SPring-8
Research Frontiers

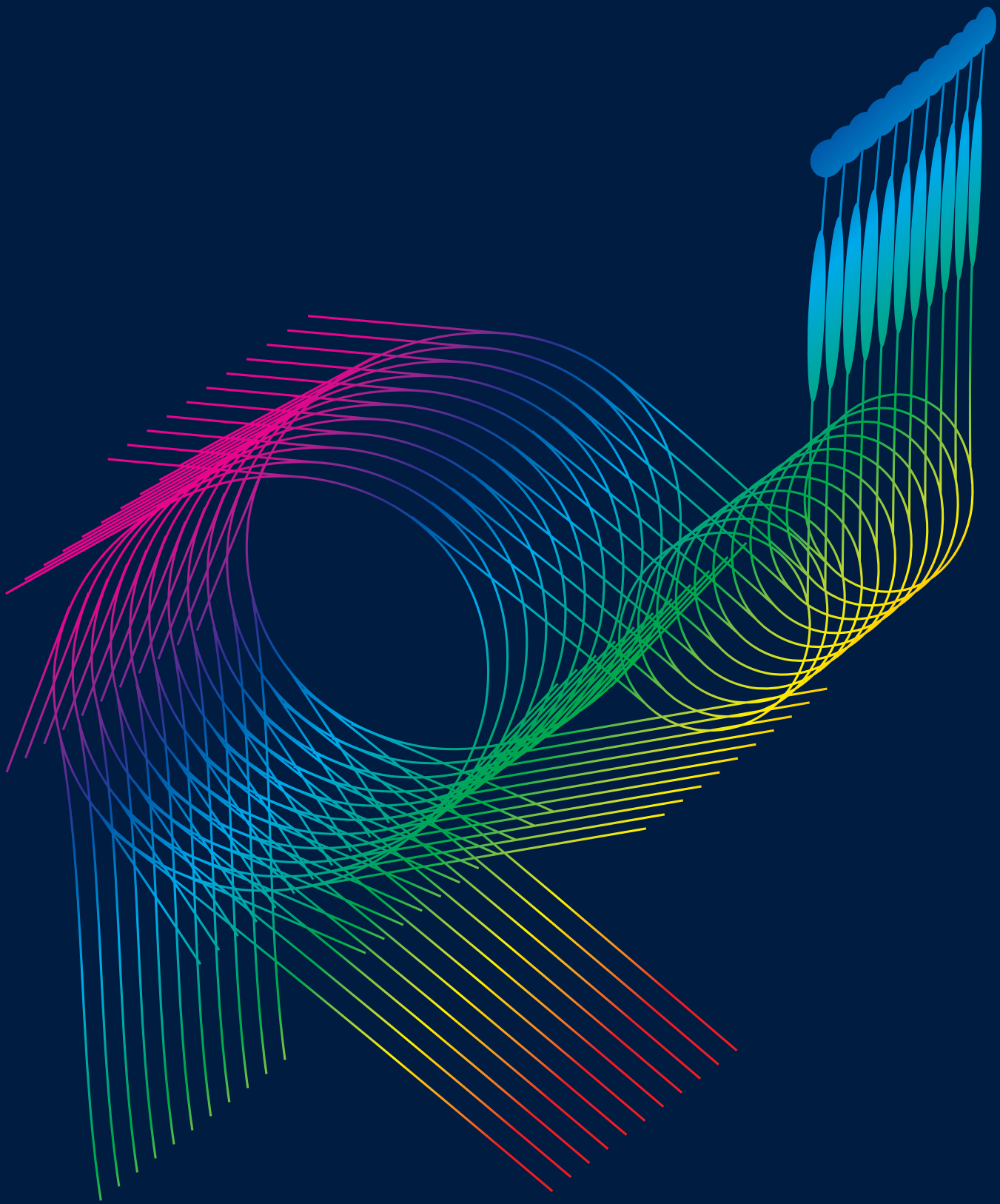

2001B／2002A

Editor's Note

SPring-8 Research Frontiers describes the outstanding scientific achievements produced at SPring-8 beamlines: public beamlines including R&D beamlines, contract beamlines, JAERI/RIKEN beamlines and an accelerator diagnosis beamline. This fifth issue "2001B/2002A" covers advances made during the two consecutive research terms, the second half of 2001 and the first half of 2002.

The number of papers published based on the research results obtained at SPring-8 has increased steadily every year. As the number of publications increased, the number of excellent papers also increased. Among the excellent results, 42 results are selected and categorized into seven research disciplines with one exception to be reported in this issue: the exception is about nuclear physics, which was obtained using -rays generated by inverse Compton scattering.

We invited seven specialists from the Proposal Review Committee to serve as the Editing Coordinators for their respective research fields:

Life Science : *Professor Masaru Tanokura* (The University of Tokyo)
Materials Science : *Professor Satoshi Sasaki* (Tokyo Institute of Technology)
Chemical Science : *Professor Inosuke Koyano* (Himeji Institute of Technology)
Earth & Planetary Science : *Professor Tetsuo Irifune* (Ehime University)
Environmental Science : *Professor Iwao Watanabe* (Osaka Women's University)
Industrial Application : *Professor Tokuhiko Okamoto* (Ritsumeikan University)
Instrumentation & Methodology : *Professor Makoto Watanabe* (Tohoku University)

We would like to express our most sincere appreciation to the Editing Coordinators for their efforts in preparing the introductory overviews and providing comments on each research field. We would also like to express our gratitude to users and facility members of SPring-8 for contributing their reports to the SPring-8 Research Frontiers.

SPring-8 Research Frontiers will be sent on request. Its full text is also available on the SPring-8 Web site (http://www.spring8.or.jp/)

CONTENTS
2001B/2002A

Preface

This issue of SPring-8 Research Frontiers contains highlights of the research results and the facility improvement at SPring-8 in its 5-th year, a period from September 2001 to August 2002. In this period, the number of publications increased steeply. SPring-8 has entered upon a phase to reap a rich harvest at many beamlines after long preparation for experiments. A government committee, which reviewed SPring-8 from the autumn of 2001 to the summer of 2002, pointed out that SPring-8 has shifted from a construction period to real utilization period.

The review committee also advised that SPring-8 should be operated in a more strategic way than it had been. In response to it, the priority policies will be applied to the beam-time allocation from the latter half of 2003. Virtually, SPring-8 has given a priority to projects, the Protein 3000 and the Nanotechnology Support, which were implemented on the basis of the government's science and technology policies.

Efforts were made to encourage the industrial applications which had not so progressed as had been expected. In November 2001, a public beamline dedicated to industrial applications in materials science started operation. It was mainly on this beamline that experiments under a Trial-Use program were conducted for industrial users who were not familiar with synchrotron radiation. Some of the results obtained in this program are included in this issue. In March 2002, a consortium of pharmaceutical companies opened a contract beamline dedicated to protein structure analysis.

I would be happy if some of the articles in this issue would stimulate readers' mind or trigger readers' new actions.

Akira Kira
Director
SPring-8 / JASRI

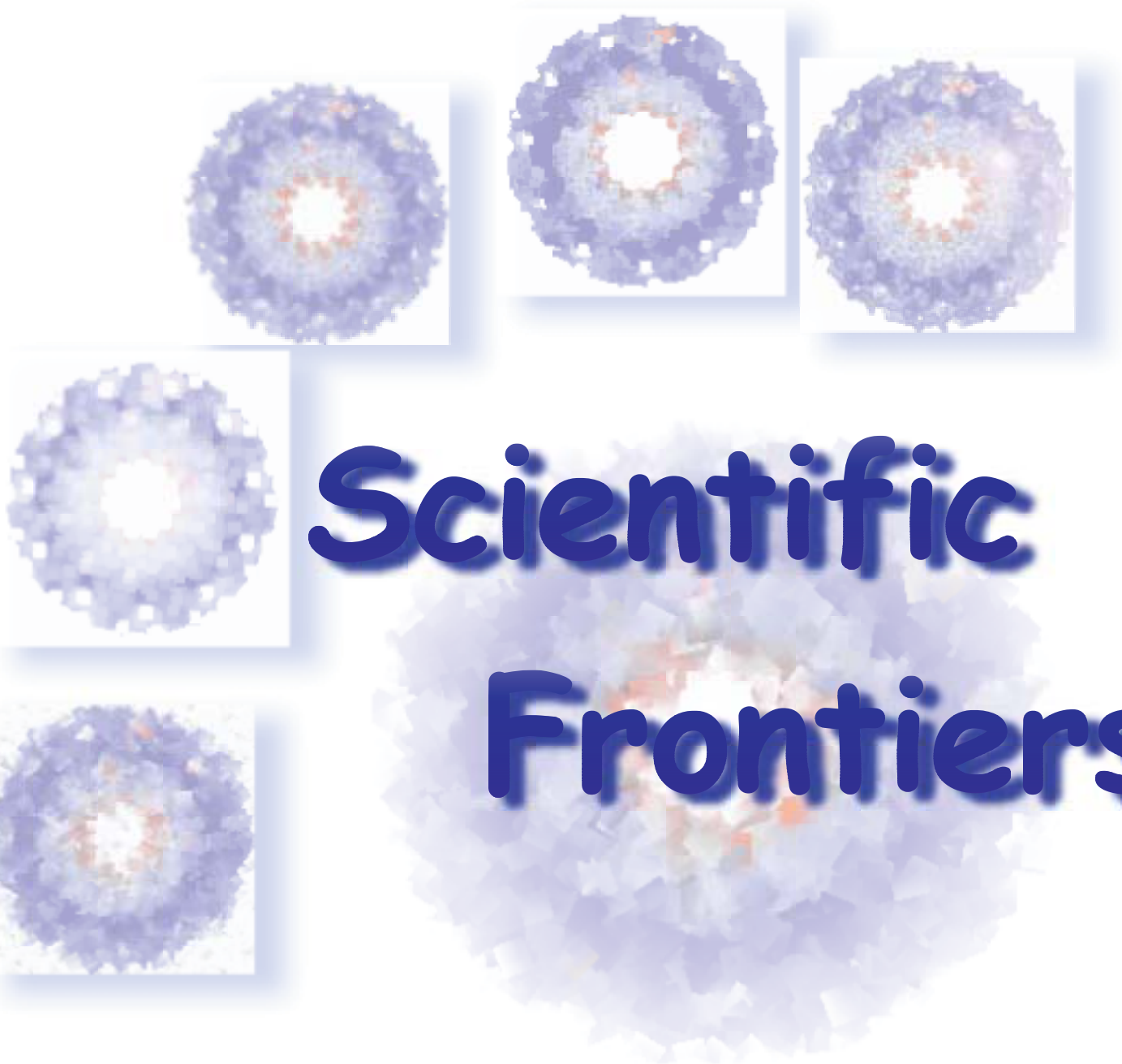

Scientific Frontiers

Life Science

SPring-8 operates several beamlines for Life Science experiments. Researchers from universities, private companies and government laboratories around the world use these facilities, and many studies not only of crystallographic, but also of biological significance, have been reported.

To data, a wide range of crystals of biological macromolecules have been analyzed at SPring-8, and their structures have been revealed. For example, the crystal structure of the xenobiotic exporter protein AcrB from *Escherichia coli*, also known as a multidrug efflux transporter, has been determined by the multiple isomorphous replacement method at BL44XU. This structure allows us to understand the molecular mechanism of efflux transportation of xenobiotics by modeling the complex structure with an outer membrane channel protein, TolC. In addition, the crystal structures of sarcoplasmic reticulum Ca^{2+}-ATPase (calcium pump) have been determined at a 2.6-Å resolution for the Ca^{2+}-bound form and at a 3.1-Å resolution for the Ca^{2+}-unbound form at BL41XU and BL44XU.

The structures of the various states of biological macromolecules are important for understanding the detailed molecular mechanisms of biological machinery. At BL45XU, the crystal structure of DNA-dependent RNA polymerase holoenzyme from *Thermus thermophilus* has been determined at a 2.6-Å resolution, and since RNA polymerase is the key enzyme of the transcription process, knowledge of the structure of the RNA polymerase holenzyme has lead to detailed elucidation of the molecular mechanism of transcription.

The crystal structure of the homologous-pairing domain of the human RAD52 protein for DNA repair ($Rad52_{1-212}$) has been determined at a 2.85-Å resolution. At BL45XU, an X-ray diffraction pattern has also been recorded from a single myofibril of muscle by generating microbeams using a pair of pinholes. This is the first example of X-ray diffraction recording from micrometer-sized hydrated, functional protein assemblies in a cell. The microfibril angle (MFA) in wood has been determined for various branch portions in Sugi, *Crypromeria japonica*, by small angle X-ray scattering (SAXS) at BL40B2. Meanwhile, at BL28B2, coronary microangiographic imaging has been carried out in isolated perfused rat heart to evaluate vascular responses.

Masaru Tanokura

X-RAY CRYSTALLOGRAPHIC ANALYSIS OF XENOBIOTIC EXPORTER PROTEINS OF *ESCHERICHIA COLI*

The xenobiotic exporter proteins, also known as multidrug efflux transporters, pump a wide variety of noxious compounds out of a cell across the cell membrane. They play an important role in multidrug resistance of pathogenic bacteria and cancer cells [1]. Genomic sequence analysis has revealed the presence of many putative xenobiotic exporter genes in chromosomes from microorganisms to mammalian cells. There are 19 transporter genes in *Escherichia coli*, which actually mediate the efflux of some drugs and toxic compounds. Among them, AcrB is constitutively expressed and is a major contributor for intrinsic drug resistance of *E. coli*. [2]. AcrB cooperates with a membrane fusion protein, AcrA, and an outer membrane channel, TolC. This AcrAB-TolC system exports an unusually wide variety of noxious compounds, *e.g.* dyes, detergents and most lipophilic antibiotics directly out of the cell, bypassing the periplasmic space driven by proton motive force. AcrB is the most important component of this system; it mediates energy coupling and determines substrate specificity (Fig. 1).

First of all we cloned a histidine-tagged AcrB into a multicopy plasmid and overproduced it in *E. coli*. Then, AcrB was solubilized and purified in the presence of a non-ionic detergent, n-dodecyl-β-D-maltopyranoside. Using the vapor diffusion method, we obtained crystals of AcrB (space group *R*32), and we employed the multiple isomorphous replacement method to solve the phase problem. A molecular model was built and refined at a resolution of 3.5 Å. All the diffraction data used for structure determination were collected at beamline **BL44XU** (Institute for Protein Research, Osaka Univ.) [3].

AcrB comprises a trimer of 1,049-residue protomers (Figs. 2(a), 2(b)), and its appearance resembles that of a jellyfish with a three-fold symmetry axis perpendicular to the membrane plane. It comprises an extra-membrane (periplasmic) headpiece approximately 50 Å × 100 Å, and a transmembrane region of dimensions 70 Å × 80 Å. The headpiece is divided into two stacked parts: the upper and lower parts are 30-Å and 40-Å thick, respectively. The side view of the upper part has a trapezoidal appearance that is ~70-Å wide at the bottom and ~40-Å wide at the top. Viewed from above, the upper part is open like a funnel, with an internal diameter of 30 Å. This funnel connected by

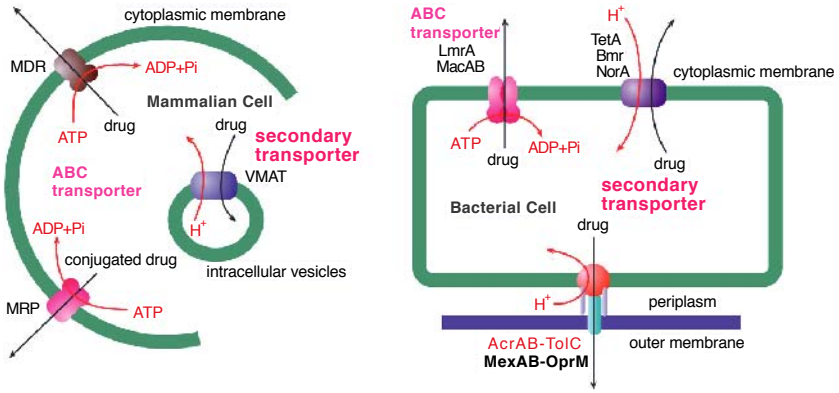

Fig. 1. Xenobiotic exporters world. A mammalian cell and a bacterial cell are illustrated.

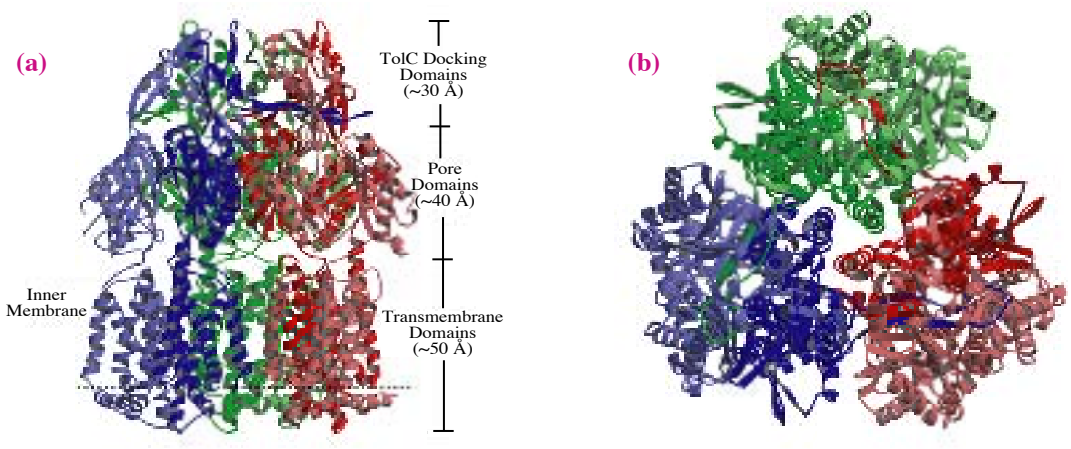

*Fig. 2. Structure of AcrB. **(a)** Side view of a ribbon representation. Three protomers are individually coloured. The N-terminal and C-terminal halves of the protomers are depicted by dark and pale colours, respectively. The extra-membrane (periplasmic) headpieces are at the top. **(b)** Top view of a ribbon representation. The protomers are individually colored as in **(a)**.*

a pore, located between the headpieces of the three protomers to a large central cavity at the interface of the headpiece and transmembrane region of the protomers. Within the membrane, the protomers are arranged like a ring with a 30-Å hole between them, which may be filled with phospholipids.

The protomers appear to be interlocked by three hairpin-like structures *ca.* 35 Å long, each protruding from one protomer into the next protomer. To achieve this mutual insertion, the protomers are tightly packed as a trimer. Between every protomer in the periplasmic domain, there are three vestibules that open wide into the periplasm and lead to the central cavity inside the headpiece, and a substrate located in the periplasmic space or on the membrane plane might gain access to the cavity through any of these vestibules (Fig. 3). The funnel opened at the top of the AcrB trimer seems to be a perfect fit for the proximal end of the TolC protein (Fig. 4(a)). The crystal structure of TolC protrudes 100 Å into the periplasm [4], thus, the sum of the periplasmic length of AcrB and TolC is ~170 Å, which is just enough to cross the periplasmic space, indicating that AcrB and TolC might direct dock with each other (Fig. 4(a)).

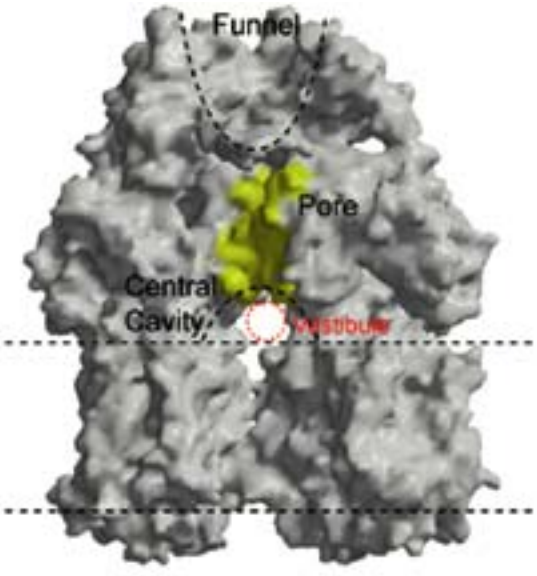

Fig. 3. A cutaway view displaying the solvent-accessible surface of AcrB. The front protomer is removed. The yellow areas of the surface are colored according to residues belonging to the pore helix.

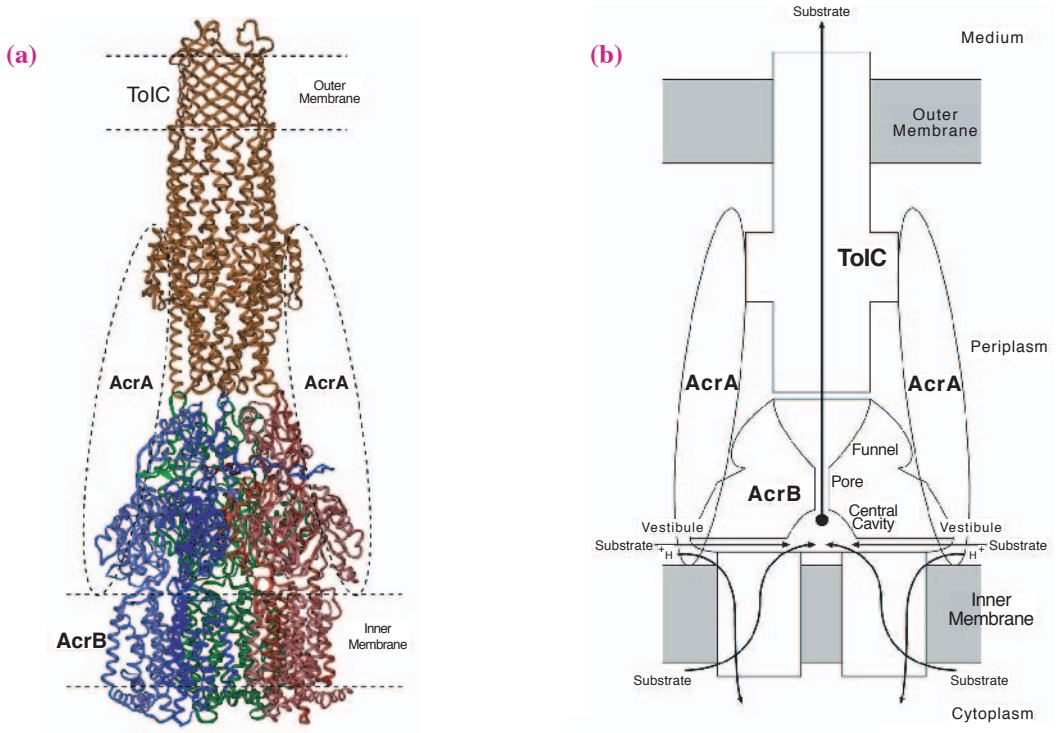

*Fig. 4. **(a)** Proposed model of the AcrB-AcrA-TolC complex. **(b)** The schematic mechanism of xenobioic export mediated by AcrAB-TolC system. The TolC structure dock with the AcrB.*

Xenobiotic substrates from the cytoplasm or inner leaflet of the membrane are transported through every protomer across the membrane and collect in the central cavity. Substrates from the periplasmic surface of the inner membrane or the outer leaflet of the membrane also gain access in the cavity through the vestibules. It appears, then, that substrates in the cavity are actively exported through the pore into the funnel and then on into the TolC tunnel.

The energy for active transport is captured in the transmembrane region and transmitted to the extra-membrane pore by a remote conformational coupling (Fig. 4(b)). This beautiful AcrB structure provides a great deal of important insight into the function of multidrug resistance mediated by xenobiotic exporters. This structure is not only the first structure of a multidrug exporter, but also the first atomic-level structure of a membrane transporter that couples with proton translocation across the membrane. Therefore, we believe that this work is a real milestone for understanding active membrane transport mechanisms based on molecular structure.

Satoshi Murakami[a,b,c], Ryosuke Nakashima[a] and Akihito Yamaguchi[a,c]

(a) Osaka University
(b) Japan Science and Technology Corporation, PRESTO
(c) Japan Science and Technology Corporation, CREST

E-mail: mura@sanken.osaka-u.ac.jp

References

[1] Okusu *et al.*, J. Bacteriol. **178** (1996) 306.
[2] Nikaido *et al.*, J. Mol. Microb. Biotechnol. **3** (2001) 215.
[3] Satoshi Murakami, Ryosuke Nakashima, Eiki Yamashita and Akihito Yamaguchi, Nature **419** (2002) 587.
[4] V. Koronakis *et al.*, Nature **405** (2000) 914.

Crystal Structure Analysis of Calcium Pump of Sarcoplasmic Reticulum

Nature uses ion gradients across cell membranes very efficiently. When cell membrane excites, ions come into cytoplasm rapidly following the ion gradients. To restore the original resting state, the ions must be pumped back. P-type ATPase is a family of ion transporting ATPases that are responsible for establishing such ion gradients. They include Na^+K^+-ATPase, sarcoplasmic reticulum (SR) Ca^{2+}-ATPase and gastric H^+K^+-ATPase among others. Of these SR Ca^{2+}-ATPase is the simplest and the best studied member. The transport is thought to be achieved by changing the binding site from high affinity and facing cytoplasm (E1 form) to low affinity and facing the extracellular side (E2 form). The reaction cycle completes by transporting another type of ion (H^+ for Ca^{2+}-ATPase) in the opposite direction. This process is called counter transport.

When muscle contracts, large amounts of Ca^{2+} stored in SR are released into muscle cells. Ca^{2+}-ATPase in the SR membrane pumps Ca^{2+} back into SR to relax muscle cells. Compared to channels, which can transfer millions of ions per second, pumps work much more slowly. Ca^{2+}-ATPase can transfer only 2 Ca^{2+} per ATP-hydrolysis or 60 Ca^{2+} per second. To make the relaxation process efficient, SR membrane is full of Ca^{2+}-ATPase (more than 60% of the proteins in SR membrane). Therefore, Ca^{2+}-ATPase is one of the most suitable membrane proteins for structural studies. Also, because Ca^{2+} is the most ubiquitous factor for regulation of cellular processes, elucidation of the mechanism of Ca^{2+}-ATPase has tremendous importance in both biological and medical aspects.

We have been working on this ATPase using X-ray crystallography and determined its structure to

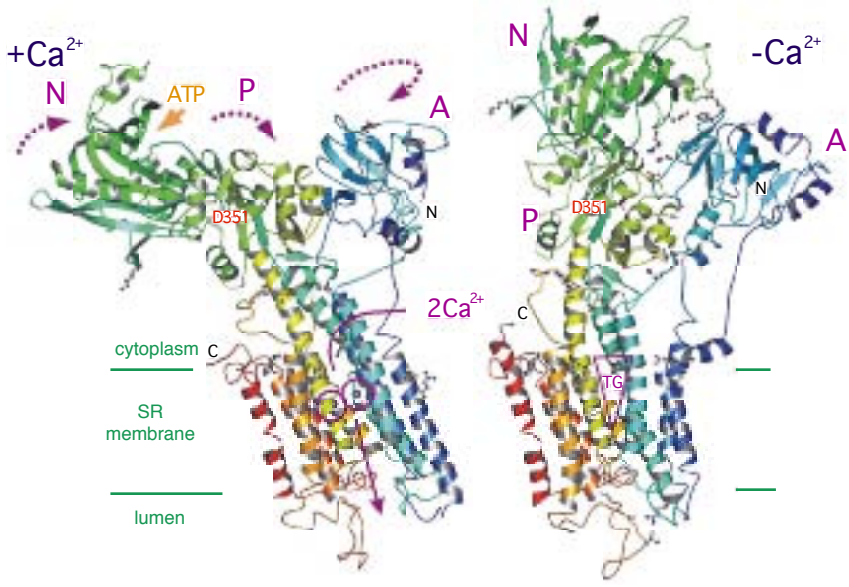

Fig. 1. Structural changes in sarcoplasmic reticulum Ca^{2+}-ATPase accompanying the dissociation of Ca^{2+}. Colour changes gradually from the N terminus (blue) to the C terminus (red). Two purple spheres in the membrane domain represent bound Ca^{2+} ions. Adenosine moiety of ATP binds to the N-domain, whereas the catalytic site (phosphorylation site) Asp351 is located in the P-domain. The binding sites for thapsigargin (TG, a potent inhibitor) is also shown.

2.6 Å resolution for the Ca^{2+}-bound (E1 Ca^{2+}) form [1] and to 3.1 Å resolution for a Ca^{2+}-unbound (E2(TG)) form stabilized by thapsigargin, a very potent inhibitor [2] (Fig. 1). Diffraction data from the E2(TG) crystals were collected at beamline **BL44XU** using imaging plates of 4000 × 4000 pixels. This was essential because one dimension of the unit cell was as large as 600 Å, yet the diffraction spots went out to 3.0 Å resolution.

SR Ca^{2+}-ATPase consists of a single polypeptide chain of 110 kDa. It comprises 3 (A, N and P) cytoplasmic domains and 10 transmembrane α-helices. The differences in structure between the Ca^{2+} -bound and unbound forms are global and very large (Fig. 1). In the transmembrane region, complicated movements of transmembrane helices are observed. In particular, it is surprising to see large (~ 5.5 Å) movements of the M3 and M4 helices normal to the membrane (Fig. 2). Because the M4 helix is a key component of the transmembrane Ca^{2+}-binding sites (Fig. 3), it is clear that such piston-like movements will abolish the binding of Ca^{2+} at site II. Also, the unwound part of M6, another key helix in Ca^{2+} coordination, rotates nearly 90 ° to destroy site I (Fig. 3). It is not obvious why such large movements of the transmembrane helices are necessary. Homology modelling of the cation binding sites of a related pump, Na^+K^+-ATPase, suggests that such movements are required for assuring the release of one type of ion and binding of the other type of ions that are counter-transported at the same time [3].

All three cytoplasmic domains show very large domain movements, keeping the structure of each domain virtually unchanged. In the Ca^{2+}-bound form, they are widely separated but gather to form a compact headpiece in the Ca^{2+}-unbound form.

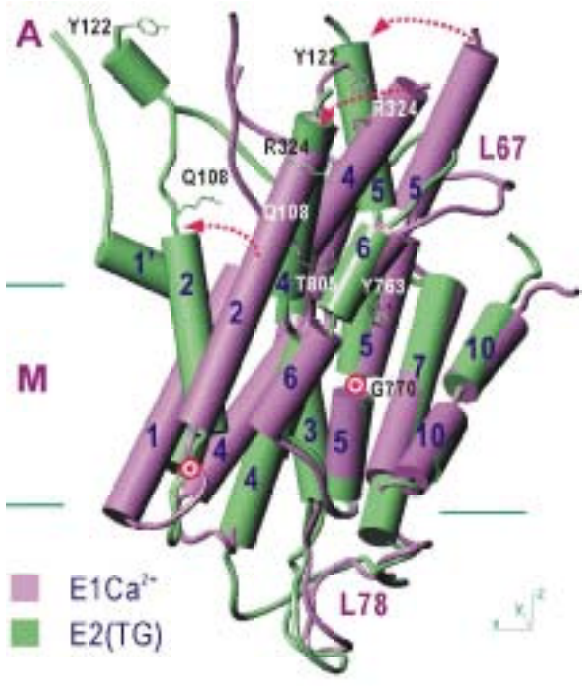

Fig. 2. Rearrangement of transmembrane helices viewed from the side opposite to Fig. 1. Cylinders represent α-helices. Double circles show pivot positions for the M2 and M5 helices. Arrows indicate the directions of movements during the change from Ca^{2+}-bound to unbound form.

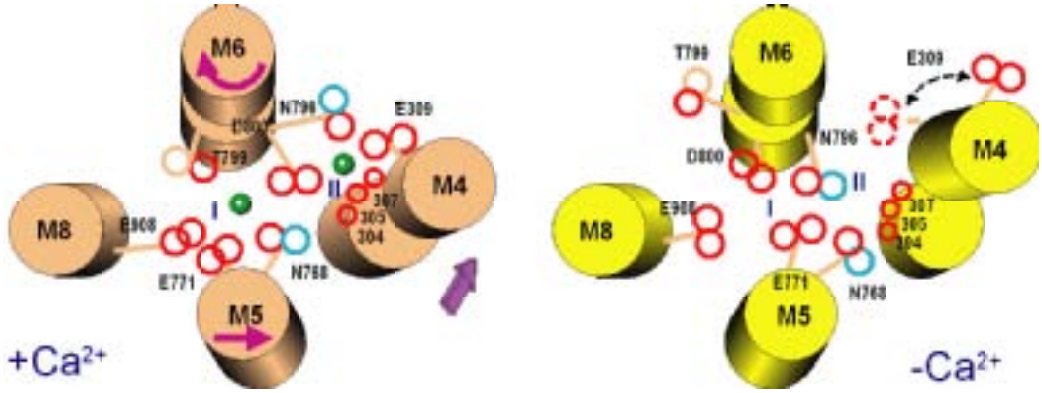

Fig. 3. Schematic diagram of the Ca^{2+}-binding sites of the Ca^{2+}-ATPase in the Ca^{2+}-bound and unbound forms. The arrows in the left panel ($+Ca^{2+}$) show the directions of movements accompanying the dissociation of Ca^{2+}. Oxygen atoms are shown in red, nitrogen in cyan, carbon in orange. Ca^{2+} ions are thought to enter into the binding sites through E309. First Ca^{2+} binds to site I and the second to site II. The binding of the second Ca^{2+} causes conformation changes that result in the hydrolysis of ATP.

Obviously these movements are linked with those of the transmembrane helices. Since no ATP or phosphorylation is required for transition between these two states, thermal energy must be able to cause such large movements. The close association of the 3 cytoplasmic domains will restrict the thermal movements of the transmembrane helices, and will limit the delivery of ATP to the catalytic site in the P-domain (D351 in Fig. 1).

Chikashi Toyoshima and Hiromi Nomura

The University of Tokyo

E-mail: ct@iam.u-tokyo.ac.jp

References

[1] C. Toyoshima, M. Nakasako, H. Nomura and H. Ogawa, Nature **405** (2000) 647.
[2] C. Toyoshima and H. Nomura, Nature **418** (2002) 605.
[3] H. Ogawa and C. Toyoshima, Proc. Natl. Acad. Sci. USA. **99** (2002) 15977.

Crystal Structure of a Bacterial RNA Polymerase Holoenzyme at 2.6 Å Resolution

The DNA-dependent RNA polymerase (RNAP) is the key enzyme of the transcription process, and is a final target in many regulatory pathways that control gene expression in all living organisms. Bacterial RNAP exists in two forms: core and holoenzyme. The core enzyme (~ 400 kDa) consists of five subunits: α-dimer(α2), β, β', and ω. The transcription cycle in bacterial cells can be divided into three major stages: initiation, elongation, and termination. Although it is catalytically active, the core enzyme is incapable of initiating transcription efficiently and with specificity. For this, it must bind an initiation factor, σ, to form a holoenzyme that can recognize specific DNA sequences (promoters) [1,2]. During initiation, the holoenzyme specifically binds to two conserved hexamers in the promoter at nucleotide (nt) positions –35 and –10 relative to the transcription start site (+1), to form a closed promoter complex. Then, it unwinds the double-stranded DNA around the –10 region (between nt –12 and +2), resulting in the open promoter complex, and initiates transcription in the presence of nucleoside triphosphate substrates [3]. After the synthesis of a 9 - 12 nt-long RNA, of which 8 - 9 are base-paired with the DNA template strand (RNA-DNA hybrid), the transcription complex passes from the initiation to elongation stage [4]. This transition is characterized by the escape of the RNAP from the promoter, the dissociation of σ from the core, and the formation of a highly processive ternary elongation complex. The σ-factor plays a key role in initiation, being directly involved in promoter recognition, DNA melting, and promoter escape and clearance [2]. The family of related σ proteins shares four regions of sequence homology, designated 1 to 4, which are further divided into several subregions [5]. The regions 4.2, 2.3 - 2.4, and 2.5 were shown to recognize the –35, –10, and the so-called "extended –10" elements of the promoter, respectively.

We have determined the crystal structure of the *T. thermophilus* RNAP holoenzyme, containing the major σ-factor (σ70), at 2.6-Å resolution (Fig. 1) at beamline **BL45XU**. The σ70 subunit is located almost entirely on the core surface, except for a short segment (σ313 - 342), which is buried within the core molecule. The modeled structure of σ70

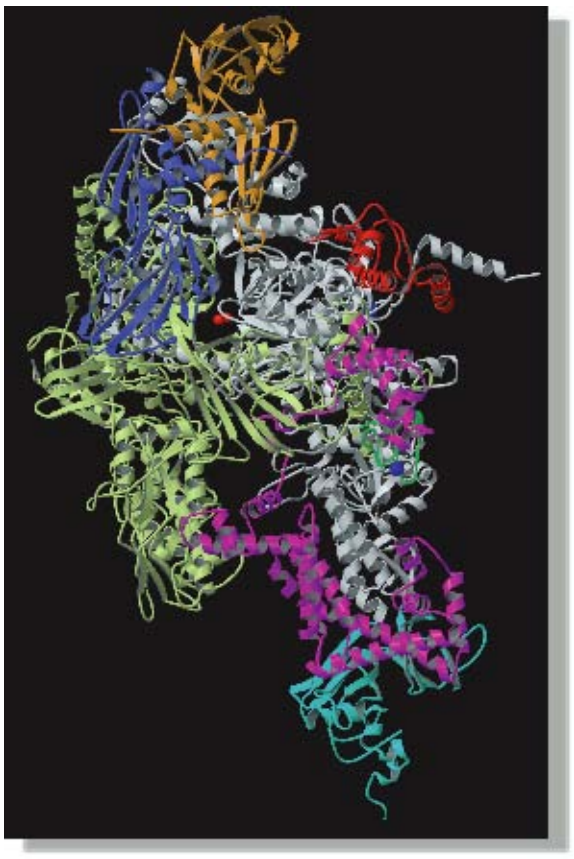

Fig. 1. Holoenzyme crystal structure. The subunits colors are: β, sage; β', white (β'163-452, cyan; β' Zn-finger, green); αI, blue; αII, light orange; σ, magenta; and ω, red. Two catalytic Mg^{2+} (red) and two Zn^{2+} ions (blue) are shown as spheres.

consists entirely of α-helices connected by either turns or loops, and it can be divided into four structural domains: N-terminal domain 1 (ND1), N-terminal domain 2 (ND2), linker domain (LD), and C-terminal domain (CD) (Fig. 2).

ND1 consists of eight α-helices (σ74-254) comprising four helix-turn-helix motifs (HtH). This domain encompasses region 1.2 up to the N-terminal half of region 2.4, including the non-conserved segment between regions 1 and 2. ND1 has a U-shaped structure, and is connected to ND2 (σ261 - 312) by a short linker loop (σ255 - 260), That lies at the C-terminus of region 2.4. ND2, corresponding to conserved regions 2.4 - 2.5 and 3.1, consists of three α-helices that fold into an α-helical bundle. The C-terminal helix of ND1 and the N-terminal helix of ND2 (σ234 - 281) form a V-shaped structure near the opening of the upstream DNA binding channel, which is likely to be a binding site for the –10 element of promoter. The 30 residue-long "linker" domain, LD (σ313 - 339), intervenes between the globular N- and C-terminal portions of σ and has a mostly extended, unfolded conformation. Roughly at its midpoint, LD forms a hairpin loop (σ318 - 329) that protrudes into the active site cleft. The C-terminal domain, CD (σ340

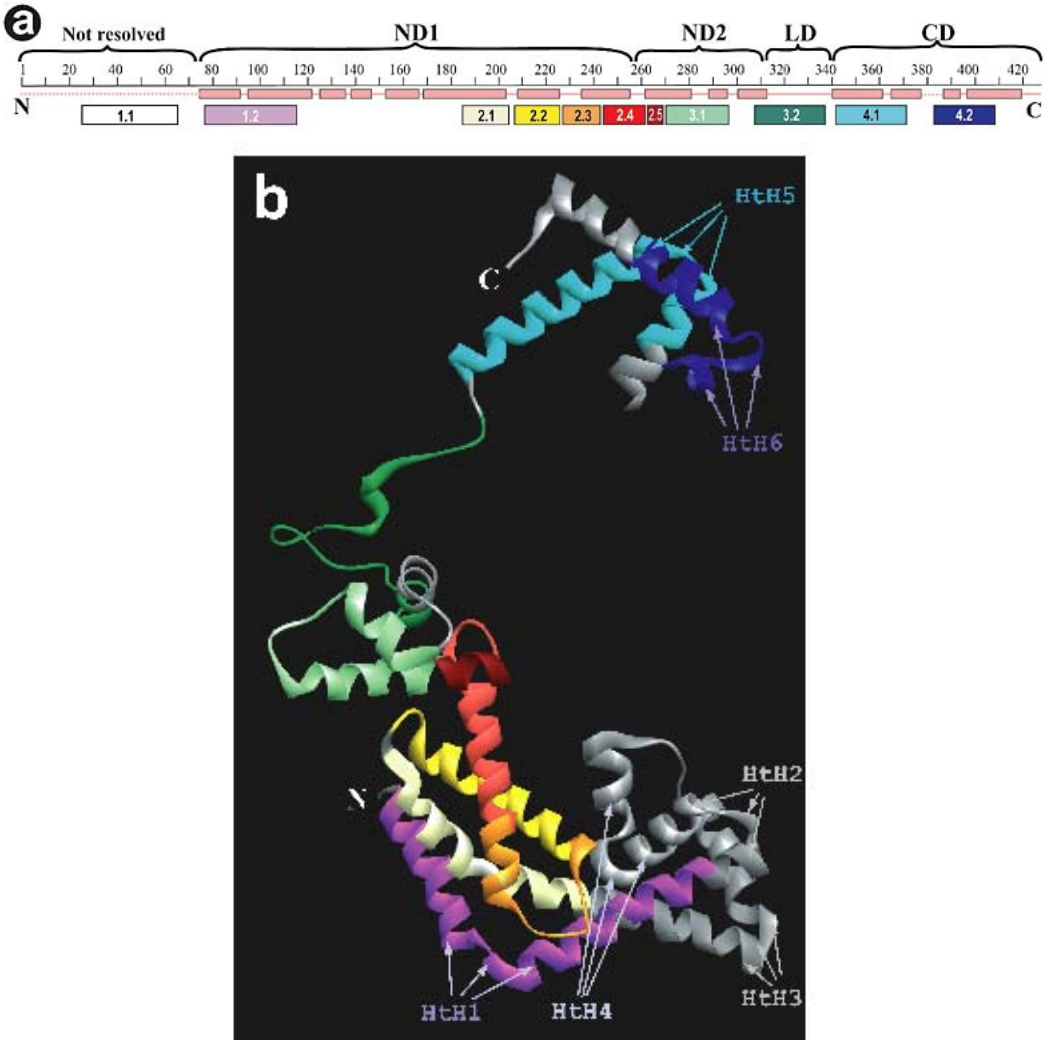

*Fig. 2. σ domain organization and structure. (**a**) Scheme of structural domains and conserved regions. (**b**) Ribbon diagram of σ. The color coding is the same as in (**a**) except for the non-conserved regions (grey).*

- 423), which includes conserved regions 4.1 and 4.2, contains four α-helices, which are arranged as a pair of HtH motifs. This site is about 57 Å from the N-terminal half of the protein, containing regions 2.3 - 2.5, that allows unambiguous modeling of promoter bound to the holoenzyme (Fig. 3).

In the holoenzyme, certain σ structural elements greatly reduce the available space in the functionally important protein cavities and channels that accommodate promoter DNA, RNA-DNA hybrid, and RNA product. Thus, the holoenzyme structure additionally restrains possible orientations and conformations of the nucleic acids in the transcription intermediates, allowing better understanding of various steps of transcription initiation.

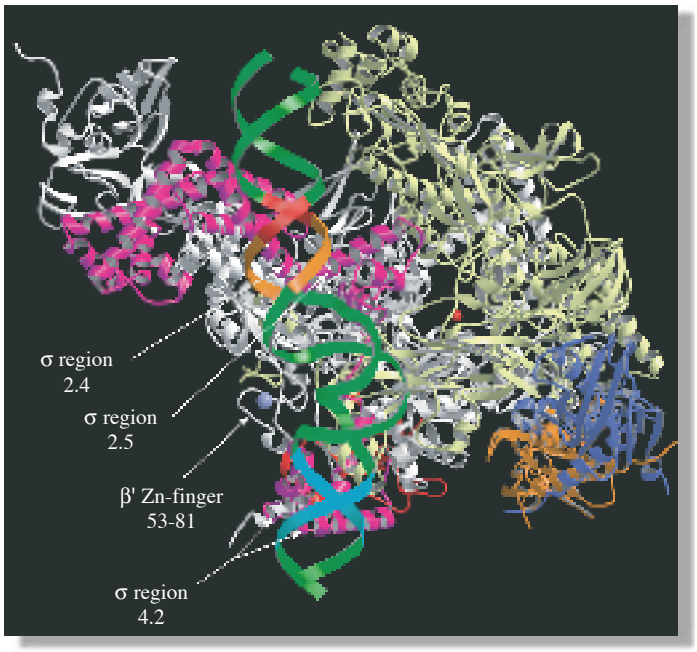

*Fig. 3. Modelling of the holoenzyme/closed promoter complex. The protein colour coding is the same as in Fig. 1(**c**), except all of β' is shown in white. The dsDNA (green) contains the –35 (cyan), –10 (red), extended –10 (orange) promoter regions. The Mg^{2+} (red) and Zn^{2+} (blue) ions are shown as spheres.*

Dmitry G. Vassylyev[a], Sergei Borukhov[b] and Shigeyuki Yokoyama[a,c,d]

(a) SPring-8 / RIKEN
(b) SUNY Health Science Center, USA
(c) RIKEN Genomic Sciences Center
(d) The University of Tokyo

E-mail: dmitry@yumiyoshi.harima.riken.go.jp

References

[1] R.R. Burgess *et al.*, Nature **221** (1969) 43.
[2] C. Gross *et al.*, Transcriptional Regulation (eds S.R. McKnight & K.R. Yamamoto) - Cold Spring Harbor Laboratory Press, Cold Spring Harbor (1992) 129.
[3] M.T.J. Record *et al.*, *Escherichia coli* and *Salmonella* (ed F.C. Neidhart) - ASM Press, Washington, D.C. (1996) 792.
[4] P. von Hippel, Science **281** (1998) 660.
[5] M. Lonetto *et al.*, J. Bacteriol. **174** (1992) 3843.

Crystal Structure of the Homologous-pairing Domain of the Human Rad52 Protein

A DNA break that remains unrepaired is lethal for any cell. Double strand breaks occur in cells exposed to ionizing radiation and chemotherapeutic agents, or naturally by replication errors and oxygen radicals generated from respiration. To repair such lesions, cells have developed efficient homologous recombinational repair systems. In budding yeast, the RAD52 epistasis group genes (*RAD51*, *RAD52*, *RAD54*, *RAD55*, *RAD57*, *RAD59*) play central roles in homologous recombination and are conserved among eukaryotes. Rad52, a key member of this group, displays two critical activities that have been demonstrated in vitro: homologous pairing and interaction with the Rad51 recombinase. These activities are likely to be essential for the initiation of homologous recombination, although no detailed molecular mechanisms are currently available.

The human Rad52 protein consists of 418 amino acid residues, and we, as well as others, have found that the N- and C-terminal halves of this protein have distinct roles in recombination. The N-terminal half of Rad52 (about 200 amino acid residues) is highly conserved among Rad52 homologs, and this region composes a structurally stable domain as suggested from limited proteolysis experiments [1]. The isolated, N-terminal domain of Rad52 binds to single-stranded DNA (ssDNA), and has homologous-pairing activity equivalent to that of the full-length protein [1]. Interestingly, alternative-splicing variants containing only the N-terminal half of Rad52 were found in humans, indicating that the isolated, N-terminal domain of Rad52 has a role in recombination [2]. The C-terminal half, by contrast, is poorly conserved among Rad52 homologs. This region physically interacts

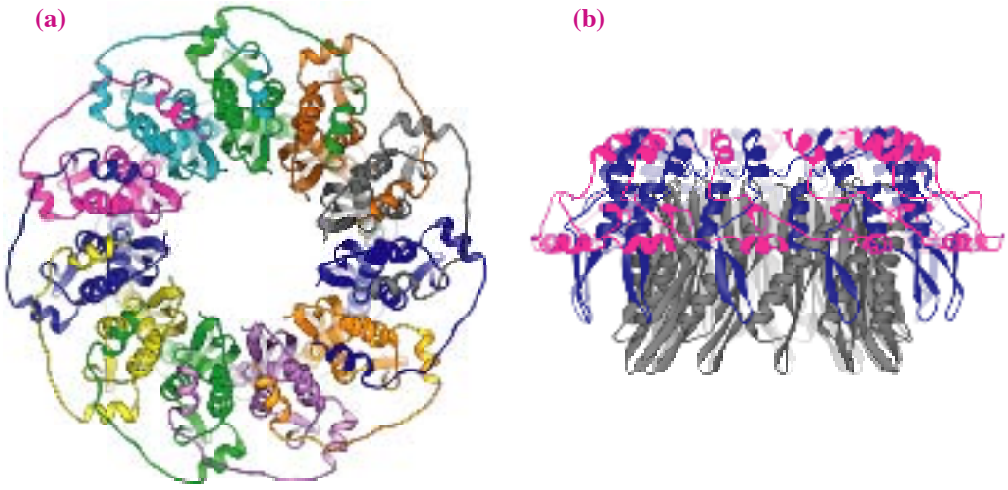

*Fig. 1. The structure of $Rad52_{1-212}$. **(a)** Ribbon diagram of the undecameric ring of $Rad52_{1-212}$, viewed down the central channel from the top of the domed cap. **(b)** The ring viewed from the side. The domed cap region is coloured in blue and magenta, and the stem region is coloured in grey. The diameter of the ring is about 120 Å, and that of the central channel is about 50 Å at the narrowest point.*

with the Rad51 recombinase [1], and may have an important role in the recombination mediated by Rad52 and Rad51. Therefore, the N-terminal half is present in both the longer (full-length) and shorter (alternative splicing variant) forms of Rad52, whereas the C-terminal half is only present in the longer form of Rad52.

To gain insight into the mechanism of homologous-pairing promoted by Rad52, the N-terminal fragment ($Rad52_{1-212}$) containing the homologous-pairing domain was designed, and crystals of this fragment were prepared for structural analyses. Data from both the native and selenomethionine-substituted $Rad52_{1-212}$ crystals were collected at the RIKEN Structural Biology beamline I (**BL45XU**), and the structure was determined by the multi-wavelength anomalous dispersion (MAD) method at 2.85 Å resolution [3]. The crystal structure of $Rad52_{1-212}$ revealed an undecameric ring, indicating that the shorter form of Rad52 is undecameric. The overall structure resembles a mushroom with a stem and a domed cap region (Fig. 1).

$Rad52_{1-212}$ has an exposed groove around the entire ring structure. This groove encircles the stem region, and is highly positive in charge, as determined from the surface potential calculations (Fig. 2). The groove has an approximate width of 10 Å and an appropriate size to accommodate ssDNA. To identify the precise DNA binding site, the basic and aromatic amino acid residues on the positively charged surface, which have the potential to interact directly with ssDNA, were replaced with alanine by site-directed mutagenesis (Fig. 3(a)). These mutants were then tested for ssDNA binding. The mutations of Arg55, Tyr65, Lys152, Arg153, and Arg156, with side chains inside the groove, clearly decreased the ssDNA binding activity (Fig. 3(b)). Therefore, the shorter form o Rad52 fits ssDNA inside the exposed groove, and wraps ssDNA around the stem region.

In contrast to the shorter form, our sedimentation equilibrium studies on the longer form of Rad52 demonstrated that the protein is heptameric in solution. Previous electron microscopic studies also concluded that Rad52 forms a heptameric ring [4]. Interestingly, the two ring forms have similar

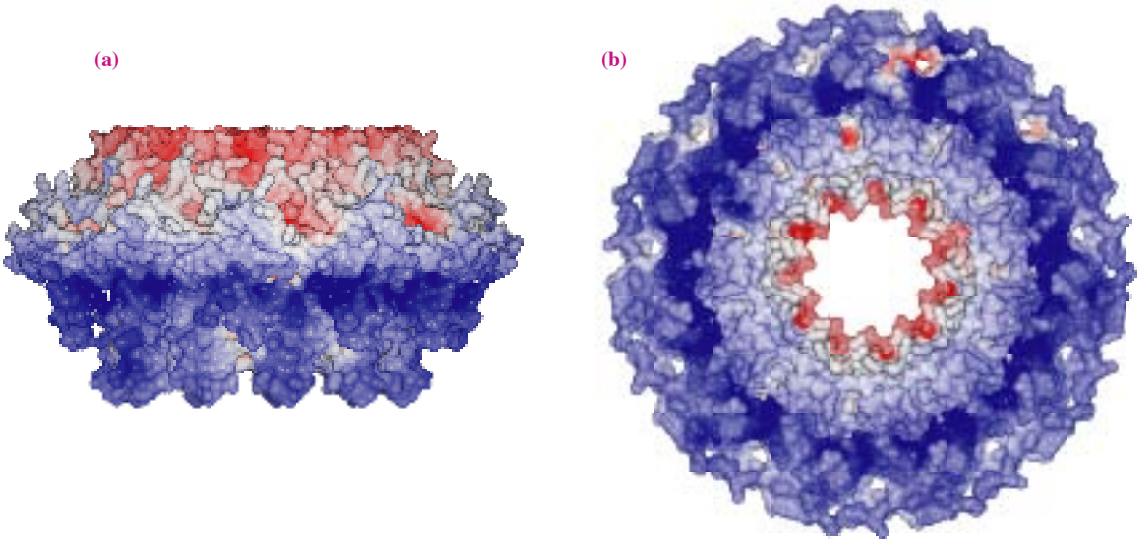

*Fig. 2. Side (**a**) and bottom (**b**) view of the surface of $Rad52_{1-212}$. The surface is coloured according to the electrostatic potential. (red) $-12\ k_BT^{-1}$ to (blue) $12\ k_BT^{-1}$.*

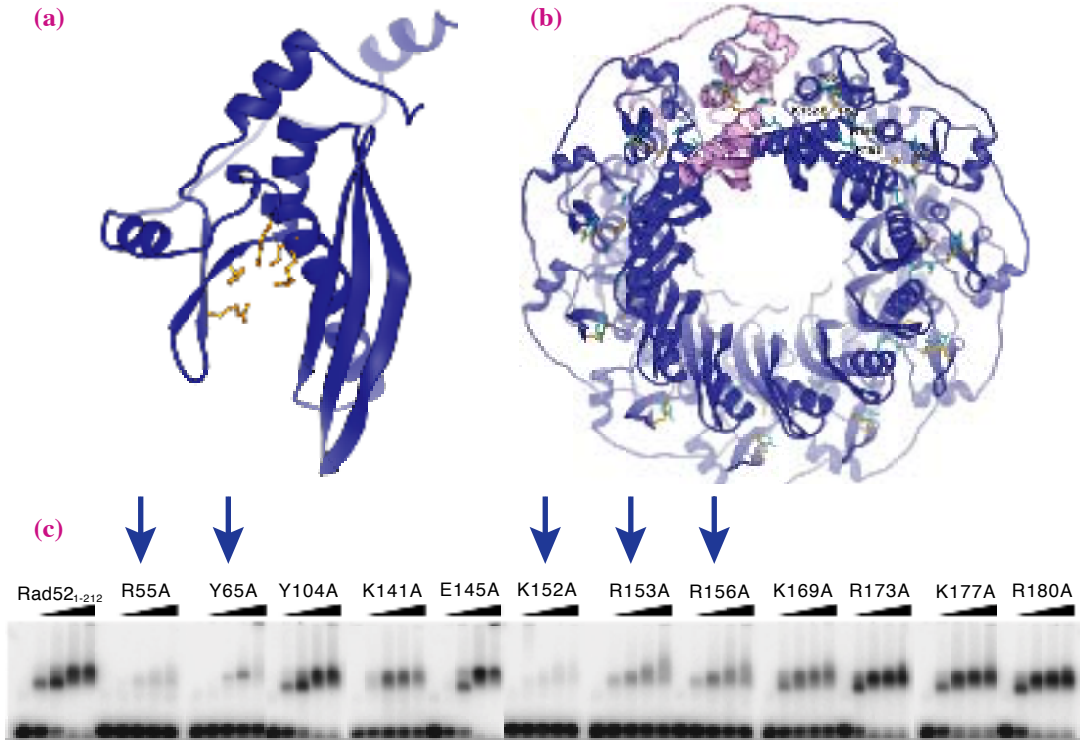

*Fig. 3. Mutagenesis and ssDNA binding. **(a)** Amino acid residues (coloured in yellow) essential for ssDNA binding mapped on the Rad52$_{1-212}$ monomer. **(b)** The residues essential for ssDNA binding are located inside the groove. **(c)** Gel shift assay of the Rad52$_{1-212}$-ssDNA complexes. The ssDNA binding was analyzed by 1% agarose gel electrophoresis.*

diameters, which allowed us to model the heptameric ring using the crystal structure of Rad52$_{1-212}$ (Fig. 4). In the resulting heptamer model, a positively charged DNA groove is present, suggesting that the groove for DNA binding is conserved in both ring forms. This is consistent with the similar ssDNA binding and homologous-pairing activities of the longer and shorter forms of Rad52 [1].

In conclusion, the crystal structure of Rad52$_{1-212}$ revealed that the homologous-pairing domain of Rad52 is organized into a ring with a circular groove essential for ssDNA binding. Mutagenesis studies demonstrated that ssDNA binds to Rad52 by wrapping around the ring structure. Both ring forms are capable of promoting homologous pairing, suggesting that ring formation is essential for the activity. On the other hand, only the heptameric form of Rad52 can interact with the Rad51 recombinase through the C-terminal half, which was predicted to be located between the monomers in the heptamer model. The two ring forms of Rad52 could be involved in different recombination pathways. The shorter form, which lacks the Rad51-interacting region, may function in recombination pathways that are independent of Rad51. By contrast, the longer form could function in Rad51-dependent recombination pathways. In both cases, our results suggest that the N-terminal half of Rad52 promotes homologous pairing in the DNA binding groove around the ring structure.

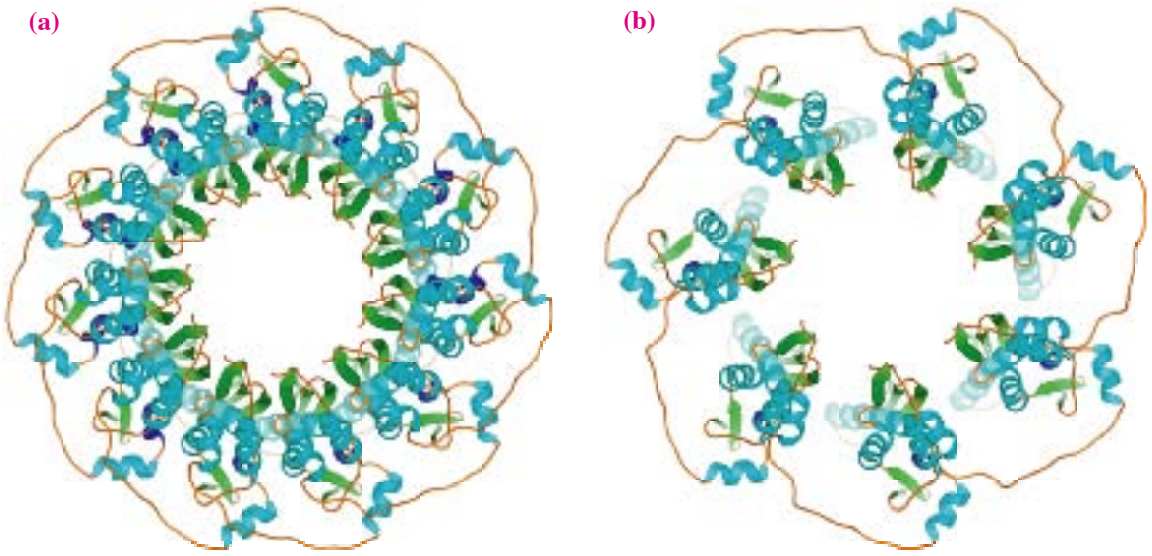

*Fig. 4. Heptamer model of Rad52. The heptameric ring of the longer form was modeled by simply removing four monomers from the undecameric ring (**a**), and spacing the remaining seven monomers evenly, without changing the diameter of the ring (**b**).*

Wataru Kagawa[a,c] , Hitoshi Kurumizaka[a,b] and Shigeyuki Yokoyama[a,b,c]

(a) RIKEN Genomic Sciences Center
(b) RIKEN Cellular Signaling Laboratory
(c) The University of Tokyo

E-mail: kurumi@jota.gsc.riken.go.jp

References

[1] W. Kagawa *et al*., J. Biol. Chem. **276** (2001) 35201.
[2] K. Kito *et al*., Biochim. Biophys. Acta **1489** (1999) 303.
[3] W. Kagawa, H. Kurumizaka, R. Ishitani, S. Fukai, O. Nureki, T. Shibata, and S. Yokoyama, Mol. Cell **10** (2002) 359.
[4] A. Z. Stasiak *et al.*, Curr. Biol. **10** (2000) 337.

X-ray Diffraction Pattern Recorded from a Single Myofibril of Muscle

Muscle contraction is caused by the interaction between two major contractile proteins, myosin and actin, within muscle cells. In striated muscle, these proteins are polymerized and form filaments with regular helical repeats, and these filaments are in turn arranged in a regular hexagonal lattice. Because of this architecture, a striated muscle gives rise to a number of strong reflections when irradiated with X-ray beam, making X-ray diffraction method a powerful tool to study the molecular mechanism of muscle contraction.

The structure of a striated muscle is shown in Fig. 1. A striated muscle is made of many muscle cells (diameter, 50 - 100 μm; length, millimeters to centimeters). Each muscle cell contains thousands of myofibrils (diameter, 1 - 3 μm). A myofibril is made of 2 - 3 μm-long sarcomeres (minimal functional unit of muscle) connected in series. A sarcomere contains a single hexagonal lattice of protein filaments as described above.

The strongest reflections of muscle, called equatorial reflections, originate from the hexagonal arrangement of filaments. Since a muscle contains an enormous number of myofibrils with random lattice orientations, the recorded diffraction pattern is basically a rotary-averaged "powder diffraction pattern (a diffraction pattern that would be recorded from ground powder of mineral crystals)", from which information about the lattice plane orientations is lost. This problem cannot be solved by the use of a single muscle cell, since it still contains a large number of myofibrils. The only solution to preserve that crucial information is to record diffraction patterns from a single myofibril, which is only 1/1000 by volume of a muscle cell, the smallest muscle specimen which has been used for X-ray diffraction studies.

The strategy was not to isolate a single myofibril from a muscle cell, but to generate X-ray microbeams by using a pair of pinholes (diameter, 2 μm) and to shoot at a single myofibril within a muscle cell without isolating it (Fig. 2). Unlike in conventional recording, the muscle cell was irradiated end-on so that the beam would pass through only one myofibril if ideally aligned. As a material, the flight muscle of an insect (bumblebee) was chosen because its myofibrils were well separated from each other and its filament lattices were of crystal quality.

Figure 3 shows representative diffraction patterns from the insect flight muscle [1] recorded in this way at beamline **BL45XU** [2]. The pattern obtained with 50-μm pinholes consists of a number of concentric circles typical of powder diffraction, since there are still many myofibrils in the beam-path

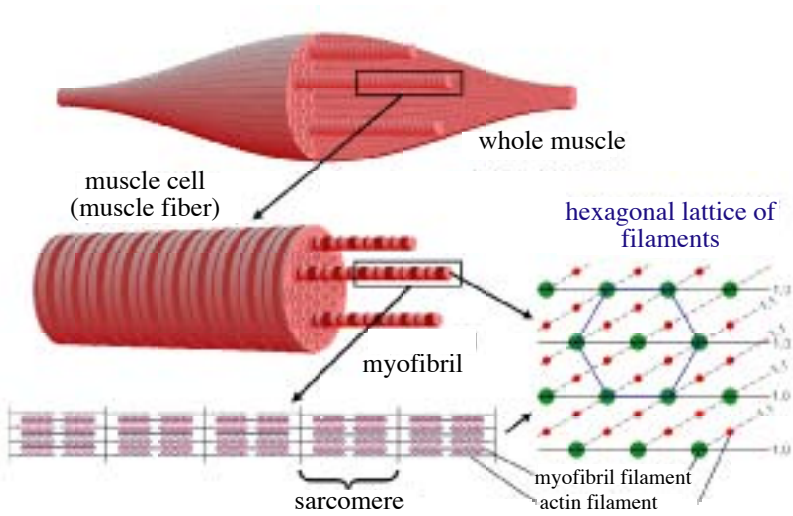

Fig. 1. Structure of vertebrate striated muscle.

(Fig. 3(a)). If, on the other hand, 2-μm pinholes are used, the reflections are spot-like and arranged in a hexagonally symmetrical fashion. These patterns are what is expected from a single hexagonal lattice. The lattice plane from which each reflection originates can be readily identified.

The muscle cells used to record the diffraction patterns were ~3 mm long, and the well-defined spot-like reflections mean that the lattices of more than 1000 sarcomeres were exactly in register; a 0.1° twist in every sarcomere would reduce the pattern to a powder diffraction as in Fig. 3(a). This extraordinary register of filament lattice could be beneficial in transmitting force effectively in the flight muscle of the insect, which exhibits sophisticated flight maneuver.

The present results represent the first example of X-ray diffraction recording from micrometer-sized hydrated, functional protein assemblies within a cell. Cells contain a variety of regular protein assemblies other than myosin-actin contractile machinery, and the success of the present recording opens the possibility that X-ray diffraction technique can also be applied to study the structure of these minute cellular protein assemblies.

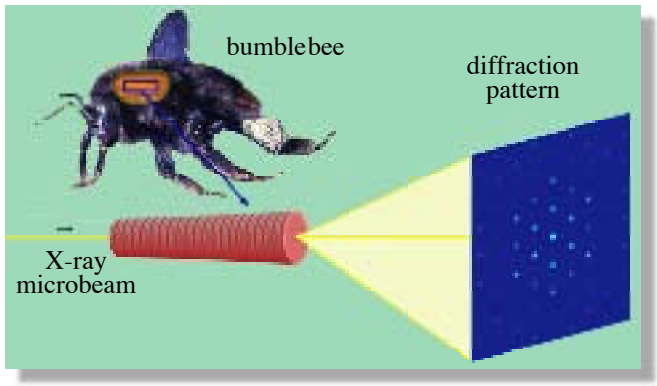

Fig. 2. Schematic diagram of recording an end-on diffraction pattern from a single myofibril in a flight muscle cell of a bumblebee.

Hiroyuki Iwamoto

SPring-8 / JASRI

E-mail: iwamoto@spring8.or.jp

References

[1] H. Iwamoto, Y. Nishikawa, J. Wakayama and T. Fujisawa, Biophys. J. **83** (2002) 1074.
[2] T. Fujisawa *et al.*, J. Appl. Cryst. **33** (2000) 797.

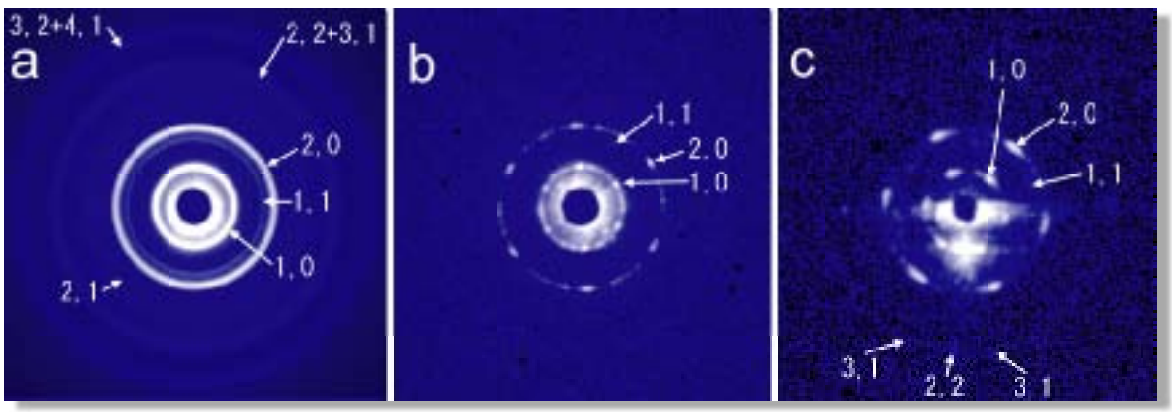

*Fig. 3. End-on diffraction patterns recorded from bumblebee flight muscle. **(a)** A pattern recorded with 50 μm pinholes. **(b, c)** Patterns recorded with 2-μm pinholes. The numbers indicate the crystallographic indices of lattice planes.*

Microfibril Angle in Wood and its Biological Significance

Cedars, firs, larches, pines and spruces belong to the order Coniferales or softwoods, which are important as lumber and as raw material. Sugi, *Cryptomeria japonica* is a unique genus, and is adapted so well to our climate that it has become one of the most planted species in Japanese forests.

Wood is a cellular composite that consists of many hollow fibrous cells primarily aligned parallel to the trunk or branch (Fig. 1). Cells are produced by cell division in the vascular cambium, a thin layer of cells located concentrically underneath the bark. The cambium produces bark towards the outside and wood towards the inside of the tree. In the temperate zone, the earlywood is formed in spring and the latewood formed at the end of the growing season. Thus the growth ring, an annual ring in this case, appears as a result of such cambial activity. Most of the cells remain as cell walls, which were once living tissue. Each cell wall is multi-layered, in which the cellulose microfibrils are encrusted by hemicellulose and lignin to achieve a so called fiber-reinforced structure.

Tracheids comprise 95% of cells in softwoods. The cell walls contain several sub-layers of cellulose microfibrils, variously oriented, and are divided into primary and secondary walls. Primary walls are formed during cell elongation, while secondary walls are formed subsequently. The microfibrils are highly ordered bundles of cellulose chains (the crystal modulus along fiber axis is greater than 100 GPa) that give strength and stiffness to the cell wall. The microfibrils in the middle layer of the secondary wall S_2 (approx. 80% of the thickness) form a right-handed spiral which makes an angle with the cell axis called the microfibril angle, MFA.

Obviously, the MFA has a strong correlation with wood quality as well as with the physicomechanical function of a tree. When a tree is young, it needs to be elastic in order to move in the wind. After some decades, however, the cells produced by mature trunk cambium have a smaller MFA for stiffness and for keeping the trunk upright. By contrast, branches have to be rather elastic, allowing them to bent with the weight of snow and shed it. Therefore, MFA needs to be larger. The MFA is thus critical to the total mechanical balance of the tree, and correct MFAs are essential for its survival.

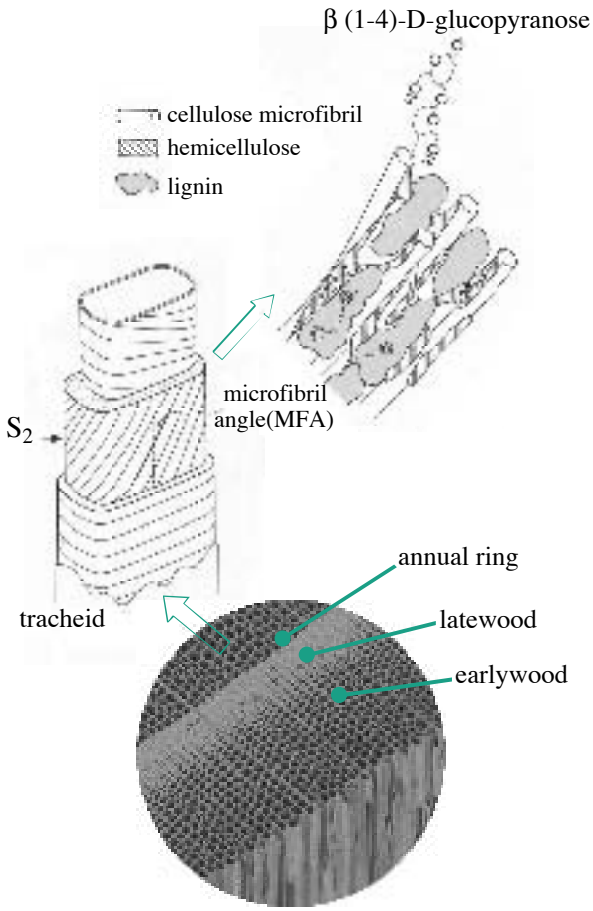

Fig. 1. Hierarchical strucuture of softwoods. From tissues to molecules. (SEM: courtesy of Dr. Fujii, FFPRI).

Traditional methods of MFA measurement based on optical microscopy, such as of the orientation of the cross-field pit apertures, or of the maximum extinction position using a polarizing microscope, demanded highly-skilled sample preparation and measurements on many samples to obtain reliable MFAs, and are thus time-consuming. In contrast, there are advantages in using X-ray diffraction techniques, which are sensitive to the dispersion of microfibril orientation. WAXS and SAXS are frequently used techniques, and in this study we performed SAXS experiments. The high flux of synchrotron radiation at beamline **BL40B2** enables us to obtain high-quality SAXS data in a short exposure, thus making large scale surveys of MFA practical.

The averaged MFAs and lateral diameters obtained form *C. japonica* are exemplified in Fig. 2 together with the corresponding SAXS patterns. The MFAs were generally found to be larger in the lower and basal parts of a branch, whereas the upper parts generally exhibited larger MFAs when the branch angle was altered. The radius of gyration, however, remained constant. Our goal is to visualize the optimization of MFAs in response to the actual mechanical demands on various parts of a tree, and the mapping of whole trunks, including those of some hardwoods, is also in progress.

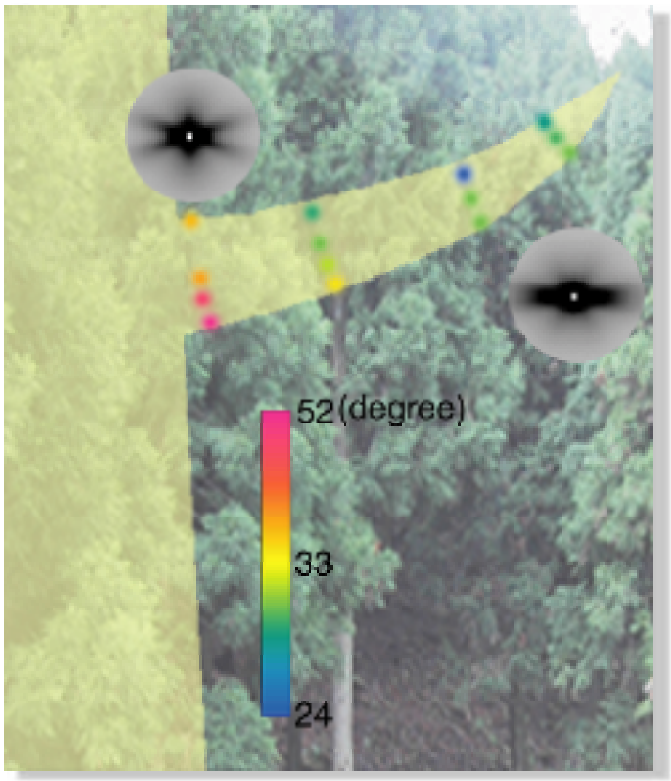

Fig. 2. Microfibril angles obtained from various portions of a branch in Sugi (C. japonica).

Ritsuko Hori[a], Junji Sugiyama[a] and Katsuaki Inoue[b]

(a) Kyoto University
(b) SPring-8 / JASRI

E-mail: junjis@kuwri.kyoto-u.ac.jp

Microangiography in Isolated Perfused Rat Heart to Evaluate Vascular Response

Organs within the body have the ability to regulate their own blood supply. Vasoconstriction decreases blood flow, while vasodilatation increases blood flow. Visualization of constriction and dilation of blood vessels with drags (vasoactive agents) is a useful research tool for evaluating vascular response. Microangiography with spatial resolution in the micrometer range was carried out to depict vascular response in an isolated perfused rat heart [1]. In imaging experiments, the rat was anesthetized, then the heart was excised. The isolated heart was mounted on a steel tube and perfused with perfusion fluid to supply nutrients and oxygen (Fig. 1); perfusion fluid was used as a substitute for blood and directed into blood vessels. The contractile function and regular heart rhythm returned to the isolated heart within a few seconds. The isolated perfused heart provides an excellent test-bed for undertaking carefully controlled dose-response studies. After administering an iodine contrast agent injection, the vascular response in small blood vessels could be visualized during the perfusion of vasoactive agents.

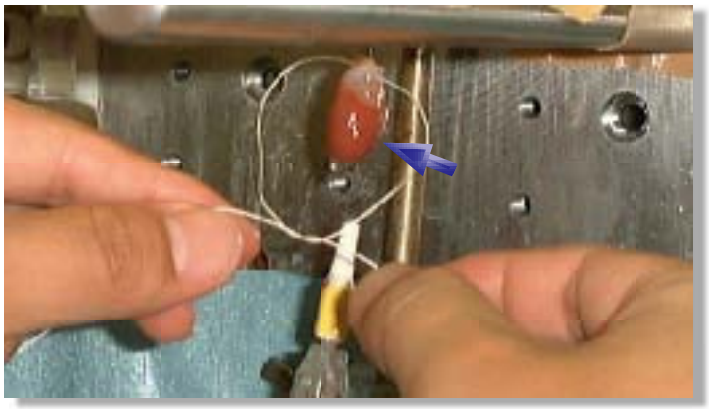

Fig. 1. Isolated perfused rat heart indicated by a blue arrow.

Coronary microangiographic imaging was carried out at the **BL28B2** bending-magnet beamline, employing a single crystal monochromator, with the monochromatic X-ray energy adjusted to 33.2 keV just above the iodine *K*-edge energy. An X-ray imaging system requires a high shutter speed (short exposure time) to produce sharp and blur-free images of fast-moving hearts, and for this purpose we developed a shutter system using a moving-coil galvanometer-based scanner. The shortest shutter open time was 3 ms.

X-rays transmitted through the object are detected by the X-ray direct-conversion type detector incorporating the X-ray SATICON pickup tube [2-4]. The X-ray camera has a resolution of 1,050 scanning lines and can record images at a maximum speed of 30 frames/s. Sequential images were obtained with an input field of view of 6.9 mm × 6.9 mm, and the equivalent pixel size projected onto the input window was 6.9 μm. Image signals are converted into a digital format and stored in a frame memory with a 1024 × 1024 pixels format and 10-bit resolution.

Acetylcholine and sodium nitroprusside were vasoactive agents used in this experiment, and with them a study to evaluate vascular responses by measuring internal diameters of small blood vessels on the baseline and under the stress of induced vasoactive agents (perfusion of agents). Sequential images of the left coronary arteries were taken at heart rates of 300 - 400 per minute. Small blood vessels of less than 50 μm in diameter were displayed in images (Fig. 2). The images show an area of 5.6 mm wide by 4.4 mm high.

Figure 2(a) shows a frame from a baseline angiographic sequence, Fig. 2(b) an acetylcholine stress sequence, and Fig. 2(c) a sodium nitroprusside stress sequence. All of these images show typical diameter changes in small coronary arteries in response to agents.

In the arterial tree, vasodilatation (white arrows) was observed in small arteries less than approximately 100 μm in diameter, whereas large arteries (yellow arrows) underwent almost no change in internal diameter due to the vasoactive agents. These agents only change the diameters of small blood vessels. Furthermore, new arterial branches of coronary arteries with diameters of 20 - 30 μm became visible in Fig. 2(c). The present imaging system enables the direct evaluation of vasodilatation in small coronary arteries of less than 50 μm diameter for this time.

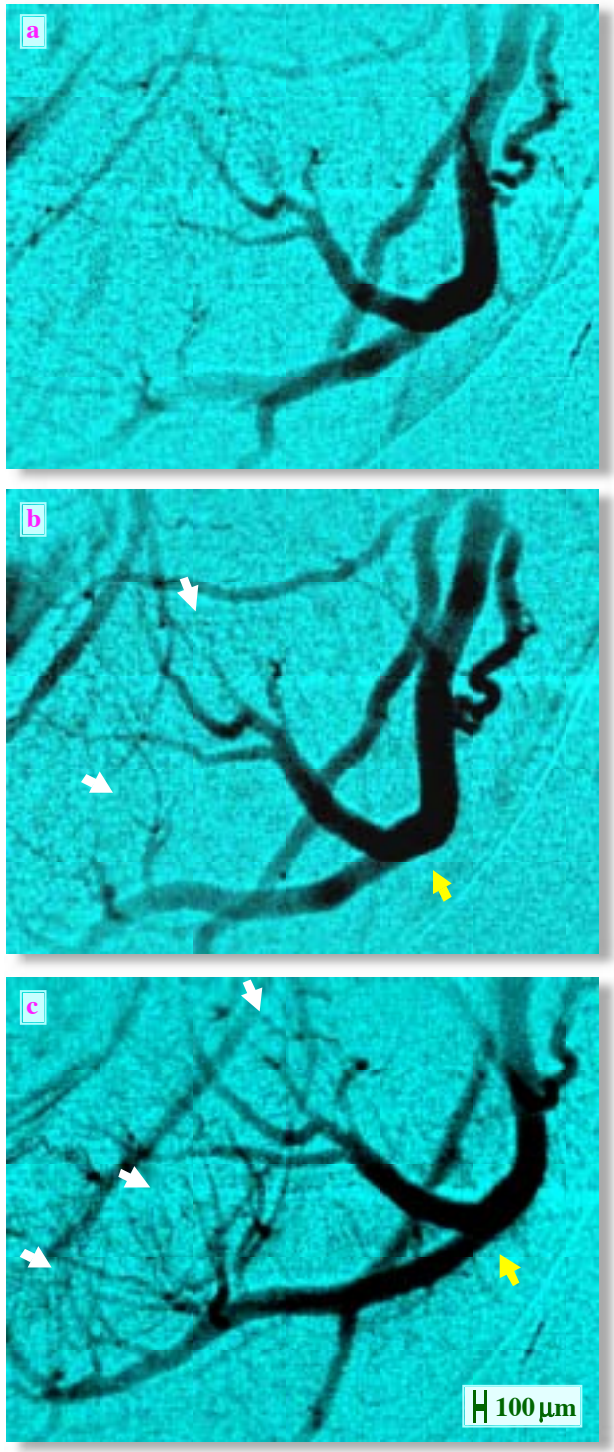

*Fig. 2. Microangiographic images **(a)** at baseline, **(b)** with acetylcholine stress and **(c)** with sodium nitroprusside stress. White arrows in **(b)** and **(c)** indicate apparent vasodilatation and new arterial branches in response to vasoactive agents, whereas large arteries (yellow arrows) underwent almost no change of internal diameter.*

Keiji Umetani[a], Kazuhito Fukushima[b] and Kazuro Sugimura [b]

(a) SPring-8 / JASRI
(b) Kobe University, School of Medicine

E-mail: umetani@spring8.or.jp

References

[1] K. Umetani *et al.*, Proc. 2002 IEEE Intl. Symp. on Biomedical Imaging: Macro to Nano (2002) 561.
[2] K. Umetani *et al.*, Anal. Sci. **17** Supp. (2001) i531.
[3] T. Yamashita *et al.*, Nitric oxide **5** (2001) 494.
[4] T. Yamashita *et al.*, Circulation **105** (2002) 3e.

Materials Science

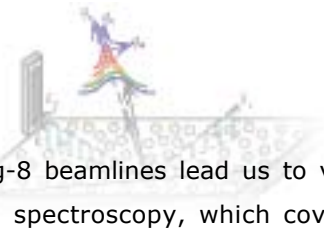

Major efforts in Materials Science using the SPring-8 beamlines lead us to various activities in the field of X-ray diffraction, scattering and spectroscopy, which cover the scientific world of solids, liquids and gases, as well as materials of technological importance. New techniques combined with the brilliant photon sources are aggressively used in such experiments as high-resolution inelastic scattering, nuclear resonant scattering, surface diffraction, holography and structural analysis under photo-excitation. In this volume, scientific interest is focused on the physics and chemistry of magnetic materials, using the techniques of resonant magnetic scattering, magnetic Compton scattering and magnetic circular dichroism to obtain results.

The experiments related to Materials Science are performed on almost all beamlines at SPring-8. Above all, the following beamlines are commonly used: BL02B1 (Crystal Structure Analysis), BL02B2 (Powder Diffraction), BL04B1 (High Pressure and High Temperature), BL04B2 (High Energy X-ray Diffraction), BL08W (High Energy Inelastic Scattering), BL09XU (Nuclear Resonant Scattering), BL10XU (Extremely Dense State Research), BL13XU (Surface and Interface Structures), BL25SU (Soft X-ray Spectroscopy of Solid), BL28B2 (White Beam X-ray Diffraction), BL35XU (High Resolution Inelastic Scattering), BL47XU (R&D) and BL12B2 (Asia and Pacific Council for Science and Technology, Taiwan). Having the requisite number of photons with sufficient resolution in energy and space, each of the beamlines supports the pioneers of vast frontiers of natural science and technology at SPring-8.

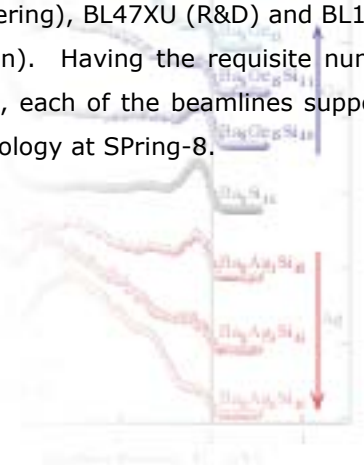

Satoshi Sasaki

Collective Excitations in Liquid Si

The structurally simplest 'semiconductor', Si, is manufactured by growing the crystal directly from the 'metallic' melt. This interplay between a metallic disordered phase and the semiconducting crystalline state has stimulated much theoretical and experimental interest in the static and dynamic properties of this system. For example, the influence of covalent bonds on the dynamics of the metallic melt was investigated in an early first-principles molecular-dynamics simulation by the originators [1]. However, the experimental investigation of the microscopic dynamics has yet been hindered by the fact that the collective longitudinal modes in liquid Si are out of reach of thermal neutrons due to the high sound velocity (~ 4,000 ms^{-1}) and the kinematic restrictions of this technique. High-resolution inelastic X-ray scattering (IXS) is another technique that permits the study of Q dependence of excitations in the meV range, but in contrast to neutron scattering, it has no kinematic restrictions and the scattered radiation is entirely coherent within the energy range of interest. Combined with a suitable high-temperature sample environment, we were able to measure for the first time the dynamic scattering law $S(Q, \omega)$ of liquid Si [2].

The experiments were carried out at beamline **BL35XU** using a horizontal IXS spectrometer [3] (energy resolution: ~1.8 meV FWHM at 21.8 keV). The hot sample (T = 1733 K) was located in a sapphire container, which was a slight modification of the so-called Tamura-type cell [4]. It was placed in a vessel equipped with continuous Be windows [5] capable of covering scattering angles between 0° and 25°.

Figure 1 shows selected spectra normalized to the respective intensity. Also given is a typical example of the resolution function (dashed line). The data clearly prove the existence of longitudinal collective short wavelength modes, which appear

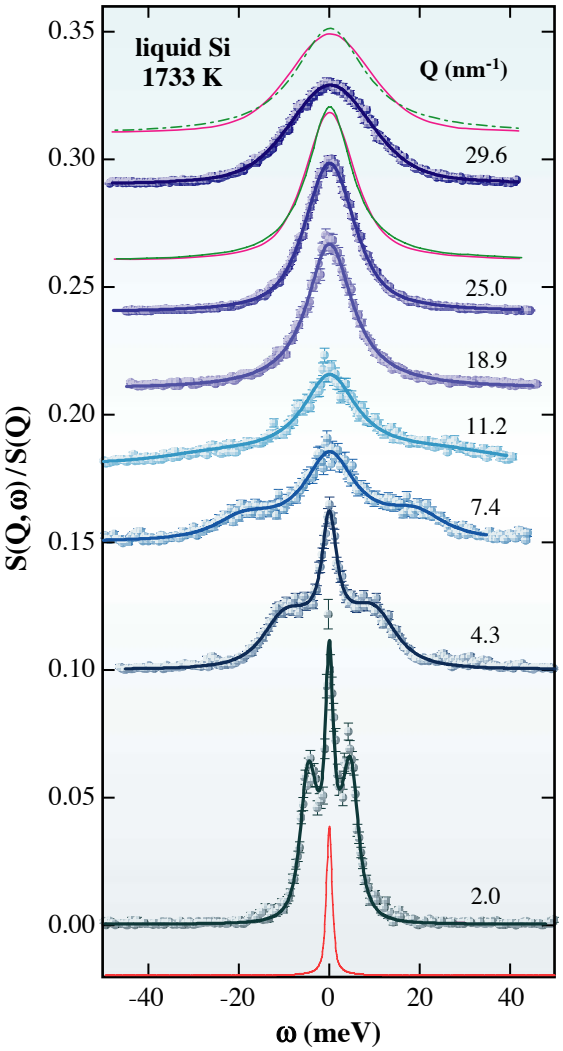

Fig. 1. Selected S(Q,ω) spectra normalized to S(Q). Experimental data are given by circles with error bars, and thick solid lines represent fits of the DHO model convoluted with the resolution function (dashed line). Dot-dashed lines show the best convoluted fits for the quasielastic lines using a Lorentzian in comparison to the quasi-Voigt fits (thin solid lines, shifted from the data).

as peaks or shoulders in the lower Q range. For the resolution correction, a model $S(Q, \omega)$ function convoluted with the resolution function was fitted to the data. For this model, we approximated the central line by a Lorentzian at lower Q values or by a pseudo-Voigt function at higher Q values (see text below), and the inelastic contribution by a damped harmonic oscillator (DHO). Using the fitted results (thick solid lines), the excitation energy ω_c and the line width Γ_Q were determined as shown in Fig. 2 . The dashed line represents the dispersion of hydrodynamic sound, and its slope is given by the bulk adiabatic sound velocity v_s = 3952 ms^{-1}. The frequencies of the short wavelength modes increase noticeably faster (~17%) with Q than predicted by classical hydrodynamics. This so-called 'positive' dispersion was already found earlier in liquid alkali metals and also in liquid Hg. The collective modes are highly damped at higher Q values compared to those in liquid alkali metals.

The usual choice, in which a quasielastic line is modelled by a Lorentzian, is not suitable for liquid Si beyond Q = 20 nm^{-1}. Instead we used a quasi-Voigt function, *i.e.*, a linear combination of a Gaussian and a Lorentzian. Dot-dashed lines in Fig. 1 show convoluted fits using a Lorentzian in comparison to the quasi-Voigt fits (thin solid line, the same as the thick ones). The quasi-Voigt function fits the data well, whereas the deviation of the Lorentzian fits is considerable. Circles and triangles in Fig. 3 represent the line width Γ_0s and the Gaussian fraction c of the quasielastic lines. The Gaussian contribution becomes noticeably important at about 20 nm^{-1} and reaches about 50% at Q ~ 30 nm^{-1}. Around the Q value where the maximum in $S(Q)$ is located, a minimum in Γ_0

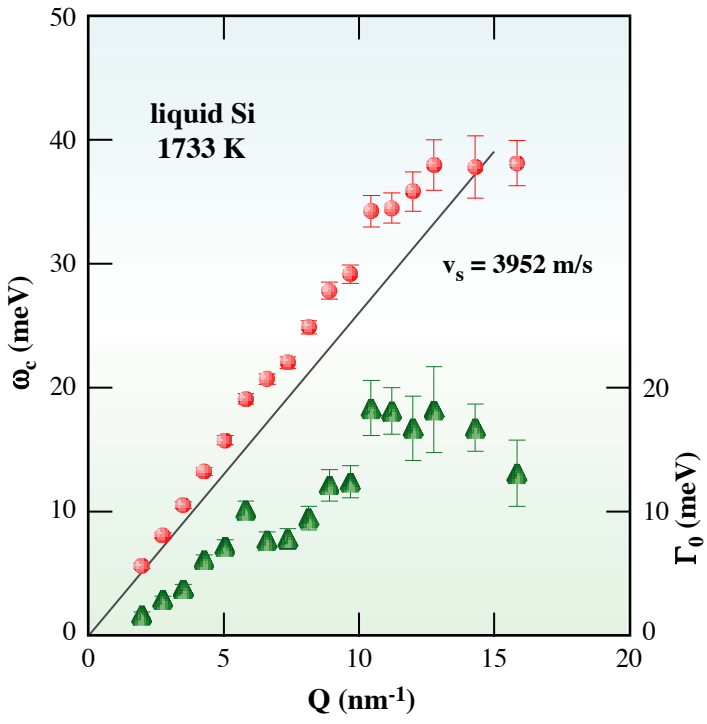

Fig. 2. Dispersion relation (circles) and line width (triangles) of the collective modes in liquid Si.

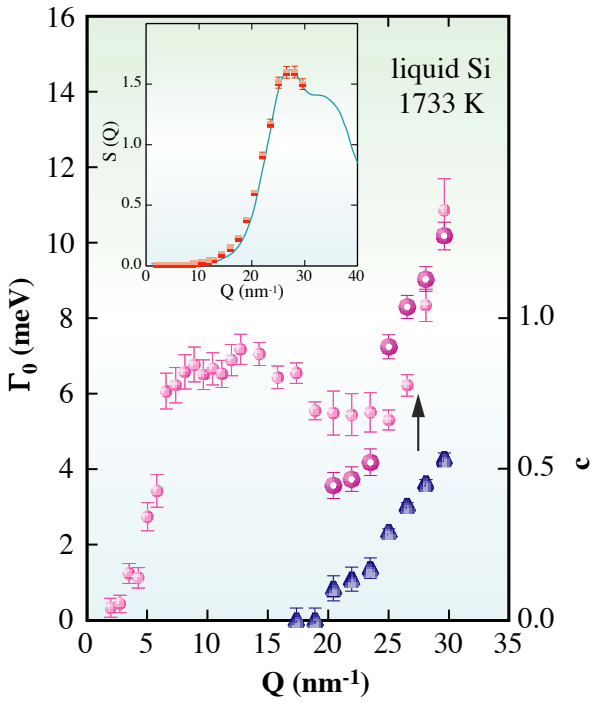

Fig. 3. Q dependence of the quasielastic line width Γ_0 (circles). With increasing Q, a Gaussian component (open circles) is needed in addition to the Lorentzian (full circles) to model the central line. Triangles give the Gaussian fraction, c. The arrow indicates the Q position of the first maximum in S(Q). Inset: S(Q) determined from the zero frequency moment of the present experiment (squares) together with the result from elastic X-ray scattering [6].

(usually Γ_{0L}) is expected, which is the well-known *de Gennes* narrowing. However it is worth noting that the minimum of Γ_{0L} is found at about 22.5 nm^{-1}, while the maximum in $S(Q)$ is located at 27.3 nm^{-1} (arrow in Fig. 3, see also $S(Q)$ given in the inset).

Besides the damped phonon modes and the anomalies in the quasielastic line, however, direct evidence for the existence of covalent bonds in liquid Si (*e.g.* localized modes) was not observed. A detailed analysis using *e.g.* a mode-coupling theory would be useful for a further understanding of the present results, and is now in progress.

Shinya Hosokawa[a], Wolf-Christian Pilgrim[a] and Yukinobu Kawakita[b]

(a) Philipps Universität Marburg, Germany
(b) Kyushu University

E-mail: hosokawa@mailer.uni-marburg.de

References

[1] I. Štich, R. Car and M. Parrinello, Phys. Rev. B **44** (1991) 4262.
[2] S. Hosokawa, W.-C. Pilgrim, Y. Kawakita, K. Ohshima, S. Takeda, D. Ishikawa, S. Tsutsui, Y. Tanaka and A.Q.R. Baron, submitted in Phys. Rev. Lett.
[3] A.Q.R. Baron *et al.*, J. Phys. Chem. Solids **61** (2000) 461.
[4] K. Tamura *et al.*, Rev. Sci. Instrum. **70** (1999) 144.
[5] S. Hosokawa and W.-C. Pilgrim, Rev. Sci. Instrum. **72** (2001) 1721.
[6] Y. Waseda and K. Suzuki, Z. Phys. B **20** (1975) 339.

Condensation of Excited Molecules under Photo-Excitation

External fields, such as magnetic fields and pressure, frequently influence the order parameters of the physical system and thus cause phase transitions. In FeRh, for example, an external magnetic field forcibly aligns the Fe local spins, and eventually induces a transition from the antiferromagnetic ground state to the ferromagnetic state at around room temperature. Since photo-irradiation selectively excites molecular units in solid systems, we can expect a new type phase transition whose order parameter is the *density of the excited molecules.* In Fig. 1, we show schematic pictures of a molecular system under photo-excitation: open and filled circles represent the molecular units in the ground and excited states, respectively. Under weak photo-excitation, the process of creating the excited molecules balances the thermal and/or quantum relaxation processes acting upon them. What happens if we further increase the excitation power? In this case, the interaction between the excited molecules will stabilize either the excited molecular pairs or the dense regions of excited molecules (hatched region in Fig. 1). In other words, the lifetime of the dense region becomes much longer than that of the isolated excited molecules. Consequently, such regions tend to grow by the subsequent photo-excitations, and eventually the excited molecules condense.

To experimentally confirm the above-mentioned scenario, we have performed *in situ* synchrotron radiation X-ray (SRX) powder structural analysis of $[Fe(ptz)_6](BF_4)_2$ under photo-excitation at beamline **BL02B2** [1]. $[Fe(ptz)_6](BF_4)_2$ (ptz = propyltetrazole), consists of $Fe(ptz)_6$ molecular units, in which a divalent Fe^{2+} ion is surrounded by six N of ptz ligands. The $Fe(ptz)_6$ unit takes two well-defined states; one is the low-spin (LS) ground state, and the other one is the high-spin (HS) exited state. The Fe-N bond distance (2.2 Å) is larger in the HS state than that (2.0 Å) in the LS state.

Figure 2 shows the powder patterns for $[Fe(ptz)_6](BF_4)_2$ at 91 K under various photo-excitation conditions. A cw laser (532 nm) beam, which selectively excites the LS molecules into the HS state, was weakly focused onto the powdered

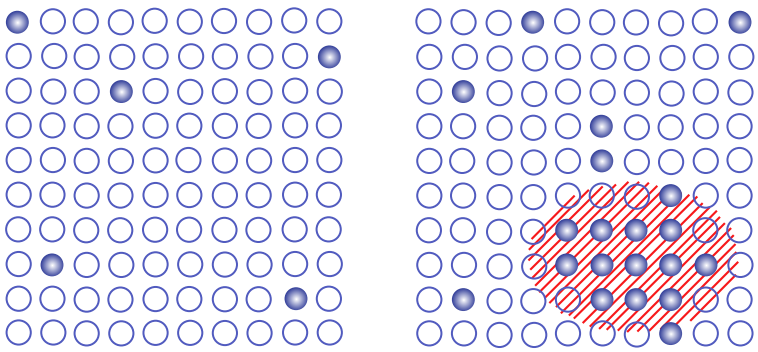

(a) Weak Excitation **(b)** Strong Excitation

Fig. 1. Schematic pictures of a molecular system under ***(a)*** *weak and* ***(b)*** *strong excitation. Open and filled circles represent the molecular units in the ground and excited states, respectively. Hatching in* ***(b)*** *indicates the dense region of the excited molecules.*

samples in a capillary; the laser spot size (*ca.* 2 mm) was larger than the collimator size (1 mm × 0.5 mm) for the SRX beam. The powder patterns showed negligible change in the weak excitation region (P < 49 mW; P is the excitation power), and were analyzed with the rhombohedral (R3; Z = 3) model [2]. At P = 55 mW and 70 mW, however, the Bragg reflection at 19.2° showed a shoulder structure in the lower-angle side. As a result, we adopted a two-phase model with the rhombohedral structures to determine the Rietveld analysis of these patterns.

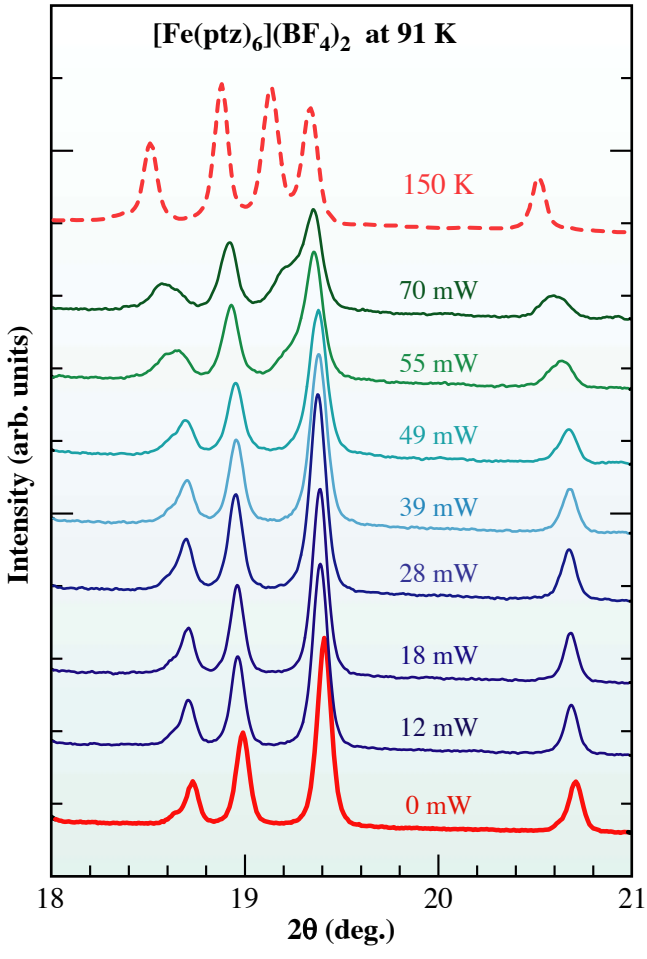

Fig. 2. In situ synchrotron-radiation X-ray powder diffraction patterns under various excitation powers for $[Fe(ptz)_6](BF_4)_2$ at 91 K. X-ray wavelength is 1.0010 Å. The thick solid curve is the powder pattern without photo-excitation. The broken curve is the powder pattern at 150 K in the high-temperature phase.

In Fig. 3 we summarized the P-dependence of physical quantities for $[Fe(ptz)_6](BF_4)_2$ at 91 K. The lattice constants (Fig. 3(a)) gradually change with P in the weak excitation region (P < 49 mW). At P = 55 mW, however, the secondary phase (square symbols) suddenly appears. The lattice constant a (10.82 - 10.83 Å) for this secondary phase is much smaller than the high-temperature value (10.89 Å), indicating that the present observation cannot be ascribed to the conventional heating effects. These structural changes are maintained only under photo-excitation, and soon disappear if we stop it. Figure 3(b) shows the P-dependence of the Fe-N bond distance $d_{Fe\text{-}N}$ determined by the Rietveld structural analysis. The longer $d_{Fe\text{-}N}$ (2.1 Å) suggests that the secondary phase should be ascribed to the condensed phase of the photo-excited HS molecules. Figure 3(c) shows the mass fraction of the secondary phase.

Now, let us investigate the interrelation between P and the order parameter, that is, density n_{HS} of the HS molecules, which can be estimated by varying the LS absorption band [3]. In Fig. 4, we plotted n_{HS} against P for $[Fe(ptz)_6](BF_4)_2$ at 77 K; solid and open circles represent the data obtained in P-increasing and decreasing runs, respectively. We used the 514.5 nm (2.41 eV) line of a cw Ar^+ laser as the excitation and probe light sources (pump & probe technique). In the weak-excitation region (P < 60 mW/cm^2), n_{HS} remains small (< 0.1). With a further increase in P, however, n_{HS} steeply increases and reaches *ca.* 0.5. Such an abrupt change of n_{HS} against P can be regarded as the phase transition into the condensed state of the HS molecules. We further observed a clear optical hysteresis, indicating that this phase transition is of the first order.

Thus, our *in situ* SRX powder structural analysis, in addition to results of the pump & probe experiment of $[Fe(ptz)_6](BF_4)_2$, suggests that condensation of excited molecules is realized under strong-excitation. Present *in situ* SRX powder structural analysis is a powerful tool for determining the atomic coordinates in the photo-excited steady state, and for exploring the physics of excited states.

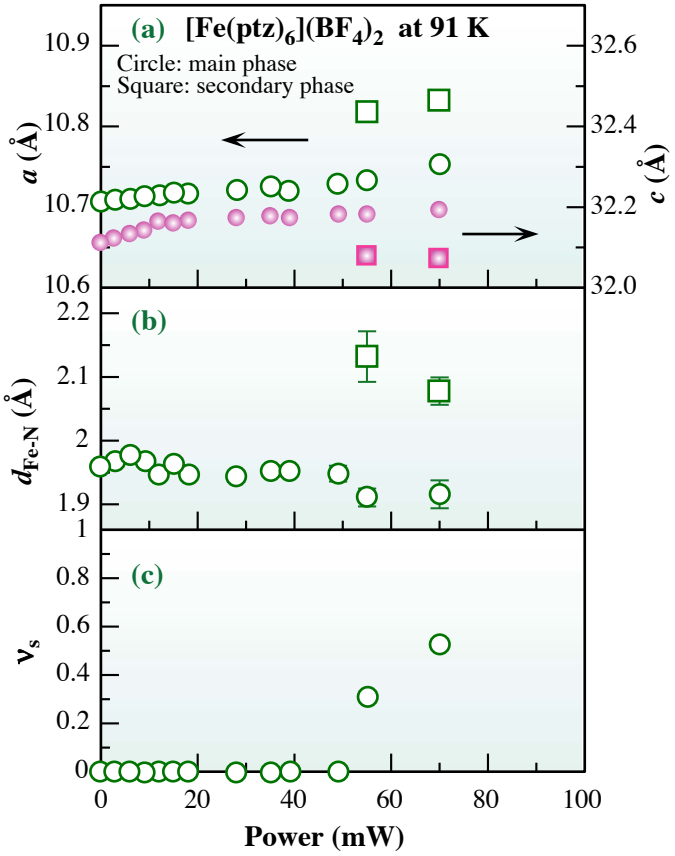

Fig. 3. Excitation power dependence of ***(a)*** *lattice constants, a and c,* ***(b)*** *Fe-N bond distance d_{Fe-N} and* ***(c)*** *mass fraction v_s of the secondary phase for $[Fe(ptz)_6](BF_4)_2$ at 91 K. Square symbols represent values for the photo-induced secondary phase.*

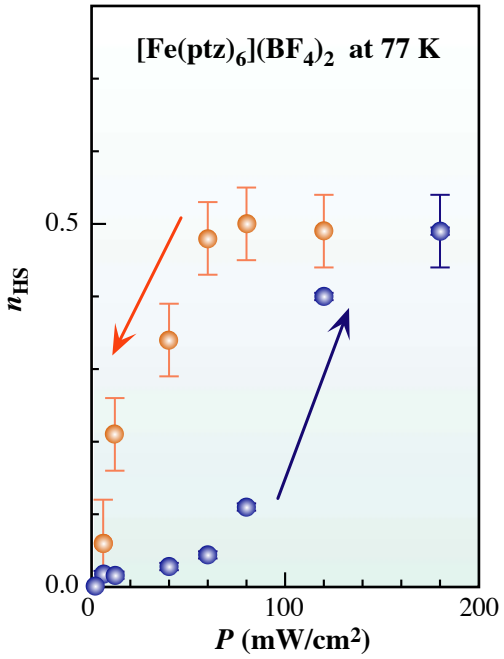

Fig. 4. Density n_{HS} of the HS molecules against excitation power density P for $[Fe(ptz)_6](BF_4)_2$ at 77 K.

Yutaka Moritomo[a], Kenichi Kato[b] and XiaoJun Liu[a]

(a) Nagoya University
(b) SPring-8 / JASRI

E-mail: moritomo@nano.nuap.nagoya-u.ac.jp

References

[1] Yutaka Moritomo, K. Kato, A. Kuriki, A. Nakamoto, N. Kojima, M. Takata and M. Sakata, J. Phys. Soc. Jpn. **71** (2002) 2609.
[2] Yutaka Moritomo K. Kato, A. Nakamoto, N. Kojima, E. Nishibori, M. Takata and M. Sakata, J. Phys. Soc. Jpn. **71** (2002) 1015.
[3] X. J. Liu, Y. Moritomo, T. Kawamoto, A. Nakamoto and N. Kojima, Phys. Rev. **67** (2003) 012102.

Composition and Strain of Semiconductor Quantum Dots

Quantum dots exhibit confinements of electronic carriers and have been a major focus of research interest in the last decade. The confinement resulted from the dot dimension, which is typically in the range of 10 nm to 50 nm. Although new fabrication techniques for various dots have greatly advanced, our fundamental knowledge of quantum dots in terms of equilibrium and kinetic properties of formation remains limited. Compared to bulk crystals or epitaxial films, the concepts of equilibrium crystal shape, surface segregation, and phase diagram all need to be developed for different quantum dot systems. To be able to experimentally determine the exact atomic positions of the dot is one of the critical steps in this research.

The method we have employed to study the structure of quantum dots is an extension of the conventional grazing incidence surface X-ray diffraction technique. The basic idea is that the dots can be divided into iso-strain slabs, which are regions with constant lateral lattice parameters [1]. X-rays scattered by different iso-strain slabs at different heights will distribute to different parts of the reciprocal space (Fig. 1). Therefore, from the detailed profile of the X-ray intensity distribution around surface Bragg peaks, we are able to reconstruct the shape and the strain field within the dots. The methodology is called Reciprocal Space Mapping (RSM) [1]. In this work, we further explore the resonant X-ray effect in RSM to study quantum dots.

For semiconductor systems, the fabrication techniques of different quantum dots have been well developed to the extent that opto-electronic devices can be commercialized. Nowadays, the most effective way to fabricate semiconductor quantum dots is by the self-assembled growth mode, which relies on strain-induced island formation via a Stranski-Krastanow epitaxial growth. Interestingly, such quantum dots are dislocation free and often exhibit a preferred shape with narrow size distribution [2]. We applied RSM to uncapped InGaAs quantum dots grown on a GaAs(001) substrate. The surface topology of a typical sample studied is shown in Fig. 2(a).

The X-ray scattering measurements were conducted at both the bending magnet beamline **BL12B2** at SPring-8 and the wiggler beamline BL17B of Taiwan Light Source. The grazing incident scattering geometry was set with $\alpha_i < \alpha_c$ of GaAs. With this scattering geometry, we explored an illuminated area of a few mm^2 containing ~10^6 quantum dots. The results obtained by non-resonant RSM of the strain and compositional distributions of the InGaAs dots are shown in Fig. 2(b) [3].

The resonant RSM method incorporates the anomalous X-ray effect near the absorption edges [4], where the dispersion corrections f' and f'' make a rather large contribution to the atomic scattering factors and vary drastically with the energy of the incident X-rays. This variation is further enhanced for weak reflections and provides a highly sensitive means to determine the composition (x) of each iso-strain slab. One can better understand the sensitivity of the method by

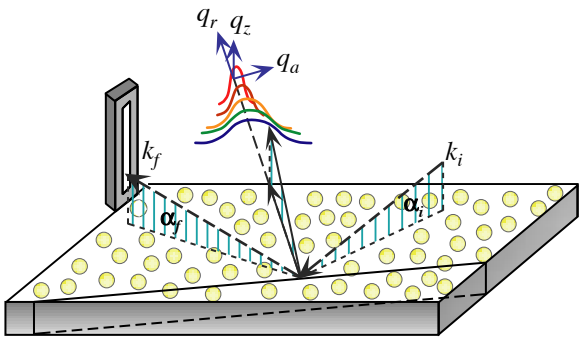

Fig. 1. A schematic of the grazing incidence scattering geometry employed in the Reciprocal Space Mapping method.

examining the structure factor of even reflections of $In_xGa_{1-x}As$, which has the zinc-blend structure, as given by

$$F_{InGaAs} = [x F_{InAs} + (1-x) F_{GaAs}]$$
$$= 4 [x (f_{In} \pm f_{As}) + (1-x) (f_{Ga} \pm f_{As})],$$

where F's and f's are the structure factors and the atomic scattering factors and the plus (minus) sign is for strong (weak) reflection, respectively. Figure 3(a) illustrates the energy dependence of normalized scattered intensities for the $In_xGa_{1-x}As$ (200) and (400) reflections with In composition x of 0.1 and 0.4. These calculated profiles agree qualitatively to the experimental ones as shown in Fig. 3(b). The obtained height-strain and composition-strain dependence clearly indicate that the In concentration is much lower than the nominal composition 0.5 near the dot/substrate interface region and grows with increasing lattice mismatch. Detailed results will be published [4].

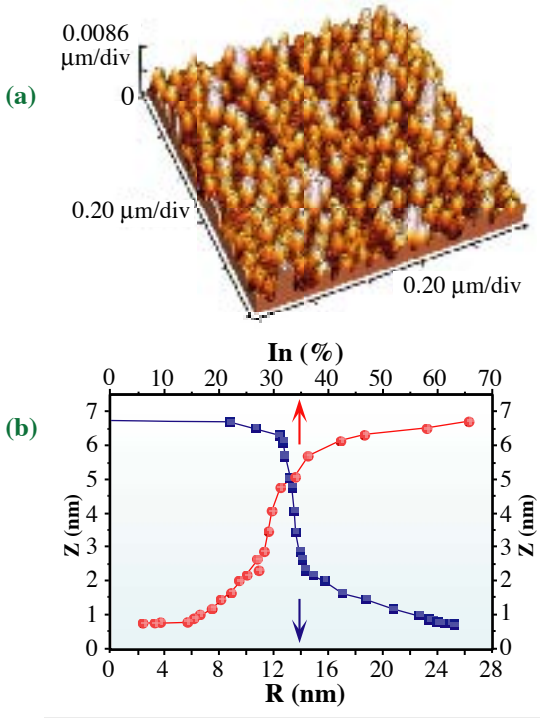

*Fig. 2. **(a)** An AFM image of uncapped $In_xGa_{1-x}As$ quantum dots formed on GaAs(001) surface with a nominal $x = 0.5$. **(b)** The variations of radius and In content of InGaAs quantum dots obtained by non-resonant RSM method.*

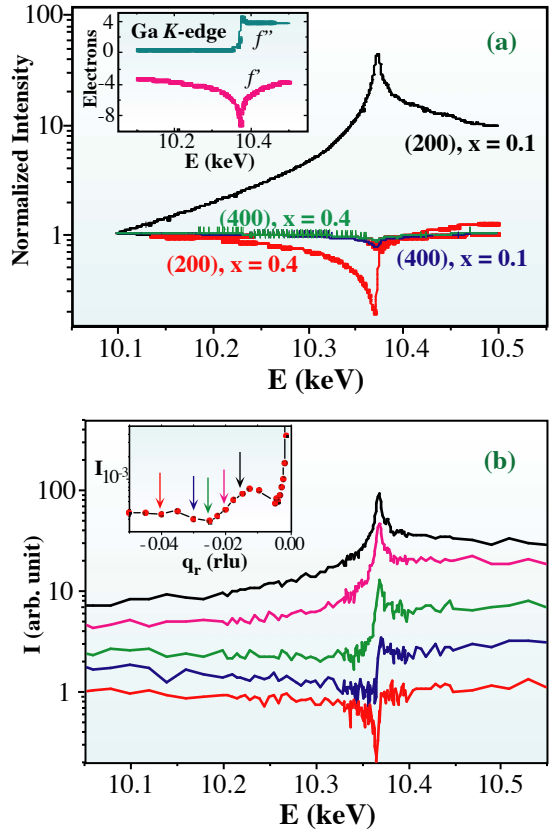

*Fig. 3. **(a)** The energy dependence of normalized scattered intensities for the $In_xGa_{1-x}As$ (200) and (400) reflections with In composition x of 0.1 and 0.4. Inset: the energy dispersion corrections f' and f" near Ga K-edge. **(b)** The experimental energy-scanned profiles at different q_r positions as indicated in the inset. Different profiles correspond to quantum dot layers with different In concentration. The curves are offset vertically for clarity.*

Keng S. Liang

National Synchrotron Radiation Research Center, Taiwan

E-mail: ksliang@srrc.gov.tw

References

[1] I. Kegel *et al.*, Phys. Rev. B **63** (2001) 35318.
[2] L.G. Wang *et al.*, Phys. Rev. B **62** (2000) 1897.
[3] C.H. Hsu *et al.*, 7th Int'l Conf. on Surface X-ray and Neutron Scattering, Sep. 2002, to appear in Physica B (2003).
[4] Y. Stestko *et al.*, to be published.

Structural Study of Si/Ge/Si(001) Crystal by a Holographic Method using X-ray Diffraction

Holography is a well-known technique to directly reconstruct an image of objects. In this technique, a detecting plate called a hologram is first created by using an interference effect between two waves: one is a reference wave coming directly from a light source to the detecting plate, while another is an object wave coming after once scattered by objects. In the second step, one can reconstruct the objects by illuminating the reference wave on the hologram. In the present work, we show a similar holographic method to reconstruct images of surface and interface atoms with an atomic resolution. Here we treat two-dimensionally ordered atoms on a substrate crystal. Hitherto similar attempts have been made as to two-dimensional structures projected on the surface [1]. In this work, however, we show the first experimental results of three-dimensional reconstructed images of surface atoms.

To analyze the structure of surface atoms on crystals, we usually measure integrated intensities for a number of diffraction spots. Then we compare the observed intensities with those calculated for possible models until we find a good model that attains a good agreement between those two intensities. In the present work, however, we could directly determine the structure of surface atoms from experimentally obtained intensities.

Figure 1 illustrates the principle of the present method. In this case the diffraction amplitude is divide dn two; one is a contribution from a surface layer to be determined, and the other is a contribution from a substrate crystal given by the sum of amplitudes from semi-infinite layers. In most cases one knows the structure of the substrate crystal, and can calculate the phase and modulus of the amplitude by crystal-truncation-rod scattering [2] based on the kinematical theory of X-ray diffraction. Thus we can regard the wave scattered from the substrate crystal as a reference wave. In this situation, we can reconstruct unknown surface atoms by a Fourier transform after proper normalization of the experimental data instead of illuminating a reference wave as in optical holography.

Figure 2 shows images of Ge atoms on Si(001) substrate crystal reconstructed from observed intensities. Here we used a sample in which a monolayer of Ge atoms are epitaxially grown on a clean Si(001) surface at 775 K. A few nanometers of an amorphous Si layer was further deposited on the sample at 295 K to withstand in the atmosphere. To reconstruct the images, we have obtained intensities about at 250 points, most of which are measured at points on the rod close to Bragg points.

Figure 3 shows a schematic illustration of the interface. Figure 2 corresponds to the hatched areas in Fig. 3. The result clearly shows that Ge atoms locate positions that Si atoms would

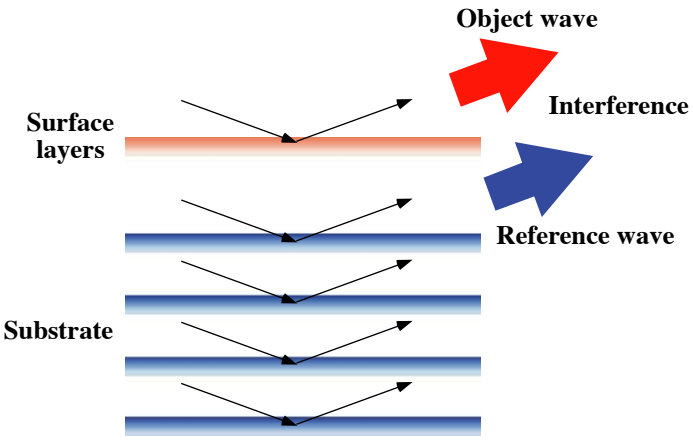

Fig. 1. Principle of the present method to reconstruct images of surface atoms using an interference effect.

otherwise occupy. The position of Ge atoms is slightly relaxed toward the surface, reflecting the difference in bond lengths between Ge and Si in crystals.

In regard to structural analysis of surfaces and interfaces, constructing an initial model is a most intricate task. However, once the initial structure is directly obtained from experimental data, one could easily refine the structure, with for instance, the use of conventional fitting procedures.

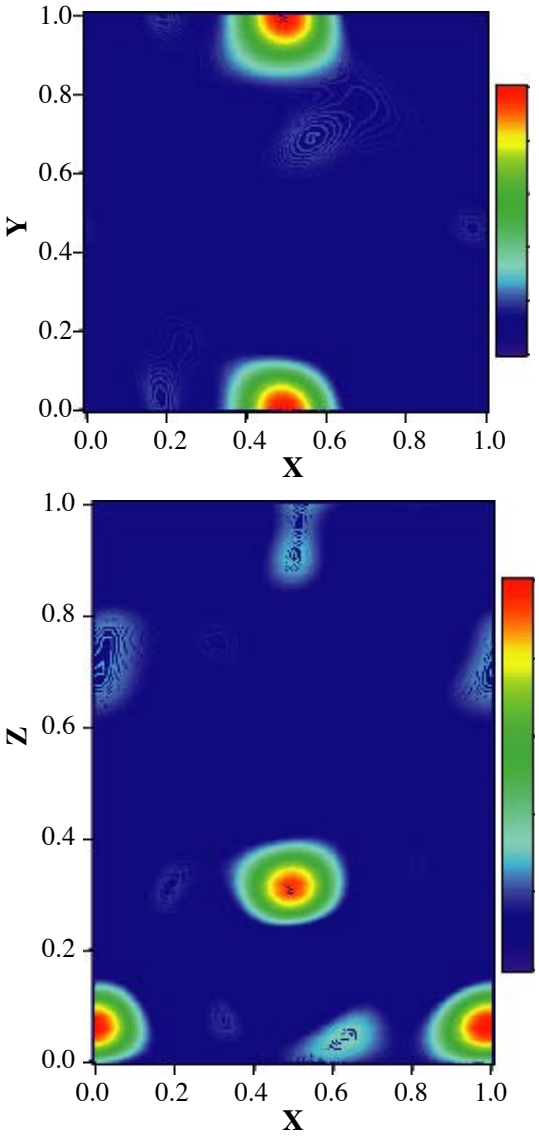

Fig. 2. Contour maps of Ge atoms on Si(001) substrate crystal at planes parallel (upper) and perpendicular (lower) to the surface. Rectangular regions correspond to the hatched areas in Fig. 3.

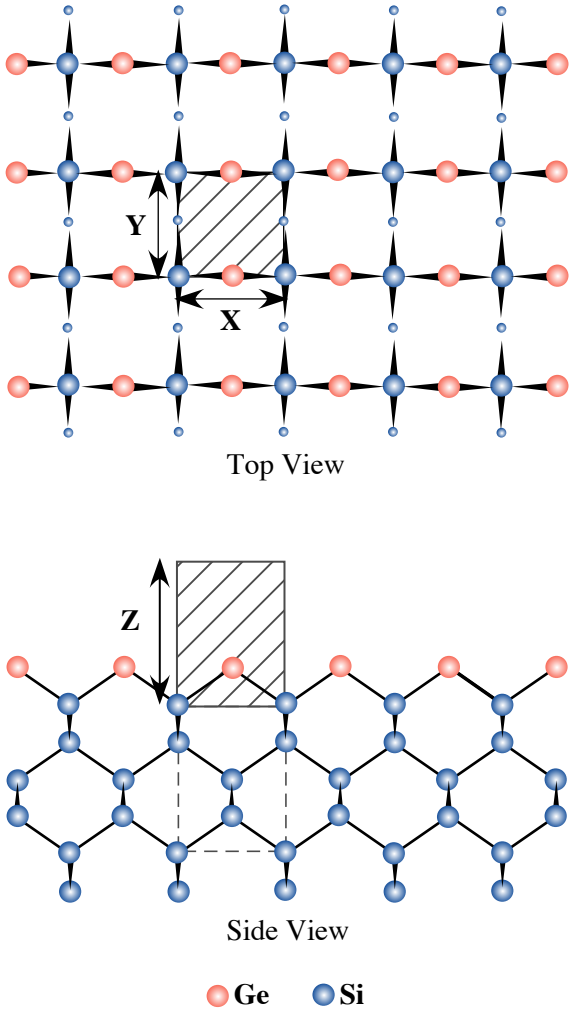

Fig. 3. Schematic illustration of reconstructed Ge atoms with respect to the Si(001) substrate crystal.

Toshio Takahashi and Kazushi Sumitani

The University of Tokyo

E-mail: ttaka@issp.u-tokyo.ac.jp

References

[1] L.D. Marks *et al.*, Surf. Rev. Lett. **5** (1998) 1087.
[2] I.K. Robinson, Phys. Rev. B **33** (1986) 3830.
[3] K. Sumitani, T. Takahashi, S. Nakatani, A. Nojima, O. Sakata, Y. Yoda, S. Koh, T. Irisawa, and Y. Shiraki, Jpn. J. Appl. Phys. **42** (2003) L189.

3-D Imaging around a Dopant in Si Crystal by X-ray Fluorescence Holography

The doping technique in crystalline Si has played an important role in the fabrication of advanced semiconductor devices, which requires state-of-the-art tailoring of a band gap. In order to understand the nature of doping-induced electronic states, it is essential to study the local structures around impurities in a doped semiconductor. The X-ray absorption fine structure (XAFS) method is commonly used for studying the local structure of particular elements. X-ray fluorescence holography (XFH) [1,2] is a promising new technique for imaging 3-D atomic arrangements around atoms emitting fluorescence photons. This technique is also applicable to investigate the environment around a dopant [3].

The "normal" and "inverse" modes exist in the XFH method. In the normal XFH method, fluorescent X-rays from atoms in a sample with and without being scattered by surrounding atoms serve as the object and reference waves, respectively. A holographic pattern is recorded by scanning a detector around the sample. In the inverse mode, fluorescence is used to detect an interference field originating from incident and scattered X-rays (Fig. 1). The holographic pattern is obtained by detecting the fluorescence while the sample's orientation is varied relative to the incident beam. The inverse mode was preferably used in the XFH experiment at this synchrotron radiation facility because the holograms can be recorded at any incident energy above the absorption edge of an emitter.

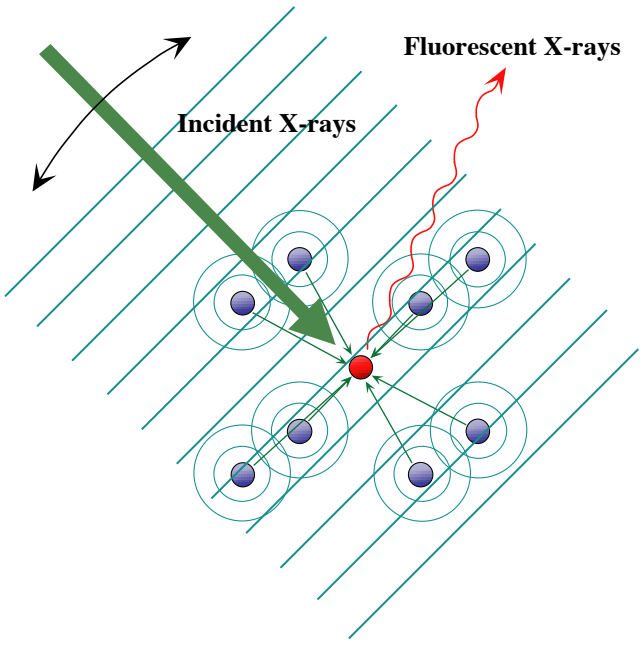

Fig. 1. The XFH principle for the inverse mode.

XFH patterns were measured at beamline **BL47XU**. An $Si_{0.999}Ge_{0.001}$ sample grown by the Czochralski method was used as the sample [4], and its dimensions were 5 × 5 × 2 mm³. Incident energies were 14.5 - 17.0 keV with 0.25 keV steps. Figure 2 shows an experimental setup for recording inverse XFH holograms. The Ge Kα (9.87 keV) X-ray fluorescence via a cylindrical LiF crystal was detected by an avalanche photodiode. The X-ray fluorescence count rate was about 200,000 cps. The fluorescence intensities were measured as a function of azimuthal angle ϕ and polar angle θ_1 within the ranges of $0° \leq \phi \leq 360°$ and $0° \leq \theta_1 \leq 76°$. The X-ray exit angle of θ_2 was fixed at 45°. In this experiment, we recorded 11 holograms at different energies.

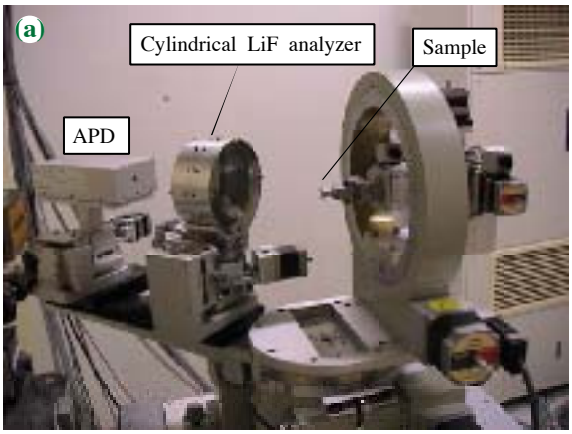

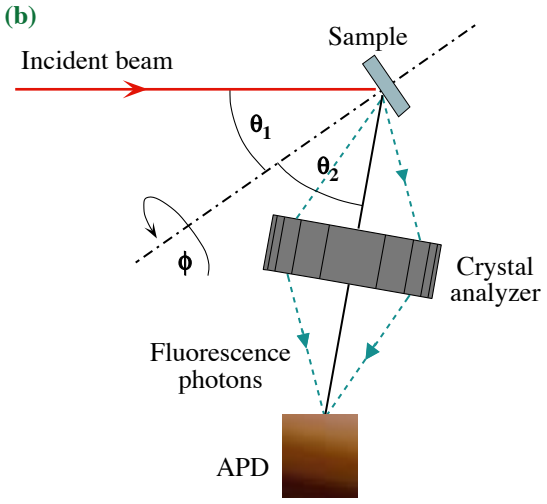

*Fig. 2. Photograph (**a**) and schematic diagram (**b**) of the experimental setup installed at SPring-8 for the structural analysis of condensed systems by XFH.*

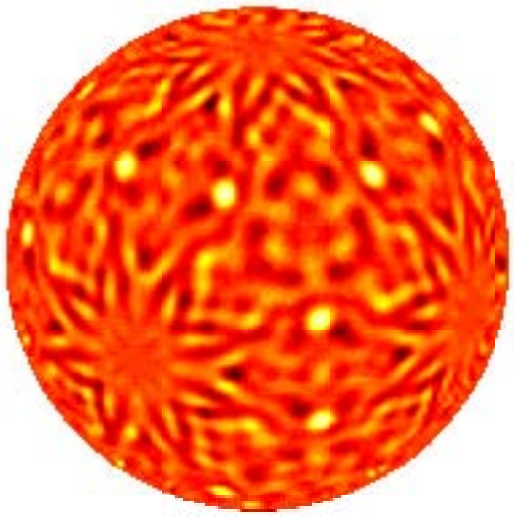

Fig. 3. Ge X-ray fluorescence hologram of $Si_{0.999}Ge_{0.001}$ recorded at 14.5 keV. The displayed pattern was obtained by symmetrization and low-pass filtering.

To handle the data, we incorporated extension of the hologram to the full sphere by using measured symmetries and low-pass filtering. Figure 3 shows the resulting hologram pattern at 14.5 keV. Multiple energy reconstruction by the Helmholtz-Kirchhoff transformation modified according to Barton was applied to these hologram data. The real space image was depicted in Fig. 4. The atomic images were extremely fine, and artifacts, which were obvious in the reconstruction by the single energy XFH, were sufficiently suppressed. The atoms up to the seventh coordination shell were recognized, though we

have only displayed the atoms up to the fourth coordination shell in the Fig. 4 because of the complication of the figure. The arrangement of the atoms in the reconstruction remarkably shows a superposition of two associated environments of a diamond structure, revealing that Ge atoms lie in two distinct crystallographic sites. Thus, we found that Ge atoms are substituted for Si sites. Taking into account the Ge concentration, most of the atomic images were regarded as being of Si. Originally, XFH was weak at imaging light atoms such as Si and O. The present result revealed that our experimental and data processing techniques significantly improved the results [5].

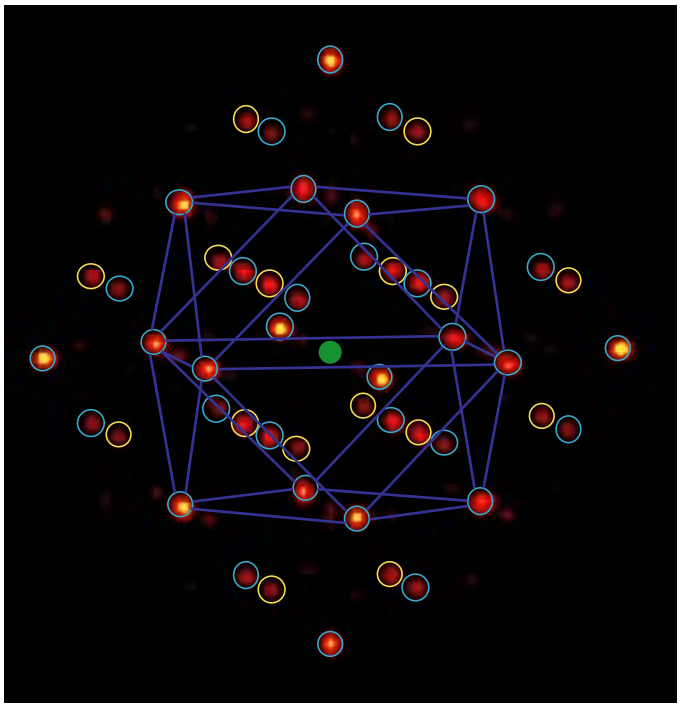

Fig. 4. 3-D image of the atomic environment around Ge in $Si_{0.999}Ge_{0.001}$.

Kouichi Hayashi, Yukio Takahashi and Ei-ichiro Matsubara

Tohoku University

E-mail: khayashi@imr.tohoku.ac.jp

References

[1] M. Tegze and G. Faigel, Nature **380** (1996) 49.
[2] T. Gog *et al.*, Phys. Rev. Lett. **76** (1996) 313.
[3] K. Hayashi, M. Matsui, Y. Awakura, T. Kaneyoshi, H. Tanida and M. Ishii, Phys. Rev. B **63** (2001) R41201.
[4] I. Yonenaga, J. Cryst. Growth **198-199** (1999) 404.
[5] K. Hayashi, J. J. Soc. Synchrotron Rad. Res. **15** (2002) 267.

Phase Separation between Electron-rich Ferromagnetic and Electron-poor Antiferromagnetic Regions on $La_{2-2x}Sr_{1+2x}Mn_2O_7$ Studied by Magnetic Compton Profile Measurement

Perovskite Mn oxides have attracted much interest because of the colossal magnetoresistance (CMR) which appears just above its metal-insulator transition temperature T_c. The ferromagnetism and metallic conductivity below T_c have been interpreted in terms of the double-exchange (DE) mechanism, where e_g orbital electrons go around Mn sites through hybridization with O 2*p* orbitals, and align the localized t_{2g} spins by the strong Hund's coupling [1]. However, the CMR phenomenon cannot be explained by the simple DE mechanism. It is currently pointed out that the orbital degree of freedom is important, as are the charge and spin ones. The determination of e_g (x^2-y^2 and $3z^2-r^2$ orbitals) and t_{2g} orbital occupation in Mn 3*d* state will provide a clue for the clear understanding of the CMR phenomenon existing in this system.

These orbital states can be distinguished on a magnetic Compton profile (MCP) by their characteristic line shapes. For instance, directional Compton profiles of x^2-y^2 and $3z^2-r^2$ atomic orbitals are shown in Fig. 1(a) and 1(b), respectively. This feature makes it possible to determine the e_g and t_{2g} orbital occupation separately [2]. Recently, the temperature dependence of MCP has been measured on a single crystal of $La_{2-2x}Sr_{1+2x}Mn_2O_7$

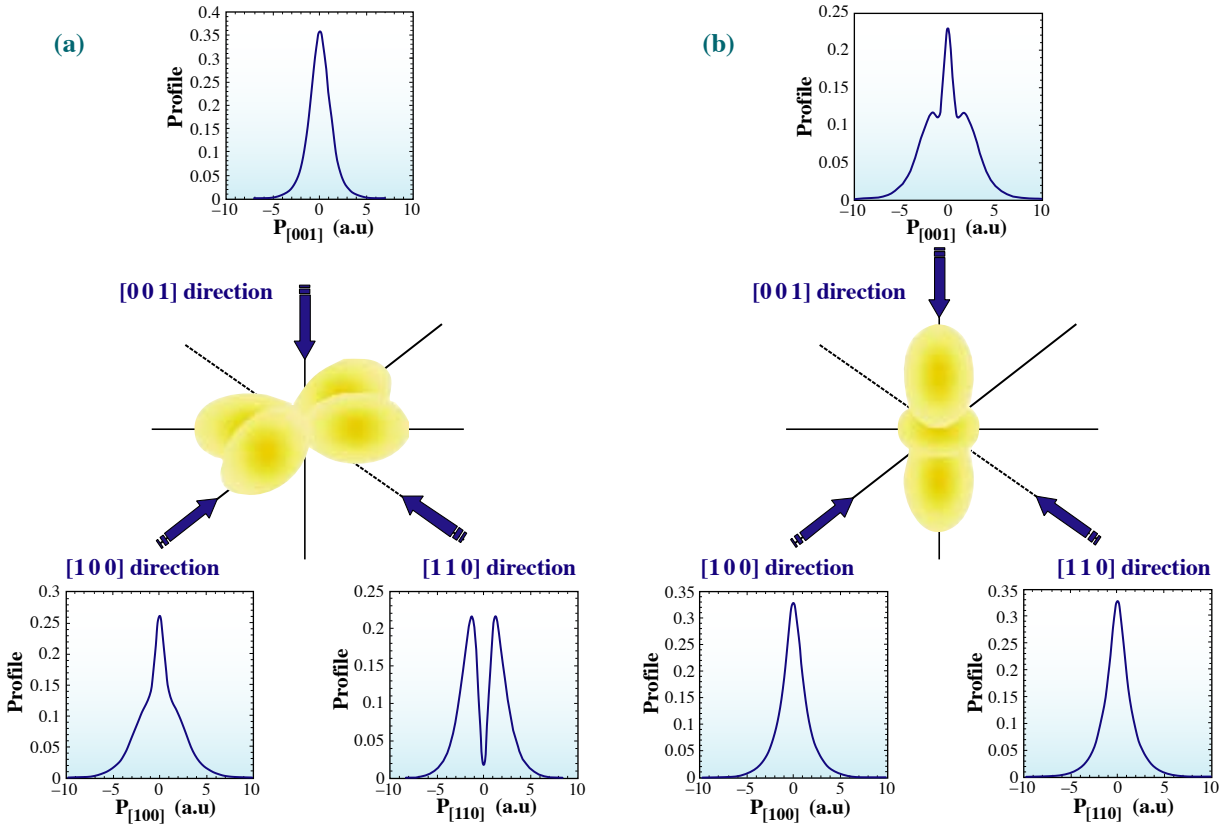

Fig. 1. Directional Compton profiles of **(a)** x^2-y^2 *and* **(b)** $3z^2-r^2$ *atomic orbitals.*

at x = 0.42 along the c-axis [3]. Experiments were made on beamline **BL08W** using circularly polarized X-rays at 174 keV. MCP's measured at 10 and 150 K are shown in Fig. 2. The area of each MCP is normalized to the magnetic moment measured at each temperature, and it should be noted that T_c lies in between these temperatures. Thus MCP at 150 K reflects a field-induced ferromagnetic state above T_c.

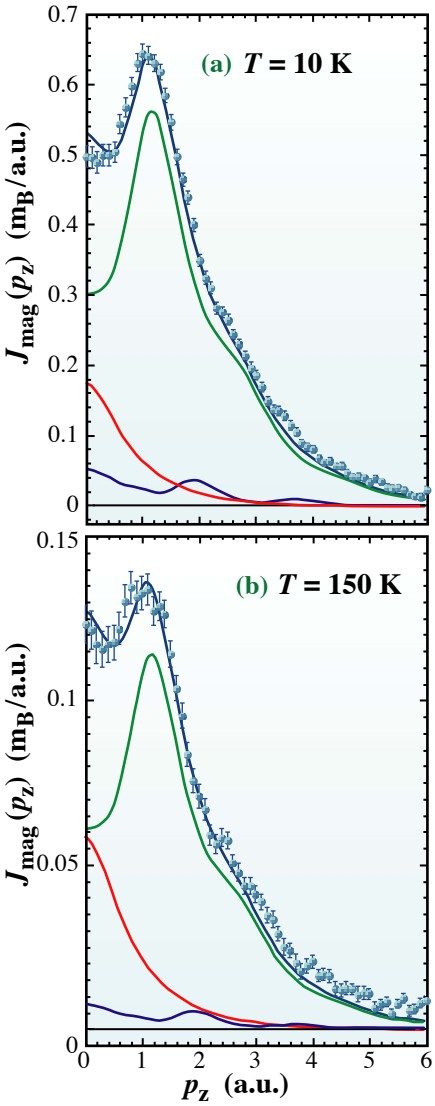

*Fig. 2. The magnetic Compton profiles of $La_{2-2x}Sr_{1+2x}Mn_2O_7$ with x = 0.42 measured at **(a)** 10 K and **(b)** 150 K. Experimental data and the fitting result are shown with solid circles and solid line, respectively. The green line represents the t_{2g} orbital contribution. The red and blue lines are for the x^2-y^2 and $3z^2-r^2$ contributions in the e_g orbital state, respectively.*

Significant change in shape is observed in a low momentum region; the dip is shallower at 150 K than at 10 K. Since the magnetic moment of the sample almost originates in the spins in Mn 3*d* orbitals, this behavior means that the ratio of e_g spin to t_{2g} increases above T_c, because the e_g-orbital profile shows a peak at p_z=0, while the t_{2g}-one has a dent. To evaluate the spin magnetic moments in the respective orbitals, a fitting analysis of each MCP was carried out using theoretical profiles of t_{2g} and e_g type orbitals obtained from an *ab initio* molecular orbital calculation for the $(MnO_6)^{8-}$ cluster. In the case of manganites, it is reasonable to assume that the electron number in each orbital is proportional to the number of spins due to the strong Hund's coupling between t_{2g} and e_g spins. If we assume that all Mn ions have the same electron number, that is, t_{2g} and e_g orbital occupations are 3 and 0.58, respectively, the e_g/t_{2g} ratio is expected to be 0.193. However, the ratio at 10 K deduced from the fitting result is 0.234, which is slightly larger than the expected ratio, and the ratio at 150 K shows an even large rvalue of 0.306. This can be interpreted in terms of the phase separation between electron-rich ferromagnetic and electron-poor antiferromagnetic regions [4], because the MCP measurement only observes the ferromagnetic component in the sample. From the ratios, it is found that the e_g electrons are highly segregated in the ferromagnetic region above T_c.

Akihisa Koizumi

Himeji Institute of Technology

E-mail: akihisa@sci.himeji-tech.ac.jp

References

[1] C. Zener, Phys. Rev. **82** (1951) 403.
[2] A. Koizumi *et al.*, Phys. Rev. Lett. **86** (2001) 5589.
[3] A. Koizumi, T. Nagao, Y. Kakutani, N. Sakai, K. Hirota and Y. Murakami, submitted in Phys. Rev. Lett.
[4] A. Moreo *et al.*, Science **283** (1999) 2034.

Phonon Density of States in *fcc*-Fe Precipitates in Cu

Since a nuclear resonant scattering method gives us information only from the resonant nuclei, if we apply this method to the precipitates of a resonant nucleus, *e.g.* ^{57}Fe, we can obtain information for the Fe-precipitates alone, apart from the host metal. Accordingly, we can study how the host metal affects and how far the effect extends to the precipitates through the interface. Nano-particle precipitates have attracted widespread attention due to their many technological applications, such as improving the mechanical properties of materials. Therefore the data obtained provide important knowledge and can contribute to the development of new materials. In this article, we report the phonon density of states (DOS) of *fcc*-^{57}Fe precipitates in a Cu matrix, investigated using the nuclear resonant inelastic scattering method at beamline **BL09XU** [1].

Even below room temperature, Fe precipitates in Cu retain the *fcc* structure, which is stable for bulk crystal of Fe above 1185 K under normal atmospheric conditions. The precipitates are known to be spherical and are coherent with the Cu matrix, as shown in Fig. 1. The sizes of the precipitates can be easily controlled by thermal treatment [2]. The particle sizes of the precipitates with diameters of 3, 8, 15, 30, 50 and 80 nm were studied at room temperature. Experimental phonon DOSs determined from the present experiment for the *fcc*-Fe precipitates at various particle sizes are given in Fig. 2. The experimental data on the isolated Fe impurities in Cu previously reported by M. Seto *et al.* are also given as zero-nm precipitates for comparison [3]. With increasing particle sizes, phonon DOS curves show continuous change up to 15 nm, but no appreciable change is found above 30 nm, indicating that the influence of the Cu host extends to about 30 nm. Since all precipitates have a common atomic mass, these changes in the phonon DOS should be attributed to the inter-atomic forces $f_{Fe\text{-}Cu}$ and $f_{Fe\text{-}Fe}$. If the $f_{Fe\text{-}Cu}$ is greatly different from the $f_{Fe\text{-}Fe}$, the phonon DOS curves for small precipitates should be composed of two parts, one from the interface area ($f_{Fe\text{-}Cu}$) and

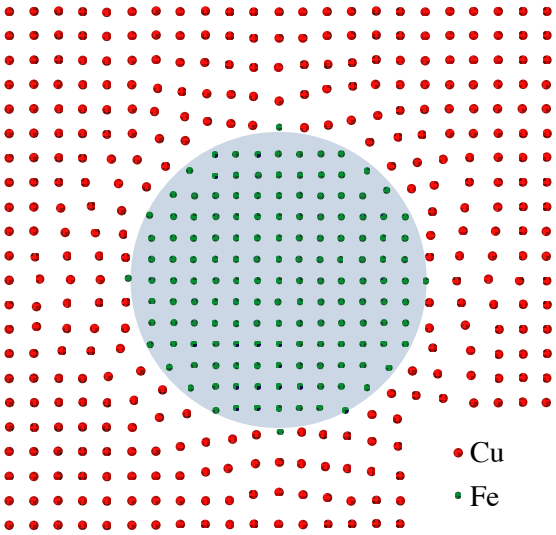

Fig. 1. Schematic illustration of coherent precipitates.

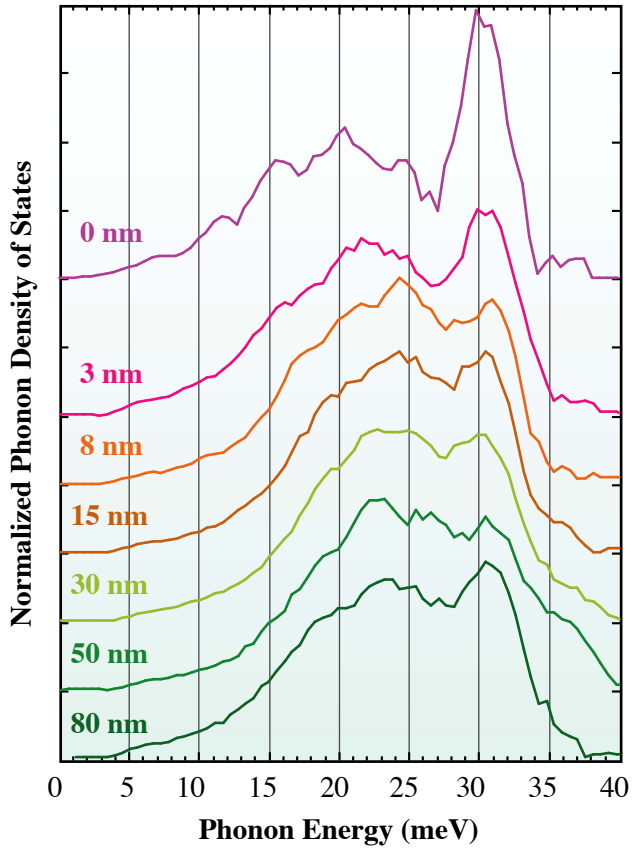

Fig. 2. Experimental phonon density of states (DOS) for various sizes of fcc-Fe precipitates in Cu measured at room temperature. Data for 0 nm indicate those for the isolated Fe impurities in Cu.

the other from inside the precipitates ($f_{Fe\text{-}Fe}$). The experimental phonon DOS changes gradually with increasing particle size. Thus, the influence of the Cu host is not confined to the interface area but uniformly extends over entire particles, and the effect should be attributed to the inter-atomic force $f_{Fe\text{-}Fe}$ itself. One possible explanation would be a change of the lattice parameter. The lattice parameter of the *fcc* -Fe precipitates is slightly smaller (0.7%) than that of Cu matrix and the precipitates are exposed to a strong expansive force. Consequently, the small precipitates have larger lattice spacing than the large ones [4], resulting in a change in the inter-atomic force $f_{Fe\text{-}Fe}$ of small precipitates.

Fcc -Fe precipitates in Cu undergo a structural phase transition at low temperature ($T_C \approx 65$ K), below which atomic positions are described by a periodic displacement wave propagating along the [1 1 0] direction with the <1 −1 0> polarization vector. Drastic softening of the sound velocity toward T_C has been reported [5]. Thus, the temperature variation of the phonon DOS for the *fcc* -Fe precipitates was also studied. Data obtained at various temperatures using the precipitates with a 50-nm diameter are given in Fig. 3. Phonon DOS curves show drastic change with decreasing temperature even though the displacement of lattices below T_C is very small. The peak intensity around 30 meV increases and the peak around 22 meV shifts toward the high-energy side with decreasing intensity. The structural phase transition is the first order, while

the change in phonon DOS appears to be continuous. The shape of the phonon DOS curve at 150 K already differs from that at room temperature, suggesting that the phonon dispersion curve, *i.e.*, inter-atomic potential starts to change far above the transition temperature. Recalling that *fcc*-Fe bulk crystal is stable only at much high temperature under normal atmospheric condition, we believe that the structural phase transition is the *fcc*-*bcc* martensitic transformation of the Fe metal. However, volume expansion and external shape change of the precipitates are tightly restricted by the host metal, and the martensitic transformation stopped at the halfway point of the transformation [6].

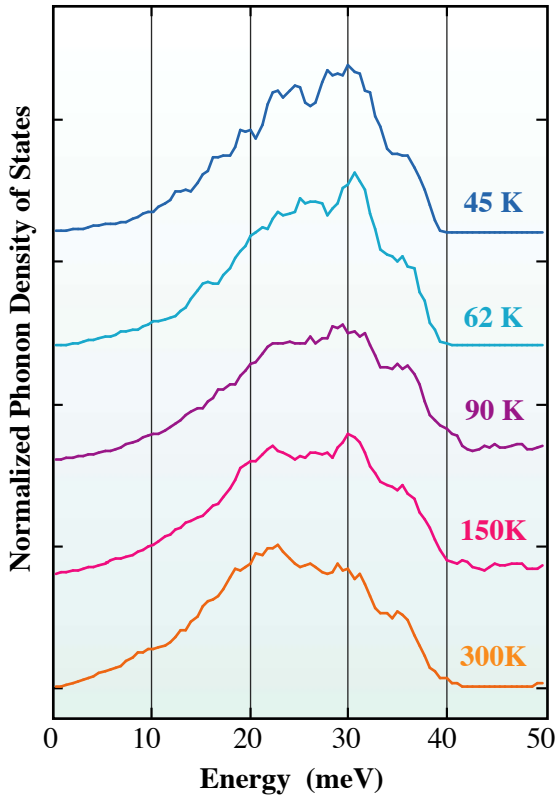

Fig. 3. Temperature variation of phonon density of states (DOS) of fcc-Fe precipitates. A specimen with precipitates of 50 nm in diameter was used.

Yorihiko Tsunoda

Waseda University

E-mail: tsunoda@waseda.jp

References

[1] Y. Tsunoda, Y. Kurimoto, M. Seto, S. Kitao and Y. Yoda, Phys. Rev. B **66** (2002) 214304.
[2] R. Borrelly *et al.*, Scr. Metall. **15** (1975) 747.
[3] M. Seto *et al.*, Phys. Rev. B **61** (2000) 11425.
[4] Y. Tsunoda *et al.*, J. Phys. F: Met. Phys. **18** (1988) 1421.
[5] Y. Tsunoda and N. Kunitomi, Solid State Commun. **54** (1985) 547.
[6] Y. Tsunoda, J. Phys. Soc. Jpn. **58** (1989) 1648.

Measurement of Long-lived Isotopes using Stroboscopic Detection of Synchrotron Radiation

Nuclear resonant elastic scattering of synchrotron radiation provides information on the hyperfine interactions between nuclei and their surroundings [1]. Traditionally, this information is deduced from the time response of the radiation to the nuclear excitation. In these experiments it is imperative that the time between two successive bunches is larger than the decay time of the nuclear ensemble. We present here an alternative to this method, called stroboscopic detection, in which the constraint on the bunch mode is significantly relieved, and which has the potential for providing complementary information.

Stroboscopic detection is performed in the heterodyne setup, meaning that two samples are put in the beamline: the sample under investigation and a single-line reference sample with known characteristics. The reference sample is given a variable velocity and thus its resonance energy is shifted by the Doppler-shift. The spectra are then taken as a function of the velocity of this reference sample. In nuclear resonant scattering experiments, it is crucial that the data corresponding to non-scattered photons is not incorporated in the spectrum because the number of non-scattered photons is several orders of magnitude larger than the number of nuclear resonantly scattered photons. This is related to the linewidth of the nuclear excited level, which is several orders of magnitude smaller than the bandwidth of the synchrotron radiation, even after the best high resolution monochromator. Because the nuclear resonantly scattered photons are delayed due to the lifetime of the nuclear excited level, they can be separated from the non-scattered photons by time-gating. Typically in stroboscopic detection, the fundamental frequency of this time-gating is equal to or is a multiple of the bunch frequency [2]. The intensity, integrated within the periodic set of time-windows as a function of the Doppler velocity is called the stroboscopic spectrum. This spectrum consists of several stroboscopic order components, each resembling a conventional Mössbauer spectrum.

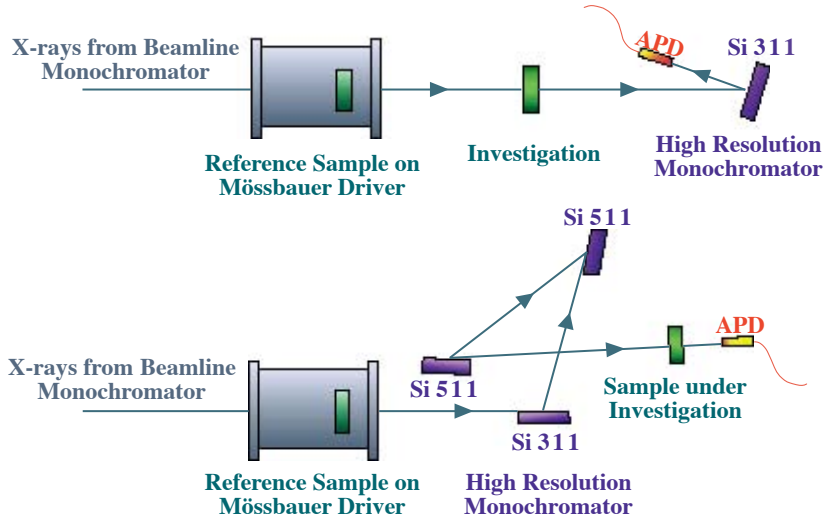

Fig. 1. Experimental setup for both experiments.

A specific property of stroboscopic detection is that the bunch mode is decorrelated from the lifetime of the nuclear isomer. The repetition frequency of the bunches is only restricted by the time response of the detector. Therefore, it is possible to study systems with a lifetime that is much longer than the bunch period, even longer than the circulation period of the electrons in the storage ring. To illustrate that resonances of long-lived isotopes can be detected using stroboscopic

detection, we performed two measurements at beamline **BL09XU** on ^{181}Ta. The lifetime of the isomeric state in a single ^{181}Ta nucleus is 8.7 μs. We used two ^{181}Ta metal foils with respective thicknesses of 3.8 μm and 2.8 μm. The decay time of the total nuclear ensemble was about 15 times shorter than the lifetime of the isomeric state in a single nucleus [3].

We performed two experiments, both in a velocity range of about 2 mm/s. The bunch mode in the first experiment was the 203-bunch mode, which has a bunch separation of 24 ns. The second experiment was performed in the 1/12 filling +10 single bunches mode. A picture of the experimental setup of both experiments can be found in Fig. 1. The delayed count rate in the first experiment was 6 counts per minute and in the second experiment this was 18 counts per minute. These low count rates are caused by the narrow linewidth of the nuclear excited level, which is linked to the large lifetime. The higher delayed count rate for the second experiment can be linked to a better efficiency of the avalanche photodiode detector [4] and a better high-resolution monochromator.

Figure 2 shows the experimental spectra. Because we are only interested in the resonance of the zeroth stroboscopic order, the shape of the time-windows is not crucial. In order to optimize from point of view of statistics, they are taken as broad as possible. For the first experiment (Fig. 2(a)), the first stroboscopic order spectrum component is out of the velocity range, and hence, only the zeroth order stroboscopic resonance can be observed. In the second spectrum, several stroboscopic resonances are generated within the velocity range. These constitute the negative sidebands in the spectrum (Fig. 2(b)).

In conclusion, with these two experiments we demonstrated the potential of stroboscopic detection to contribute to the research on long-lived isotopes. Thereby, the strength of stroboscopic detection is that there is no inherent restrictions on the lifetime of the nuclear levels to be investigated.

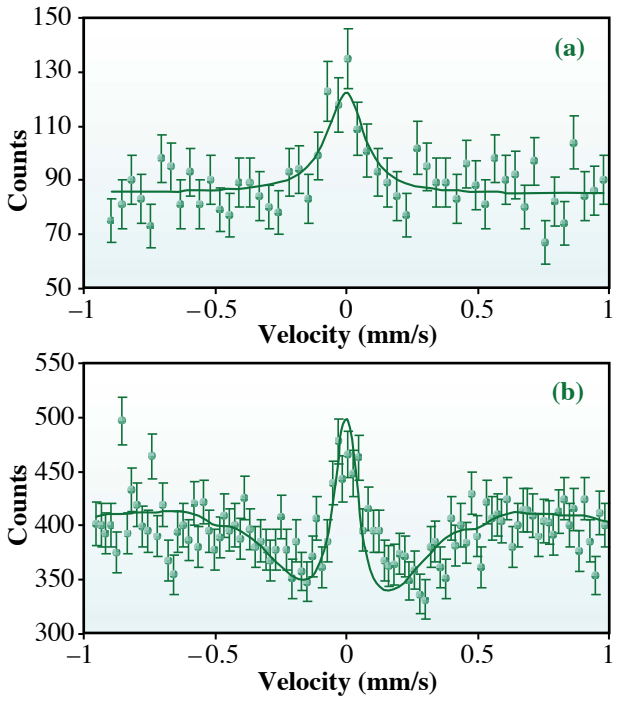

*Fig. 2. Stroboscopic spectra of two ^{181}Ta metal-foils with a bunch-mode of **(a)** 203 single bunches and **(b)** 1/12 filling + 10 single bunches.*

Romain Coussement, Riet Callens and Inge Serdons

Instituut voor Kern- en Stralingsfysica, K.U. Leuven, Belgium

E-mail: romain.coussement@fys.kuleuven.ac.be

References

[1] E. Gerdau and H. de Waard, Hyperfine Interact. **123-125** (2000) and references therein.
[2] R. Callens, R. Coussement, C. L'abbe, S. Nasu, K. Vyvey, T. Yamada, Y. Yoda, and J. Odeurs, Phys. Rev. B **65** (2002) 160404(R); R. Callens, R. Coussement, T. Kawakami, J. Ladriere, S. Nasu, T. Ono, I. Serdons, K. Vyvey, T. Yamada, Y. Yoda and J. Odeurs, Phys. Rev. B **67** (2003) 104423.
[3] A.I. Chumakov *et al.*, Phys. Rev. Lett. **75** (1995) 549.
[4] A.Q.R. Baron, Hyperfine Interactions **125** (2000) 29.

Soft X-ray Magnetic Circular Dichroism of c(2×2) CuMn Ordered Surface Alloy

Crystalline Mn is known as an antiferromagnetic or a paramagnetic material with quite a small magnetic moment. However, once Mn atoms crystallize with non-magnetic elements, such as Sb and even an oxygen atom, ferromagnetism appears as is found in MnSb or in $La_{1-x}Sr_xMnO_3$ [1]. Very small amounts of Mn in a semiconductor can also derive a degree of ferromagnetism, as discovered in (Ga, Mn)As [2]. One may extend this idea to a low dimensional case. An example is an Mn-based alloy fabricated on noble metal surfaces.

Wuttig *et al*. discovered that Mn based two-dimensional (2-D) ordered alloy can be formed on a clean Cu(001) surface at a coverage of 0.5 ML, where Mn and substrate atoms are alternatively placed forming a c(2×2) "checkerboard" structure, as shown in Fig. 1 [3]. A low energy electron diffraction (LEED) *I-V* measurement shows that the c(2×2) CuMn surface alloy has a pronounced corrugation in which Mn atoms in the first layer are displaced outwards by $\delta_Z = 0.30 \pm 0.02$ Å, which is 17% with respect to the atomic distance in the bulk [3]. Such a remarkable atomic displacement is surprising because the other c(2×2) ordered surface alloy systems with non-magnetic elements, namely c(2×2) CuAu/Cu(001) and c(2×2) CuPd/Cu(001) show only small relaxations of 6% and 1%, respectively, instead of the larger atomic radii of Au (1.442 Å) and Pd (1.375 Å) compared to that of Mn (1.365 Å) as listed in Table I.

A theoretical band structure calculation predicts that the most stable magnetic state for c(2×2) CuMn ordered surface alloy is a ferromagnetic structure in the ground state [3]. The theory also explains that the observed large relaxation of the Mn atoms are derived from the magnetism [3]. However, no experimental evidence of the ferromagnetic state of this surface alloy has been obtained so far. The lack of the experimental evidence possibly comes from the lower ferromagnetic transition temperature (Curie temperature) as usually found in ultra-thin films with

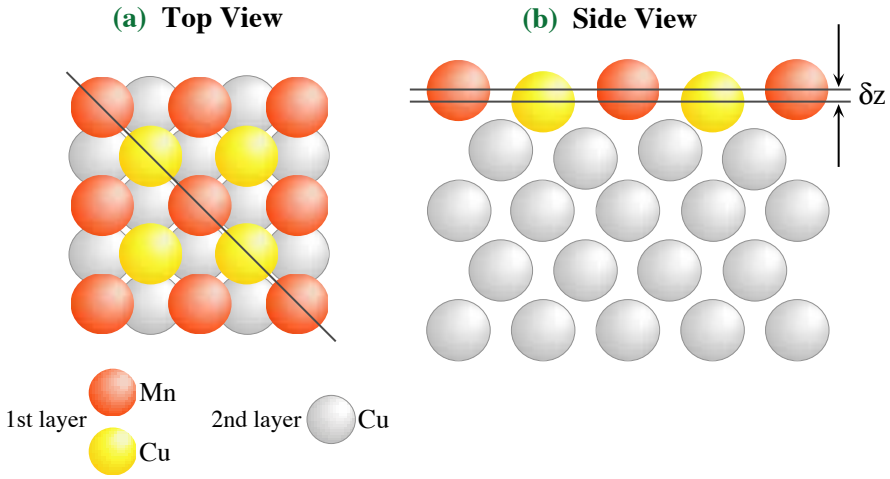

Fig. 1. Surface structure viewed from the top ***(a)*** *and from the side* ***(b)*** *of c(2×2) CuMn/Cu(001) 2-D ordered surface alloy as determined by LEED I-V analysis [3].*

Table I. *Atomic relaxation values determined by the LEED I-V analysis for several c(2×2) 2-D surface alloys [3].*

Structure	δz (Å)	Relaxation	Atomic radius (Å)
c(2×2) CuAu/Cu(001)	0.1	6 %	1.442
c(2×2) CuPd/Cu(001)	0.02 ± 0.03	1 %	1.375
c(2×2) CuMn/Cu(001)	0.30 ± 0.03	16.6 %	1.365
c(2×2) NiMn/Ni(001)	0.25 ± 0.03	14.2 %	1.365

a couple of 3*d* transition metal monolayers. For this reason, we have tried to observe the soft X-ray magnetic circular dichroism (XMCD) spectra in the Mn 2*p* core absorption region at low temperature at beamline **BL25SU**.

Soft X-ray magnetic circular dichroism (XMCD) in core level absorption spectrum provides us with useful information related to electronic states of magnetic materials. It is noted that the XMCD not only gives us element speeific magnetic moments, but also tells us how much an orbital (a spin) magnetic moment contributes to their total magnetic moments. Figure 2 shows an example of a submonolayer Mn grown on Ni(110) substrate [4]. One finds a clear XMCD of Mn and Ni 2*p* edges, and the polarities of the XMCD signals are the same for both Mn and Ni, meaning the directions of the magnetic moments are parallel between the Mn and the substrate Ni [4]. Thus one can surely obtain the element-specific information of the magnetic moments by conducting core-excited XMCD experiments.

The Mn 2*p* XAS and XMCD spectra of the c(2×2) CuMn/Cu(001) are shown in Fig. 3 [5]. We have observed several fine structures on all spin-orbit split components of the Mn 2*p* XAS spectrum.

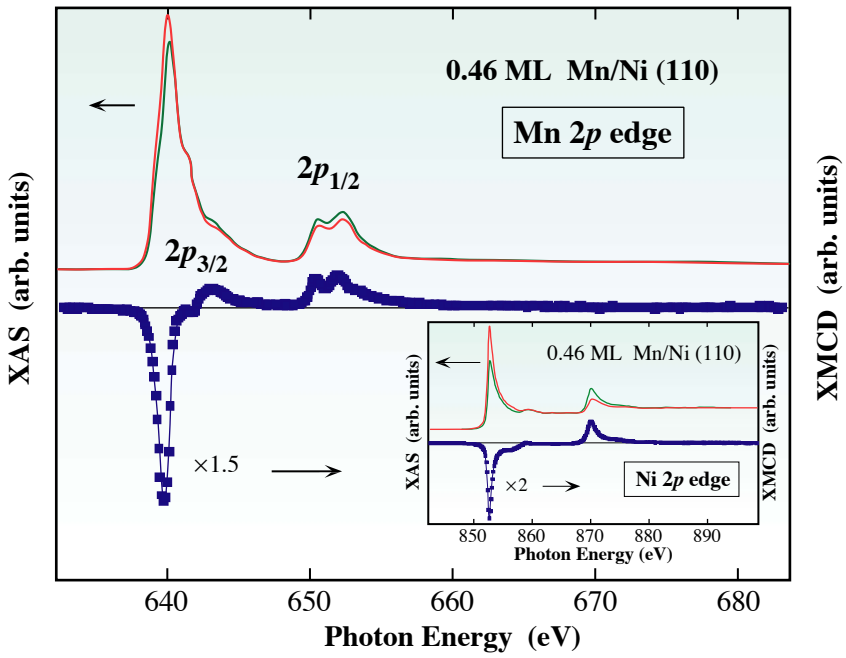

Fig. 2. Mn 2p XAS (upper) and XMCD (lower) spectra of 0.46 ML Mn ultrathin film on Ni(110). The inset shows the Ni 2p XAS (upper) and XMCD (lower) spectra of the same system. The ferromagnetic coupling between the Mn layer and the Ni substrate is clear. (see text)

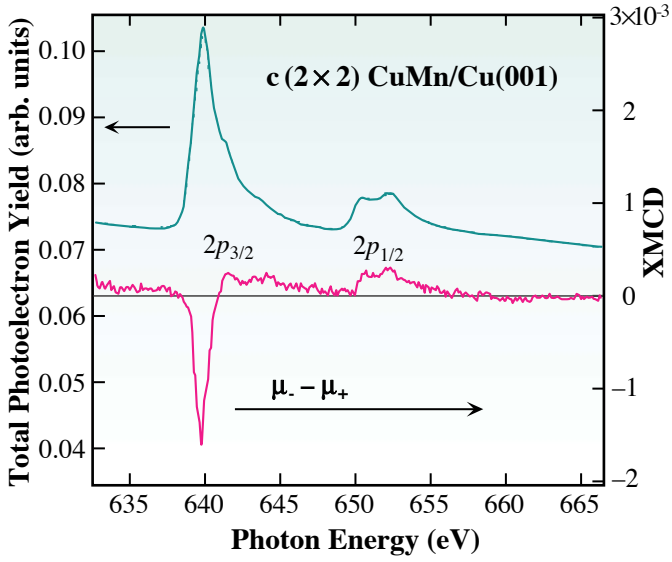

Fig. 3. Mn 2p XAS (upper) and XMCD (lower) spectra of c(2×2)CuMn/Cu(001) 2-D ordered surface alloy measured at T = 25 K. The XAS spectra are normalized by the incident photon flux. The XAS (XMCD) intensity scale is indicated at the left (right) axis.

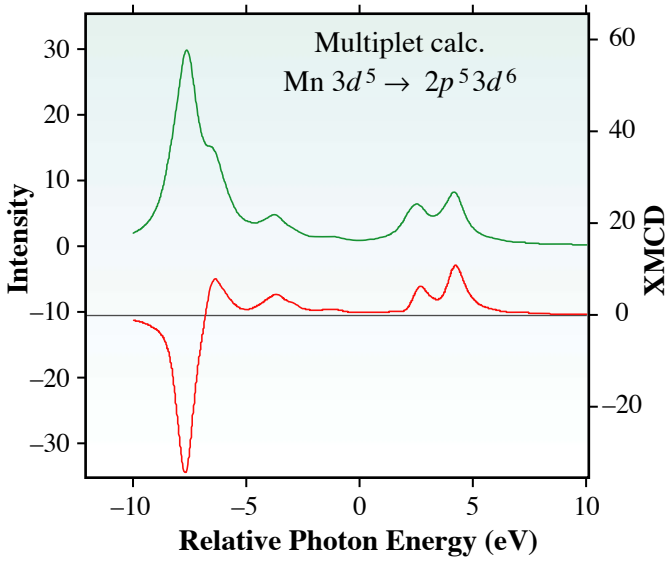

Fig. 4. Calculated Mn 2p XAS (upper) and XMCD (lower) spectra with Mn $2p^5 3d^6$ final state multiplets.

We found two shoulder states at energies ~1 and ~2 eV higher than that of the $2p_{3/2}$ main peak. Furthermore, a doublet peak structure was found for the $2p_{1/2}$ component. However, we have clearly observed the XMCD signal at T = 25 K as shown in the lower part of Fig. 3, which indicates the existence of the long-range ferromagnetic order under the external magnetic field (~1.4 T). The present XMCD spectrum shows the negative structure followed by the weaker positive structure with increasing hν in the $2p_{3/2}$ core excitation region, whereas the double peak structure with the positive sign exits in the $2p_{1/2}$ region.

We now compare the experimental Mn 2*p* XAS and XMCD spectra with the calculated Mn $2p^5 3d^6$ final state multiplets with assuming the $3d^5$ as the ground state configuration [5]. As shown in Fig. 4, we find excellent correspondence with the experimental XMCD spectrum as well as the XAS one, which shows that the observed several fine structures are derived from the multiplet effects. This result clearly indicates an almost half-filled electron nature leading to the high spin magnetic moment of the Mn atom.

Akio Kimura

Hiroshima University

E-mail: akiok@hiroshima-u.ac.jp

References

[1] M. Imada, A. Fujimori and Y. Tokura, Rev. Mod. Phys. **70** (1998) 1039.
[2] H. Ohno, J. Magn. Magn Mater. **200** (1999) 110.
[3] M. Wuttig *et al.*, Surf. Sci. **292** (1993) 189; M. Wuttig *et al.*, Phys. Rev. Lett. **70** (1993) 3619.
[4] T. Xie *et al.*, Jpn. J. Appl. Phys. **42** (2003) - in press.
[5] A. Kimura, T. Kanbe, T. Xie, S. Qiao, M. Taniguchi, T. Muro, S. Imada and S. Suga, Jpn. J. Appl. Phys. **42** (2003) - in press.

Soft X-ray Photoelectron Spectroscopy in Silicon Clathrate Superconductors

Silicon clathrate compounds consist of fullerene-like polyhedral Si-cages, which share their faces to form a three-dimensional Si-sp^3 covalent network. Guest elements such as an alkali atom or an alkali-earth one can be encapsulated in the cage. Recently, these compounds have attracted strong interest due to the discovery of superconductivity in a metal-doped silicon clathrate, $Ba_6Na_2Si_{46}$ [1], as well as the potential for thermoelectric applications.

Barium encapsulated type-I silicon clathrate, Ba_8Si_{46}, has been reported to show superconductivity below $T_c \sim 8$ K [2], which is the highest T_c observed in the silicon clathrate family. As schematically shown in Fig. 1, the crystal structure of Ba_8Si_{46} consists of two types of polyhedral cages, *i.e.* dodecahedral (Si_{20}) and tetrakaidecahedral (Si_{24}) cages. In an ideal-composition phase, Ba atoms occupy all of the cages resulting in the chemical formula of Ba_8Si_{46} per cubic unit cell. In Ba_8Si_{46}, we can substitute Ag atoms for Si atoms in 'Si (1)' sites shown in Fig. 1, where the chemical formula becomes $Ba_8Ag_xSi_{46-x}$ ($0 \le x \le 6$). The solid solution of Si and Ge clathrate, $Ba_8Ge_ySi_{46-y}$ ($0 \le y \le 40$), and pure germanium clathrate Ba_8Ge_{43} also have been synthesized. In both cases, the superconducting transition temperature T_c has been found to systematically decrease with increasing Ag or Ge concentration.

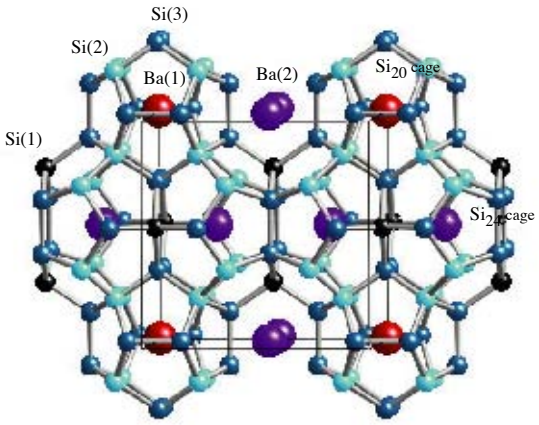

Fig. 1. Schematic illustration of crystal structure of silicon clathrate Ba_8Si_{46}. Two types of fullerene-like polyhedral cages, i.e. Si_{20} and Si_{24} cages, share their faces to form the sp^3 covalent network. A Ba atom is encapsulated in each cage.

Photoelectron spectroscopy (PES) allows us to directly observe the electronic structures in the valence band in addition to the core electrons in solid substances. Recently, it has been recognized that high-resolution PES using relatively high-energy soft X-ray is quite a powerful tool for investigating the bulk-states of solids. In the present study [3], PES was carried out by using a synchrotron radiation soft X-ray to investigate the electronic structure of silicon clathrate family. The relationship between the electronic structure and the systematic change of superconducting nature of silicon clathrate family is discussed.

Polycrystalline samples of clathrates $Ba_8Ag_xSi_{46-x}$ ($0 \le x \le 6$), $Ba_8Ge_ySi_{46-y}$ ($0 \le y \le 40$) and Ba_8Ge_{43} (pure germanium clathrate) were prepared by using a high-pressure synthesis technique as reported in previous works [1, 2]. Photoelectron spectra were measured at beamline **BL25SU** with various photon energies $h\nu$ between ~240 and ~1200 eV. The total energy resolution was ~150 meV at $h\nu$ ~ 800 eV . Samples were cooled down to 20 K. obtain clean surfaces, samples were fractured under the ultrahigh vacuum of $\sim 1 \times 10^{-10}$ Torr just before the measurements were taken.

The valence-band photoelectron spectra of Ba_8Si_{46} are shown in Fig. 2. The horizontal axis indicates the binding energy E_B, where 0 eV corresponds to the Fermi energy E_F. Red and blue dots are measured by using excitation photon energy of $h\nu \sim 785$ and ~776 eV, respectively. The former corresponds to the Ba 3*d* to 4*f* transition

energy, called 'on resonance,' and the latter is below the Ba 3*d* to 4*f* transition energy, called 'off resonance.' The letters A-D indicate four prominent structures. The overall spectral shape is similar to the density of states (DOS) calculated by using local density approximation (LDA) [4]. The structures A-C are assigned to the *s* -, *sp* - and *p*-like bands characteristics to the sp^3 bonded Si_{46} network. The extremely narrow band D, with the width of ~ 0.3 eV, is seen beside the *p* -band with a gap of ~ 1.2 eV. In a previous work [5], however, ultraviolet photoelectron spectra (UPS) showed a broad extra peak in the gap between C and D. It was proposed that the discrepancy between the UPS and the calculated DOS were caused by electron-correlation effects. The UPS, however, may include surface-state components due to a short photoelectron mean free path.

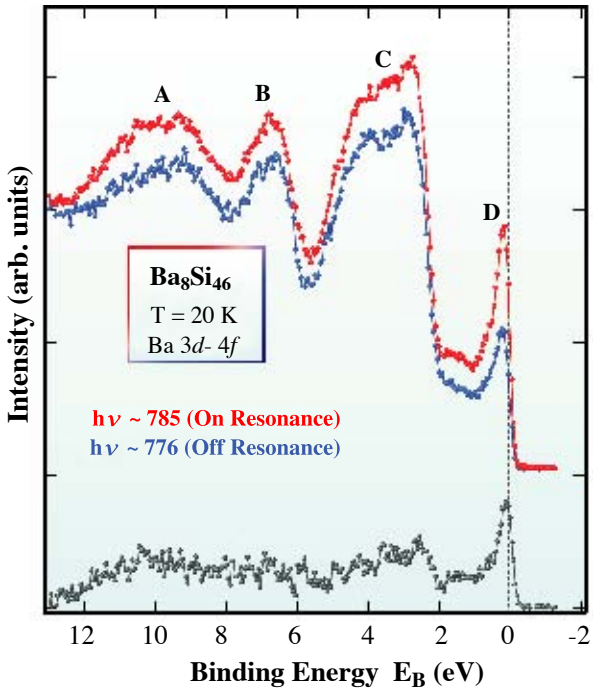

Fig. 2. Valence-band photoelectron spectra of silicon clathrate Ba_8Si_{46}. Red and blue dots are measured by using excitation photon energy of hν~ 785 and ~ 776 eV, respectively. The former corresponds to the Ba 3d to 4f transition energy, called 'on resonance,' and the latter is below the Ba 3d to 4f transition energy, so called 'off resonance.' The black dots show the difference spectrum between the 'on resonance' and the 'off resonance' spectra.

The present results, which are more bulk-sensitive spectra, basically support the LDA calculation, indicating that the electron-correlation effects are not so strong in Ba_8Si_{46}. It is noticed that the Fermi level E_F is located at the band D, resulting in the high DOS at E_F. The black dots in Fig. 2 show the difference spectrum between the 'on resonance' and the 'off resonance' spectra. Generally speaking, this spectrum corresponds to the Ba related partial DOS in the valence band. The band D is obviously enhanced by the Ba 3*d* - 4*f* resonance excitation; therefore, it is confirmed that the Ba orbital strongly contributes to the band D. The LDA calculation has predicted the narrow band at E_F, constructed by a hybridization of Ba 5*d* orbital and the conduction band of the Si_{46} network. The high DOS at E_F is expected to be responsible for the relatively high T_c in terms of the Bardeen-Cooper-Schrieffer (BCS) theory for phonon-mediated superconductivity. Furthermore, Ba-related states seem to spread widely over in the valence band, as seen in the difference spectrum in Fig. 2. It may originate from the hybridization between *s*-like state of Ba and valence band of the Si_{46} network.

The valence-band photoelectron spectra of $Ba_8Ag_xSi_{46-x}$, $Ba_8Ge_ySi_{46-y}$ and Ba_8Ge_{43} are shown in Fig. 3. The intensity of the band D systematically decreases with increasing Ag concentration in $Ba_8Ag_xSi_{46-x}$, as seen in the lower half of Fig. 3. Simultaneously, new states appear between the C and D bands at E_B = 0.5 ~ 2 eV, whose intensity increases with the Ag concentration. Similar phenomena are also observed in the solid solution of Si and Ge clathrate as shown in the upper half of Fig. 3. In Fig. 4, the superconducting transition temperature T_c of clathrates is plotted as a function of the integrated intensity of the band D. It is clear that the sample with higher T_c has a band D with higher intensity. The decrease in the intensity of the band D means the decrease in DOS at E_F. This must be responsible for the decrease in T_c in

the clathrates, $Ba_8Ag_xSi_{46-x}$ and $Ba_8Ge_ySi_{46-y}$, in terms of the BCS theory.

The core level spectra of Si 2*p*, Ag 3*d* and Ba 4*d* show systematic change with increasing x in $Ba_8Ag_xSi_{46-x}$. From the analysis of the chemical shift of core level spectra, it is found that there is systematic electron transfer from Ba atoms to the Ag + Si network with increasing x. This may weaken the hybridization between Ba and the Si network, resulting in the decrease of the band D. The new state at E_B = 0.5 ~ 2 eV may be constructed by acceptor states originating from the Ag and Si hybridization in $Ba_8Ag_xSi_{46-x}$. On the other hand, in $Ba_8Ge_ySi_{46-y}$ and Ba_8Ge_{43}, the core level spectra of Ge 3*d* and Ba 4*d* show systematic change with increasing the Ge concentration. The Si 2*p* spectra, however, does not show any change. The new states at E_B = 0.5 ~ 2 eV may be constructed by the Ge and Ba hybridization, in $Ba_8Ge_ySi_{46-y}$ and Ba_8Ge_{43}. Consequently, the weakened hybridization between Ba and Si network results in the decrease in the band D.

In conclusion, we have investigated the electronic structure of silicon clathrate superconductors by using the bulk-sensitive PES. We have clarified the relationship between the electronic structure and the systematic change of superconducting nature of the silicon clathrate family.

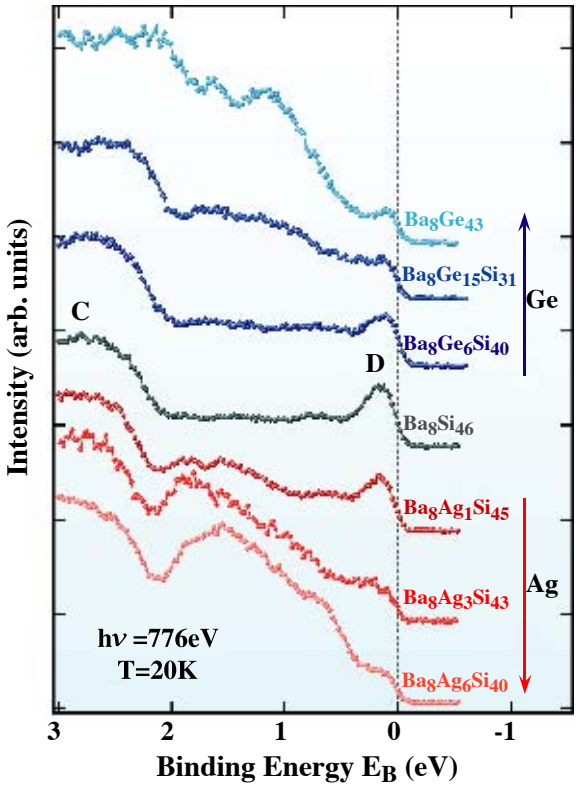

Fig. 3. Valence-band photoelectron spectra of silicon clathrates $Ba_8Ag_xSi_{46-x}$, $Ba_8Ge_ySi_{46-y}$ and Ba_8Ge_{43} measured by using excitation photon energy of hν ~ 776 eV.

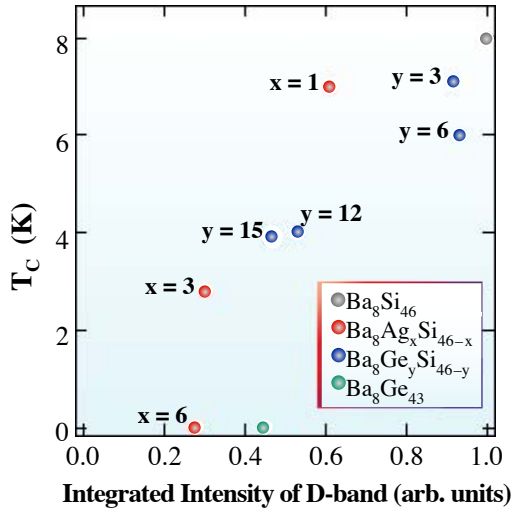

Fig. 4. Relationship between the superconducing transition temperature T_C and the intensity of the band D (see Fig. 2 and 3) in valence-band photoelectron spectra of silicon clathrates $Ba_8Ag_xSi_{46-x}$, $Ba_8Ge_ySi_{46-y}$ and Ba_8Ge_{43}.

Takehito Nakano and Keisuke Kobayashi

SPring-8 / JASRI

E-mail: nakano@spring8.or.jp

References

[1] H. Kawaji *et al.*, Phys. Rev. Lett. **74** (1995) 1427.
[2] S. Yamanaka *et al.*, Inorg. Chem. **39** (2000) 56.
[3] T. Nakano, N. Kamakura, Y. Ikemoto, K. Kobayashi, T. Muro, Y. Nozue, H. Fukuoka, S. Yamanaka and S. Shin - in preparation.
[4] K. Moriguchi *et al.*, Phys. Rev. B **61** (2000) 9859.
[5] T. Yokoya *et al.*, Phys. Rev. B **64** (2001) 172504.

Chemical Science

The chemical sciences cover a broad range of subjects dealing with chemical changes and related phenomena of substances, including free molecules, clusters, surfaces, and solids. The highly brilliant light from SPring-8, covering a whole range of wavelengths from hard X-rays to far infrared, is evidently very useful for the study of various aspects of chemical reactions. In this section, four conspicuous topics in Chemical Science are selected from the experimental reports 2001B and 2002A.

Soft X-ray undulator beamlines play a central role in the study of spectroscopy and dynamics because the inner-shell excitation/ionization energies of elements of chemical interest lie in the soft X-ray region. By taking advantage of very high resolving power of these beamlines, an increasing number of high quality studies have been performed over the years since the commissioning of each beamline. Progress in this field during the last year includes the successful extension of the coincidence momentum imaging technique to the study of photoelectron angular distribution in the molecular frame (article by De Fanis *et al.*).

Another important and widely-used technique in Chemical Science is the X-ray diffraction. With the dramatic increase in the capability by combining with the 3rd generation synchrotron radiation, both the single-crystal and powder diffraction techniques are increasingly being used to probe rather exotic systems; such studies include the characterization of intermediate states of a laser-induced chemical reaction in a solid (article by Ozawa and Toriumi), the study of the structure of adsorbed or deposited layers on metal electrodes (article by Nakamura and Ito), and the direct observation of the molecular state adsorbed in the nanoporous metal-organic solid (article by Kitagawa). All of these pioneering works are yielding intriguing new results.

Inosuke Koyano

Inner-Shell Photoemission from Free Molecules in the Molecular Frame Probed by the Electron-Ion Coincidence Momentum Imaging Technique

Photoelectrons from molecules are scattered by the anisotropic molecular potential. One can study such scattering effects by measuring photoelectron emission in the molecular frame. The experimental technique we use for such a study is momentum imaging, which is based on the time of flight measurement combined with the measurement of the position of detection for the charged particles. A momentum imaging apparatus was installed on beamline **BL27SU** a couple of years ago and was first used for measuring three-dimensional (3-D) momentum of fragment ions produced via the core excitation of CO_2 molecules [1]. One can also employ this technique for molecular inner-shell photoelectrons. The measurement of the 3-D momentum of a photoelectron in coincidence with fragment ions, emitted over 4π sr, allows us to obtain photoelectron angular distributions in the molecular

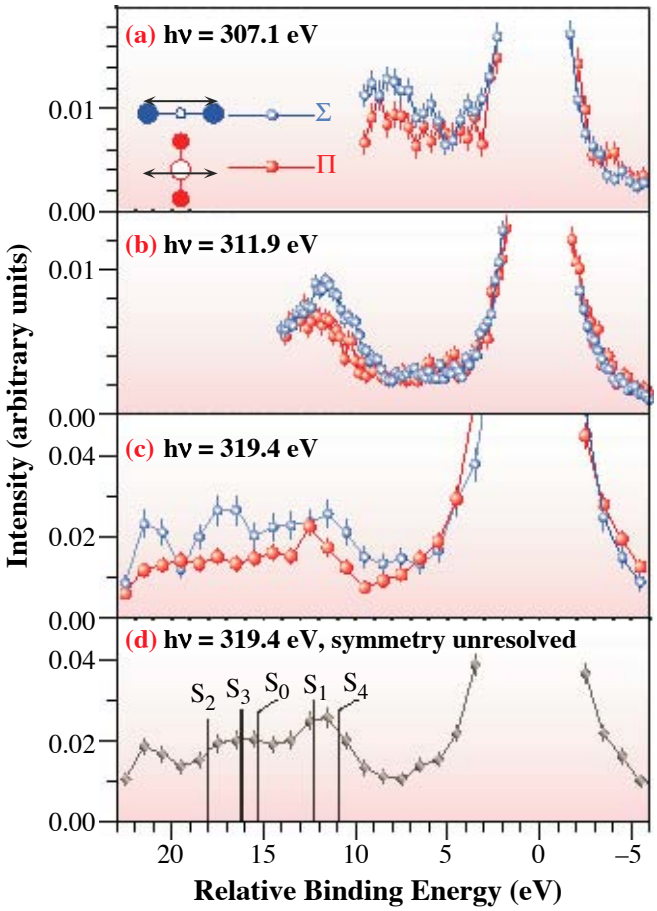

*Fig. 1. Photoelectron spectra of CO_2 for the molecular axis fixed in space parallel (Σ), and perpendicular (Π) to the direction of the electric vector of the incident light, **(a-c)**, and without selection of the molecular axis **(d)**.*

frame, as well as photoelectron spectra of selected symmetries for the ionization continuum. Here we present such a photoemission study of CO_2 molecules and the argon dimers.

In Fig. 1, we present CO_2 C1*s* photoelectron spectra for selected symmetry of the ionization continuum with resolution sufficient to resolve the satellite structure. This satellite structure is attributed to the excitation of a valence electron to the unoccupied molecular orbital accompanying core ionization. The energy scale represents the binding energy relative to the main photoline, and the intensity is normalized so that the integrated area of each spectrum is unity. For Σ and Π symmetries of the ionization continuum the molecular axis is parallel and perpendicular, respectively, to the electric vector of the incident light. Thus, we can resolve the symmetries of the continuum channel by filtering the fragment ions emitted at 0° or 90° with respect to the electric vector. From these symmetry-resolved photoelectron spectra, one can learn that the creation of the satellites is more efficient for the Σ rather than the Π channel, stemming from the fact that the slow photoelectron interacts more strongly with the valence electrons when the photoelectron is emitted along the molecular axis [2].

Figure 2 presents photoelectron angular distributions (PAD) for C1*s* ionization of CO_2 molecules in the molecular frame, with the molecular axis oriented along, at 45°, and perpendicular to the electric vector of the incident light. The major features of these measured PADs are fairly accurately reproduced by calculations employing a relaxed-core Hartree-Fock approach, as can be seen in the figure. In contrast to the well-known PAD for N 1*s* ionization of N_2, which exhibits a rich structure dominated by the f-wave ($\ell = 3$) at the shape resonance [3], the PAD for C 1*s* photoionization of CO_2 is quite unstructured over the entire observed range

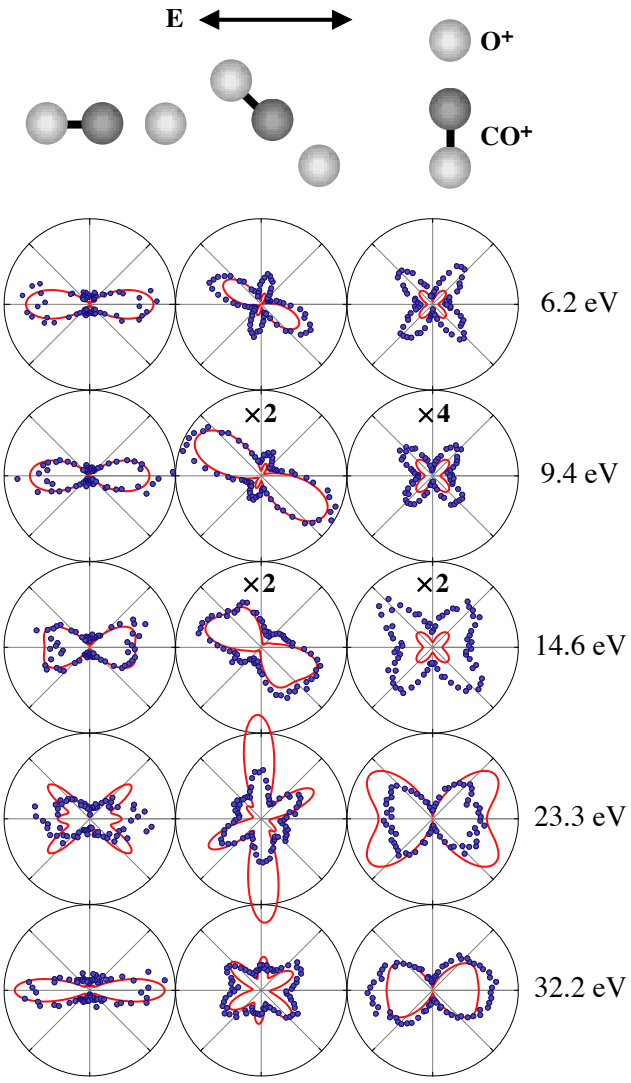

Fig. 2. Polar plots of C 1s photoelectron angular distributions of CO_2 molecules in a molecular frame, at electron kinetic energies of 6.2, 9.4, 14.6, 23.3 and 32.2 eV. The dots and curves correspond to measurements and calculations, respectively. The direction of the electric vector of the incident light, E, is horizontal. The molecular axis is at 0°, 45°, and 90° with respect to E.

across the shape resonance, illustrating that more than one partial wave contribute to the formation of the shape resonance, and that these waves interfere with each other [4].

In Fig. 3, we present PADs for the argon 2*p*-shell ionization of argon dimers. Here the PAD's dependence on the direction of the electric vector of the incident light has been removed by integrating over all relative orientations of the dimer axis with respect to the electric vector. The photoemission events belonging to the dimers have been filtered out with the momentum imaging of two Ar^+ ions by requiring momentum conservation for the fragments; the event is attributed to the dimer only if the two Ar^+ have opposite momentum vector. Comparison with *ab initio* calculation is necessary to interpret the process, and this will be performed in the near future.

In the future we intend to systematically extend this electron-ion coincidence momentum imaging technique to a photoemission study of three-dimensional polyatomic molecules.

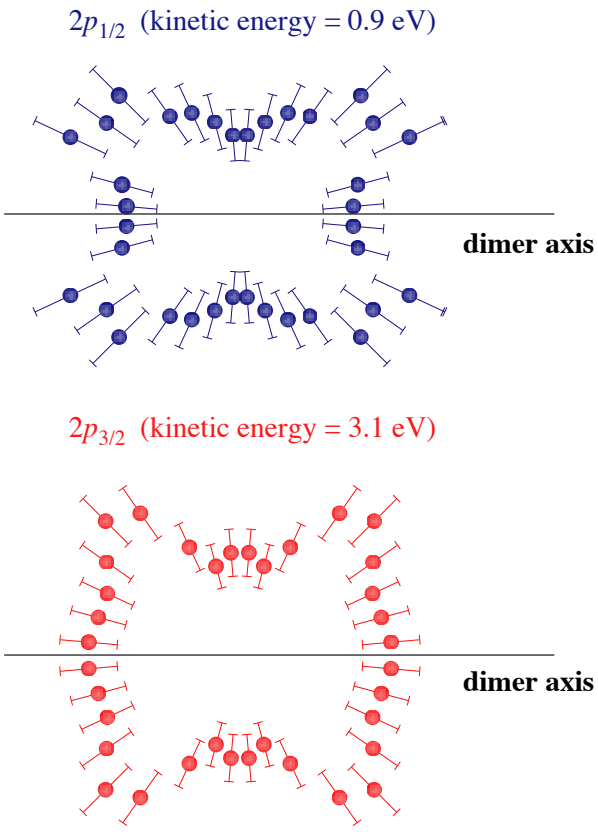

Fig. 3. Polar plots of Ar $2p_{1/2}$ and $2p_{3/2}$ photoelectron angular distributions of argon dimers in the molecular frame. The dependence on the relative orientation between the dimer axis and the electric vector of the incident light is removed by integrating over the all possible relative orientations.

Alberto De Fanis[a], Norio Saito[b] and Kiyoshi Ueda[c]

(a) SPring-8 / JASRI
(b) National Institute of Advanced Industrial Science and Technology
(c) Tohoku University

E-mail: defanis@spring8.or.jp

References

[1] see for example Y. Muramatsu *et al.*, Phys. Rev. Lett. **88** (2002) 133002.
[2] A. De Fanis *et al.*, Phys. Rev. Lett. **89** (2002) 023006.
[3] E. Shigemasa *et al.*, Phys. Rev. Lett. **74** (1995) 359.
[4] N. Saito, A. De Fanis, K. Kubozuka, M. Machida, M. Takahashi, H. Yoshida, I.H. Suzuki, A. Cassimi, A. Czasch, L. Schmidt, R. Dörner, K. Wang, B. Zimmermann, V. McKoy, I. Koyano and K. Ueda, J. Phys. B: At. Mol. Opt. Phys. **36** (2003) L25.

Photoexcited Molecular Structure of Diplatinum (II) Complex by Single-Crystal X-ray Structure Analysis

Direct observation of geometrical changes following photo-excitation of molecules provides essential information on transient species such as metastable states of chemical reactions and excited states, which are sometimes difficult to describe by molecular orbital calculations. Although single-crystal X-ray structure analysis is a powerful and conventional tool for obtaining accurate molecular geometry and structural parameters, there are some difficulties to be overcome to determine the structure of photo-excited molecules using ordinary diffractometers. Because of the extremely small populations and small geometrical changes of excited-state molecules in crystals, photo-excited crystallography requires more accurate measurements of diffraction intensities. We have developed a new low-temperature vacuum (LTV) X-ray camera installed on beamline **BL02B1** (Fig. 1), in addition to a special data collection system, the multiple-exposure IP method for excited-state crystallography. We report here the instrumentation and its first application to the luminescent diplatinum(II) $[Pt_2(pop)_4]^{4-}$ complex.

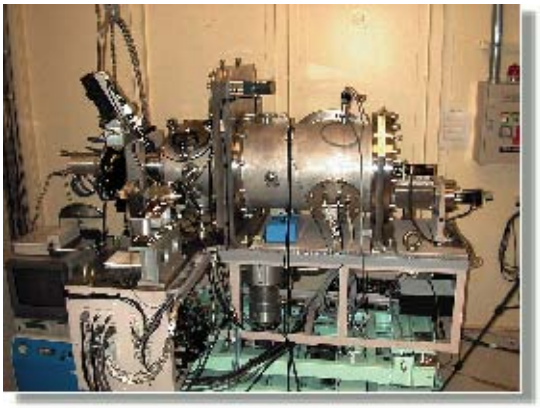

Fig. 1. Low-temperature vacuum X-ray camera.

The LTV camera is specially designed for accurate diffraction measurements with high S/N ratios at low temperature (< 80 K). To obtain diffraction images with extremely low background, an image plate (IP) is placed in a vacuum chamber preventing X-ray scattering from air and vacuum windows. A crystal specimen is mounted on a cold head of He refrigerator and can be cooled down to 20 K under a high vacuum. Crystal rotation, IP positioning, and the IP readout system are fully computer controlled for phi-oscillation and screenless Weissenberg modes. An additional feature of this camera is the multiple-exposure mode, in which both diffraction patterns under light-irradiated (light-on) and non-irradiated (light-off) conditions are recorded on the same IP frame. The first exposure by phi-oscillation mode under the light-off condition is followed by the second one under the light-on condition after a slight shift (1 to 2 mm) of the IP holder, and these processes are repeated several times to minimize systematic errors in the intensity measurements (Fig. 2). The doubly-recorded diffraction images can be read at the same time under the same conditions, giving accurate measurements of intensity change for each reflection. A laser light for photo-excitation can be introduced through fiber optics into the vacuum chamber and focused on the crystal (Fig. 3).

The $[Pt_2(pop)_4]^{4-}$ complex ion consists of two Pt(II) atoms bridged by four pyrophosphate ligands (Fig. 4). Two PtP_4 square planer moieties are stacked with an eclipsed configuration, and the Pt-Pt distance is 2.93 Å. Formally, there are no direct metal-metal bonds. Spectroscopic investigations of the complex show strong green luminescence,

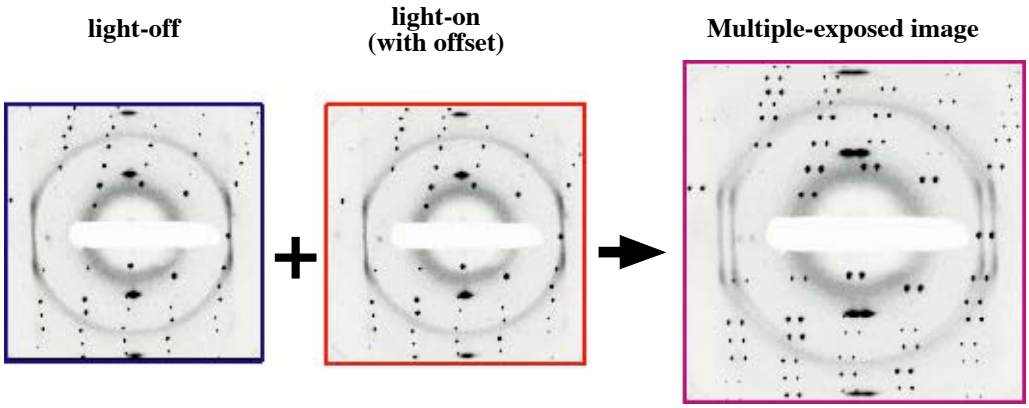

Fig. 2. Multiple-exposure IP method. The first X-ray exposure is followed by the second one after a 1 - 2 mm shift of the IP holder without readout or erasing processes. The doubly-recorded images are read at one time.

which has been attributed to $^3A_{2u} \rightarrow {}^1A_{1g}$ phosphorescence [1]. Emission spectra of the Ba^{2+} salts at 5 K exhibit fine structures with a spacing of 150 cm^{-1}, which are assigned to Pt-Pt stretching vibration in the $^3A_{2u}$ excited state [2]. The frequency of the vibrational structure in the excited states is higher than that in the ground state (116 cm^{-1}), suggesting an effective Pt-Pt bond formed in the excited states. The $^1A_{1g} \rightarrow {}^1A_{2u}$ absorption corresponds to the $5d\sigma^* \rightarrow 6p\sigma$ electronic transitions.

A single crystal of $(n\text{-}Bu_4N)_2H_2[Pt_2(pop)_4]$ situated on top of carbon fiber supports was mounted on the camera, and was kept at 54 K. A He-Cd blue CW laser (442 nm/100 mW) was used for photo-excitation, continuously illuminating during the light-on period to maintain the crystal in a pseudo-steady state. The multiple-exposure oscillation photo comprising alternating light-off and light-on periods for 24 seconds each was repeated ten times to record one IP frame. 52 frames of oscillation photo were subjected to intensity data processing. Standard crystal structure analyses were performed using each light-on and light-off intensity data sets independently. Lattice constants for the light-on data set were slightly larger than that for the light-off set. However, standard structural analysis showed that there were no differences in atomic parameters except an increase in temperature factors for the light-on data set. These results indicate that the heating effect by laser irradiation has caused a small temperature rise that led to expansion of the unit-cell volume in the light-on condition.

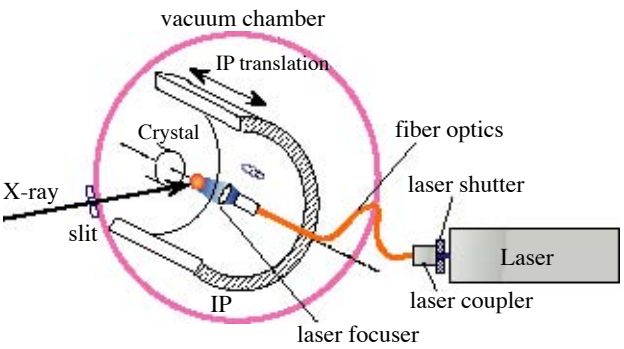

Fig. 3. Schematic layout of the LTV camera with laser irradiation optics.

To reveal small changes of crystal structure between the light-on and light-off data sets, difference Fourier syntheses were performed for $|F_{on}| - |F_{off}|$ using the phase factors calculated by the atomic parameters of the light-off data set. The observed electron density map (Fig. 4) shows positive and negative peaks with heights of 1 - 2 e/Å^3 near the Pt atoms, indicating that a small portion of the metal atoms moves toward the positive peaks in the light-on crystal. The Pt(1) atom shifts toward the Pt(2) position, while the Pt(2) atom shifts within the plane perpendicular to the Pt-Pt vector. These results clearly reflect shrinkage in the Pt-Pt distance. Changes in the geometrical parameters of the Pt atoms were analyzed quantitatively by least-squares calculations based on the response ratio (defined as $\eta = (I_{on} - I_{off})/I_{off}$) [3]. The positional and occupancy parameters of the Pt atoms in the excited states reveal that the Pt(1*)–Pt(2*) distance in the excited state is 2.70 (4) Å, which is 0.23 Å shorter than that of the ground state (Pt(1)–Pt(2) 2.9289 (2) Å) [4].

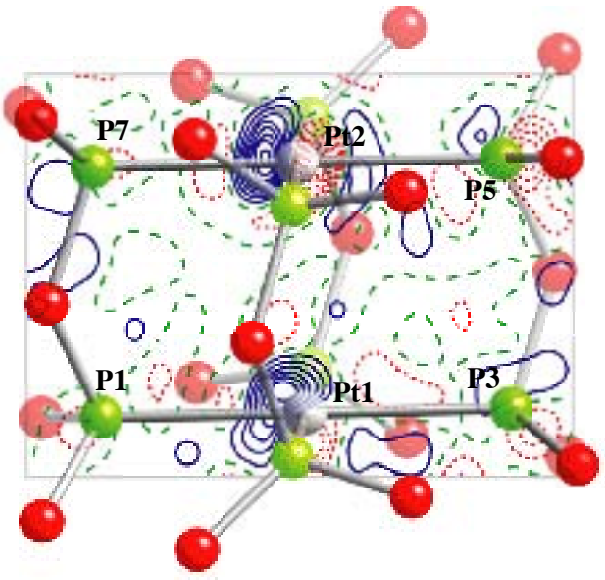

Fig. 4. Difference Fourier map (superimposed with a molecular diagram) of $|F_{on}| - |F_{off}|$ in a plane containing Pt(1)–Pt(2) vector and coordinated four P atoms of the ligands. Continuous lines and dashed lines indicate positive and negative density, drawn at every 0.2 e/Å^3, respectively.

Yoshiki Ozawa and Koshiro Toriumi

Himeji Institute of Technology

E-mail: toriumi@sci.himeji-tech.ac.jp

References

[1] D. M. Roundhill *et al.*, Acc. Chem. Res. **22** (1989) 55.
[2] A. P. Zipp, Coord. Chem. Rev. **84** (1988) 47.
[3] Y. Ozawa *et al.*, J. Appl. Cryst. **31** (1998) 128.
[4] Yoshiki Ozawa, Madoka Terashima, Minoru Mitsumi, Koshiro Toriumi, Nobuhiro Yaduda, Hidehiro Uekusa and Yuji Ohashi, Chem. Lett. **32** (2003) 62.

Structures of Electrode Surfaces Studied by *In Situ* Surface X-ray Diffraction: New Structures of Water Adsorbed on Au(1 1 1) Electrode Surface

The adsorption of a water molecule and coadsorption of a water molecule with electrolyte ions on a metal electrode surface is a fundamental issue of electrochemical surface science. So far, the role of the hydration water molecule in electrode reactions on an electrode surface remains unclear. The two-dimensional structure of water molecules on a surface gives an insight into important mechanisms concerning electron and proton transfer or weak interactions of water molecules with surfaces. Recent studies of water adsorption on metal surfaces are almost entirely limited to the adsorption of water under UHV conditions. *In situ* observation of water adsorption on a real electrode surface is quite difficult due to the hindrance of electrolyte solution on the electrode surface. To understand the role of hydration water molecules on electrochemical double layers on an electrode surface, it is imperative to reveal the structure of hydration water molecules in the double layers under an electrode potential control.

It is well known that water forms a tetrahedral network structure not only in ice (solid), but also in liquid (solution) phases. The density of these phases is approximately one unit. Recently, however, the existence of a high-density water (1.5 - 2.0) has been observed for a water structure on an electrode surface [1]. Thus, it might be possible to find a new two-dimensionally extended water phase on a metal electrode surface. Recent progress with synchrotron radiation has made it possible to observe structures extended on surfaces or interfaces by two- or three-dimensional structure analysis, and we have applied this surface X-ray diffraction technique to one of the most important systems of electrochemistry : the underpotential deposition (UPD) of copper on an Au(111) electrode surface. Figure 1 shows a cyclic voltammogram (CV, current-potential curve) associated with copper deposition on an Au(111) electrode surface in H_2SO_4 solution. In general, metal monolayer deposition was observed to occur at a certain "undervoltage" with respect to the equilibrium Nernst potential of the reaction M(z+) + ze$^-$ → M. Here, M(z+) designates a metal ion in

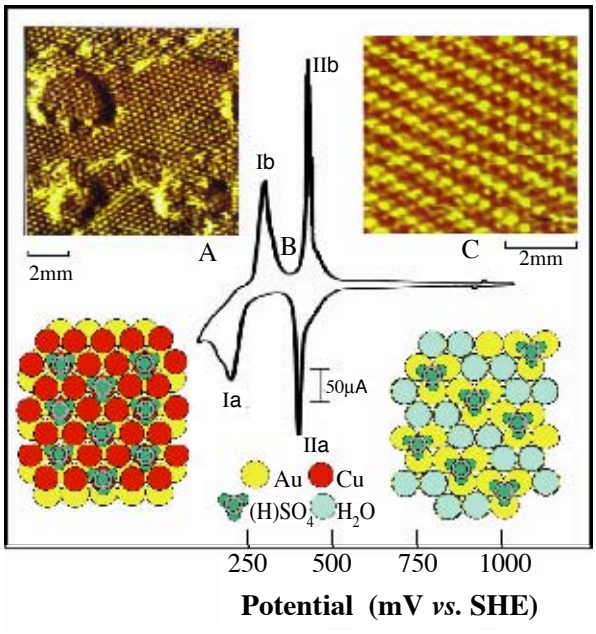

Fig. 1. CV of an Au(111) electrode in 0.5 M H_2SO_4 + 1 mM $CuSO_4$ at a scan rate of 50 mV/s. In situ STM images at the A range (0.35V RHE) and C range (1.20 V, RHE) of adsorbed molecules on the Au(111) electrode in 0.5 M H_2SO_4 + 1 mM $CuSO_4$ solution are shown in the inset. STM (A range): in situ STM of sulfate + UPD copper adsorbed on the Au(111) electrode surface. I_t = 2.8 nA, V_{bias} = –65.6 mV. STM (C range): in situ STM of HSO_4^- + $H_5O_2^+$ adsorbed on the Au(111) electrode surface. I_t = 4.2 nA, V_{bias} = –967.2 mV.

solution, and M, a metal atom in a lattice position on a surface. It was recognized that the undervoltage results energetically from the contribution of the heat of adsorption of the metal atoms on the inert substrate metal electrode surface on the energy of activation of the discharge reaction. The current peaks, IIa and IIb, are attributed to adsorption or deposition of Cu and desorption or stripping of Cu^{2+} in honeycomb copper atoms (2/3 coverage), respectively. The peaks, Ia and Ib, appear to be those of honeycomb-centered copper atoms for 1/3 coverage, respectively. We have determined the structures in those three potential ranges at A (more negative than Ia), B (between Ia and IIa) and C (more positive than IIa).

The *in situ* specular X-ray reflectivity measurements were carried out using a multi-axis diffractometer installed on beamlines **BL09XU** and **BL13XU**. The wavelength of X-ray radiation was 0.130 nm. The total number of unique reflections observed for the symmetry (P31m) was 53 at the potential of 0.32 V (RHE: Reversible Hydrogen Electrode) where UPD copper forms a honeycomb structure. The final R-factor converged to 8.8%. Figures 2 and 3 show the Cu UPD honeycomb structure formed on the Au(111) electrode in 0.5 M H_2SO_4 + 1 mM $CuSO_4$ solution at 0.32 V in the potential range B. We succeeded in locating the hydration water molecules on top of each UPD copper atom, so that a 1×1 closest-pack oxygen adlayer dominates on the UPD copper Au(111) surface.

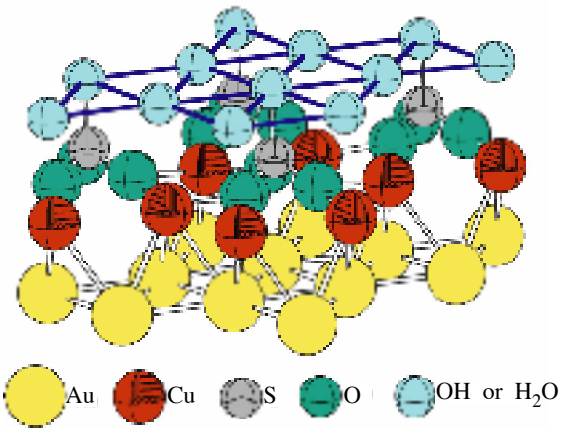

Fig. 2. ORTEP drawing of the structure based on the final positional parameters and temperature factors for Cu UPD on the Au(111) electrode in 0.5 M H_2SO_4 + 1 mM $CuSO_4$ solution. Electrode potential was 0.32 V (RHE).

The honeycomb copper layer on Au(111) does not show a metallic state. The difference in diameter between copper (0.256 nm) and gold (0.288 nm) causes a gap in the copper-copper distance of the honeycomb structure. The hydration water that is formed on copper is a new phase of water with a high density. The hydration water phase consists of a 1×1-O structure on the Au(111) surface, 1/3 of which is an oxygen atom of sulfate O and 2/3 of which is hydration water molecule on each copper atom. The distance (OH...O), 0.288 nm, is typical of the hydrogen bonding value of O...O seen in an ice structure under high pressure. The important point is that all of the oxygen atoms form a coplanar structure, which is in remarkable contrast to an ice structure. The ice structures have the common feature of tetrahedral bonding of water oxygen atoms. In contrast, the new water phase is formed by a closest-packed oxygen structure with a coplanar layer.

In region C, with a more positive potential than the small dip in CV at 940 mV, the *in situ* STM image shows a $\sqrt{3} \times \sqrt{7}$ structure as seen in the inset in Fig. 1. Intensities in a non-integer reflection (1/5, 1/5, 0.2) and its equivalent reflections, developed in region C, measure the growth of $\sqrt{3} \times \sqrt{7}$ structure domains of bisulfate anion on the surface. The ball model in Fig. 1 shows the best fit of the observation. The bright and the dimmer spots in the STM image correspond to the HSO_4^- anion and proton dimer $H_5O_2^+$ molecules, respectively. There exist a number of hydrogen bonding pairs between anions and water molecules. The ideal and most stable OH...O hydrogen bonding distance of 0.280 nm matches

the substrate Au lattice unit, yielding a high degree of stabilization due to the hydrogen bond network formation. In the ball model, oxygen atoms occupy the top surface of gold atoms which exhibit closest packing accommodation of oxygen, although the oxygen is not coplanar in this case.

In region A, which has a more negative potential than the current peak Ia in CV, where 1×1 full monolayer coverage of copper or further overlayers (OPD) of copper are deposited on the Au(111) electrode surface, high-intensity at (1/3, 1/3, 1.5) reflection continues to evolve even at the potential more negative than 100 mV, where multilayers of copper deposit epitaxially on Au(111). The further-enriched intensity of the reflection at potentials more negative than 100 mV indicates that hydration water and sulfate anions still form the similar $\sqrt{3} \times \sqrt{7}$ structure shown in Fig. 2 on 1×1 epitaxially grown copper layers on the Au(111) electrode.

We have recently observed zinc UPD on Au(111) in 0.1 M KH_2PO_4 and 1 mM $Zn(ClO_4)_2$ solution. While the surface structure of the Au(111) electrode in the topmost layer of copper UPD is the same as a bulk structure(1×1), and lifting of a surface reconstruction takes place at a surface, surface reconstruction of the Au(111) electrode continues to occur in the case of zinc UPD associated with a zinc phosphate formation(Zn-UPD), even in very negative electrode potential ranges [3]. This indicates that copper sulfate with a closest-packed hydration water sheet causes a strong interaction with the Au(111) electrode, whereas the Zn-phosphate surface complex is only weakly adsorbed on the Au(111) electrode. Consequently, the top layer gold surface is only weakly affected by the overlayer Zn-phosphate complex, resulting in the occurrence of surface reconstruction.

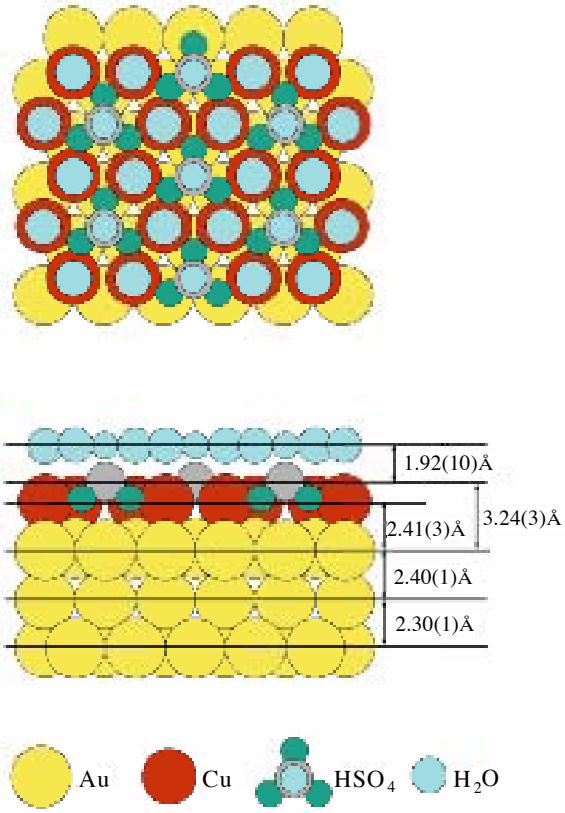

Fig. 3. Schematic model (top and side view) of UPD copper, hydration water molecule and sulfate anion adsorbed on an Au(111) electrode at the potential, 0.32 V (RHE).

Masashi Nakamura and Masatoki Ito

Keio University

E-mail: masatoki@chem.keio.ac.jp

References

[1] M.F. Toney *et al.*, Nature **368** (1994) 444.
[2] M. Nakamura *et al.*, Surface Science **514** (2002) 227.
[3] M. Nakamura, K. Matsunaga, K. Kitahara, M. Ito and O. Sakata, to be published in J. Electroanal. Chem.

Direct Observation of O_2 Molecules Adsorbed in a Nanoporous Metal-Organic Solid

One-dimensional regular assembly of dioxygen molecules, which cannot be realized under normal conditions, has long been one of the most fascinating targets in chemistry and physics because of the keen interest in its magnetic and photophysical properties that are characteristic of low dimensionality [1]. One approach to the formation of a one-dimensional specific assembly of dioxygen molecules is to use a uniform nano-sized channel in a microporous compound. Molecules tend to be condensed in a nano-sized channel by a type of confinement effect resulting from dispersion-type attractive interactions of contiguous pore walls, which eventually form an ordered assembly well suited to regulated pore geometry. A clue to a regular one-dimensional assembly is the creation of well-regulated channel structures. Crystalline microporous coordination polymers possessing uniform low-dimensional channels are relevant for a host framework where guest molecules are confined in their channels [2-4]. Here we report the first direct observation of dioxygen molecules physisorbed in nano-channels of a microporous copper coordination polymer by the MEM (Maximum Entropy Method)/Rietveld Method using *in situ* high-resolution synchrotron X-ray powder diffraction measurements on beamline **BL02B2** [5].

For this purpose, we employed a microporous copper coordination polymer with pillared layer structure (**CPL-1**), which possesses one-dimensional nano-channels with a cross section of 4 × 6 Å^2. Figure 1 shows *in situ* powder X-ray diffraction patterns of as-synthesized **CPL-1** and anhydrous **CPL-1** with oxygen at 80 KPa over a temperature range of 300 to 90 K. The powder diffraction pattern changes significantly (i) after heating under reduced pressure to remove water molecules, (ii) during the cooling process between 130 K and 150 K, and (iii) during the reheating

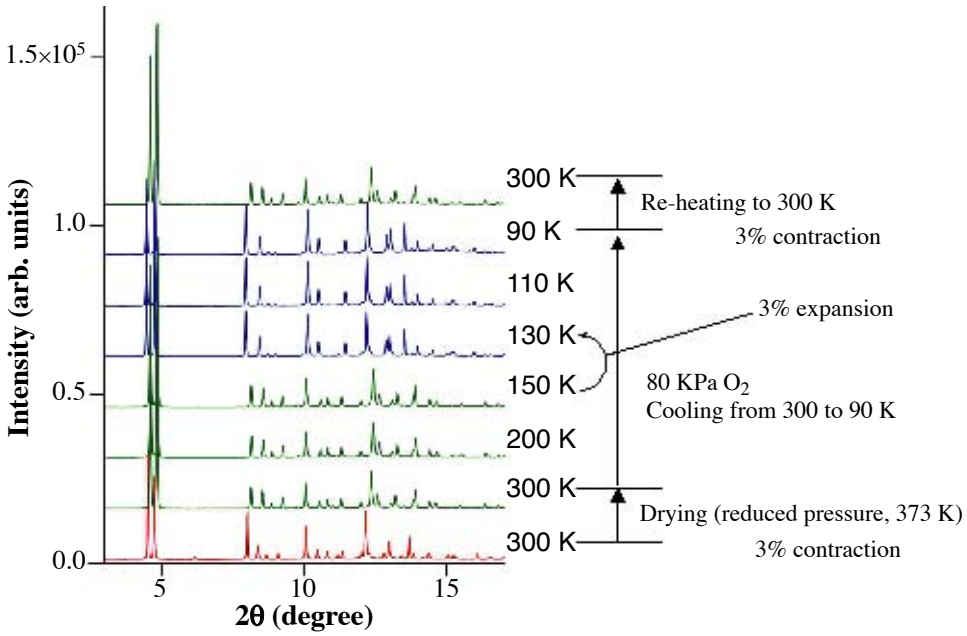

Fig. 1. Temperature-dependence of synchrotron XRD patterns of CPL-1 at 80 KPa of O_2.

process from 90 K to 300 K. No change was observed without any oxygen molecules over the whole temperature range studied.

Crystal structure of anhydrous **CPL-1** at 90 K without O_2 molecules determined by Rietveld analysis revealed that the porous structure was identical to as-synthesized **CPL-1** with slight structure distortion. MEM/Rietveld analysis proved significantly that no water molecule exists in the nano-channel (Fig. 2(a)).

Cell parameters of the anhydrous **CPL-1** with O_2 of 80 KPa at 90 K (space group $P2_1/c$) were determined by Rietveld analysis as follows: a is 4.68759(4) Å, b 20.4373(2) Å, c 10.9484(1) Å, and β 96.9480(6)°.

The reliability (R) factor based on the Bragg intensities R_I and the weighted profile R factor R_{wp} of the final Rietveld fitting were 3.9% and 2.1%, respectively. The final electron densities, obtained by the maximum-entropy method with reliability factor R_F of 1.5%, clearly reveal the 3-D pillared-layer structure, which is consistent with single-crystal data. Figure 2(b) shows the perspective view of the electron density distribution map along the a-axis; front view and side view. The earthnut-shaped electron densities, which are presumably due to O_2 molecules, are clearly recognized in the mid of channels. The relatively small value of isotropic displacement parameter (B 4.1(2)) and no disorder of O_2 molecules indicate that O_2 molecules adsorbed in the nano-channel is like solid state rather than liquid state at 90K which is much higher than the freezing point of O_2, 54.4 K at atmospheric pressure. Interestingly, two O_2 molecules align parallel with each other along the a-axis with intermolecular distance of 3.28(4) Å which is much smaller than the one corresponding to the minimum of the Lennard-Jones potential (Re = 3.9 Å). This intermolecular distance is comparable to the distance between the two nearest molecules in solid α-O_2, which is stable below 24 K at atmospheric pressure. This indicates that O_2 molecules adsorbed in the nano-channel form van der Waals dimers ($(O_2)_2$), whose successful structural characterization has not been reported yet. Each dimer aligns along the a-axis to form 1-D ladder-like structure.

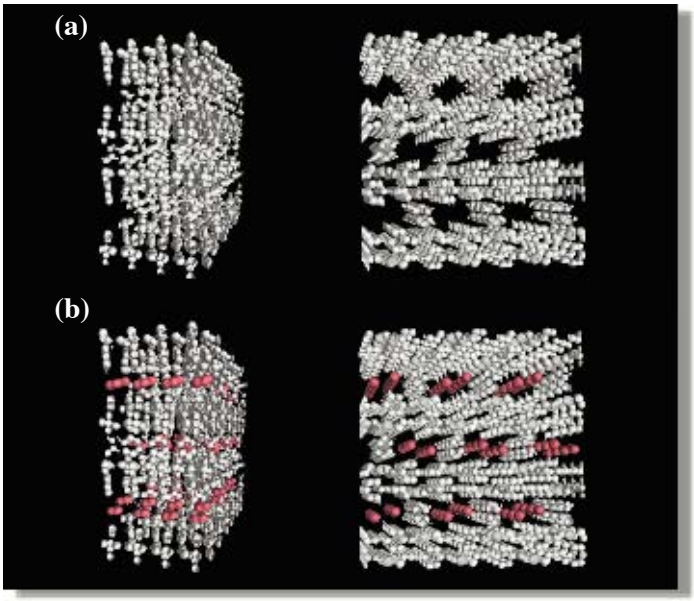

Fig. 2. MEM electron density maps of ***(a)*** *anhydrous CPL-1 without O_2 molecules at 90 K and* ***(b)*** *CPL-1 with adsorbed O_2 at 90 K as an equal –density contour surface. The equicontour level is 1.0 e Å^{-3}.*

Susumu Kitagawa

Kyoto University

E-mail: kitagawa@sbchem.kyoto-u.ac.jp

References

[1] W. Mori *et al.*, Mol. Cryst. Liq. Cryst. **306**(1997) 1.
[2] R. Kitaura, K. Seki, G. Akiyama, S. Kitagawa, Angew. Chem. Int. Ed. **42** (2003) 428.
[3] R. Kitaura *et al.*, Angew. Chem. Int. Ed. **41** (2002) 133.
[4] M. Kondo *et al.*, Angew. Chem. Int. Ed. **38** (1999) 140.
[5] Ryo Kitaura, Susumu Kitagawa, Yoshiki Kubota, Tatsuo C. Kobayashi, Koichi Kindo, Yoshimi Mita, Akira Matsuo, Michihiro Kobayashi, Ho-Chol Chang, Tadashi C. Ozawa, Megumi Suzuki, Makoto Sakata, Masaki Takata, Science **298** (2002) 2358.

EARTH & PLANETARY SCIENCE

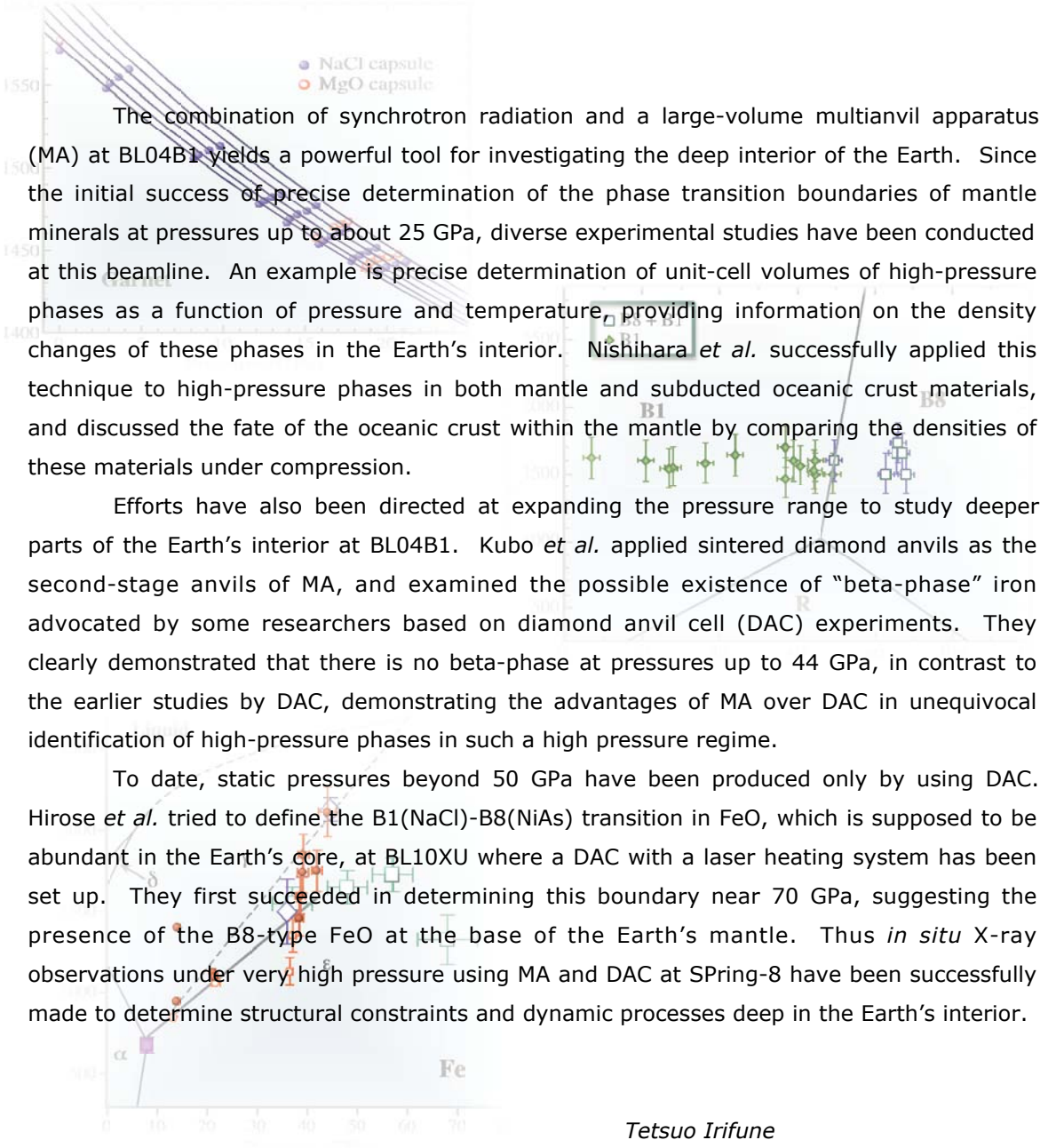

The combination of synchrotron radiation and a large-volume multianvil apparatus (MA) at BL04B1 yields a powerful tool for investigating the deep interior of the Earth. Since the initial success of precise determination of the phase transition boundaries of mantle minerals at pressures up to about 25 GPa, diverse experimental studies have been conducted at this beamline. An example is precise determination of unit-cell volumes of high-pressure phases as a function of pressure and temperature, providing information on the density changes of these phases in the Earth's interior. Nishihara *et al.* successfully applied this technique to high-pressure phases in both mantle and subducted oceanic crust materials, and discussed the fate of the oceanic crust within the mantle by comparing the densities of these materials under compression.

Efforts have also been directed at expanding the pressure range to study deeper parts of the Earth's interior at BL04B1. Kubo *et al.* applied sintered diamond anvils as the second-stage anvils of MA, and examined the possible existence of "beta-phase" iron advocated by some researchers based on diamond anvil cell (DAC) experiments. They clearly demonstrated that there is no beta-phase at pressures up to 44 GPa, in contrast to the earlier studies by DAC, demonstrating the advantages of MA over DAC in unequivocal identification of high-pressure phases in such a high pressure regime.

To date, static pressures beyond 50 GPa have been produced only by using DAC. Hirose *et al.* tried to define the B1(NaCl)-B8(NiAs) transition in FeO, which is supposed to be abundant in the Earth's core, at BL10XU where a DAC with a laser heating system has been set up. They first succeeded in determining this boundary near 70 GPa, suggesting the presence of the B8-type FeO at the base of the Earth's mantle. Thus *in situ* X-ray observations under very high pressure using MA and DAC at SPring-8 have been successfully made to determine structural constraints and dynamic processes deep in the Earth's interior.

Tetsuo Irifune

Density Difference between Subducted Oceanic Crust and Ambient Mantle in the Mantle Transition Zone

Since the beginning of plate tectonics, the oceanic lithosphere has been continually subducted into the Earth's deep mantle for 4.5 Gy. The oceanic lithosphere consists of an upper basaltic layer (oceanic crust) and a lower olivine-rich peridotitic layer. The total amount of subducted oceanic crust in this 4.5 Gy period is estimated to be at least ~3×10^{23} kg, which is about 8% of the weight of the present Earth's mantle. Thus, the oceanic crust, which is rich in pyroxene and garnet, may be the source of very important chemical heterogeneity in the olivine-rich Earth's mantle. To clarify behavior of the oceanic crust in the deep mantle, accurate information about density differences between the oceanic crust and the ambient mantle is very important.

We determined pressure-volume-temperature relations (*P-V-T* equation of state) of related minerals at high-pressure and high-temperature conditions, to precisely evaluate the density difference. Garnet and ringwoodite are the most abundant minerals in the oceanic crust and the ambient mantle, respectively, in the conditions of the mantle transition zone (410 – 660 km deep). However, *P-V-T* equation of state for the natural compositions of these minerals are not well constrained.

We conducted *in situ* X-ray diffraction experiments at up to 21 GPa and 1273 K, using the SPEED-1500 multi-anvil high-pressure apparatus installed at beamline **BL04B1** [1], and simultaneously determined *P-V-T* equations of state for majorite garnet with oceanic crust composition and ringwoodite with natural Fe-bearing composition. The garnet and the ringwoodite were synthesized from natural abyssal basalt and natural olivine, respectively. These starting materials were packed separately into NaCl or MgO sample chamber with a mixture of gold and MgO, and compressed in the same high-pressure cell. The pressure was determined by the cell volume for gold using an equation of state of gold [2], and the temperature was measured by a thermocouple. The cell volumes of garnet and ringwoodite were determined by least squares calculations using the positions of X-ray diffraction peaks. The samples were compressed to the desired pressure at room temperature and heated to the maximum temperature to release non-hydrostatic stress.

Pressure-volume-temperature data were collected under 47 different conditions. Figure 1 shows *P-V-T* data for garnet. The data collected by using an NaCl capsule after heating to above 873 K and the

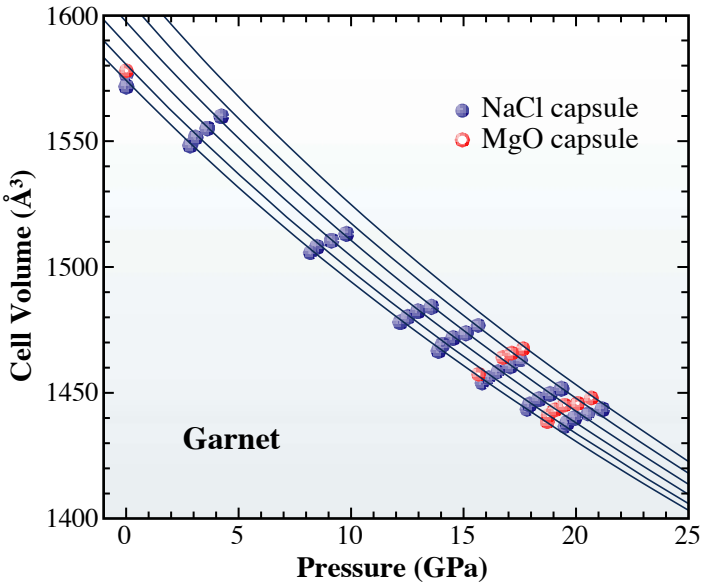

Fig. 1. Pressure-volume-temperature data for garnet with oceanic crust composition with calculated isothermal compression curves. Closed and open circles denote data collected using NaCl and MgO capsules, respectively. The isotherms (from lower cell volumes, 300, 473, 673, 873, 1073 and 1273 K) are fit to high-temperature equation of state.

data collected using an MgO capsule after heating to 1273 K showed consistent results, and the sample conditions are considered to be nearly hydrostatic. Thus, we could determine the *P-V-T* equations of state for garnet and ringwoodite precisely.

In spite of its high Si, Ca, Fe and Na contents, the present *P-V-T* equation of state for garnet shows excellent agreement with that of $Mg_3Al_2Si_3O_{12}$ garnet [3,4]. The present equation of state for ringwoodite yields significantly higher thermal expansivity than that derived by diamond anvil experiments on Mg_2SiO_4 ringwoodite to 30 GPa and 700 K [5]. The discrepancy may be due to limited temperature range (700 K at maximum) in the previous study.

The density of oceanic crust and ambient mantle the mantle transition zone were calculated by using present results, previously reported thermoelastic parameters of related minerals and phase relations in oceanic crust and pyrolitic mantle (Fig. 2). Because *P-V-T* equations of state for garnet and ringwoodite were determined in the same high-pressure experiments, the calculated density difference between the oceanic crust and the ambient mantle in the lower part of the transition zone (520 – 660 km deep) is considered to be valid even after considering fluctuations in the mantle temperatures, and inaccuracy of pressure determination in the *P-V-T* experiments, possible error in mineral physics parameters used, etc. Accordingly, the oceanic crust is denser than the ambient mantle across the entire range of the mantle transition zone along geotherms. Present results provide important information for clarifying the behavior of the oceanic crust in the deep mantle.

Yu Nishihara* and Eiichi Takahashi

Tokyo Institute of Technology

*present address : Yale University, U.S.A.

E-mail: yu.nishihara@yale.edu

References

[1] W. Utsumi *et al.*, Rev. High Pres. Sci. Tech. **7** (1998) 1484.
[2] O.L. Anderson *et al.*, J. Appl. Phys. **65** (1989) 1534.
[3] Y. Wang *et al.*, Phys. Earth Planet. Int. **105** (1998) 59.
[4] L. Zhang *et al.*, Phys. Chem. Minerals **25** (1998) 301.
[5] Y. Meng *et al.*, Phys. Chem. Minerals **21** (1994) 407.

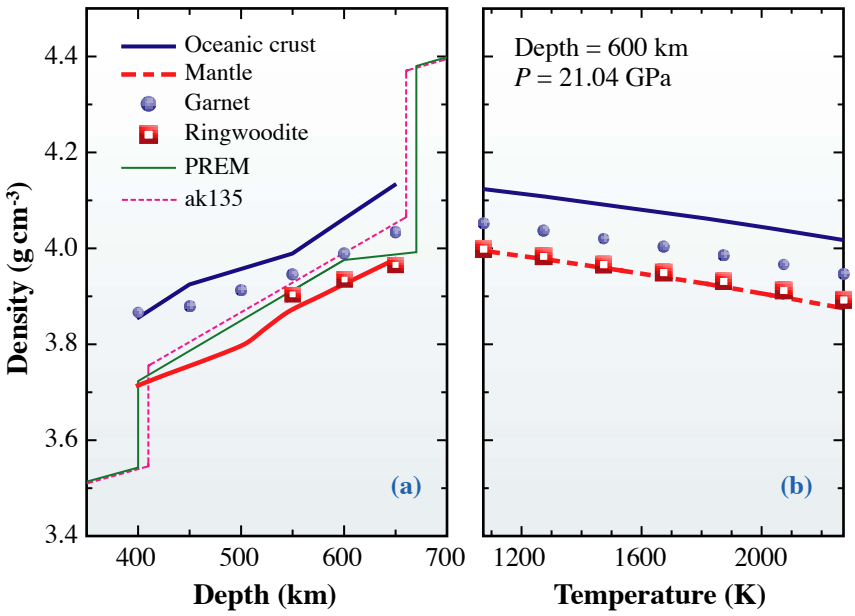

*Fig. 2. Density changes in the oceanic crust and the ambient mantle (**a**) against depth along the geotherm and (**b**) against temperature at a depth of 600 km (pressure is 21.04 GPa). The bold solid and dashed lines are the oceanic crust and the pyrolitic mantle, respectively. Solid circles and open squares are garnet in the oceanic crust and ringwoodite in the mantle, respectively, which are calculated using present P-V-T equations of state. Seismic observations are shown as thin solid (PREM) and dashed (ak135) lines.*

Absence of β-iron up to 44 GPa and 2100 K: *In situ* X-ray Observation of Iron using Kawai-type Apparatus Equipped with Sintered Diamond

The properties and states of iron at high-P/T have been extensively studied by Earth scientists, leading them to understand Earth's core that is composed of iron. By the 1970s, four polymorphs of iron, namely α (bcc), γ (fcc), ε (hcp) and δ (bcc), were known. In the 1990s, however, based on experiments using a diamond anvil cell (DAC), a fifth phase called β was claimed to be present under conditions typically higher than 35 GPa and 1500 K. If the β phase really does exist, we might replace ε-iron as the most likely phase to constitute Earth's inner core with β phase. However, both the existence and structure of β phase are controversial; two different crystal structures have been proposed for β (double-hcp (dhcp) [1] and orthorhombic [2]), while the absence of β up to 84 GPa and 3500 K has also been reported [3]. So far, exploration of β-iron has been impossible when using an eight cubic anvil system (Kawai-type apparatus) equipped with tungsten carbide, because the maximum attainable pressure was limited to less than 30 GPa. Nevertheless, by adopting sintered diamond (SD) as the anvil material [4], it has become possible to generate pressure exceeding 40 GPa by using the Kawai-type apparatus. Under these circumstances, we studied the phase relations of iron using a Kawai-type apparatus equipped with SD, whose geometry aids considerably in providing a quasi-hydrostatic environment for the sample.

The sample consisted of fine iron powder mixed with MgO in a 1:1 weight ratio to suppress grain growth of the iron at high temperature. The sample was put into a semi-sintered MgO sleeve (Fig. 1) that served as the pressure standard. High pressure was achieved by compressing the octahedral specimen assembly (Fig. 1) in a Kawai-type apparatus using "SPEED 1500" press installed at beamline **BL04B1** [5]. Energy dispersive X-ray diffraction profiles for both the sample and the MgO standard were collected along temperature cycling at fixed press loads of 660 and 800 tons at up to 1850 and 2100 K, respectively. Pressure was determined from the measured unit cell volume of the MgO pressure standard.

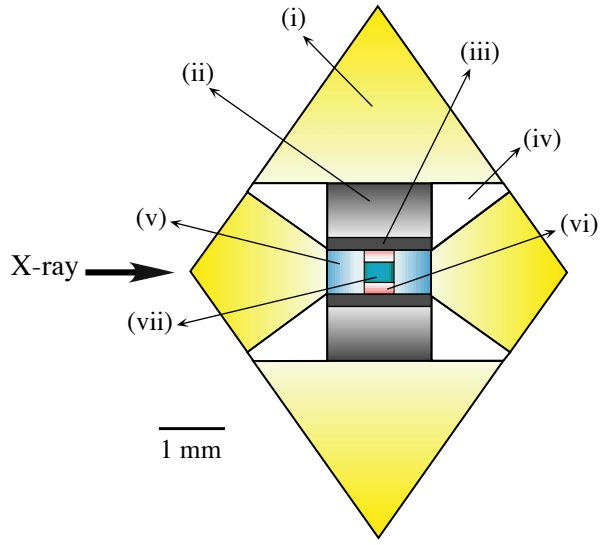

*Fig. 1. A cross-section of the octahedral specimen assembly. **(i)** Pressure medium (MgO+5wt% Cr_2O_3), **(ii)** Thermal insulation sleeve ($LaCrO_3$), **(iii)** Cylindrical heater (Re), **(iv)** Wedge-shaped electrode (Cu), **(v)** Diamond powder, **(vi)** Sample sleeve (pressure standard) (MgO), **(vii)** Sample (MgO+Fe). A thermocouple (W97/Re3-W75/Re25, not shown) is placed perpendicular to the paper and in contact with the outer surface of the heater. The incident X-ray beam (arrow) was collimated to 0.05 mm horizontally and 0.1 mm vertically, which made it possible for us to acquire diffraction patterns from the sample and the pressure standard independently.*

Several diffraction profiles of the sample are reproduced in Fig. 2. In the first cycle at 660 tons, iron initially assumed the ε phase at 37 GPa and 300 K, and it persisted at 1370 K and 38.4 GPa (Fig. 2(a)) upon heating. Diffraction peaks of γ appeared at 1450 K and 38.4 GPa and intensified simultaneously with reduction of ε as the temperature increased to 1850 K and 39.2 GPa (Fig. 2(b)). A substantial amount of ε still survived at 1850 K due to the temperature gradient through the sample. Upon cooling, enhancement of peaks for ε was noticed with a simultaneous reduction of γ at 1350 K and 37.1 GPa, but a certain amount of the γ phase remained even after quenching to 300 K and 34 GPa (Fig. 2(c)). In the second cycle at 800 tons, no change was observed up to 1700 K. At 1750 K and 41.9 GPa, the growth of γ was recognized together with a reduction of ε, which was rapid with increasing temperature up to 2100 K and 44 GPa (Fig. 2(d)). The mutual growth relations of the γ and ε phases corresponding to heating and cooling completely deny the presence of any phase between the stability fields of γ and ε up to 44 GPa. Moreover, we could not find any characteristic

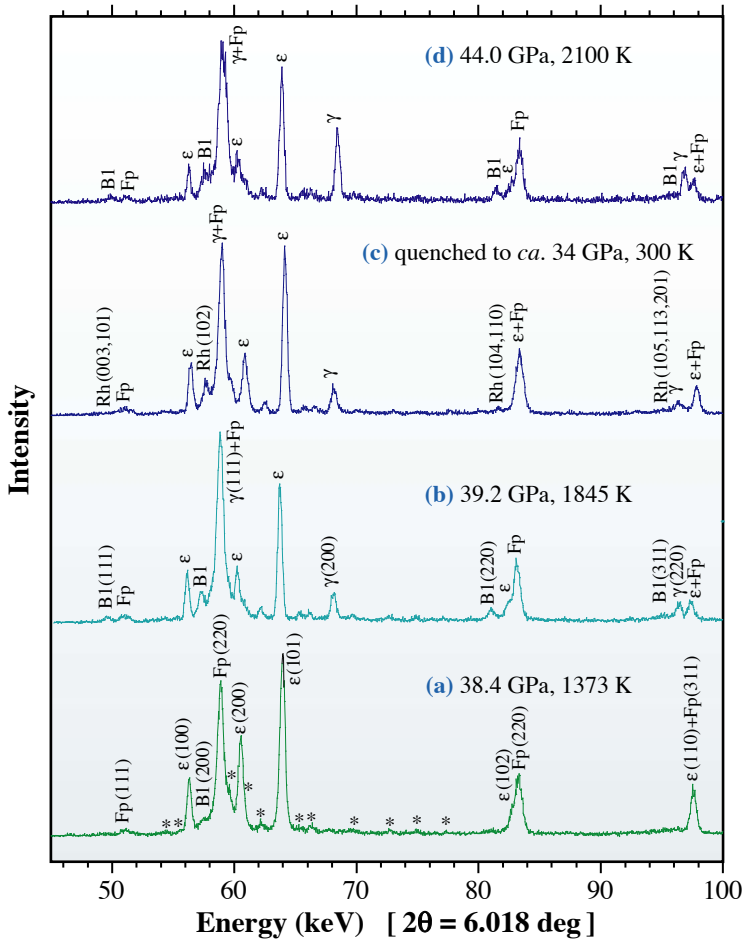

*Fig. 2. Examples of diffraction profiles of the sample. **(a)**, **(b)**, and **(c)** are on the first cycle at 660 tons and **(d)** is on the second cycle at 800 tons (see text). ε: ε-iron, γ: γ-iron, Fp: MgO mixed with the iron sample, B1; (Fe, Mg)O with the B1 structure, Rh: (Fe, Mg)O with the rhombohedral structure, asterisk: Fe_3C. Numbers in parentheses are Miller indices. In addition to iron, diffraction peaks of MgO (mixed with the iron) were also observed.*

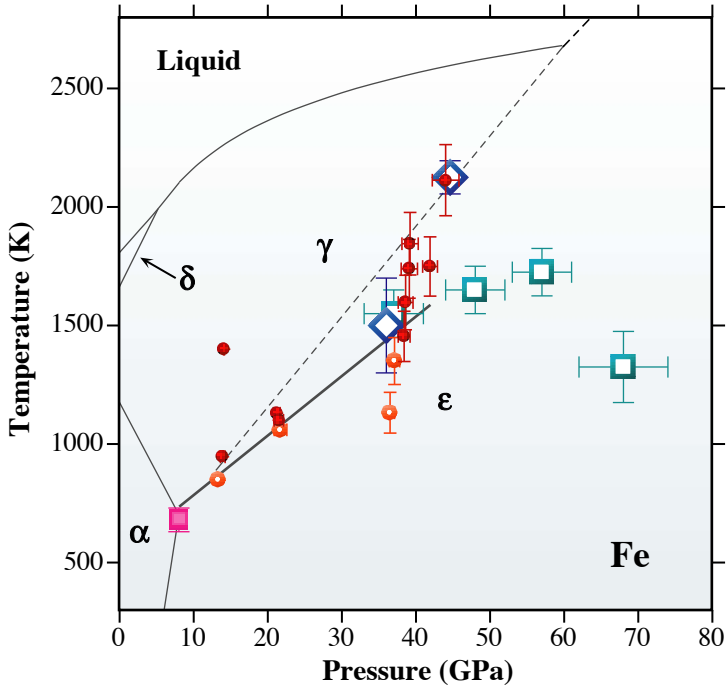

Fig. 3. Summary of the experimental results. The solid and open circles denote the conditions at which the growth of γ and ε phases were observed, respectively. The thick line shows the ε-γ boundary constrained in the present study. The open squares and diamonds are the conditions under which β phases of dhcp and orthorhombic structures were reported, respectively [1, 2]. The solid square indicates α-γ-ε triple point [6]. The dashed lines are the previously reported melting curve and ε-γ boundary of iron [3]. Bars indicate error in temperature and pressure. Note that we observed growth of the γ phase at the P/T conditions where β phase has been reported as a stable phase in previous studies [1, 2].

peaks of dhcp- and orthorhombic iron in any of the diffraction profiles. All the identified phases of iron are plotted on a P/T space along with selected previous results (Fig. 3). As the β phase(s) has been observed in DAC without using pressure medium [1] or using high-strength pressure media [2], strong uniaxial stress on the sample might cause an incomplete phase transition from ε to a "metastable" β phase.

Atsushi Kubo[a], Eiji Ito[a] and Kenichi Funakoshi[b]

(a) Okayama University
(b) SPring-8 / JASRI

E-mail: akubo@misasa.okayama-u.ac.jp

References

[1] S. K. Saxena and L. S. Dubrovinsky, Am. Mineral. **85** (2000) 372.
[2] D. Andrault *et al*., Am. Mineral. **85** (2000) 364.
[3] G. Shen *et al*., Geophys. Res. Lett. **25** (1998) 373.
[4] E. Ito *et al*., Geophys. Res. Lett. **25** (1998) 821.
[5] W. Utsumi *et al*., Spec. Issue Rev. High Press. Sci. Technol. **6** (1997) 512.
[6] T. Uchida *et al*., J. Geophys. Res. **106** (2001) 21799.
[7] Atsushi Kubo, Eiji Ito, Tomoo Katsura, Toru Shinmei, Hitoshi Yamada, Osamu Nishikawa, Maoshuang Song and Kenichi Funakoshi, Geophys. Res. Lett. **30** (2003) 1126.

High Pressure and High Temperature Phase Transitions of FeO

FeO is one of the most abundant oxide components in Earth's mantle and is also likely incorporated in the core. FeO crystallizes with the NaCl-type structure (B1) under ambient conditions and transforms to a rhombohedral phase above 17 GPa at 300 K [1]. The resistance-heated diamond anvil cell (DAC) experiments showed the transition from rhombohedral to NiAs-type (B8) structure above 90 GPa at 600 K [2]. Fei and Mao [2] further suggested the transition from the B1 to the B8 structure around 70 GPa at high temperature (>1000 K) to be consistent with earlier shock compression studies [3] and electrical resistance measurements [4]. This B1 to B8 transition has never been confirmed at high temperatures.

High-pressure and high-temperature experiments were performed at beamline **BL10XU** using DAC coupled with heating by a Nd:YAG laser [5]. We collected X-ray diffraction patterns of the sample at *in situ* high pressure and temperature conditions up to 87 GPa and 1730 K. A fine powder of $Fe_{0.954}O$ mixed with Fe (2:1 by mole ratio) was used as a starting material. It was loaded into a 100-μm hole drilled in a rhenium gasket preindented to a thickness of 50 μm, together with a pressure medium of Al_2O_3 polycrystalline pellets. The size of the heating spot was more than 50 μm. The X-ray diffraction data were collected from an area 20 μm in diameter. Exposure times were one to five minutes.

We observed a transition from the B1 to the B8 structure above 70 GPa at 1600 K (Fig. 1). The typical diffraction patterns of FeO with either the B1 or B8 structure are shown in Fig. 2. The relative intensities of diffraction peaks of the B8 structure may indicate the metallic polytype NiAs structure, which is a mixture of inverse (O at Ni site) and normal structures (Fe at Ni site), as proposed by Mazin *et al.* [6]. The metallic features of the polytype NiAs can explain the metallization of FeO

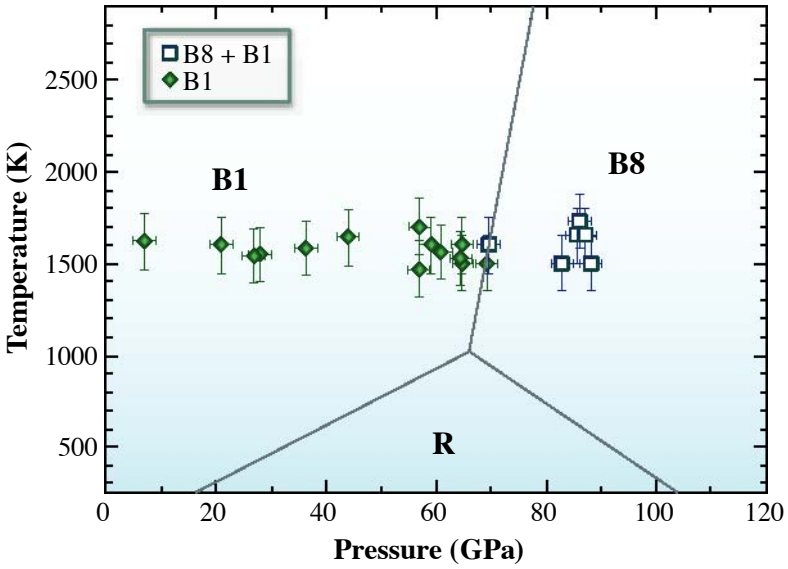

Fig. 1. Phase diagram of FeO. The B1-R and R-B8 transition boundaries are from Fei and Mao [2]. B1, NaCl-type; B8, NiAs-type; R, rhombohedral structure.

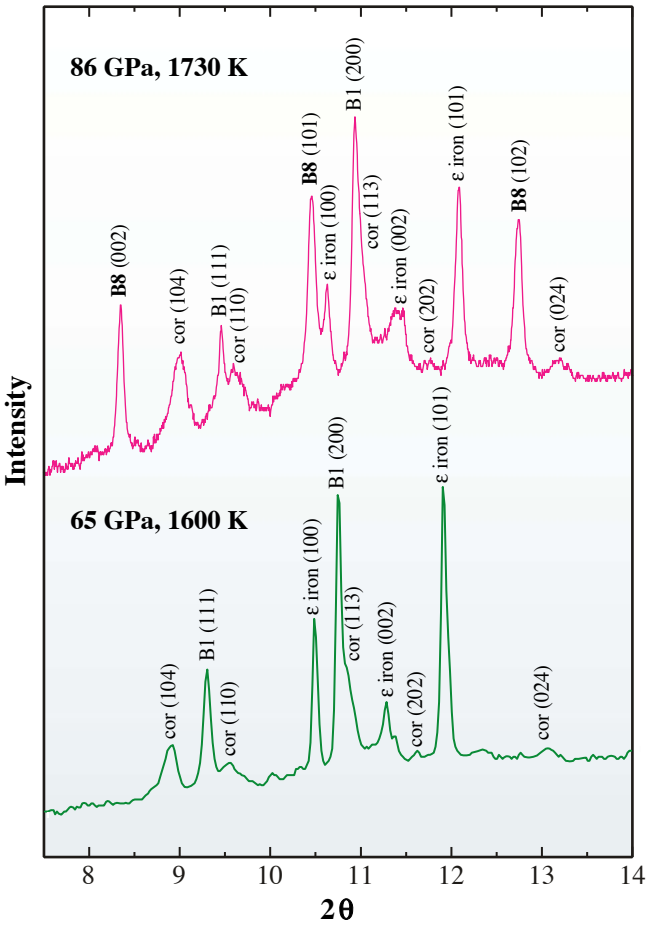

Fig. 2. Examples of X-ray diffraction patterns showing the B1 and B8 structures of FeO together with ε-Fe and corundum.

inferred from the resistance measurements [4]. The transition to a metallic phase of FeO could enhance oxygen solubility in molten iron. A structural difference between the B1 structure of MgO and the B8 structure of FeO could lead to an immiscibility gap in the MgO-FeO solid solution above 70 GPa. The lowermost mantle could be enriched with FeO as a result of chemical reactions between silicate perovskite and liquid iron. The FeO-rich (Mg,Fe)O phase with the B8 structure is likely to be present together with MgO-rich ferropericlase in the deep lower mantle. The presence of the B8 phase should increase the electrical and thermal conductivity, which may explain the nature of a highly electrically conductive layer observed at the bottom 200 m of the Earth's mantle.

Kei Hirose

Tokyo Institute of Technology

E-mail: kei@geo.titech.ac.jp

References

[1] T. Yagi *et al.*, J. Geophys. Res. **90** (1985) 8784.
[2] Y. Fei and H. Mao, Science **266** (1994) 1678.
[3] R. Jeanloz and T. Ahrens, Geophys. J. R. Astr. Soc. **62** (1980) 505.
[4] E. Knittle and R. Jeanloz, Geophys. Res. Lett. **13** (1986) 1541.
[5] T. Watanuki *et al.*, Rev. Sci. Instrum. **72** (2001) 1289.
[6] I. Mazin *et al.*, Am. Miner. **83** (1998) 451.

Environmental Science

This section covers wide topics reported by researchers working in a vast variety of disciplines. They may not have common terminologies. They may talk about their own science and technology by using the same words but with different meanings. However, there is an important objective in common: they are all aiming at a better and healthier environment for us and our posterity.

The first topic by Nishihata *et al.* is concerning a new catalyst for exhaust gas from automotive engines. As is well known, the catalyst converts the air-pollutant-emission to harmless gas. The drawbacks of the catalysts used today are their limited life and requirement of large amounts of precious metals. Here is a new catalyst that seems to have an eternal life and is expected to dramatically reduce the demand for the precious metals. The authors describe how this catalyst works.

The next topic also concerns the reduction of the exhaust gas from automobiles. The ultimate goal of absolutely non-air-polluting vehicles is now within our reach. Last year Japanese automobile makers sent fuel-cell-powered passenger cars to the market. The fuel-cell is fed with hydrogen gas, an energy source, but then the car needs a hydrogen gas storage tank. Noritake is searching for efficient hydrogen storage materials. He describes here how hydrogen is stored in magnesium hydride, which is one of the candidate materials. Such knowledge, he believes, will orient us toward finding better materials.

Another environmental hazard we are confronted with is heavy metal ions leaching out from incinerator residue. Since the daily accumulation of residue is huge, trace amounts of hazardous ions emanating from it can be a problem for us. Tsuyumoto analyses the chemical state of heavy metal ions in cement. Cement has been widely used to solidify the incinerator ash, and therefore, one must know the chemical state of the ions to predict the long term stability of residue in cement.

The last report concerns DNA damage by photo-irradiation. Yokoya *et al.* installed an EPR spectrometer in a beamline. Their EPR system detected radicals as transient species when the DNA bases were irradiated with soft X-rays. They think that these are the keys to solving the baffling problem of how the genetic transformations relevant to mutation and carcinogenesis occur.

Iwao Watanabe

Self-regeneration of a Pd-perovskite Catalyst: A Philosopher's Stone for Today's Automotive Engine

The important role of automotive catalysts is widely recognized for the conversion of three pollutant-emissions, such as carbon monoxide (CO), nitrogen oxides (NOx) and unburned hydrocarbons (HC) in engine exhaust gases. The conventional catalysts disperse fine particles of precious metal on ceramic-support materials. However, the catalytic activity deteriorates owing to the agglomeration and growth of metal particles during vehicle use (see the lower sequence in Fig. 1). Thus, an excess amount of precious metals is usually incorporated to guarantee continued catalytic activity after running the vehicle over 80,000 km. A state-of-the-art automotive gasoline engine is operated close to the stoichiometric air-to-fuel ratio to convert the pollutant-emissions simultaneously [1], accompanying with redox (reduction and oxidation) fluctuations in exhaust-gas composition by adjusting the air-to-fuel ratio. A perovskite-based catalyst, $LaFe_{0.57}Co_{0.38}Pd_{0.05}O_3$, has maintained its high activity with high dispersion of precious metals. In this study, we have found self-regeneration of the perovskite-based catalyst with environmental fluctuations, using X-ray diffraction and XAFS performed at beamline **BL14B1** [2].

The palladium-containing perovskite (Pd-perovskite) catalyst was prepared by the alkoxide method [3,4]. The thermal ageing procedure was carried out in three steps to simulate the redox fluctuations of an automotive exhaust gas: at first the powdered catalyst was oxidized in the air at 800 °C for 1 hour, then reduced in an atmosphere of 10% H_2/ 90% N_2 at 800 °C for 1 hour, and finally re-oxidized in the air at 800 °C for 1 hour. Figure 2(a) depicts the powder diffraction pattern for the three samples. Two Bragg reflections (100) and (110) were observed for the oxidized catalyst. The Bragg reflections shifted and a few additional peaks appeared for the reduced catalyst, indicating lattice expansion and partial demolition of the perovskite crystal in a reductive atmosphere. Surprisingly, the

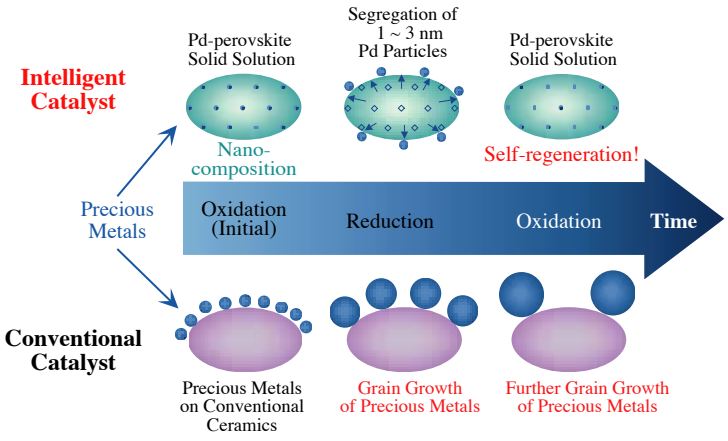

Fig. 1. Self-regeneration of the intelligent catalyst (upper sequence) and deterioration of the conventional catalyst (lower sequence) in the exhaust-gas of the state-of-the-art gasoline engine.

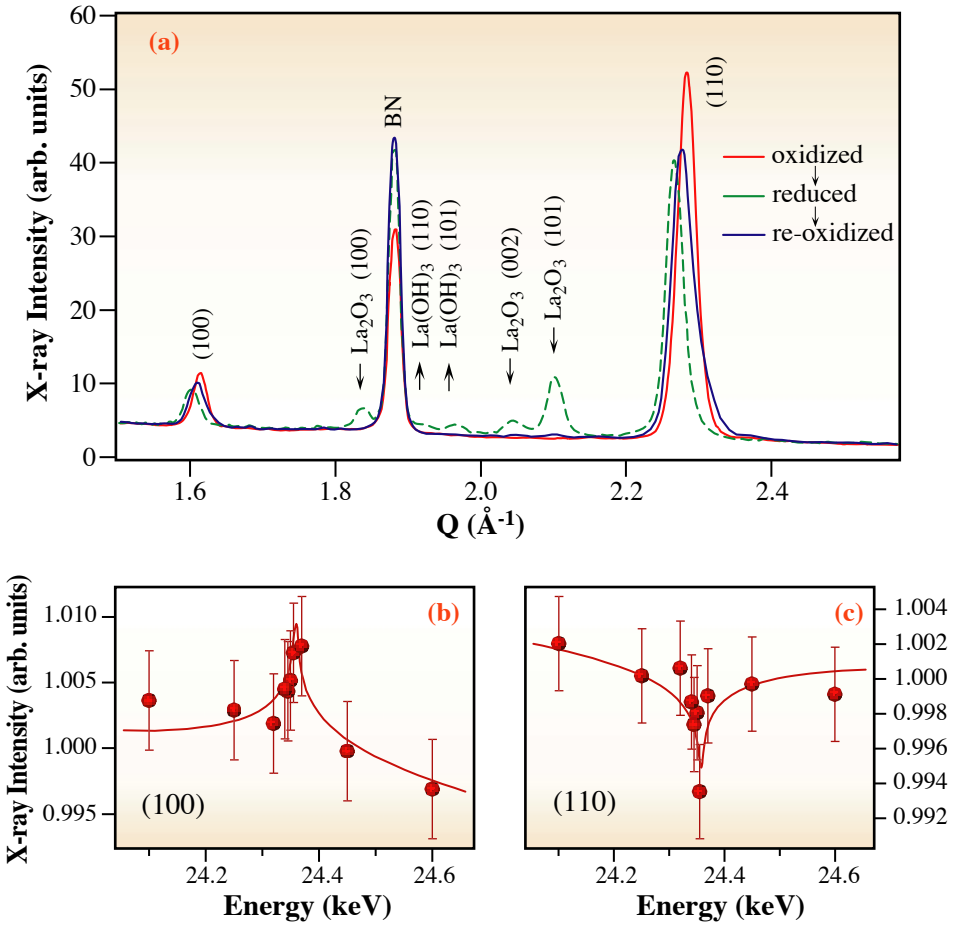

Fig. 2. X-ray powder diffraction. ***(a)*** *Powder X-ray diffraction pattern for three aged catalysts, $LaFe_{0.57}Co_{0.38}Pd_{0.05}O_3$, which were pressed into pellets with a BN binder after the ageing. Two Bragg peaks from the catalysts were assigned as a pseudocubic cell of the perovskite structure. The perovskite crystal in a reductive atmosphere was partially destroyed and transformed into $La(OH)_3$ through La_2O_3. Energy dependence of the intensity for* ***(b)*** *(100) and* ***(c)*** *(110) reflections near the Pd K-edge indicates that the B-site of the perovskite structure is occupied with Pd in the oxidized catalyst.*

diffraction pattern recovered at the re-oxidizing step: the Bragg reflections shifted back and the additional peaks disappeared completely. The catalyst retains a predominantly perovskite structure throughout the redox cycle. The increase of (100) and the decrease of (110) reflection intensities at the Pd *K*-edge clearly show that Pd occupies the B-site (6-fold coordination) of the perovskite lattice in the oxidative atmosphere (Figs. 2(b) and 2(c)).

Figure 3(a) shows XANES spectra for Pd-perovskite catalysts after the each ageing step to estimate the valence state of Pd. The chemical shift of the edge position implies that the valence of Pd in the oxidized or re-oxidized catalyst is higher than the normal bivalence as seen in PdO. On the other hand, Pd is in the metallic state in the reduced catalyst. The local structure around Pd also reversibly changes, depending on the redox atmospheres (Fig. 3(b)). The first peak of the radial

structure function can be fitted as 6 oxygen atoms of a PdO_6 octahedron for the oxidized and re-oxidized catalysts, while it can be fitted as Pd and Co atoms in a Pd-Co alloy particle for the reduced catalyst.

It has been proved that the particle growth of the precious metal can be suppressed as a result of this Pd movement between inside and outside the perovskite lattice due to the structural responses to the redox fluctuations in exhaust-gas composition with the state-of-the-art gasoline engine (see the upper sequence in Fig. 1). Therefore, this catalyst can refresh by itself to maintain the activity while the vehicle is being driven, and can reduce by 70 - 90% the amount of precious metals needed to meet the ultra-low emission vehicle standards.

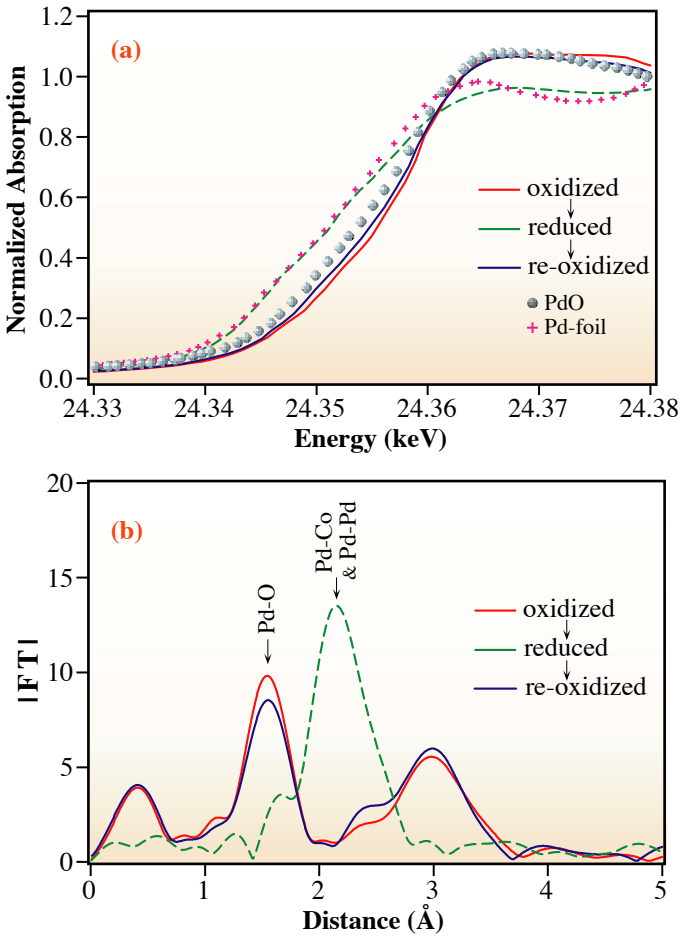

*Fig. 3. Comparison of XAFS. (**a**) X-ray absorption spectra near the Pd K-edge, which were measured in transmission mode, for three aged catalysts, $LaFe_{0.57}Co_{0.38}Pd_{0.05}O_3$. Those for PdO and a Pd-foil are also shown as reference materials. The valence of Pd changes reversibly in a redox cycle. (**b**) Radial structure function around Pd: Magnitude of Fourier transform (FT) of the k^3-weighted EXAFS oscillations for the catalysts. Neighbours seemingly appear closer to the X-ray absorbing atom because the phase shift of the photoelectron was not taken into account. The local structure around the Pd atom changes reversibly, too.*

Yasuo Nishihata[a] and Hirohisa Tanaka[b]

(a) SPring-8 / JAERI
(b) Materials Research & Development Division, Daihatsu Motor Co., Ltd.

E-mail: yasuon@sp8sun.spring8.or.jp

References

[1] R.M. Heck and R.J. Farrauto, Catalytic Air Pollution Control: Commercial Technology (Van Nostrand Reinhold, New York, 1995) 94.
[2] Y. Nishihata, J. Mizuki, T. Akao, H. Tanaka, M. Uenishi, M. Kimura, T. Okamoto and N. Hamada, Nature **418** (2002) 164.
[3] H. Tanaka *et al.*, Science and Technology in Catalysts 1994 (eds. Y. Izumi, H. Arai & M. Iwamoto) (Kodansya-Elsevier, Tokyo, 1994) 457.
[4] H. Tanaka *et al.*, Topics in Catalysts (eds N. Kruse, A. Frennet & J.-M. Bastin-Kluwer Academic, New York) **16-17** (2001) 63.

Chemical Bonding of Hydrogen in MgH_2

Hydrogen is considered to be one of leading candidates for clean energy sources in the future. For safe and efficient hydrogen storage, developments of new hydrogen storage materials are currently being researched [1]. The hydrogen storage capacity per unit weight of typical metal alloys is very low (about 2.0 mass %) and not sufficient for use in a fuel cell vehicle. Therefore, alloys containing light elements are focused on as high-performance storage materials. Magnesium in particular has a high storage capacity (7.6 mass %). For this reason, magnesium and its alloys are considered to be some of the most important candidates for reversible hydrogen storage materials. Unfortunately, magnesium hydrides are thermodynamically stable, and the dehydrogenation of magnesium hydrides requires high temperatures (> 550 K). Understanding the bonding nature of magnesium and hydrogen is essential in order to improve its fundamental dehydrogenation performance.

To further understand the nature of bonding, charge density distribution is typically investigated by X-ray diffraction analysis. However, the diffraction intensity from hydrogen atoms in metal hydrides is very weak, although we have overcome that difficulty with the highly brilliant X-ray source of SPring-8. In our result, the diffraction intensities from hydrogen could be measured precisely and the positions of hydrogen in metal hydrides were determined by the analysis based only on the X-ray diffraction data. Furthermore, the MEM/Rietveld method, which is a combination of the MEM (maximum entropy method) and the Rietveld refinement [2], was applied to metal hydrides. By employing this method and precise X-ray diffraction data, the charge density distribution measurement, which has not so far succeeded, became possible for the first time, and the bonding nature of hydrogen in MgH_2 was revealed experimentally [3].

The MgH_2 sample was prepared by hydrogen activation treatment of pure magnesium powder.

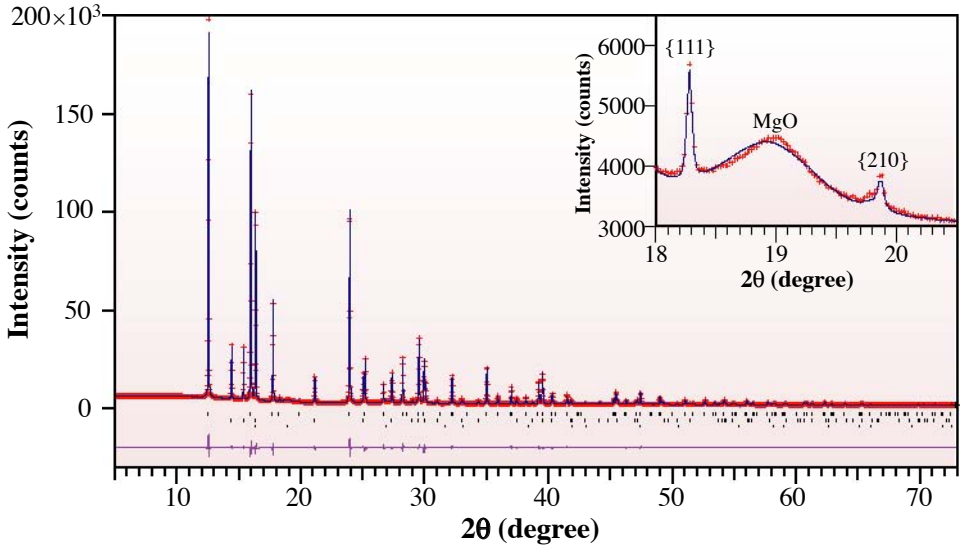

Fig. 1. Rietveld analysis pattern of the MgH_2 sample. Red + marks are measured intensity, the blue line is calculated intensity, black | marks are peak positions, and the purple line is the deviation of measurement and calculated intensity. MgH_2, Mg and MgO are included in this sample. The enlarged pattern of the region from 18.0° to 20.5° is shown in the inset.

The obtained fine powder was inserted into a glass capillary (diameter: 0.1 mm) for measurement and the X-ray diffraction experiment was carried out using a large Debye-Scherrer camera with imaging plate as detector at beamline **BL02B2** [4]. The wavelength of the incident X-ray was 0.696 Å. The X-ray diffraction intensities were obtained with 0.02° steps from 5.0° to 73.0° in 2θ. The experimental data were analyzed by the MEM/Rietveld method using the computer programs ENIGMA [5] and RIETAN [6].

The powder sample was composed of three phases, MgH_2, Mg and MgO. By Rietveld analysis, the mass fractions for each phase were determined as 69, 27 and 4 mass%, respectively. The lattice parameter of MgH_2 is a = 4.5180(6) Å, c = 3.0211(4) Å, which is a little larger than that of MgD_2. The weighted profile reliability factor, R_{WP}, and the reliability factor based on integrated intensities, R_I, of the Rietveld analysis were 2.9% and 1.7%, respectively. The fitting result of the Rietveld analysis is shown in Fig. 1. The inserted figure clearly shows the {111} reflection at 18.2° and the {210} reflection at 19.8°, which are attributed to the sub-lattice of only H atoms.

In MEM analysis, the reliability factor R was 1.0%, which is small enough to determine the charge densities of hydrogen and its bond nature. Figure 2 illustrates the crystal structure of MgH_2 (rutile type). The charge density distribution of (001) and (110) plane in the crystal of MgH_2 is shown in Fig. 3(a) and Fig. 3(b). The charge density distribution around Mg is spherical, whereas the lower charge density distribution around H is non-spherical and spreads slightly in the direction of the nearest neighbor Mg and H atoms. At the bond midpoint, the charge density is 0.26, 0.21 and 0.25 e/Å^3 for the apical Mg–H, the equatorial Mg–H and the H–H bonds, respectively. These values are much lower than those of typical covalent bonds in diamond (1.4 e/Å^3) and Si (0.7 e/Å^3) [2]. The results suggest that there are weak but significant covalent bonds between Mg and H as well as between H and H. The charge density in the interstitial region is extremely low, 0.02 e/Å^3, which could deny the existence of the metallic bonding nature. The number of electrons within the spherical region was estimated as 10.09 e and 1.26 e for Mg (radius: 0.95 Å) and H (radius: 1.00 Å). These values indicate that ionic charge of Mg and

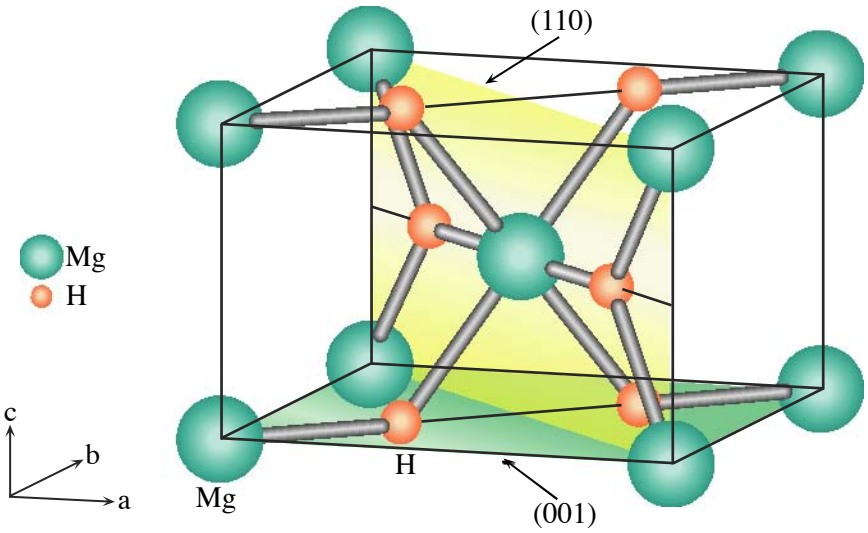

Fig. 2. The crystal structure of MgH_2 (rutile type).

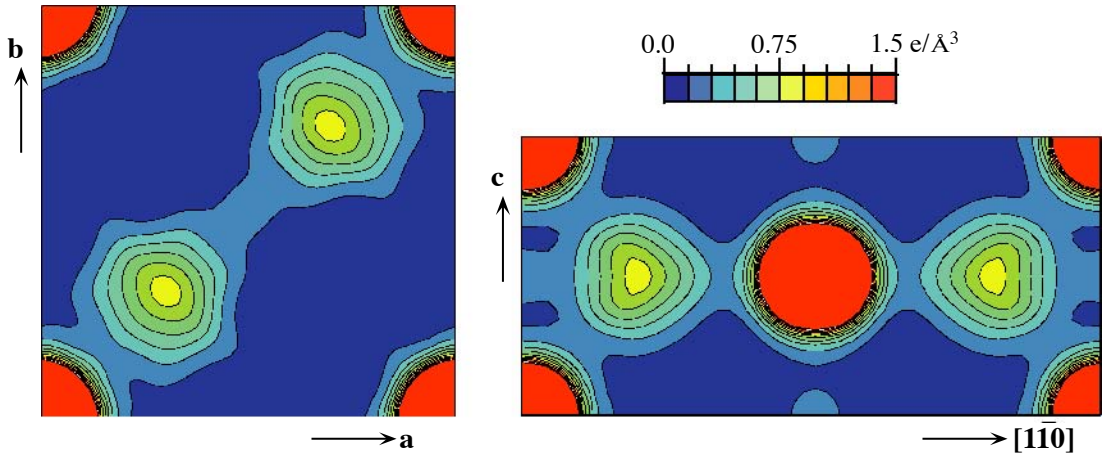

Fig. 3. MEM charge density maps of (001) and (110) plane in MgH_2. The contour lines are drawn from 0.0 to 1.5 at 0.15 e/Å^3 intervals.

H are represented as $Mg^{1.91+}$ and $H^{0.26-}$. Hydrogen is far more weakly ionized than magnesium.

Experimentally, the bonding nature of MgH_2 has been revealed by the charge density distribution measurement. As a result, we consider that it is necessary to make its ionic bonding even weaker to improve the dehydrogenation performance of MgH_2. In the future, it will be necessary to find an effective method to weaken the bonding strength by the selection of a suitable crystal structure, adding elements and so on. The electronic states and formation energy of metal hydrides have been theoretically calculated [7]. The next step is to undertake experimental and theoretical investigations into the bonding nature of hydrogen to develop efficient hydrogen storage materials.

Tatsuo Noritake

Toyota Central R & D Labs., Inc.

E-mail: e0553@mosk.tytlabs.co.jp

References

[1] L. Schlapbach and A. Züttel, Nature **414** (2001) 353.
[2] M. Takata *et al.*, Z. Krystallogr. **216** (2001) 71.
[3] T. Noritake, M. Aoki, S. Towata, Y. Seno, Y. Hirose, E. Nishibori, M. Takata, M. Sakata, Appl. Phys. Lett. **81** (2002) 2008.
[4] E. Nishibori *et al.*, Nucl. Instrum. Meth. in Phys. Res. A **467-468** (2001) 1045.
[5] F. Izumi, The Rietveld Method, Ed. R. A. Young (Oxford Univ. Press, 1993) chap. **13**.
[6] H. Tanaka *et al.*, J. Appl. Crystallogr. **35** (2002) 282.
[7] K. Miwa and A. Fukumoto, Phys. Rev. B **65** (2002) 155114.

Chemical State Analysis of Trace Heavy Metals in Normal Portland Cement using X-ray Absorption Fine Structure

Cement has been widely used to stabilize and solidify waste materials containing heavy metals, and long-term leachability of the cement-stabilized residues is an important factor when assessing potential hazards. Elution of hexavalent chromium from cement itself has also become an environmental problem, because cement contains trace amounts of chromium derived from raw materials such as iron slag and refractory bricks. Techniques to manufacture cements from the incineration ash of urban refuse and sewage sludge have been developed [1]. We should pay close attention to the use of such waste materials because trace heavy metals incorporated in cement may bring about a hazardous risk. Thus it is essential to evaluate the behavior of trace heavy metals in cement by analyzing their chemical states during hydration in order to assess a potential environmental risk. We present here the chemical state changes observed for trace amounts of chromium [2,3] and zinc by X-ray absorption fine structure (XAFS) [4].

A normal Portland cement sample was supplied by the Japan Cement Association. The cement paste sample had a water / cement ratio of 0.5. The concentrations of hexavalent chromium, total chromium, and zinc were determined by conventional wet analysis at 6.4 ppm, 58.4 ppm, and 205.1 ppm, respectively. These chromium and zinc properties are intrinsic to cement materials and are supposed to be derived from the natural raw materials and the refractory bricks.

XAFS spectra were recorded at beamline **BL38B1**. An Si(111) double-crystal monochromator was used, and higher harmonics were eliminated with Rh-coated mirrors. The spectra of unhydrated and hydrated cement samples were collected in the fluorescence mode using a Ge 19-element SSD (GL0110S, Canberra Industries Inc.).

Figure 1 shows Cr *K*-edge XANES spectra of cement and reference materials. A peak due to hexavalent chromium was observed at 5993 eV in the pre-edge region of the spectrum in Fig. 1 (indicated by an arrow). We used the intensity of the Cr *K* pre-edge peak for quantitative analysis of the hexavalent chromium (Cr(VI)) in cement matrix. We found that the peak area due to the hexavalent chromium decreased monotonically with the

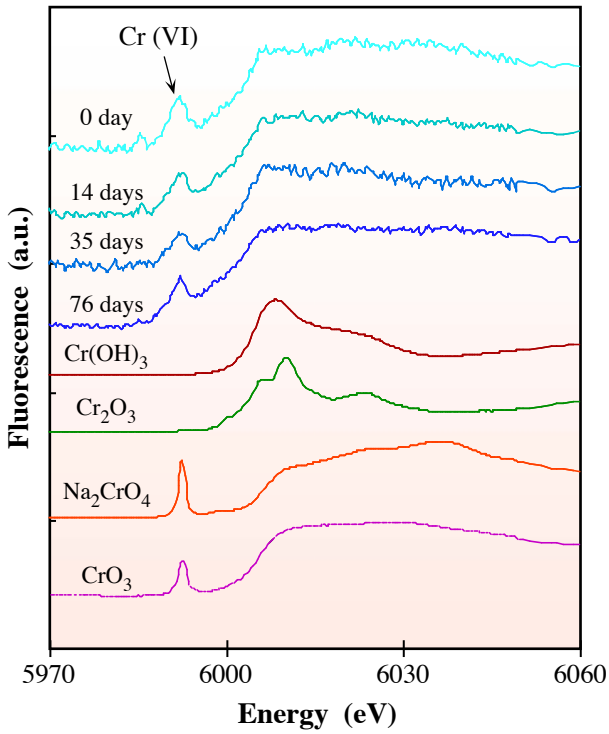

Fig. 1 Cr K-edge XANES spectra for normal Portland cement at the age of 0, 14, 35, and 76 days, along with $Cr(OH)_3$, Cr_2O_3, Na_3CrO_4 and CrO_3 for reference.

material's age, *i.e.*, with the cement hydration (Fig. 2). This indicates that the trace hexavalent chromium intrinsically contained in cement is gradually reduced to trivalent chromium during the hydration process and thus its toxicity and solubility decreases with time. This suggests that the reduction of the hexavalent chromium to the trivalent chromium is involved in the hydration reaction.

Figure 3 shows Zn *K*-edge XANES spectra of cement and reference materials. Two peaks peculiar to ZnO were also observed for cement, and their intensities monotonically decreased with the hydration of cement (indicated by arrows). This indicates that zinc atoms coordinated by four oxygen atoms decreased with the hydration of cement. It should be noted that zinc atoms intrinsically existing in the cement matrix change their chemical state drastically during hydration of the cement.

Our results indicate that chemical states of trace amounts of chromium and zinc are transformable with hydration of cement matrix. Monitoring of trace amounts of hazardous heavy metals by an automated routine analysis will be necessary in future for quality control in the cement industry and for hazard assessment of industrial wastes landfilling. We believe XAFS analysis will be a powerful tool for such purposes.

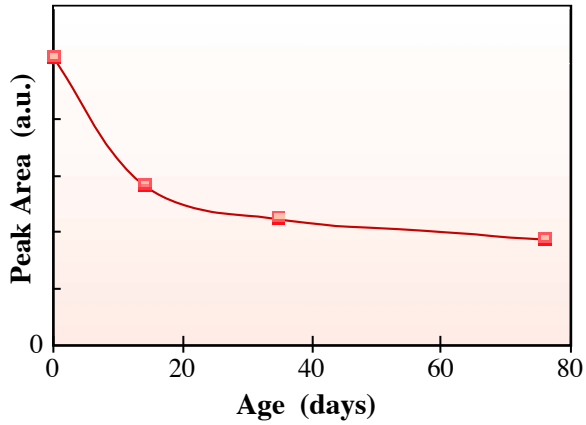

Fig. 2. Normalized area of the hexavalent pre-edge peak versus material age after mixing with water of the normal Portland cement. The curve is added to guide the eye.

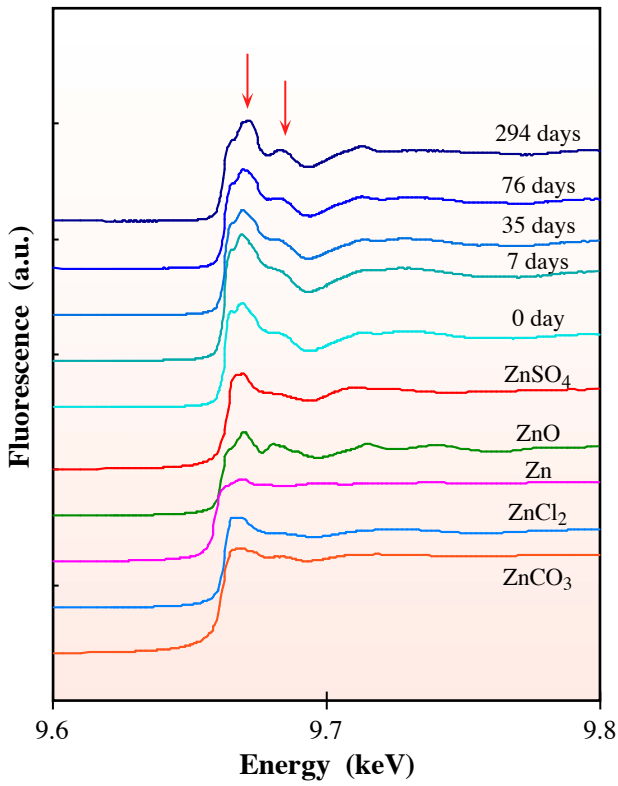

Fig. 3. Zn K-edge XANES spectra for normal Portland cement at the age of 0, 7, 35, 76 and 294 days, along with $ZnSO_4$, ZnO, Zn, $ZnCl_2$ and $ZnCO_3$ for reference.

Isao Tsuyumoto

Kanazawa Institute of Technology

E-mail: tsuyu@neptune.kanazawa-it.ac.jp

References

[1] H. Uchikawa *et al.*, World Cement **26** (1995) 33.
[2] I. Tsuyumoto and H. Uchikawa, J. Ceram. Soc. Jpn. **111** (2003) 70.
[3] I. Tsuyumoto and H. Uchikawa, accepted in J. Ceram. Soc. Jpn.
[4] I. Tsuyumoto and H. Uchikawa, submitted in J. Am. Ceram. Soc.

Study of Soft X-ray-Stimulated Free Radicals Inducing DNA Base Damage

Studies employing synchrotron soft X-rays as probes to investigate genetic changes have highlighted the biological effects, such as mutation or carcinogenesis, related to the molecular process in DNA damage [1]. Site-selective photoabsorption in a DNA molecule is one of the most powerful techniques for understanding the physicochemical mechanism of DNA damage, which induces the radiobiological effects. We have developed an EPR (Electron Paramagnetic Resonance) spectrometer (Fig. 1) installed in a synchrotron soft X-ray beamline at SPring-8 to observe free radical species as intermediates leading the complicated DNA damage [2]. This system enables us to investigate the radical process *in situ* in DNA molecules by core-excitation with irradiation by the soft X-rays [3].

The experiments were performed at the Biological Application Station in the JAERI soft X-ray beamline **BL23SU**. The measured sample was a pellet of guanine and thymine bases, which were chosen as typical purine and pyrimidine bases in a DNA molecule. The oxygen in the bases was selected as a target atom for *K*-shell excitation in the molecules. The sample pellet was irradiated with soft X-ray photons in a microwave cavity mounted in a vacuum chamber (< 10^{-6} Pa). The sample temperature was controlled from 15 to 300 K, and relatively low microwave power ranging 0.1 - 7 mW was used to avoid power saturation of EPR signals. Monochromatic soft X-ray photons were provided using a grazing incidence monochromator equipped with varied-line-spacing-plane-gratings (VLSPGM). The resolution power E/ΔE is ~ 10,000 in the 0.5 keV region, and a photon flux of the order of 10^{11} (photons/sec/100 mA ring current/0.02% band width) was realized.

Obtained EPR spectra show the induction of short-lived unstable radicals clearly distinguished from stable ones which still exist after exposing to soft X-rays. The signal intensity of a short-lived doublet signal observed in the guanine spectrum at 77 K (Fig. 2(a)) linearly increases with an increase of the photon flux density. The signal immediately

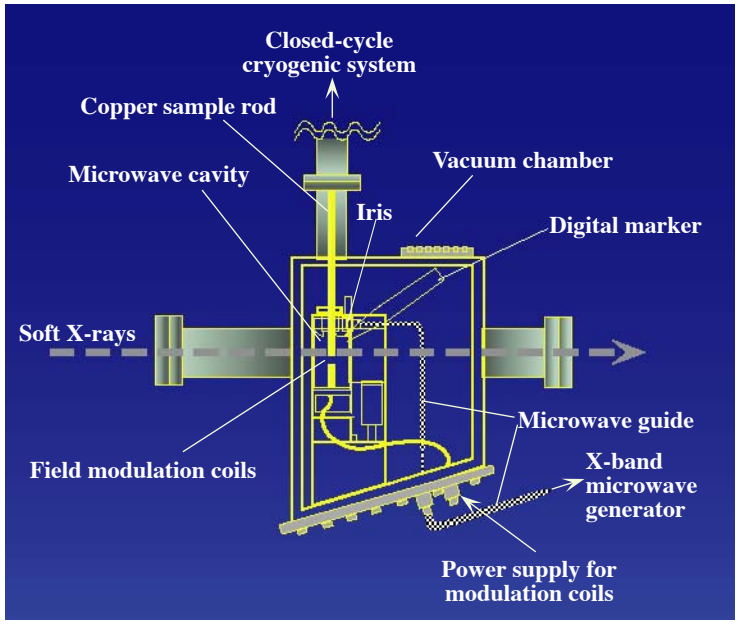

Fig. 1. The microwave cavity of the EPR apparatus mounted in the high vacuum chamber. The sample is set on a copper rod and installed in the narrow gap between field modulation coils. X-band microwaves are guided into the chamber via copper wave-guides connected with a vacuum-sealed junction.

disappeared by beam-off. Only a singlet signal (Fig. 2(b)), which is consistent with previous data on a guanine cation (one electron oxidation) [4] remained on the spectrum. It is inferred that the lifetime of the short-lived radical should be longer than 10 μsec due to the magnetic field modulation of 100 kHz for the EPR spectrometer. Considering the experimental time response limit, the presence of a doublet signal would indicate a transient radical species following the Auger final state that promptly decays within a psec. Thus, we propose a pathway for forming a final guanine lesion in DNA, such as 7,8-dihydro-8-oxo-guanine (8-oxo-G), shown in Fig. 2.

In the case of thymine, a strong singlet signal appeared during irradiation by soft X-rays (Fig. 3(a)). In contrast to guanine, however, over 10^{16} photons were needed obtain the detectable signal of stable radical at room temperature. The stable doublet signal with an additional minor structure (Fig. 3(b)) is similar to thymine anion radical previously reported [5]. Based on these aspects, we propose a possible pathway for forming a final thymine lesion as shown in Fig. 3. The anion radical would be induced by a secondary reaction with photo or Auger electrons to thymine in bulk condition.

These results strongly indicate that the *in situ*

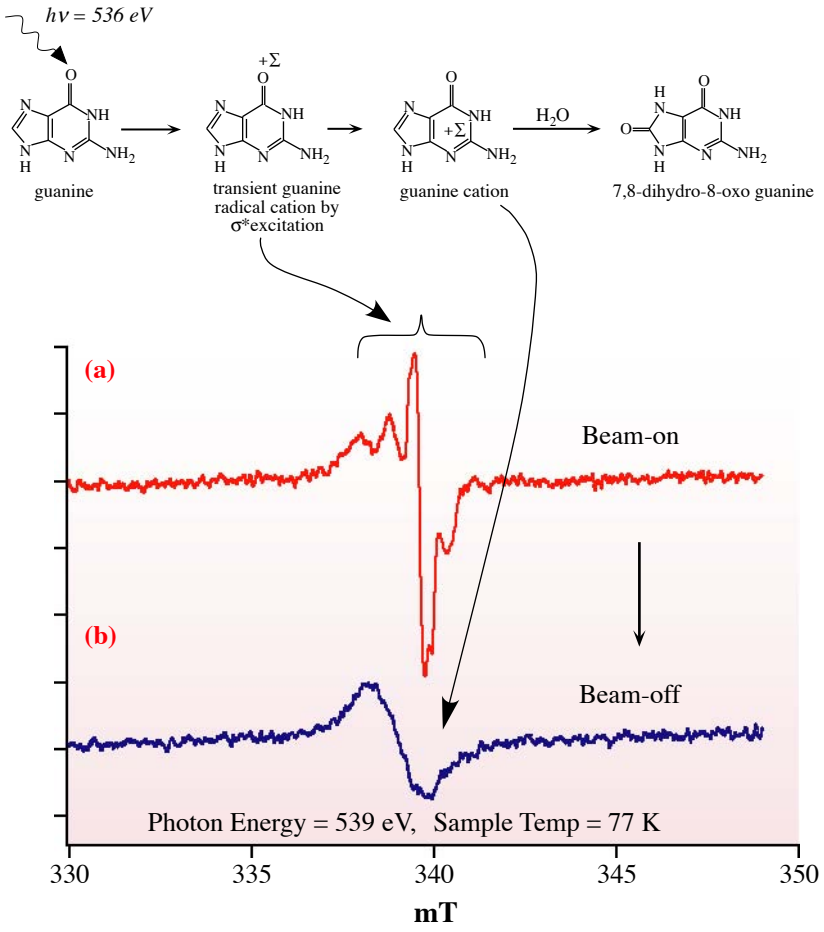

*Fig. 2. EPR spectra of guanine during irradiation by soft X-rays (536 eV) at 77 K (**a**), and just after exposure (**b**). The microwave power was 200 μW and the width of the magnetic field modulation of 100 kHz was 0.5 mT.*

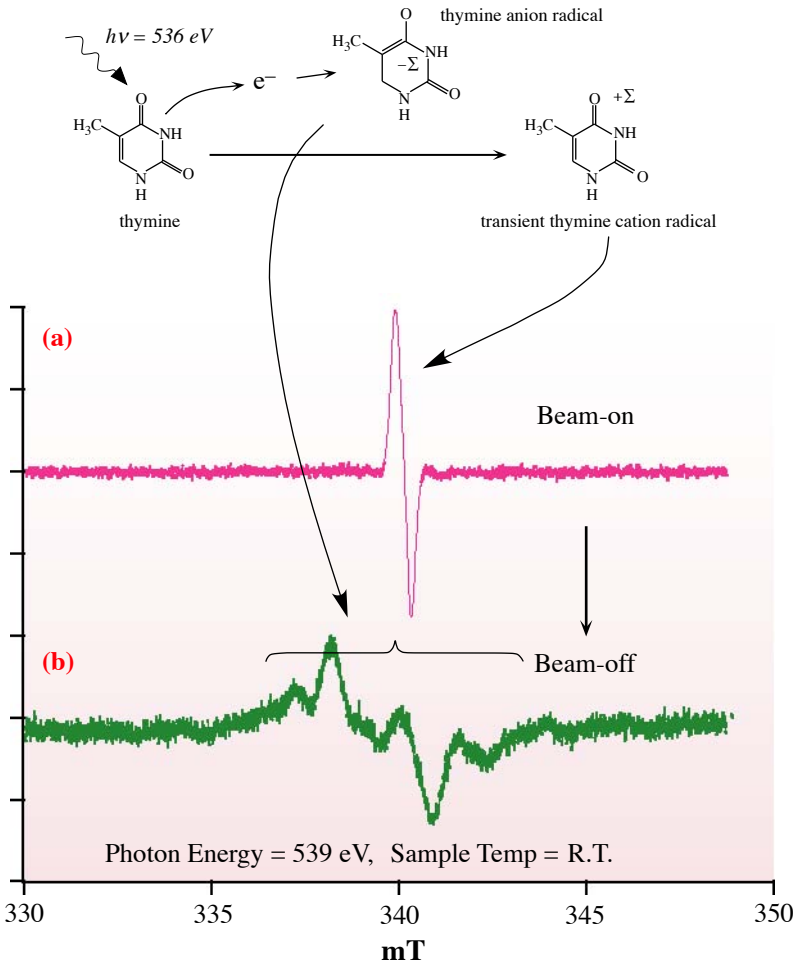

Fig. 3. ***(a)*** *EPR spectrum of thymine during irradiation of soft X-rays (536 eV) at room temperature. The microwave power was 1 mW and width of the magnetic field modulation of 100 kHz was 0.5 mT.* ***(b)*** *EPR spectrum of thymine after exposure of a high flux of about 1016 photons. The microwave power was 7 mW and width of the magnetic field modulation of 100 kHz was 0.5 mT. The gain was two times larger than that for* ***(a)****.*

EPR measurement provides evidence of the transient radical species induced, presumably, as single-electron oxidation by core level excitation. These are inferred to be precursors of chemically stable DNA base lesions. Our findings will open discussions on physicochemical processes of DNA damage induction by ionizing radiation.

Akinari Yokoya, Ken Akamatsu and Kentaro Fujii

SPring-8 / JAERI

E-mail: yokoya@spring8.or.jp

References

[1] K. Hieda and T. Ito, in: S. Ebashi, M. Koch and E. Rubenstein (Eds.), Handbook on Synchrotron Rad., North-Holland, Amsterdam **4** (1991) 431.
[2] A. Yokoya and K. Akamatsu, Nucl. Instrum. Meth. A **467-468** (2001) 1333.
[3] A. Yokoya, K. Akamatsu and K. Fujii, Nucl. Instrum. Meth. B **199** (2003) 366.
[4] D.M. Close, E. Sagstuen and W. Nelson, J. Chem. Phys. **32** (1985) 4386.
[5] H.C. Box and E.E. Budzinski, J. Chem. Phys. **62** (1975) 197.

INDUSTRIAL APPLICATION

Many researchers place their hopes on the use of a synchrotron radiation facility as a tool for the development of new materials or new products. For these purposes, collaborations have been vigorously initiated between companies, or between companies and universities or public institutes at some of SPring-8's beamlines.

The subjects proposed to clarify the problems for improving or creating many interesting materials, and addressing the applications. To assess these proposals, measurements using X-ray diffraction, X-ray reflection, phase contrast imaging, and X-ray absorption fine structure techniques were carried out.

Here, six carefully selected experiments successfully accomplished in 2001B and 2002A are presented. The very interesting topics referred in this section were achieved by using the following three different beamlines, namely, one topic using Hyogo beamline, BL24XU, two topics using the public beamline for Engineering Science Research, BL19B2, and three topics using the contract beamline for Industrial Consortium ID (SUNBEAM-ID), BL16XU.

These studies include very important matters or scientific technologies for industrial use, and it is certain that they will be continued in greater detail because the technology has made remarkable progress lately and there is strong international competition to win the race of making better products.

Tokuhiko Okamoto

Measurement of Strain in Silicon-on-Insulator Layers by using Synchrotron X-ray Microbeam

Semiconductor device characteristics are, more or less, influenced by crystalline defects such as dislocations. Therefore, from points of view of scientific and device performance improvement, the study of local strain distribution not only in starting bulk materials but also in some device-processed ones are of great importance. To analyze local minute strain in materials, we have provided an X-ray microbeam 7 μm × 6 μm in size with a narrow angular divergence of less than 2 arcsec in both the vertical and the horizontal polarization directions of synchrotron radiation by using successive asymmetric Bragg reflections [1] at an energy of 15 keV, on beamline **BL24XU**. By scanning the microbeam along a line on the sample surface, a series of X-ray rocking curves, which is referred to as rocking curve maps, RCMs, have been obtained. By putting an analyzer crystal behind the sample, reflection-intensity maps in a reciprocal lattice space (q_x, q_y), which is referred to as reciprocal space maps, RSMs, have been drawn for various local points on the surfaces.

Silicon-on-insulator (SOI) materials consisting of top-Si/buried-SiO_2 ("BOX" layer)/Si-substrate are expected to be some of the most promising silicon substrates for extending three-dimensional metal-oxide-silicon (MOS) devices. We have applied present X-ray microbeam diffraction techniques to analyze the strain fluctuation in bonded SOI crystals [2]. Since lattice plane of the SOI layer and that of the substrate are not completely parallel, the X-ray rocking curves usually reveal two peaks of the Bragg reflection, one coming from the SOI layer and the other from the substrate. Figure 1 shows one of the 004 reflection RCMs measured for a 5-μm-thick SOI sample. It is interesting to

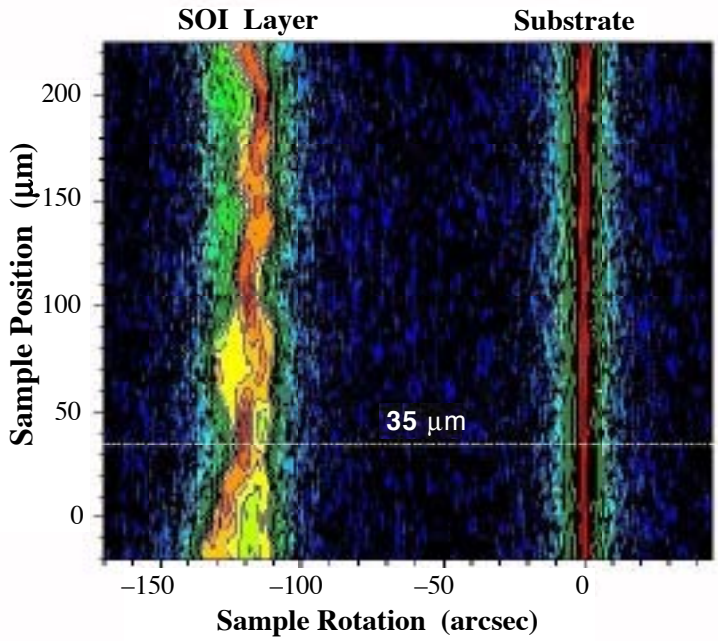

Fig. 1. RCM of 004 reflection taken from a 5-μm-thick SOI layer. The vertical axis indicates the positions of the sample irradiated by the scanning X-ray microbeam.

point out that the peak profiles and the half-widths corresponding to the SOI layer vary depending on the irradiated positions, while a vertical line of high intensity corresponding to the substrate on the right hand side of Fig. 1 is quite straight.

Then, RSMs were taken at some fixed positions of the SOI peaks in Fig. 1. Figure 2 shows an example of the RSM measured for the SOI layer at the dotted line (Z = 35 μm) in Fig. 1. It is clear from this figure that the lattice distortion in the SOI layer is mainly due to the lattice tilt variation because several high-intensity centers at different ω can be seen at $\Delta d/d = 0$. This fact suggests the existence of several crystal grains of an equivalent lattice tilt angle.

It is interesting to see how the equi-tilted lattice planes extend in the SOI layer. The sample was scanned against the microbeam and the reflection intensity was recorded at a fixed tilt angle of the crystal rotation (ω). Both images in Fig. 3 show the intensity distribution maps (so-called equi-tilt maps) for an area of about 300 × 300 μm² of the SOI layer, measured at two different rotation angles, (a) ω = −7.9 and (b) ω = +7.9 arcsec. Those images clearly show that magnitude of the lattice tilt varies in total more than 16 arcsec within the measured area. Typical spatial sizes of the equi-tilt grains range from 20 to 80 μm in this sample.

A similar feature of the lattice tilt was also observed in a SIMOX wafer, which is another type of SOI crystal. Analysis revealed that the SOI layers formed on the BOX layer are more or less strained and fluctuated, and magnitude of the lattice tilt depends on the SOI and the BOX thicknesses and the SOI layer processing conditions. At present, the major reason for such a large lattice tilt in the SOI layer has not yet been clarified. It can be safely said that the SOI surface polishing effects can be excluded, because there was no peak shift with a wide angular width observed for samples with a thicker (more than 60 μm) SOI layer.

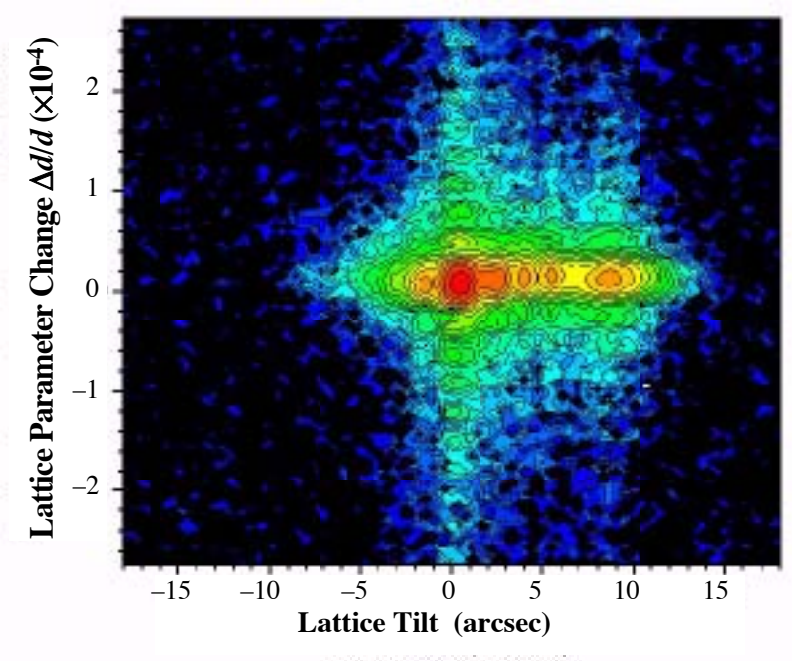

Fig. 2. RSM of a SOI layer measured at the dotted line position of the RCM shown in Fig. 1. Intensity spots in the horizontal direction at Δd/d = 0 show lattice tilt of the grains in the SOI layer. Additional spot arrays lying along the vertical direction are due to thickness fringes belonging to each small grain in the SOI layer.

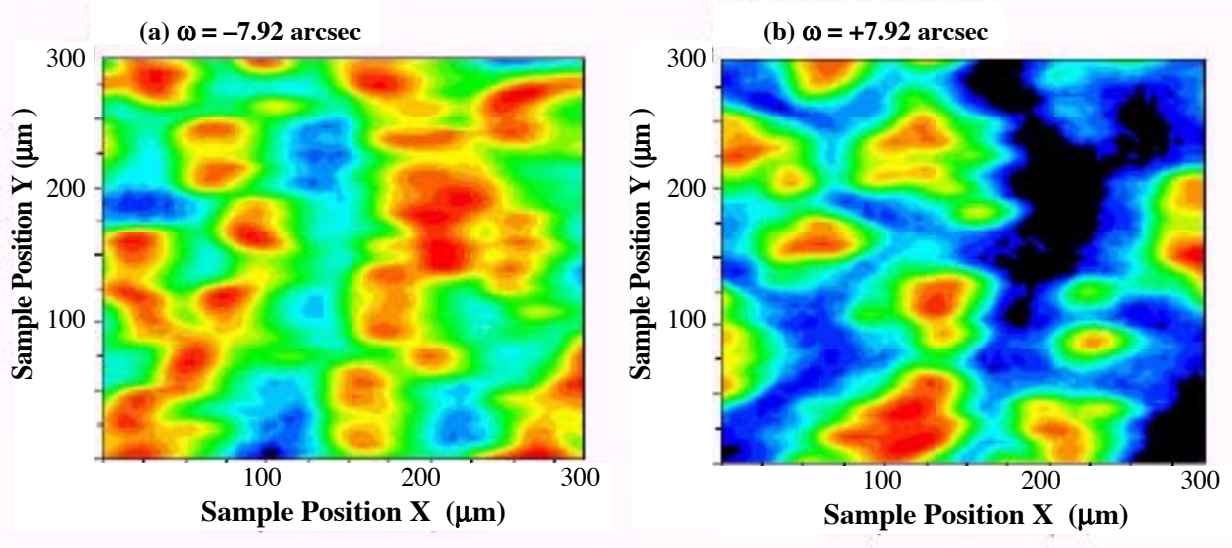

Fig. 3. Equi-tilt maps taken at two different angles around the Bragg peak. Contrasts seem to be complementary between (a) and (b).

Junji Matsui

Himeji Institute of Technology

E-mail: matsui@sci.himeji-tech.ac.jp

References

[1] Y. Tsusaka *et al.*, Jpn. J. Appl. Phys. **39** (2000) L635.
[2] Y. Tsusaka, M. Urakawa, K. Yokoyama, S. Takeda, M. Katou, H. Kurihara, F. Yoshida, K. Watanabe, Y. Kagoshima and J. Matsui, Abstracts of 3rd Int'l Conf. Synchrotron Radiation in Materials Science, also appearing in Nucl. Instrum. & Meth. in Phys. Res. B **199** (2003) 19.

In situ X-ray Radiography for Compression Test of Foam Aluminum

In recent years, it has become increasingly important to reduce the weight of automobiles because of energy and environmental problems. Moreover, the popularization of aluminum use in automobiles is expected to improve human safety. Foam aluminum has features such as lightness, a high modulus of rigidity, and high crashworthiness (shock resistance), etc. Particularly, foam aluminum has several excellent properties for both reducing vehicle weight and improving human safety. However, neither the technology for evaluating its mechanical properties nor the technologies for its practical use in car parts have yet been established for foam aluminum. Therefore, practical uses of foam aluminum have stalled. In recent years, however, some examples on foam aluminum characterization using synchrotron radiation have been reported in Europe and the U.S.A [1-3]. This report includes its first use in Japan in an X-ray phase-contrast imaging experiments with synchrotron radiation. The results will be used to develop in situ technology for determining the high-speed distortion of the porous structure in foam aluminum [4]. This research is expected to lead to the establishment of a basic structural design of automotive material with foam aluminum and the improvement of its crushability properties. In this study, we aimed to take pictures of the *in situ* image of the porous structure, and also aimed to clarify how the porous structure influence on the pressure-displacement curve. Once the basic information has been obtained, it can be fed back to a basic structural design and be incorporated into structural materials for automobiles.

The *in situ* experiment on X-ray phase-contrast imaging of the foam aluminum cause by the reflection effect was done in the third hutch of beamline **BL19B2**. A continuous X-ray from the synchrotron radiation source was monochromatized by an Si(311) double crystal monochromator to 33 keV. The X-ray detector adopted was a 1280 × 1024 pixel CCD camera with a 6.7-μm pixel size (C4742-95, Hamamatsu photonics K.K). The distance between the sample and the camera was

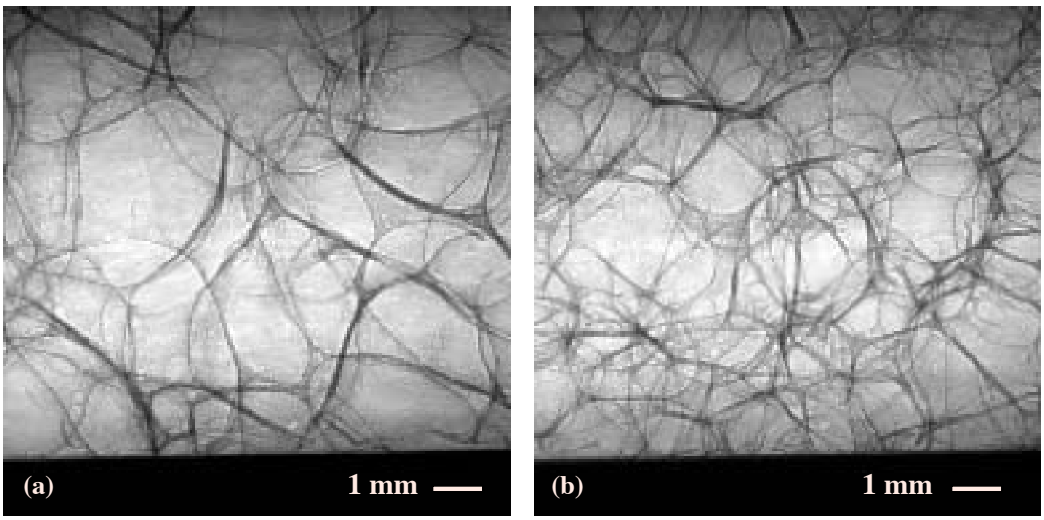

Fig. 1. Static image of two types of foam aluminum by X-ray radiography. The foam size is about 5.0 mm in ***(a)*** *and about 1.7 mm in* ***(b)****. The foam size of both types can be clearly distinguished.*

determined to be about 3 m by using the equation $L = D^2 / \lambda$, where L the distance from the sample to the detector, D the space resolution of detection, and λ the X-rays wavelength. The X-ray imaging data was stored in the process of compressing the sample with the speed of 1 mm/min, using the compression testing machine (AGS-H Shimadze Co. Ltd.) onto a PC (DOS/V, Windows 2000), one by one every two seconds. Static images of two kinds of foam aluminum with foam sizes of 5.0 and 1.7 mm are shown in Fig. 1(a) and (b), respectively. The difference in foam size could be identified by comparing each X-ray image. Figure 2 (a-c) shows three *in situ* images for a compression test. The foam with a size of $15^l \times 15^w \times 10^h$ mm^3 begins to collapse from both top and bottom edges of the sample. The sample center keeps its shape for a while. It is understood that the foam collapse once catastrophically, and then the remaining form collapses again.

In the sample with small-scale foam, it is understood that the stress induced under the transformation decreases and the displacement to complete destruction increases. In addition, it was observed that there were two types of processes operating in the destruction of the foam as seen in the movie of the foam aluminum impact test. One was buckling destruction and the other was an explosion. The compression speed of the sample was estimated at 1 mm/min in the actual experiment, taking into account the X-ray intensity and space resolution. Base d on the results of the actual experiment, we are planning to speed up the CCD camera's reading speed from seconds to milliseconds to record the destruction of the foam. That type of data will be of practical use for developing automotive materials from foam aluminum. In the near future, we plan to do further compression tests, bending tests, and modulus of rigidity tests on foam aluminum, which will help to increase the variety of applications for the material.

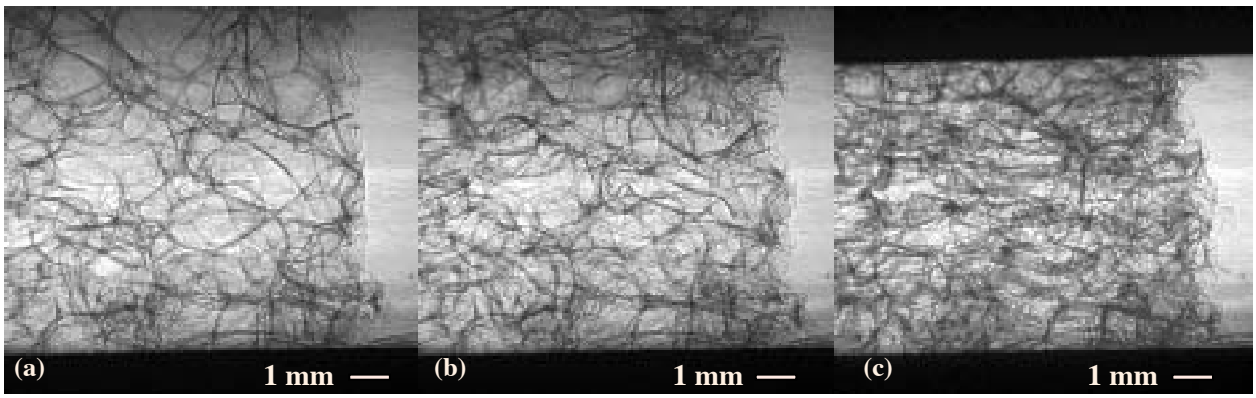

Fig. 2. Three scenes of an in situ image monitored by X-ray radiography when a compression test is done on foam aluminum. ***(a)*** *Foam aluminium begins to collapse at top and bottom.* ***(b)*** *Foam aluminium is collapsing. The center keeps its shape.* ***(c)*** *All the foams seem to be almost destroyed.*

Takashi Watanabe[a], Tetsuji Miyoshi[b] and Koichi Makii[c]

(a) Kobelco Research Institute, Inc.
(b) Shinko Wire Co., Ltd.
(c) Kobe Steel Ltd.

E-mail: watanabet@kobelcokaken.co.jp

References

[1] J. W. Elmer *et al.*, Scripta. Mater. **43** (2000) 751.
[2] L. Helfen *et al.*, Highlights 2000 ESRF (2001) 83.
[3] J. Banhart *et al.*, Appl. Phys. Lett. **78** (2001) 1152.
[4] T. Watanabe, Y. Ariga, T. Miyoshi and K. Makii, Adv. in X-ray Chem. Anal. Jpn. **34** (2003) 187.

Performance of X-ray Reflectometry for 1-nm Thick Gate Oxide

In a recent development of metal oxide semiconductor (MOS) devices, the thickness of a gate oxide has been reduced to 1 nm or even less. X-ray reflectometry is a useful tool for evaluating the thickness, density profiles and surface/interface roughness for thin films. This method is even applicable for very thin films, although it is not easy to evaluate films less than 1 nm thick. We studied the feasibility of evaluating such ultrathin films based on synchrotron radiation in comparison to the conventional X-ray source.

It is well known that the angular dependence of reflected intensity of X-rays from thin films shows the oscillation known as the Kiessig fringe, which provides the information on the layers. The oscillation intervals ($\Delta 2\theta$), which come from the interference of X-rays at a thin film, can be approximated as $\Delta 2\theta = \lambda / t$ [1], where λ is the X-ray wavelength, t is a layer thickness, and θ is the glancing angle of an X-ray. According to the equation, the interference interval increases with decreasing layer thickness. This relation indicates that the measurement of wide area of θ is requested to precisely evaluate a thin film. Since the reflected X-ray quickly decreases as $1/\theta^4$, a high-flux X-ray is required for obtaining data at high θ angles.

We compared the performance of X-ray reflectometry for a 1-nm-thick gate oxide using synchrotron radiation from a bending magnet and from an undulator in addition to the laboratory X-ray generator.

In the experiment using synchrotron radiation, an X-ray wavelength of 1.4 Å was selected by the double crystal monochromator. A Rh-coated X-ray mirror in the beamline was used to suppress higher harmonic X-rays which contaminate the monochromatized X-ray.

In reflectivity measurements, a wide intensity range of X-rays needs to be detected, and for this we used the NaI scintillation detector with a Cu attenuator of appropriate thickness to measure each angular division. The Cu attenuator also contributes to the suppression of higher harmonic X-rays with its high attenuation rate above the absorption edge. Vacuum pipes were inserted in the X-ray path to prevent the absorption of X-rays by air, as shown in Fig. 1.

After the measurement, reflectivity from each angular division was corrected for the dead time loss and concatenated into the reflectivity of the whole region.

In the reflectivity measurements taken at high angles, the background events become comparable to specularly reflected X-rays. We measured the background intensity at the off-specular configuration and removed it from the specular intensity.

A thermally grown 1-nm-thick SiO_2 layer on an Si substrate was measured with these techniques. At the bending beamline **BL16B2**, we obtained the reflectivity with the intensity range over 8 decades

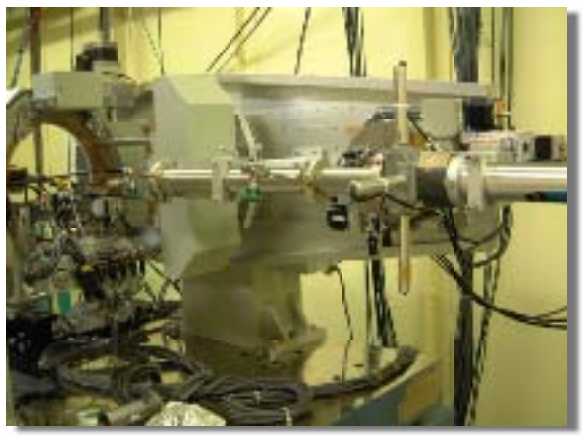

Fig. 1. Diffractometer at BL16XU used for the reflectivity measurement. Vacuum pipes are placed at upstream of the sample and between the sample and the detector to prevent absorption of X-rays in air.

and angular range around 10° (2θ) as shown in Fig. 2. On the other hand, at high-intensity undulator beamline **BL16XU** the intensity range of 12 decades and angular range around 40° was successfully obtained as shown in the same figure. In the figure, the reflectivity obtained from the laboratory equipment (Rigaku RGXR, 60kV-300 mA at 1.54 Å) is also shown for comparison, where an intensity of around 7 decades and angular range up to 6° (in 1.4 Å equivalent angle) was obtained.

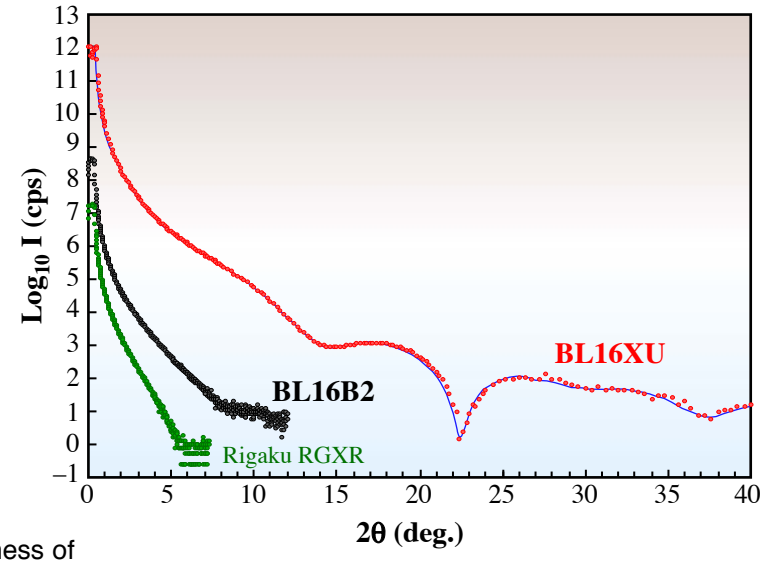

Fig. 2. Reflectivity profile for 1-nm SiO_2/Si. The solid line indicates the results of model calculation.

Based on Equation (1), the layer thickness of 1 nm corresponds to the angular interval of 8°, which indicates that the laboratory equipment is insufficient, even for determining its thickness. The measurement at the bending beamline can determine the thickness around to 1 nm. However, it is insufficient for determining the density profile within a film. The measurement taken at the undulator beamline can provide precise information that includes a density profile for the advanced gate oxide below 1 nm.

We analyzed the reflectivity obtained at the undulator beamline by using model optimization based on the matrix formalism of Vidal and Vincent [1]. In the model, we sliced the layer into 0.1-nm (1 Å)-thick sublayers with different densities. The solid line in Fig. 2 (BL16XU data) shows the results of the model calculation, and in Fig. 3 the corresponding density profile is shown. In this 0.1-nm regime, these density profiles give information not only on the compactness of SiO_2 [2], but also on the location of silicon and oxygen atoms in films grown layer by layer [3] through their different electron densities.

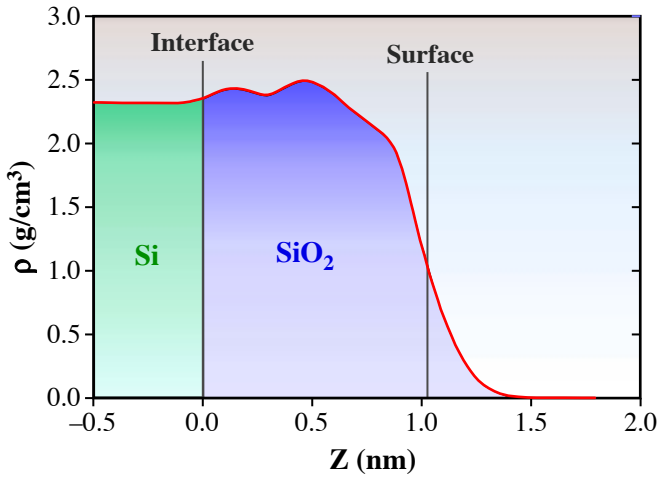

Fig. 3. Density profile obtained with the 0.1-nm sublayer model.

Naoki Awaji

Fujitsu Laboratories LTD.

E-mail: awaji@ccg.flab.fujitsu.co.jp

References

[1] B. Vidal and P. Vincent, Appl. Opt. **23** (1984) 1794.
[2] N. Awaji, Y. Sugita, T. Nakanishi, S. Ohkubo, K. Takasaki, and S. Komiya, J. Vac. Sci. Technol A **14** (1996) 971.
[3] M. Fujimura *et al.*, Ext. Abstr. Int. Conf. on Solid State Devices and Materials, Hamamatsu, Japan (1997) 542.

Structure Analysis of Co-based Alloy Thin Film Magnetic Media

The recording density of hard disk drives (HDD) used in personal computers is increasing by about 60% a year. The key components of HDDs are magnetic heads and magnetic recording media. A magnetic recording medium consists of layered thin films such as a Co-based alloy polycrystalline magnetic thin film on an Al or a glass substrate, and it is produced by a sputtering deposition system. With increasing recording density, the thickness of the magnetic film has decreased to about 10 nm.

The two most important factors for high density recording media are small grain size for small recording bits and excellent magnetic properties including high coercivity for thermal stability of small recording bits. Magnetic coercivity depends on the magnetic materials used, the strain in the magnetic layer and the preferred orientation of c-axes in Co micro-crystals [1,2]. Because the c-axis of a *hcp*-Co crystal is the easiest axis to magnetize, the preferred orientation of the c-axis to the surface plane is important in longitudinal magnetic recording media. The preferred c-axis orientation and the strain in the magnetic layer depend on both deposition conditions and layered structures including underlayers. Conventionally, CoCr alloy is used as the magnetic layer, and *bcc* -Cr or a Cr-based alloy is used as an underlayer. They are deposited on a heated substrate disk.

Grazing incidence X-ray diffraction, especially in-plane diffraction, by synchrotron radiation is useful for the crystallographic analysis of such thin films in recording media, because the highly brilliant X-rays of synchrotron radiation causes high sensitivity and high accuracy [1,2].

XAFS is also expected to be a useful method for the local structure analysis of Co atoms and additional atoms, because magnetic properties depend on the composition and atomic arrangement of the magnetic layer.

Recently we have studied a new type of recording media prepared with non-heating process. Figure 1 shows the layered structure. This type of medium has a CoPt alloy magnetic layer and an intermediate layer of Ru and shows high magnetic coercivity [3]. To clarify the role of the Ru intermediate layer, we investigated the crystallographic structure of each layer and the dependence of the structure on the deposition conditions and on Pt content of the magnetic layer [4]. We have also studied the local structure of Co atoms in the CoCrPt magnetic layer.

We conducted 2θ scan measurements of in-plane diffraction with an X-ray energy of 10 keV (λ = 0.124 nm) or 12.4 keV (λ = 0.1 nm) at beamline **BL16XU**. The grazing incidence angle was 0.25° or 0.2° in the total reflection condition. The incidence

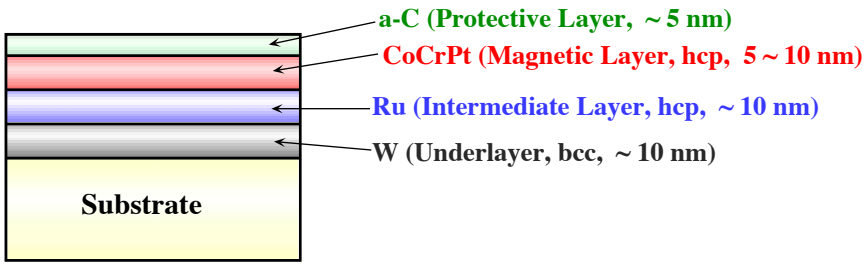

Fig. 1. The layered structure of magnetic recording media prepared with the non-heating process.

slit was 1 mm(V) × 0.1 mm(H).

Figures 2(a) and 2(b) show the in-plane 2θ scan diffraction profiles of magnetic layers and Ru layers respectively. Preferred in-plane c-axis orientation of *hcp* -Ru increases largely with a changing Ru deposition condition, from A to C, and that of *hcp* -Co in the magnetic layer also increases depending on the crystallographic orientation of Ru. The coercivity Hc also increases with the changing Ru deposition condition, from A to C, as a result of increasing preferred c-axis orientation of Co.

The Ru crystal has the same *hcp* structure as Co; but it has lattice constants several % larger than those of Co. Therefore, the Ru intermediate layer is considered to play an important role in controlling the preferred c-axis orientation of the CoPt alloy magnetic layer in the case of using non-heating process.

Figure 3 shows the in-plane 2θ scan diffraction profiles of three CoCrPt-alloy magnetic thin films with different Pt contents. With increasing Pt content, magnetic coercivity increases and the preferred in-plane c-axis orientation of Co crystals also increases suggesting a correlation between them. Diffraction peaks of Co also shift to lower diffraction angles with increasing Pt content, indicating that lattice spacing of Co crystals increases through CoPt alloying. This result suggests that the increase in preferred c-axis orientation is caused by a decrease in the lattice misfit between the CoCr alloy and Ru.

We also measured Co *K*-edge XAFS spectra of these three CoCrPt alloy magnetic films. XAFS measurements are performed in the fluorescence

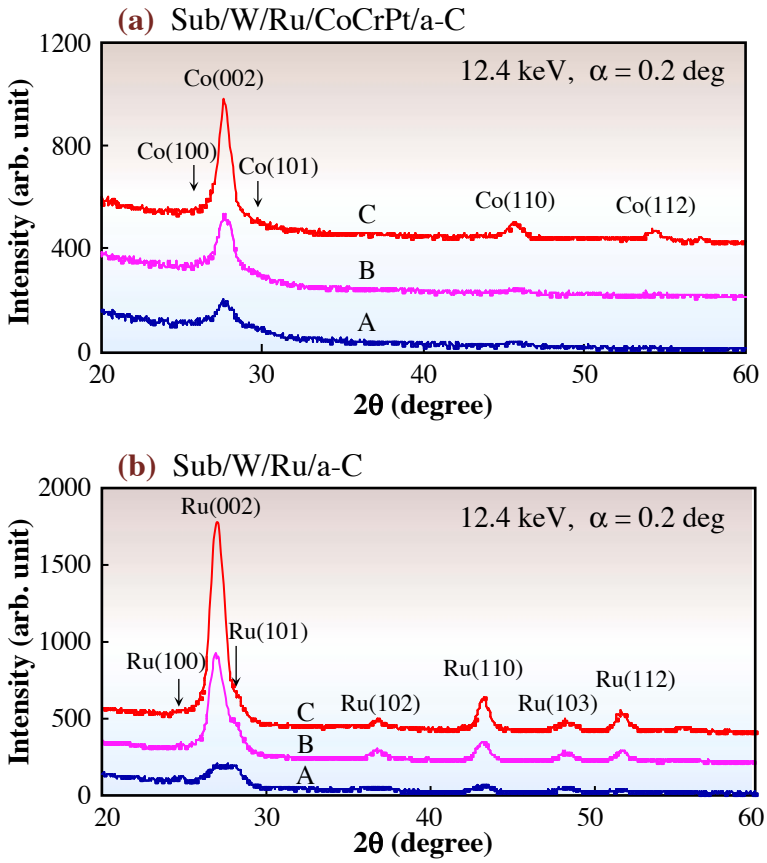

Fig. 2. In-plane diffraction profiles of ***(a)*** *CoCrPt magnetic layers and* ***(b)*** *Ru intermediate layers for the Ru deposition conditions, A, B, C, of magnetic media prepared with the non-heating process. Magnetic coercivity Hc are A: 2452Oe, B: 3671Oe, C: 3909Oe.*

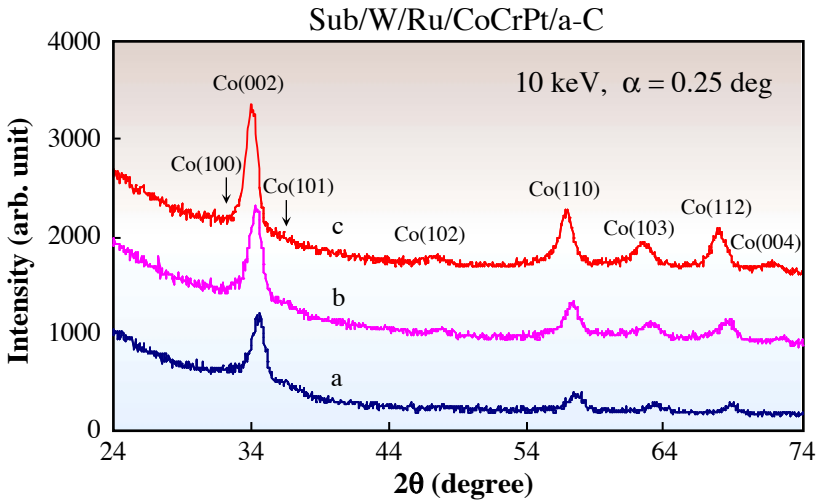

*Fig. 3. In-plane diffraction profiles of three CoCrPt magnetic films of magnetic media for Pt content. Pt content is **a**: low, **b**: middle, **c**: high. Magnetic coercivity increases with increasing Pt content. Magnetic coercivity Hc are A: 3567Oe, B: 4685Oe, C: 7052Oe.*

yield mode at beamline **BL16B2**.

XANES spectra of CoCrPt thin films are shown in Fig. 4. The intensity of the Co-Kα fluorescent X-ray decreases with increasing Pt content. The absorption at the *K*-edge is probably influenced by Pt. XANES spectral shapes of the three CoCrPt films are almost the same, suggesting that the electronic environments of Co atoms are almost the same.

We revealed that, in the new-type magnetic recording media with an Ru intermediate layer, the Ru intermediate layer plays an important role in controlling the preferred c-axis orientation of the CoPt alloy magnetic layer. Experimental results suggest that the increase in coercivity with increasing Pt content is caused, partly at least, by the decrease in the lattice misfit between the CoPt alloy and Ru.

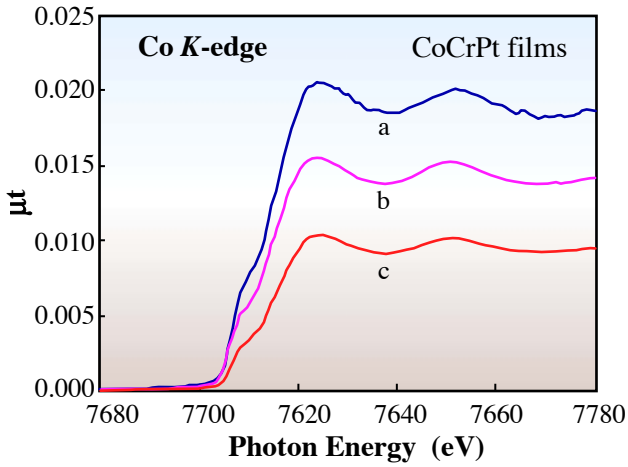

*Fig. 4. XANES spectra of three CoCrPt magnetic films of magnetic media for Pt content. Pt content is **a**: low, **b**: middle, **c**: high.*

Michio Ohsawa

Fuji Electric Corporate Research & Development Ltd.

E-mail: ohsawa-michio@fujielectric.co.jp

References

[1] T. Hirose *et al.*, IEEE Transactions on Magnetics, No.5, **33** (1997) 2971.
[2] M. Ohsawa *et al.*, Jpn. J. Appl. Phys. **38** Suppl.38-1 (1999) 365.
[3] H. Ohmori *et al.*, IEEE Transaction on Magnetics, No.4, **37** (2001) 1488.
[4] M. Ohsawa *et al.*, Fuji Electric Journal (in Japanese), No.9, **75** (2002) 501.

X-RAY MICROBEAM CHARACTERIZATION OF Cu WIRES

Recent progress in large-scale integrated circuit (LSI) technology has been remarkably fast. Rapid progress made in the storage capacity of dynamic random access memories (DRAMs). Improvement in the performance of microprocessors (MPUs) is widely recognized. The International Technology Roadmap of Semiconductors [1], which forecasts future trends in the worldwide development of fabrication technology for semiconductor devices, indicates that the minimum feature size of an MPU will be 25 nm and the chip frequency will reach around 7 GHz by 2007, as shown in Table I.

Year of production	'03	'05	'07	'16
DRAM half pitch (nm)	100	80	65	22
MPU gate length (nm)	45	32	25	9
Chip frequency (GHz)	3.09	5.17	6.74	28.7

Table I. *Roadmap about main issues in semiconductor device technology (ITRS 2001).*

As explained in the Roadmap, various new materials and techniques are being introduced into the fabrication processes. Copper interconnect technology [2], first introduced by IBM, is the best example. To achieve a higher performance and more reliable MPUs, copper was introduced as a new material instead of the conventional Al alloy. Copper has lower electric resistivity and a longer lifetime than Al. Copper, however, is very difficult to pattern using conventional subtracting methods like plasma etching. An alternative patterning method used now is the "damascene" method. Here, Cu is deposited in trenches that form nanometer-sized electric circuits.

Such dramatic changes in both materials and patterning methods require tremendous research efforts to understand the interconnect technology. To produce high-performance devices, we must physically understand the reasons of certain failure phenomena, such as interconnect breakdown, occur. For example, Cu atoms in the fine lines migrate due to a strong "wind" of electrons, and this generates voids and hillocks in the metal lines (Fig. 1(a)). This is called electromigration (EM). A second example concerns the mechanical

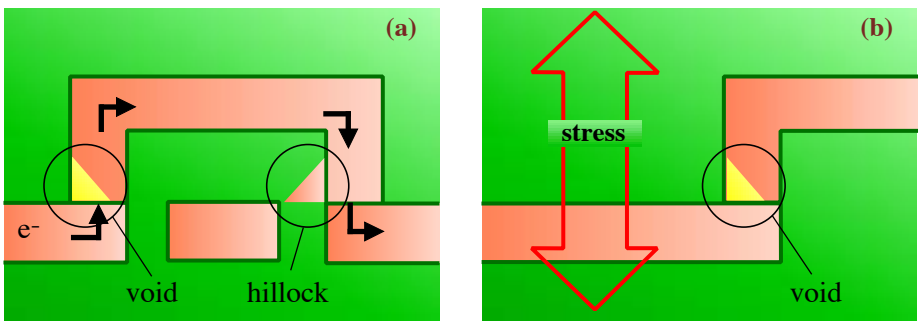

Fig. 1. Interconnect failure mechanism. ***(a)*** *Electromigration (EM). Strong electron "wind" blows Cu atoms.* ***(b)*** *Stress migration (SM). Stress gradient causes migration of Cu atoms.*

environment where stress distribution in interconnects causes voids to form. This is called stress migration (SM) (Fig. 1(b)). These atomic migrations are serious problems for the reliability of MPUs. Crystallographic grains and grain boundaries of Cu metal lines greatly affect the migrations. Consequently, the status of grains must be studied microscopically.

Measurement techniques used in the study of interconnects are scanning electron microscope (SEM), transmission electron microscope (TEM), and X-ray diffraction (XRD) measurements. SEM and TEM have excellent spatial resolutions, but, unfortunately, they cannot see the metal lines buried in dielectric materials in actual chips. Conventional XRD measurement provides precise data about strain in thin films, but its spatial resolution is around several tens of microns, even in the most sophisticated apparatus. To observe the the microscopic and the crystallographic status of fine metal lines without any destructive sample preparations, a new measurement technique is required.

An X-ray microbeam is a promising tool for such a purpose. The X-ray microbeam can penetrate thick dielectric materials, and scanning with the microbeam provides a microscopic image of the metal lines buried in the dielectric layer. Moreover, by using the X-ray microbeam, an X-ray micro-diffraction measurement [3] can be taken to measure the strains of the grains in the fine metal lines. We are currently studying physical mechanisms of interconnect failure using X-ray microbeams of 1 μm, which are available in the SUNBEAM beamline **BL16XU**.

Figure 2 shows the preparation and results of the experiment we conducted to observe Cu atom migration paths. Because there was no distinction between migrating Cu atoms and atoms in Cu

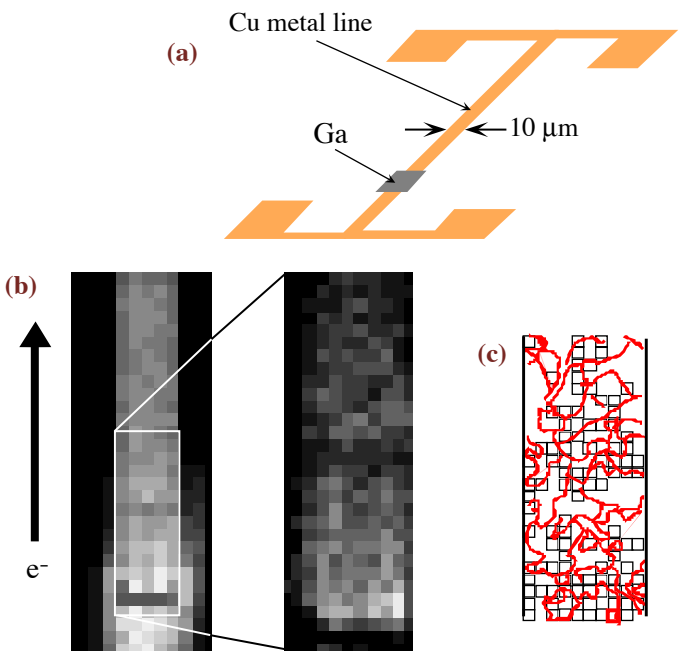

*Fig. 2. Experiment for observing Cu atom migration paths. (**a**) Initial distribution of Ga atoms. (**b**) Gallium distribution after current loading. (**c**) Coincidences between grain boundaries and the Ga distribution.*

grains, direct microscopic observation of Cu migration paths has not been done previously. This experiment was the first attempt at observing Cu migration paths by means of tracer atoms. We distributed Ga atoms locally before current loading and observed the redistribution of the atoms due to EM. Figure 2(b) gives the results of Ga X-ray fluorescence (XRF) mapping, obtained by X-ray microbeam scanning, and shows Ga atom distribution after the current was turned off. Figure 2(c) shows both the points of high Ga concentration and the grain boundaries to illustrate the coincidences between grain boundaries and the Ga distribution. This method thus reveals the diffusion paths of Cu, and should be useful when developing the fabrication processes for high-resistance interconnects against EM failure.

Figure 3 shows the microscopic X-ray diffraction experiment. The inset photograph shows diffracted X-ray spots from a 0.3-μm Cu damascene line

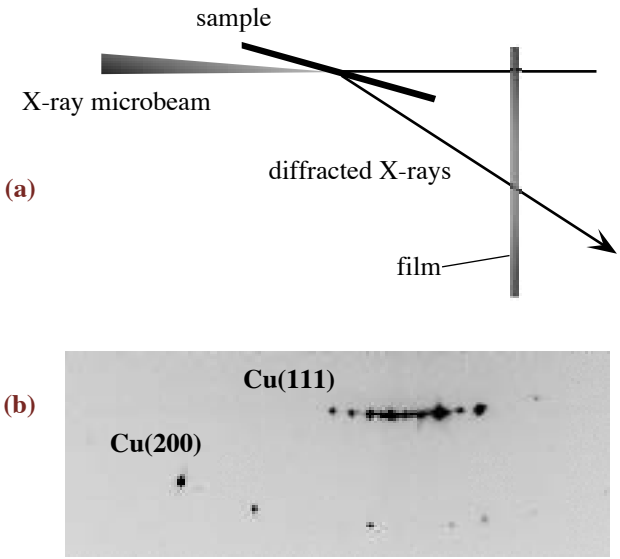

*Fig. 3. X-ray diffraction experiment using X-ray microbeam. **(a)** Experimental setup. **(b)** Diffraction spots from 0.3 μm Cu interconnect.*

irradiated with an X-ray microbeam. The diffraction angles on individual grains at the local area can be estimated from the positions of these spots. Detailed analysis of these spots provides information on the strain state of the individual grains in the metal line. As the stress gradient of the grains is a driving force of SM, these microscopic crystallographic measurements should become important tool for understanding the mechanism of stress migration.

Masaki Hasegawa

Central Research Laboratory, Hitachi Ltd.

E-mail: mhasegaw@crl.hitachi.co.jp

References

[1] http://public.itrs.net/
[2] D. Edelstein, Multilevel Interconnect Technology II, Proc. SPIE **3508** (1998) 8.
[3] M. Hasegawa and Y. Hirai, J. Appl. Phys. **90** (2001) 2792.

In situ Observation of Formation of Fe-Zn Intermetallic Compounds During Galvannealing Process by X-ray Diffraction

Galvannealed steel sheets are widely used in the automotive industry to protect car bodies from corrosion. In the industrial process of galvannealed steel sheets, steel substrates are dipped in molten zinc containing a small amount of aluminum, then annealed in a furnace at about 500 ℃. Since the coating of the galvannealed steel sheets mainly consists of Fe-Zn intermetallic compounds, such as $FeZn_7$ (δ_1 phase) and $FeZn_{13}$ (ζ phase), it is very important to study the growth behavior of those compounds during a galvannealing process to understand the roughness or the mechanical properties of the coating after the process.

As summarized by Horstmann [1], many reports on hot-dip galvanizing reactions have been presented. However, because those reactions occur in a short period up to 60 seconds, it is very difficult to detect them with static analyses using the specimen quenched after annealing, such as a cross-sectional observation of the coating with an electron microscope or the measurement of the iron content of the coating. Therefore, a rapid detection system is required to observe those reactions dynamically, *i.e.*, "*in situ* observation." In order to perform the "*in situ* observation," penetration depth of the X-ray and time definition of the detector are important factors because it is necessary to observe the whole coating with a 10 ~ 20 μm thickness, and to observe the reaction finishing within 60 seconds. An easy way to achieve good time definition of the detector is to increase the source intensity. Therefore, the X-ray source, being able to penetrate deeply, *i.e.*, having high energy and high intensity, is necessary for the "*in situ* observation."

In this study, synchrotron radiation was used as

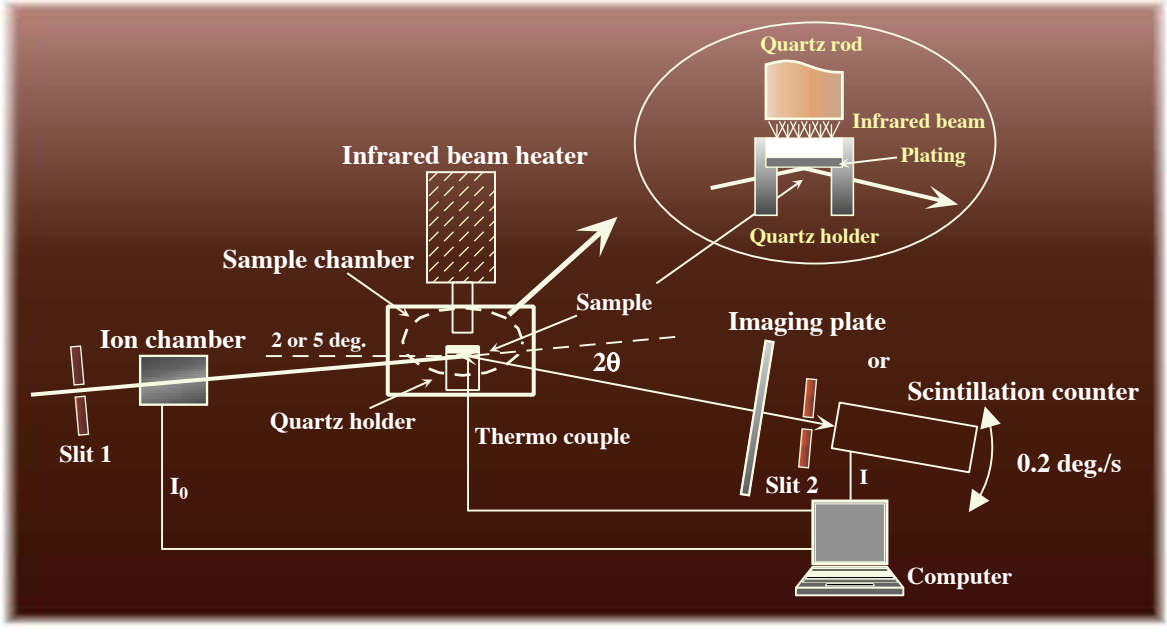

Fig. 1. Schematic illustration of the in situ observation system.

the X-ray source and the experiments were performed at beamline **BL19B2** [2]. The schematic illustration of the *in situ* observation system is shown in Fig. 1. The galvanized steel sheet sample was mounted on a quartz holder in the sample chamber filled with N_2 gas, and was heated from the polished side with the infrared beam heater (Thermo Riko: GA152) mounted on the 8-axis goniometer. We obtained heating time-dependent diffraction peak profiles with either a scintillation counter or an imaging plate. When the scintillation counter was used, the peak profiles were measured at intervals of 5 seconds while being scanned at an angle velocity of 0.2 degrees per second. When the imaging plate was used, the peak profiles were measured every second.

Figures 2(a) and 2(b) show diffraction peak profiles obtained with a scintillation counter and an imaging plate, respectively. The samples had zinc coatings containing small amounts of aluminum. Heating time shown in the figures was started to be counted when the coating fully melted. An increase in the diffraction peak intensity identified as δ_1(330) was successfully observed in the profiles. The diffraction peak could not be observed in profiles up to 20 seconds after the coating melted in Fig. 2(a), therefore, it is considered that the 30-μm coating, was too thick to allow detection of the diffraction peaks of the δ_1 phase growing near the interface between the coating and the steel substrate at the beginning of the annealing process.

On the other hand, the diffraction peak could not be observed up to 7 seconds after the coating melted in Fig. 2(b). In this measurement, the thickness of the coating does not affect the observation of the diffraction peaks of the δ_1 phase growing near the interface as mentioned above, because the steel substrate's diffraction peak was obtained clearly. It is well known that aluminum in the coating forms an Al-rich layer between the

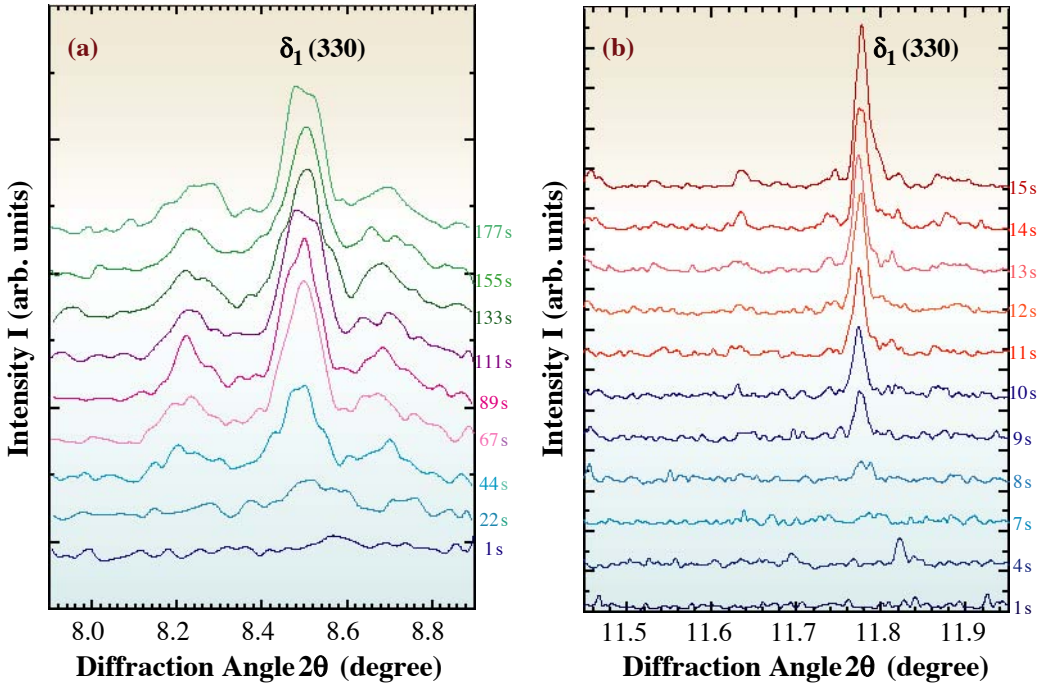

*Fig. 2. Diffraction profiles obtained from galvanized steel sheet during annealing. **(a)** Wavelength of incident X-ray: 0.0319 nm; thickness of the coating: 30 μm; detector: scintillation counter. **(b)** Wavelength of incident X-ray: 0.0443 nm; thickness of the coating: 10μm; detector: imaging plate.*

coating and the steel substrate, retarding the growth of Fe-Zn intermetallic compounds [3]. Therefore, the variation of peak profiles indicates that the Al-rich layer prevents the growth of δ_1 phase at the beginning of the annealing process. The period from the beginning of annealing to the beginning of Fe-Zn intermetallic compound growth is called an "incubation period."

Assuming that the δ_1 phase grows in a layer-by-layer manner, the time dependence of thickness was estimated as shown in Fig. 3. The estimated thickness of the δ_1 phase increased by the parabolic law with annealing time, taking into account the incubation period (t_{inc}). These results suggest that the growth of δ_1 phase is dominated by a diffusion of Fe atoms and Zn atoms in the coating.

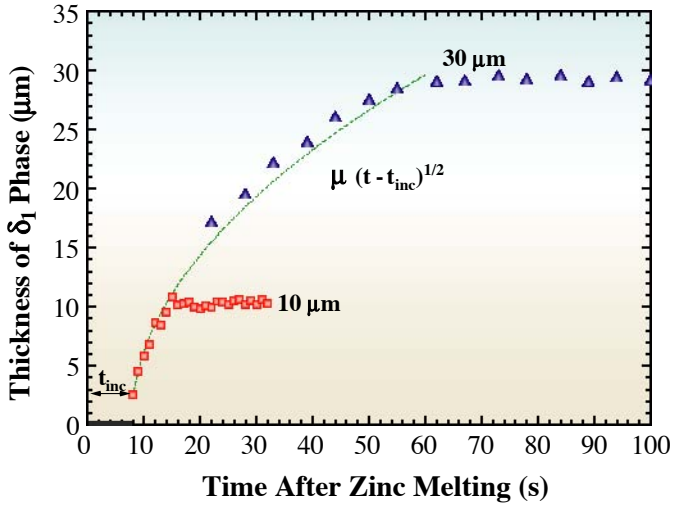

Fig. 3. Relationship between estimated thickness of the δ_1 phase and annealing time.

Akira Taniyama

Corporate R&D Laboratories, Sumitomo Metal Industries, Ltd.

E-mail: akira@pca.amaken.sumitomometals.co.jp

References

[1] D. Horstmann and F.K. Peters, Stahl u. Eisen **90** (1970) 1106.
[2] A. Taniyama, T. Takayama, M. Arai, H. Kawata, M. Sato, I. Hirosawa, T. Fukuda and J. Mizuki, Proc. Int. Conf. on Designing of Interfacial Structures in Advanced Materials and their Joints, Osaka, Japan (2002) 385.
[3] H. Bablik, Galvanizing (Hot Dip), 3rd ed., Spon Ltd., London (1950) 204.

INSTRUMENTATION & METHODOLOGY

The highlights over the last year in this section have been developments in high-resolution techniques for energy, time and space, and the construction of new beamlines for structural genomics. The first report describes the high-energy-resolution beamline for inelastic X-ray scattering with meV bandwidth. The article second reports on the unique time-resolving technique (100 fs) using a Hanbury-Brown-Twiss type interferometer. Reports of 3, 4, 5 and 6 address the advanced techniques of high spacial-resolutions in different types of imaging. They report, respectively, three-dimensional diffraction microscopic imaging with a resolution of 50 nm (2-D: 8 nm) utilizing coherence of undulator radiation, the performance of sputtered-sliced Fresnel zone plates (FZP) for hard X-ray region with a resolution of 0.1 μm, microscopic tomography using FZP with a resolution of 0.6 μm, and the blurring suppression of the phase contrast image of biological samples by using a lamella as a half-mirror of a Bonse-Hart interferometer. The seventh report describes the new beamlines, which are equipped with very powerful automated sample-preparing and measuring instruments for protein crystallography. These developments will surely open new scientific opportunities in various fields.

Makoto Watanabe

Performance of BL35XU for High Resolution Inelastic X-ray Scattering

Investigation of sample dynamics at meV energy scales and Å length scales is now possible at beamline **BL35XU** [1] using inelastic X-ray scattering (IXS). IXS offers some unique advantages as compared to neutron scattering techniques, but comes at the expense of an extremely technically demanding setup. The primary advantages of IXS appear in measurements of disordered materials and small samples. More precisely, kinematic restrictions in neutron scattering can make it difficult to work at small momentum transfers, which is a crucial region for observing collective modes in non-crystalline materials [2]. In addition, typical neutron beam sizes are ~ cm^2, so that comparably large samples are needed. This may be compared to an X-ray beam from a 3rd generation synchrotron source that can easily be focused to a spot of ~ 100 μm or less in diameter. This is a great advantage for the investigation of materials that are difficult to prepare, or for the use of extreme sample environments (high pressure and/or high temperature).

The technical difficulty of IXS stems from the extremely high energy resolution required. Whereas meV resolved measurements using neutrons with ~ 20-meV energy require resolutions of $\Delta E/E$ ~ %, with X-rays of energy a few tens of keV, the required resolution jumps some five orders of magnitude to $\Delta E/E \sim 10^{-7}$, leading to a commensurate increase in difficulty. Despite this, BL35XU has gone from the very first tests of the spectrometer using a single analyzer in May and June of 2001 to a working setup with four analyzer crystals having 2-meV resolution in the space of five months, (including the two and a half month summer shutdown), very much faster than any comparable facility. Since the first user experiments in October 2001, steady progress has improved the resolution to between 1.5 and 1.8 meV (depending on the analyzer crystal) with as much as 5×10^9 photons/s in a 0.8-meV bandwidth and a ϕ 75-μm spot at the sample.

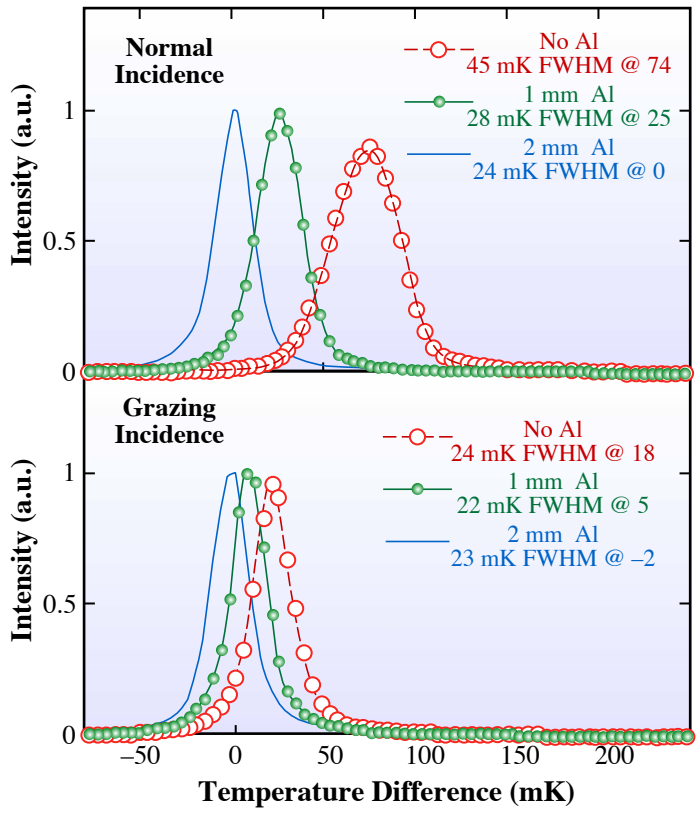

Fig. 1. Energy resolution for different power loads on the backscattering monochromator at 21.75 keV. A flat crystal (at fixed temperature) was used to analyze the beam reflected during a temperature scan of the monochromator. Each mm of aluminum reduces the incident power by a factor of 2. The grazing incidence geometry removes all of the broadening caused by the ~100 mW of beam (no Al). It also reduces the shift that occurs because the temperature sensor is not exactly at the beam spot. (Note: the relevant scale factor is about 18 mK/meV at this X-ray energy).

Here, we briefly discuss some of the instrumentation that has made this possible.

Two essential components in the operation of the spectrometer are the high resolution backscattering monochromator and the analyzer crystals. The monochromator, having to accommodate only the divergence of the undulator beam (some 15×40 μrad^2, or less) is the easier one, but, even so, it provided one notable surprise (beyond the expected difficulty of dealing with mK temperature control). In particular, it was found that the beam from the high heat load (Si (111)) monochromator, ~100 mW of power, caused local heating and distortion of the backscattering crystal over the beam spot. Thus, it was necessary to reduce the power density onto the backscattering monochromator in order to achieve resolution better than 2 meV. This was done by replacing the normal incidence backscattering monochromator with a grazing incidence version: working at a grazing angle of some 2.5 degrees reduced the power density by a factor of 20, and removed nearly all the effects of the heat load, as is evident in Fig. 1.

The analyzer crystals are more difficult, as they must accommodate a solid angle of $\sim 10 \times 10$ mrad^2, some five orders of magnitude more than the monochromator. Thus there has been an ongoing R&D program with NEC Fundamental Research Laboratory over the last four years to achieve good quality crystals. We have been following a prescription similar to that of [3]: first a flat wafer is cross-cut to produce many free-standing crystallites with a thin common back-wall; then these crystallites are bonded to a substrate of appropriate curvature; and finally the common back wall is removed, leading to many independent and, importantly, unstrained crystallites with the correct orientation. This process remains a bit of an art, but slow and mostly steady progress has led to a set of four crystals giving resolutions of 1.5, 1.6, 1.6 of 1.8 meV (operating at a 10-m radius, without any limiting apertures) using the Si (11 11 11) reflection at 21.75 keV. Presently, a 60- or 70-μm thick saw blade is used to cut 2.9 mm into a flat wafer on a 750 μm pitch. The crystallites are then bonded to a spherically curved substrate using a high temperature gold diffusion bond, and the back-wall is removed, leaving about 15000 independent crystallites with the appropriate geometry (rms deviation from the 9.8-m radius of the substrate is ~15 μrad, or better). Notably, after all etching, the active area of the crystallites is 60 to 65% of the substrate area, which is rather good. Figure 2 shows one of the analyzer crystals, while the Table I gives detailed

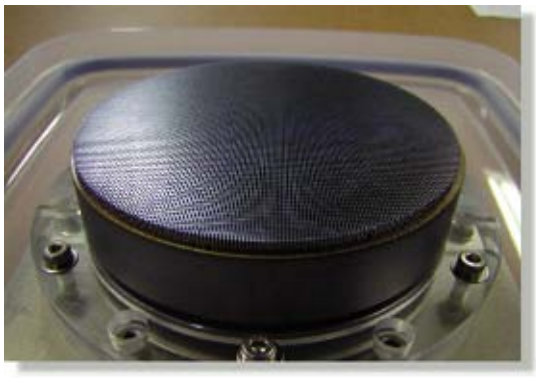

Fig. 2. 10-cm diameter analyzer crystal. Resolutions are presented in the Table I.

Table I. *Resolution at various silicon orders with the best analyzer crystal.*

Energy	Si (n n n)	FWHM (meV)	FWM/10 (meV)	FWM/100 (meV)	Rel. Flux
15.81	(8 8 8)	6.1	15.3	47	8
17.79	(9 9 9)	3.1	8.3	29	2
21.75	(11 11 11)	1.5	4.2	16	1

FWHM = Full Width at Half Maximum
FWM/X = Full Width at Maximum over X

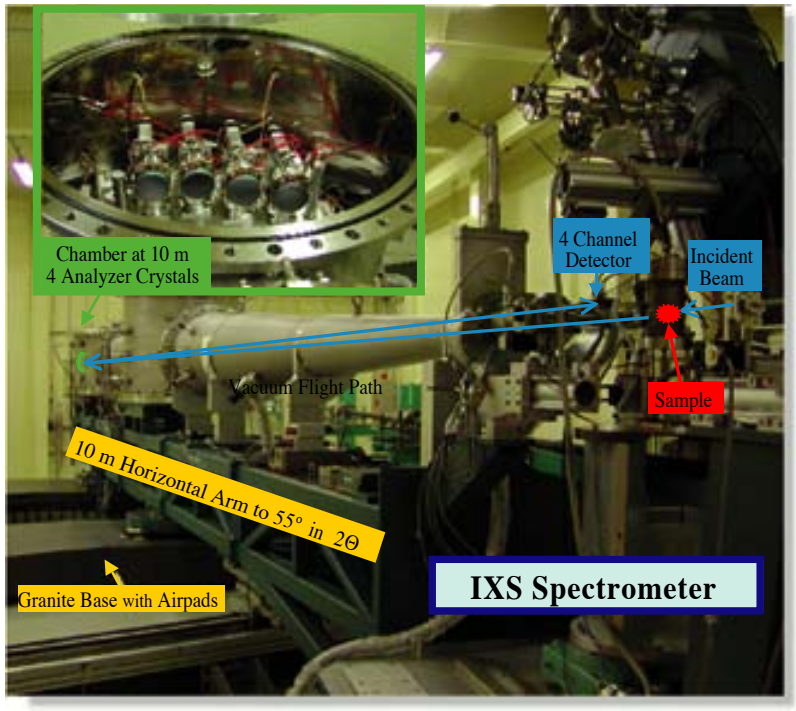

Fig. 3. The horizontal arm of the IXS spectrometer. Focused, highly monochromatic beam is incident from the right and is scattered by the sample into a set of four analyzer crystals that focus it into four detectors, allowing simultaneous measurement of four momentum transfers.

parameters. We are presently working to improve all crystals to the same 1.5-meV level of resolution.

The IXS spectrometer is shown in the final figure (Fig. 3). In the 19 months since first beam from a single analyzer crystal, and the 14 months since opening for user operation, the spectrometer has been used by many user groups to investigate a variety of liquid and solid materials, including several types of molten metals, mercury near the liquid-gas critical point (so both at high temperature and high pressure), and many crystalline materials, including several types of superconductors and one quasi-crystal.

Alfred Q. R. Baron, Yoshikazu Tanaka and Satoshi Tsutsui

SPring-8 / JASRI

E-mail: baron@spring8.or.jp

References

[1] A.Q.R. Baron, Y. Tanaka, S. Goto, K. Takeshita, T. Matsushita and T. Ishikawa. J. Phys. and Chem. Solids **61** (2000) 461; A.Q.R. Baron, Y. Tanaka, D. Miwa, D. Ishikawa, T. Mochizuki, K. Takeshita, S. Goto, T. Matsushita and T. Ishikawa, Nucl. Instrum. and Meth. in Phys. Res. A **467-468** (2001) 627.
[2] F. Sette *et al.*, Science **280** (1998) 1550; S. Hosokawa *et al.*, in this issue of SPring-8 Research Frontiers.
[3] C. Masciovecchio *et al.*, Nucl. Instrum. and Meth. B **111** (1996) 181.

Measurement of X-ray Pulse Widths by Intensity Interferometry

Ultrafast X-ray pulses provide a powerful probe for investigating structural dynamics in biological and material sciences. The upcoming linac-based undulator sources are capable of generating brilliant X-ray pulses of ~100 femtoseconds (fs). Although measurement of such ultrafast pulse width is crucial, no methods applicable to hard X-rays are currently available. In this report, we show that intensity interferometry, which is a technique initially developed by Hanbury-Brown and Twiss [1] and recently extended to the X-ray region [2,3], is capable of measuring X-ray pulse width (32 ps in FWHM) at SPring-8 [4]. Notably, the method can be easily extended to fs region by using simpler monochromators.

Most hard X-ray sources that are either currently available or under development including self-amplified spontaneous emission (SASE) free electron laser (FEL) in the linear regime, are considered to generate chaotic light. In this case, intensity interference is observed as an enhancement of the coincidence rate between the two detectors that receive the spatially and temporally coherent portions of the beam. In particular, when the method is applied to pulsed beam, the enhanced ratio includes information on the temporal pulse width s_t with respect to the longitudinal coherence time σ_t. Because the coherence time σ_t is directly given by the energy bandwidth ΔE of light, evaluation of the enhanced ratio with knowledge of the bandwidth enables to determine the pulse width s_t.

Experiments were performed using beamline **BL19LXU**, which is equipped with a 27-meter undulator, the most brilliant X-ray source currently available. The experimental setup is shown in Fig. 1. A monochromator consisting of 4-bounced asymmetric reflections (horizontal diffractions of Si 11 5 3, asymmetric angles α = 78.4°) was used as

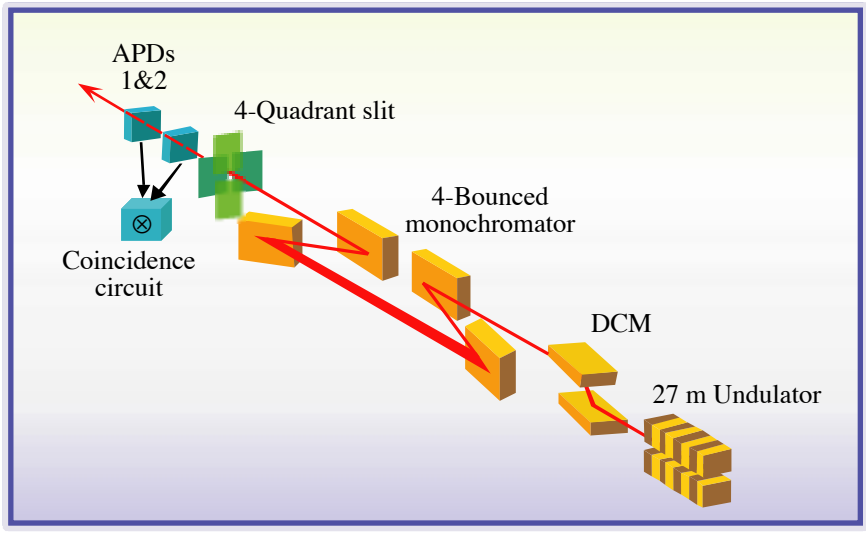

Fig. 1. Schematic view of the experimental setup. Undulator radiation is premonochromatized with a Si 111 double crystal monochromator (DCM). The 4-bounced monochromator and the 4-quadrant slit were employed to extract the longitudinally and transversely coherent portion of the beam, respectively. Two semi-transparent avalanche photo diodes (APDs) were aligned in tandem on the light axis. Outputs of the detectors were connected to the coincidence circuit.

an energy filter. The energy bandwidth was controlled by slight shift of the incident energy. A 4-quadrant slit was employed to the extract spatially coherent area of the monochromatic beam. The true coincidence rate, C_S, and the accidental one, C_N, were measured with coincidence circuits and an electric delay of 4.79 μs that corresponds to the revolution frequency of the storage ring.

The enhancement $R = C_S/C_N - 1$ of the coincidence rate is given by the inverse of the temporal mode number M_t, which means an average number of intensity fluctuation in a single pulse. We plotted the mode number M_t as a function of the bandwidth ΔE, as shown in Fig. 2. Assuming that the pulse envelope and the temporal coherence profiles are of both Gaussian distributions, M_t is given by $[1+(s_t/\sigma_t)^2]^{1/2}$ from theory, where s_t is the pulse width in FWHM and σ_t is the coherence time given by $(2\ln 2)h/(\pi\Delta E)$ (h is the Planck constant). The data were fitted with one fitting parameter, that is, the pulse width s_t. The width was determined to be 32.7±1.6 ps in FWHM. This value was compared to that measured with a streak camera, 32 ps [5]. This level of agreement was excellent.

Intensity interferometry combined with various X-ray monochromators is capable of determining X-ray pulse widths in the timescale from ns down to fs. This is because the monochromators can cover a wide range of bandwidth from 10^{-4} to 10 eV, which corresponds to values of σ_t between 10 ps and 0.1 fs. Importantly, the method can be easily extended to faster pulse regions because the optics required are much simpler than those used in the present work. The time resolution is unaffected by the timing jitter of the incident pulses and of the trigger signal. This method provides a unique technique for characterizing ~100-fs pulse profiles generated with the forthcoming linac-based, coherent X-ray sources, in addition to much faster X-ray pulses produced by proposed slicing technique of chirped pulses or ultrafast Bragg switches.

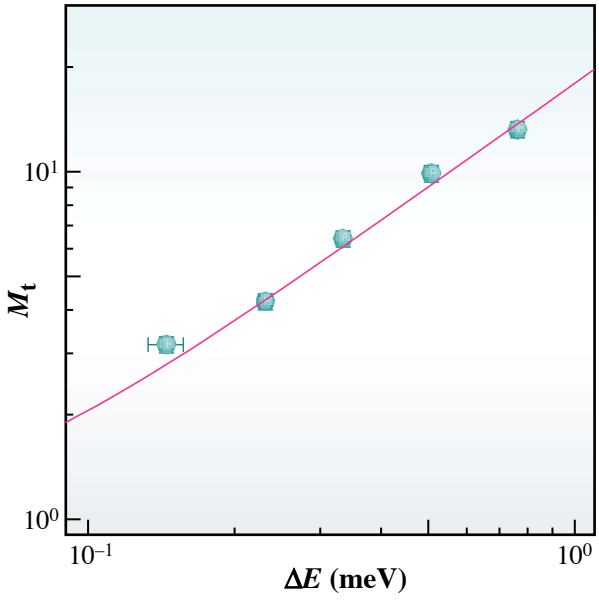

Fig. 2. The longitudinal mode number M_t vs. the energy bandwidth ΔE. The line shows the fit result with a pulse width st of 32.7 ps.

Makina Yabashi

SPring-8 / JASRI

E-mail: yabashi@spring8.or.jp

References

[1] R. Hanbury-Brown and R. Q. Twiss, Nature (London) **177** (1956) 27.
[2] E. Ikonen, Phys. Rev. Lett. **68** (1992) 2759; Y. Kunimune *et al.*, J. Synchrotron Rad. **4** (1997) 199; E. Gluskin *et al.*, *ibid.* **6** (1999) 1065.
[3] M. Yabashi *et al.*, Phys. Rev. Lett. **87** (2001) 140801.
[4] M. Yabashi, K. Tamasaku and T. Ishikawa, Phys. Rev. Lett. **88** (2002) 244801.
[5] H. Ohkuma *et al.*, Proc. of the 2001 Particle Accelerator Conference, Chicago, (2001) 2824.
[6] M. Cornacchia *et al.*, Linac Coherent Light Source (LCLS) Design Study Report. *Report SLAC-R-524* (Stanford Linear Accelerator Center, Stanford, California, 1998); R. Brinkmann *et al.*, DESY Report DESY97-048 (Deutsches Elektronen Synchrotron, Hamburg, 1997).

Towards Atomic Resolution 3-D X-ray Diffraction Microscopy

Due to the fact that X-ray wavelengths are on the order of the size of atoms, scientists have long dreamed of atomic resolution X-ray microscopes which could visualize arrangement of atoms in three dimensions. However, X-rays are much more difficult to focus than electrons. The smallest X-ray focal spot currently achievable is around 30 nm [1].

This limitation can be overcome by using coherent X-ray diffraction and the oversampling phasing method. When a finite specimen is illuminated by coherent X-rays, the weakly scattered X-ray photons form a continuous diffraction pattern in the far field. This continuous pattern can be sampled at spacings finer than the Nyquist frequency (*i.e.* the inverse of the specimen size), which we call "oversampling". Oversampling a diffraction pattern corresponds to surrounding the electron density of the specimen with a no-density region. The higher the sampling frequency, the larger the no-density region. When the no-density region is larger than the electron density region, the phase information is in principle available from the diffraction pattern itself and can be directly retrieved by using an iterative algorithm [2]. The first demonstration experiment of this form of microscopy was carried out by using coherent soft X-rays in 1999 [3]. More recently, it has been extended to image the shapes of nano-crystals by using hard X-rays [4]. However, the experiments that have been carried out thus far have been limited to imaging 2-D samples, and the highest resolution achieved to date is around 70 nm [3,4].

Here, we describe the first experiment to image the 3-D structure of a non-crystalline material at 50-nm resolution, which was reported in Phys. Rev. Lett. [5]. The experiment was carried out at the undulator beamline **BL29XU**. Figure 1 shows a schematic layout of the experimental instrument in which all the components are in vacuum with a pressure of ~10^{-6} torr. The sample, fabricated by electron beam lithography, consists of two single-layered Ni patterns (each with a size of 2.5 ×2 ×0.1 μm) rotated 65° relative to each other in-plane and separated by a distance of 1 μm. The sample is supported by a thin silicon nitride membrane window. Figure 2(a) shows a scanning electron microscopy (SEM) image of the sample. Due to the 1 μm separation of the two layers, the SEM image shows the pattern in the top layer, and the pattern in the bottom layer is visible only as a soft blur.

Figure 2(b) shows a 2-D diffraction pattern at a resolution of 8 nm recorded from the sample by using coherent X-rays with a wavelength of 2 Å. The total exposure time of the diffraction pattern is about 45 minutes using unfocused X-rays from the undulator beamline. By using the oversampling phasing method, the diffraction pattern was directly converted to the high-resolution image shown in Fig. 2(c). The top and bottom layered patterns are clearly seen as overlapped in this 2-D image projection, and the variation of the electron density at the nanometer scale is also visible. To obtain the 3-D structural information, a series of thirty-one 2-D

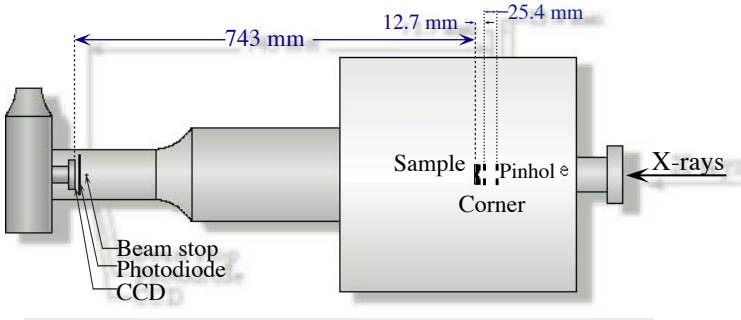

Fig. 1. Schematic layout of the experimental instrument used to record the coherent X-ray diffraction patterns.

diffraction patterns were recorded from the sample with the rotation angles ranging from –75° to 75° in 5° increments. The 2-D diffraction patterns were then assembled to produce a 3-D diffraction pattern. By using a 3-D phase retrieval algorithm [5], the 3-D structure of the non-crystalline material was successfully reconstructed at a resolution of 50 nm. Figure 2(d) shows a 3-D iso-surface rendering of the reconstructed image. The finest division in the z-axis corresponds to 25 nm and the distance between two patterns is about 1 μm, which is consistent with the known characteristics of the sample.

We anticipate that this form of microscopy will have wide applications in both materials and biological sciences. For materials science samples, which are less sensitive to radiation damage, this form of microscopy can, in principle, achieve atomic resolution in three dimensions. In biology, this form of microscopy can be applied to image the 3-D structures of whole cells, cellular organelles and supramolecular structures at high resolution, while the resolution will be mainly limited by radiation damage to the specimens.

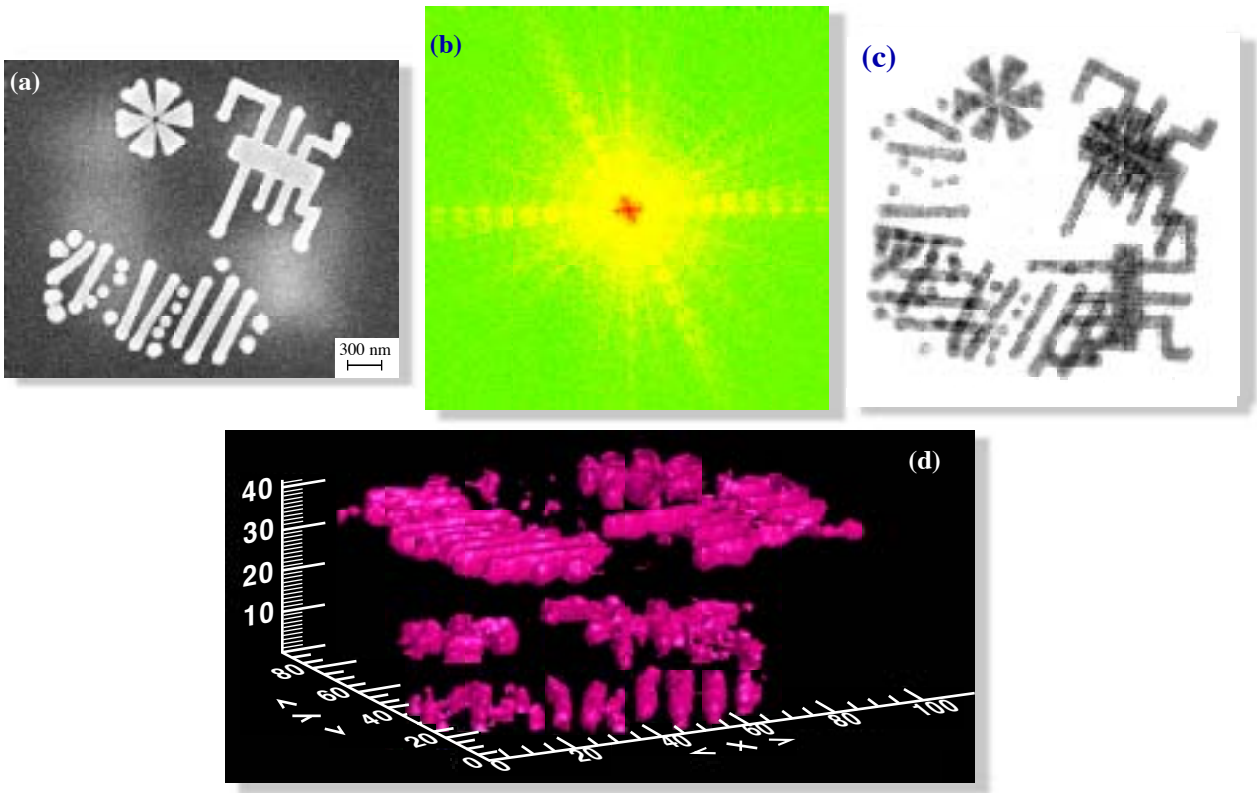

Fig. 2. ***(a)*** *An SEM image of an Ni sample with buried structures.* ***(b)*** *A high-resolution diffraction pattern recorded from the sample.* ***(c)*** *A high-resolution image reconstructed from* ***(b)****.* ***(d)*** *The reconstruction of a 3-D nanostructured material at 50 nm resolution (displayed in iso-surface rendering). [Reproduction from ref. 5.]*

Jianwei Miao[a], Tetsuya Ishikawa[b] and Keith O. Hodgson[a,c]

(a) Stanford Synch. Rad. Lab., Stanford Univ., USA
(b) SPring-8 / RIKEN
(c) Stanford University, USA

E-mail: Miao@SLAC.Stanford.EDU

References

[1] J. Kirz *et al.*, Q. Rev. Biophys. **28** (1995) 1.
[2] J. Miao *et al.*, J. Opt. Soc. Am. A **15** (1998) 1662.
[3] J. Miao *et al.*, Nature **400** (1999) 342.
[4] I. K. Robinson *et al.*, Phys. Rev. Lett. **87** (2001) 195505.
[5] J. Miao, T. Ishikawa, B. Johnson, E. H. Anderson, B. Lai and K. O. Hodgson, Phys. Rev. Lett. **89** (2002) 088303.

Characterization of Sputtered-sliced Fresnel Zone Plate at BL20XU: High-Resolution Hard X-ray Microbeam Experiments

X-ray microprobe/microscopy, which has been extensively developed in the soft X-ray domain, is now being extended to higher photon energies (> 8 keV). This extension will promote the various domains of basic science and technology, such as the observation and characterization of thicker materials, including medical-biological samples and industrial materials. The success of high spatial resolution studies of materials of sub-micron size is due to the X-ray brilliance combined with the availability of various micro-focusing optics. The expected applications of the microprobe in hard/high-energy X-ray regions are microscopy, microanalysis, micro-spectroscopy and micro-diffraction.

The Fresnel zone plate (FZP) fabricated by lithography technique realizes the highest spatial resolution in the soft X-ray domain, it is not thick enough to be used in the hard X-ray domain

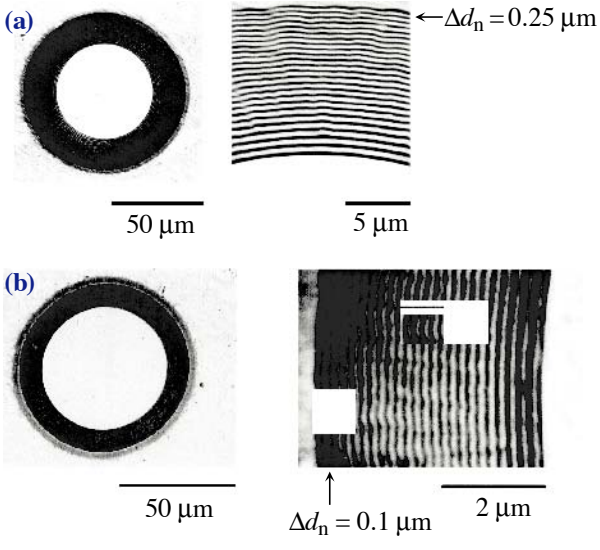

*Fig. 1. SEM micrographs showing cross sections of Cu/Al concentric mulilayers on Au wire core. Fresnel zone plate with an outermost zone widths of **(a)** 0.25 μm and **(b)** 0.1 μm.*

domain (aspect ratio (height/width): around 8:1). Compared with the FZP made by lithography technique the sputtered-sliced FZP (ss-FZP) can be made thick enough with no aspect ratio limitation and is proven to work even at quite high X-ray energies (over 100 keV) [1,2].

The ss-FZP composed of alternating transparent (Al) and opaque (Cu) layers (total 50 ~ 100 layers) was fabricated by physical vapor deposition (dc planar magnetron sputtering) on a fine gold wire core with a smooth surface and having a radius of 25 μm at a rotation speed of 15 ~ 50 rpm [3]. After deposition, the wire sample was sliced normal to the wire axis and its thickness was adjusted to 20 ~ 40 μm by mechanical polishing.

Here, two types of ss-FZP with outermost zone widths of 0.25 μm (#FZP1) and 0.1 μm (#FZP2) were fabricated. Figure 1 shows SEM micrographs of these two FZPs. The parameters are given in Table I. They were characterized using knife-edge scanning method (former) and the scanning microscopic method with a test pattern (latter). The experiment was performed at the end station of beamline **BL20XU** (hutch #2). This beamline is a unique beamline, having a 248 m-long beam path equipped with an in-vacuum undulator source and

Table I. Zone plate parameters (Cu/Al system)

Zone plate	#FZP1	#FZP2
Outermost zone width	0.25 μm	0.1 μm
Central stop diameter (Gold wire core diameter)	50 μm	50 μm
Primary focal length at 12.4 keV (λ = 1Å)	220 mm	68 mm
Number of zone	50	50
Zone plate diameter	80 μm	70 μm
Zone plate thickness	~20 μm	~40 μm

double-crystal monochromator covering the energy range 8 keV ~ 37.7 keV. The monochromator was placed 46 m downstream from the source point. A liquid-nitrogen cooling system is employed for the monochromator.

First, we performed a characterization of #FZP1. The X-ray energy was chosen to be 12.4 keV. A quadrant slit (50 μm in horizontal width) was installed in the beamline 200 m upstream from the FZP to create a stable pseudo light source, and knife-edge scanning was performed in transmission geometry. The minimum focusing size obtained was 0.3-μm full width at half maximum (FWHM) for the horizontal direction as shown in Fig. 2, and the focal length obtained was 220 mm. A schematic view of the experimental set-up is shown in Fig. 3.

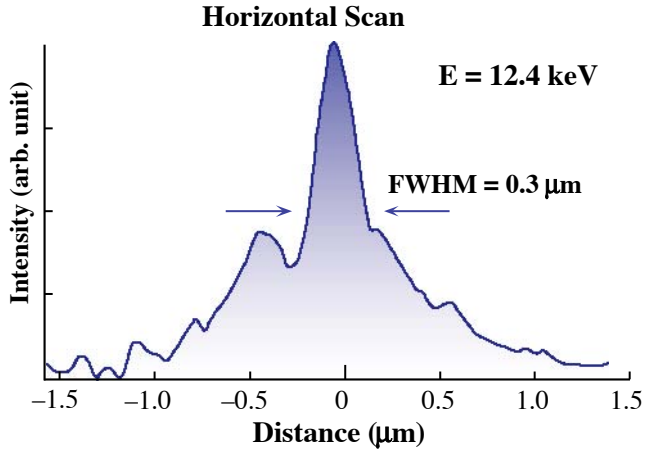

Fig. 2. Focused beam profile measured by a knife-edge horizontal scan at 12.4 keV. The full-line curve is the numerical derivative of the raw intensity data.

The diffraction limit of the first order focus of the FZP, 1.22 d_n (where d_n is the outermost zone width: 0.25 μm) is 0.3 μm. The focused beam size determined by the geometrical optics, 0.06 μm, is smaller than the diffraction-limited resolution of #FZP1. The focusing size obtained here (0.3 μm) agrees well with the theoretical limit of the FZP with outermost zone width of 0.25 μm. Diffraction efficiency for the first-order light was estimated by comparing the incident beam intensity through the order sorting aperture (OSA) and the total intensity of the focused beam through the OSA. The observed efficiency of approximately 15% agrees well with that of the calculated one at 12.4 keV.

Secondly, a scanning microscopy experiment was conducted on #FZP2. Employing scanning

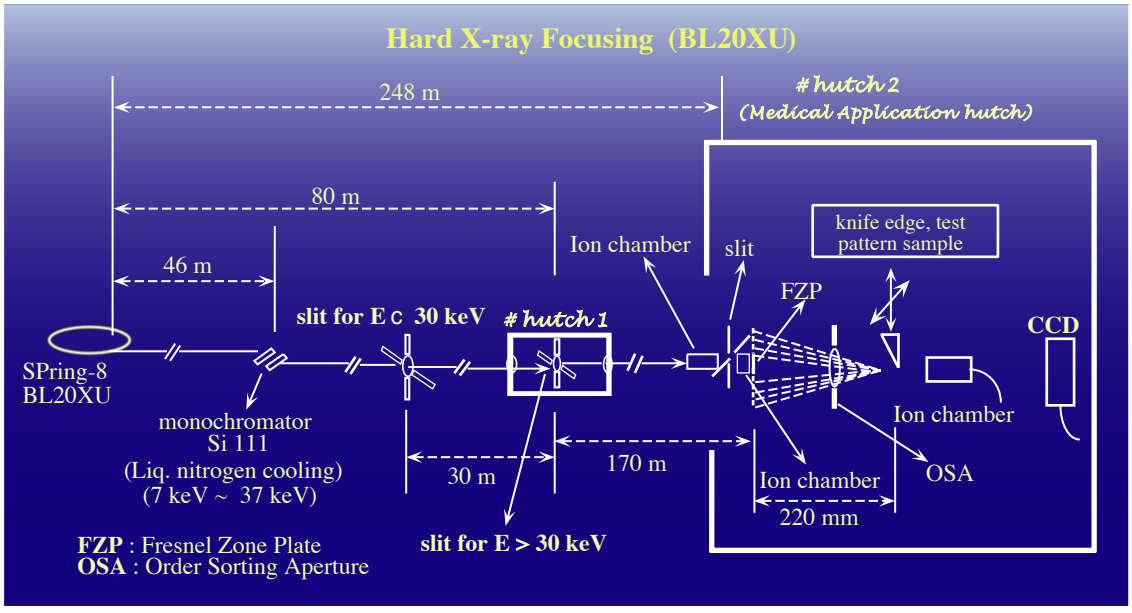

Fig. 3. Schematics of optical system of Fresnel zone plate evaluation and scanning X-ray microscopy.

microscopy to create images of the test pattern with fine structures is one method that may be used for measuring the focal beam size [1]. The X-ray energy was chosen to be 15 keV. A quadrant slit (100 μm × 100 μm) was installed in the beamline 200 m upstream from the FZP.

The designed outermost zone width of #FZP2 used here is 0.1 μm. Thus, the diffraction limit of the first-order focus of the FZP is 0.12 μm. The scanning experiment was conducted using a test pattern made of 0.5 μm-thick tantalum with seven periodic steps of 0.1 and 0.2 μm line-and-space deposited on an Si_3N_4 membrane. The result of the scanning image is shown in Fig. 4. Here, the transmitted intensity was detected using an ion chamber. The fine pattern of 0.1-μm wide was clearly resolved in the measured image. Therefore, the resolution limit of the microscope is estimated to be 0.1 ~ 0.2 μm, which is close to the diffraction-limited resolution of #FZP2. The total flux of the microbeam obtained is ~10^9 photons s^{-1}.

In conclusion, ss-FZPs have now been proven to be a genuine X-ray focusing element. It is possible to work in awide X-ray energy range (8 ~ 100 keV), even though their numerical aperture are quite small (in the order of 10^{-4}).

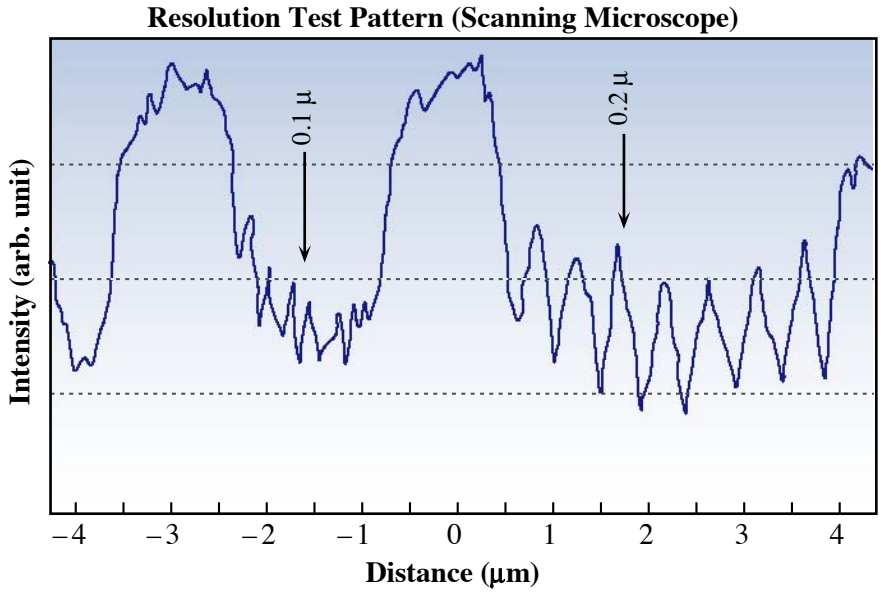

Fig. 4. Scanning microscopy image of a test pattern. Scanning step: 0.025 μm. X-ray wavelength: 0.82 Å.

Nagao Kamijo

Kansai Medical University

E-mail: fe2n-kmjy@asahi-net.or.jp

References

[1] Y. Suzuki *et al.*, Nucl. Instrum. Meth. A **467-468** (2001) 951.
[2] N. Kamijo, Y. Suzuki, M. Awaji, A. Takeuchi, H. Takano, T. Ninomiya, S. Tamura and M.Yasumoto, J. Synchrotron Rad. **9** (2002) 182.
[3] S. Tamura *et al.*, J. Synchrotron Rad. **9** (2002) 154.

3-D Imaging Tomography with Sub-micrometer Resolution Using Fresnel Zone Plate Optics

X-ray microtomography has been developed for use in various fields such as biology, materials science, petrology, and medical diagnosis. This method's setup commonly consists of a simple projection geometry with a high-resolution imaging detector and a highly collimated beam, *e.g.*, a microfocussing X-ray tube or synchrotron radiation source, which can result in a spatial resolution of about 1 μm [1]. Achieving a higher resolution with this method, however, is difficult for two reasons: one is the image blurring caused by beam deflection (both refraction and diffraction), and the other is the limited spatial resolution of the imaging detector (~1 μm).

One promising way to overcome those problems is combining X-ray imaging microscope optics using an X-ray imaging device as an objective – so called "imaging microtomography." Various types of X-ray imaging devices whose theoretical spatial resolutions are in order of 10 - 100 nm have now been developed, and almost all of them have already attained the sub-micrometer resolution; even 100-nm-resolution has been achieved with some of them [2]. Since the imaging microscope setup enables magnification of the X-ray image, spatial resolution of the imaging detector is not a serious problem.

We have developed an imaging microtomography setup at beamline **BL47XU** using a Fresnel zone plate (FZP, fabricated at NTT-AT) which is one of the X-ray imaging devices utilizing X-ray diffraction. The experimental setup is shown in Fig. 1, and the X-ray energy was set to 8 keV. In this setup, a high coherent beam is not suitable for illumination because the images tend to be degraded by unwanted interference patterns such as speckle noise. Therefore, a "beam diffuser" made of graphite powder packed with Kapton films was installed in order to reduce the coherence. The measured spatial resolution of the microscope system, comprising the illumination system, a FZP objective, and a high-resolution imaging detector, was 0.6 μm [3]. The sample was mounted on the high precision rotating stage with a wobbling accuracy of 0.1 μm. One CT scan took approximately 4 - 8 hours with this system. More details about the system are described in refs. [3,4]. Spatial resolution and the time required for the CT scan are currently being improved.

Figures 2(a) - 2(d) show reconstructed images of a diatom fossil (*Achnanthidium lanceolata*).

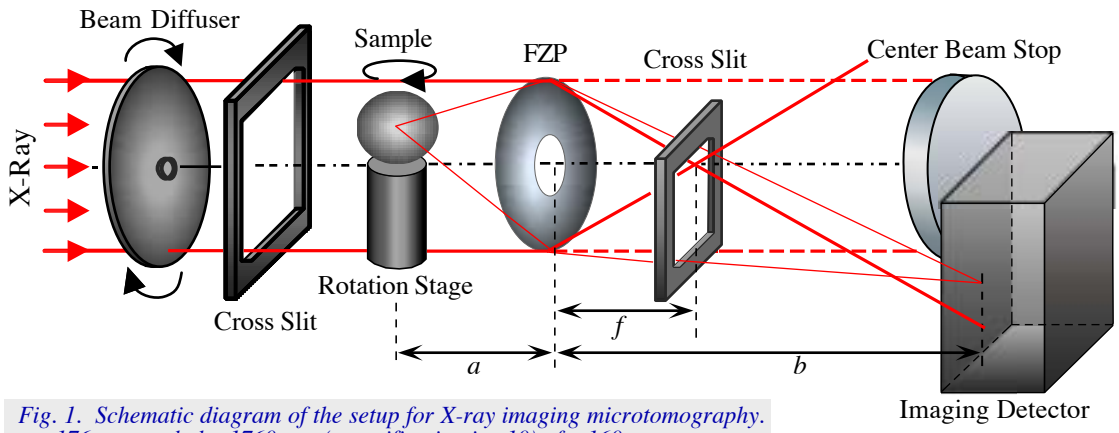

Fig. 1. Schematic diagram of the setup for X-ray imaging microtomography. a = 176 mm and b = 1760 mm (magnification is ×10), f = 160 mm.

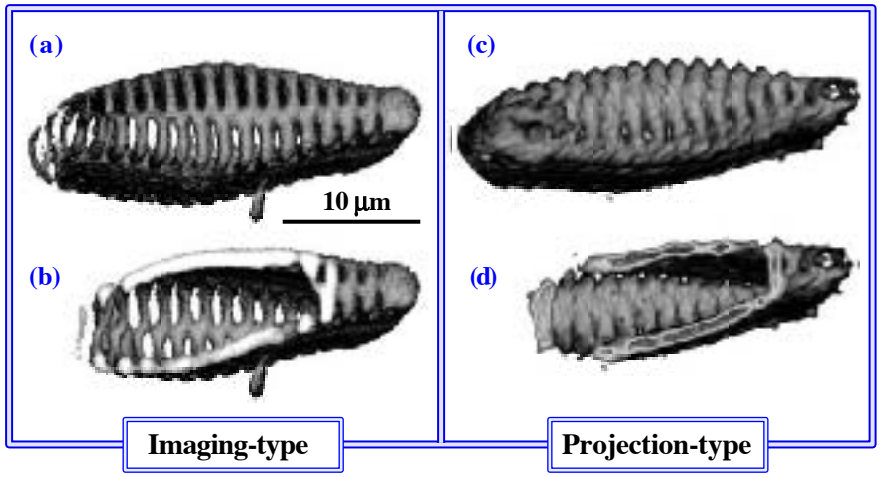

*Fig. 2. X-ray tomographic reconstructed images of diatom fossil (Achnanthidium lanceolata): **(a)** 3-D image of the outer structure, **(b)** inner structure revealed by cropping one part of the 3-D image, and **(c)** and **(d)** reconstructed images taken with projection-type microtomography [1].*

Figure 2(a) shows a whole three-dimensional image, while Fig. 2(b) shows a cropped one. For comparison, reconstructed images of the same sample taken with a projection-type microtomographic system with a spatial resolution of about 1 μm [1] are shown in Fig. 2(c) (whole image) and Fig. 2(d) (cropped image). The nesting fine structure (about 1.5 μm pitch) of the diatom was much cleaner in the imaging-type system (Figs. 2(a) and 2(b)) than in the projection-type one (Figs. 2(c) and 2(d)). Comparing both cropped images, the edge-enhancement effect due to X-ray refraction is clearly seen in the cropped section with the projection-type system (Fig. 2(d)) image, while it is not seen in the imaging-type image (Fig. 2(b)). These results demonstrate that imaging-type microtomography has a higher spatial resolution and a much smaller X-ray deflection effect than projection-type imaging.

Figure 3(a) shows the three-dimensional reconstructed image of a piece of stony meteorite (Allende), which has a complex texture made of silicates and metal-sulfides, and Fig. 3(b) shows its sliced image. Small cracks and holes are seen in the sliced image. The brighter area at the bottom of the sliced image is an iron-rich region that could be identified by comparing the images above and below the *K*-edge of iron.

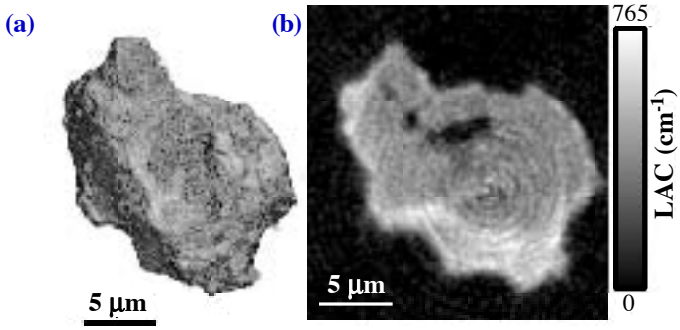

*Fig. 3. X-ray tomographic reconstructed images of a piece of Allende meteorite: **(a)** three-dimensional image and **(b)** sliced image (LAC: linear absorption coefficient).*

Akihisa Takeuchi

SPring-8 / JASRI

E-mail: take@spring8.or.jp

References

[1] K. Uesugi *et al.*, Proc. SPIE **4503** (2001) 291.
[2] A. Takeuchi, Y. Suzuki and H. Takano, J. Synchrotron Rad. **9** (2002) 115.
[3] Y. Suzuki *et al.*, Jpn. J. Appl. Phys. **40** (2001) 1508.
[4] A. Takeuchi *et al.*, Proc. SPIE **4499** (2001) 29.

Phase-contrast Tomography using X-ray Interferometer having 40-μm Lamella

Recently, various imaging techniques that produce contrast images from X-ray phase information have been proposed. Biological imaging is their main target because of expected sensitivity up to 1000 times higher than absorption-contrast X-ray imaging, whose performance is insufficient for soft tissues. Three-dimensional tomographic imaging using X-ray phase information has also been achieved [1,2] using an X-ray interferometer [3]. Its high sensitivity enables us to observe tissue structures, such as vessels, cancerous lesions, fibrous tissues, without the use of contrast media.

The method's spatial resolution (roughly 30 μm × 30 μm × 60 μm), however, was not satisfactory for histological observation; the spatial resolution was not limited by our image detector, but by the X-ray interferometer itself, which was made by cutting the body out of a crystal. The interferometer produces interference fringes by generating and recombining two coherent X-ray beams using the dynamical diffraction at a set of lamellae. A blurring mechanism is involved in this process; that is, the wave field of X-rays downstream of the sample is altered by the third lamella, which functions as an X-ray half-mirror, due to the process of dynamical diffraction. We therefore fabricated a new X-ray interferometer with a 40-μm lamella (Fig. 1(a)), which was effective for suppressing the image blurring.

The interferometer successfully produced interference fringes and was installed at beamline **BL20XU**, where we developed an apparatus for phase-contrast tomography. In the measurements, we used 12.4 keV X-rays with a CCD-based image detector, whose pixel size was 6.5 μm × 6.5 μm. Tissue pieces (2 ~ 3 mm in diameter) were observed in a cell filled with formalin. The experimental setup shown in Fig. 1(b).

Figure 2(a) shows tomographic images obtained for a piece cut out of the cortex of a rat kidney fixed in formalin [4]. Convoluted tubules and vessels are revealed. Figure 2(b) shows an optical image of

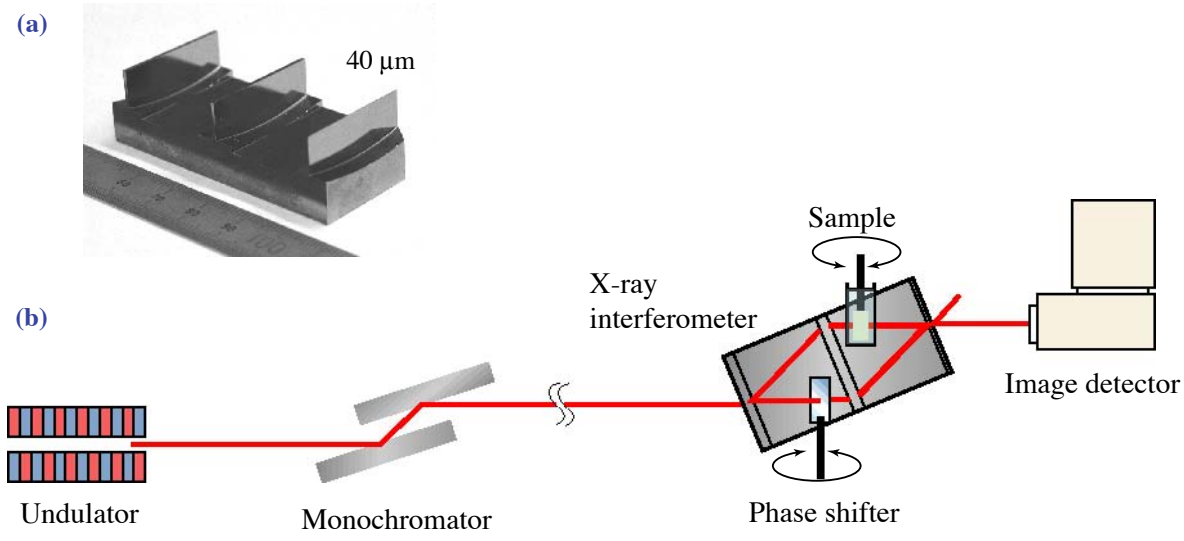

Fig. 1. X-ray interferometer with a 40 μm lamella ***(a)*** *and experimental setup for phase-contrast X-ray tomography* ***(b)****.*

the corresponding specimen sliced after the X-ray measurement for comparison. Glomeruli can also be identified in Fig. 2(a) in comparison with Fig. 2(b). Figure 2(c) shows a 3-D rendered view of the tomographic data. In earlier experiments [5], the structures could not be revealed as clearly as the present image.

Structures corresponding to 2 or 3 pixels could be resolved in the tomogram. Thus, present spatial resolution is estimated to be between 13 μm and 20 μm. It is speculated, however, that the influence of the detector's spatial resolution was not negligible; therefore, in parallel with employing a better image detector, X-ray interferometers will be further improved to achieve higher spatial resolution.

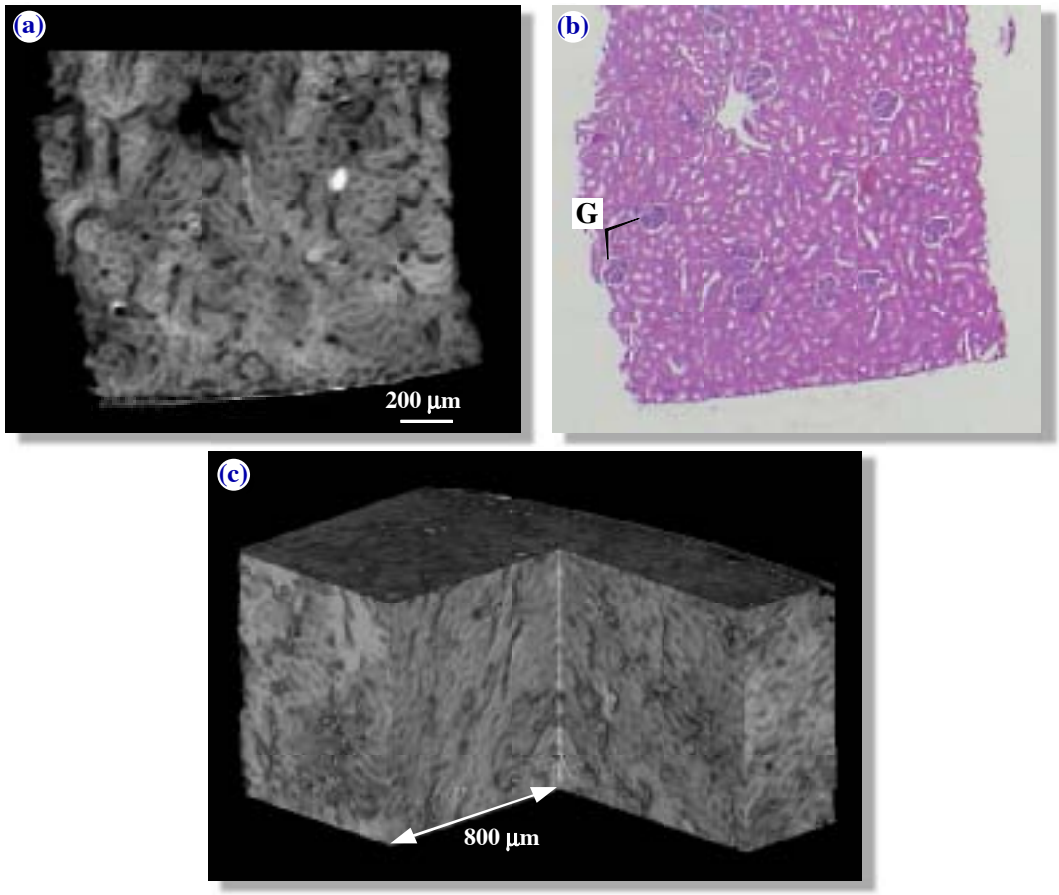

Fig. 2. Phase-contrast tomographic image of a cortex part of a rat kidney ***(a)*** *and an optical image of the corresponding specimen sliced after X-ray measurement* ***(b)****. G: glomeruli.* ***(c)*** *3-D rendered tomographic view.*

Atsushi Momose[a,b], Ichiro Koyama[a,b] and Tohoru Takeda[c]

(a) The University of Tokyo
(b) SPring-8 / JASRI
(c) University of Tsukuba

E-mail: momose@exp.t.u-tokyo.ac.jp

References

[1] A. Momose, Nucl. Instrum. Meth. A **352** (1995) 622.
[2] A. Momose *et al.*, Nature Medicine **2** (1996) 473.
[3] U. Bonse and M. Hart, Appl Phys. Lett. **6** (1965) 155.
[4] A. Momose, I. Koyama, Y. Hamaishi, H. Yoshikawa, T. Takeda, J. Wu, Y. Itai, K. Takai, K. Uesugi and Y. Suzuki, Proc. 7th Int. Conf. X-ray Microscopy, to be published in J. de Physique IV.
[5] A. Momose *et al.*, SPIE Proc. **3659** (1999) 365.

R&D for Structural Genomics: A Fully Automated Crystallization and Observation Robot System "TERA" and "Sample Auto Changer" for SPring-8 Structural Genomics Beamlines

In the post-genomic era, there is great hope that protein research will reveal the structure and function of genome-coded proteins as live nano-robots. Structural genomics is one of the major post-genomic research fields engaged in determining the number of protein structures at the atomic level based on the information of full-genome sequences from various organisms, including humans from all over the world. At SPring-8, the Highthroughput Factory (Fig. 1) has been established as an integrated protein X-ray crystallography facility. Its investigations range from protein production to protein structural analysis using the synchrotron radiation (SR) source of the RIKEN Structural Genomics Beamlines, **BL26B1** and **BL26B2**. These beamlines are part of the Japanese structural genomics project, "TANPAKU 3000, National Project on Protein Structural and Analyses of Ministry of Education, Culture, Sports, Science, and Technology (MEXT)."

First, we are trying to overcome the bottlenecks in protein crystallization and data collection. However, in practice there remain many bottlenecks in high-throughput structure determination for structural genomics.

We designed and developed the full-automated crystallization and observation robot system, "TERA," by the oil-sitting drop method (Fig. 2) [1] based on pilot studies using a commercially available manual crystallization robot, IMPAX1-5 (Douglas Instruments, UK) [2] using the original initial crystallization conditions and a standard scoring system to attempt large-scale protein crystallization. We are currently conducting unique

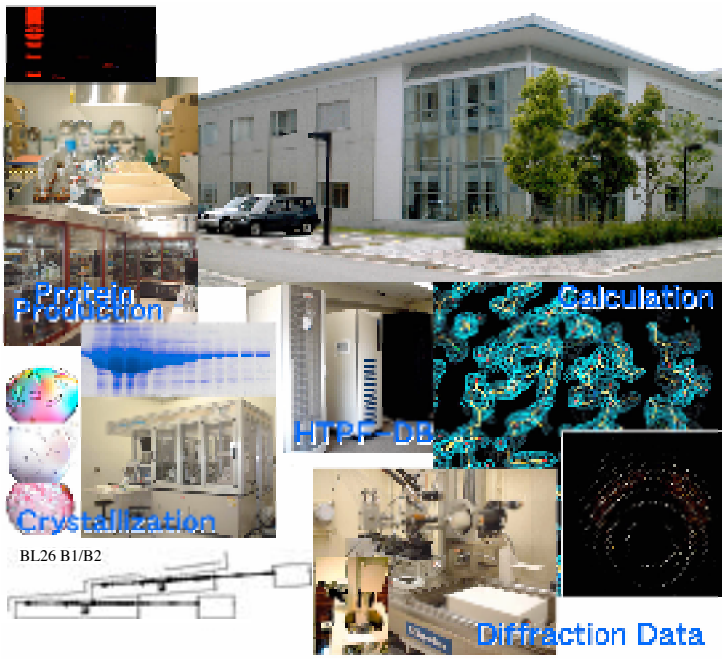

Fig. 1. RIKEN Highthroughput Factory (HTPF) for integrated protein structure determination. HTPF possesses full-functionality of SR crystallography, from protein production to crystallographic calculation. It includes RIKEN structural genomics beamlines with the integrated laboratory information system (HTPF-DB) developed in collaboration with HITACHI Software Engineering.

Fig. 2. Full-automatic protein crystallization and observation robot system, "TERA," jointly developed by Takeda Rika Kogyo, Stec and AdvanSoft. It has four components: (1) a liquid-handling robot for dispensing the crystallization setup robot at the right front, (2) microscopic photo system with CCD camera and XY plate loader at center front, (3) storage for 2,500 crystallization micro-plates and 125 crystallization reagent plates in the back, and (4) control software for managing operations with the data-base at left front. Close-up views: parts of the microscopic photo system (bottom-center panel) and the crystallization robot (bottom-right panel). Upper right panel shows various protein crystals.

crystallization experiments in the three screening steps: sparse initial, secondary for optimizing, and tertiary for additives [3].

The RIKEN Structural Genomics Beamlines have been designed to perform the high-throughput diffraction data collection for protein crystallography. In order to increase beam time efficiency and the ability to handle many crystals, the goal of this beamline development is the automated operation. During X-ray diffraction experiments, users would have to mount, dismount, centering and orientating many crystals. Therefore, a novel sample changing system has been developed to manipulate a number of crystals with the "Sample Auto Changer" as the core component (the left-hand in Figs. 3(a) and 3(b)) [4].

A small crystal of a few hundred microns or less is mounted on the originally designed plastic screw chips, called "Sample Pin," with a turnbuckle-like figure (Figs. 3(e) and 3(g)). The pin is screwed and mounted at the tapped hole of the goniostat head (the right-hand side in Figs. 3(a) and 3(f)). Contrary to a Hampton-like pin mounted on the gonio-head by a magnet, the orientation and positioning of the sample can be placed automatically at the X-ray beam center repeatedly after being aligned to the center by the operator. The mounted crystal is inserted into the tapped long tube the at arm-end of the Sample Auto Changer within 5 sec of changing the sample.

We can perform 24-hour X-ray data collection by using the Sample Auto Changer. This operation is controlled by the Beamline Scheduling Software (BBS) with a link *via* a unique crystal and tray ID to the Highthroughput Factory Database (HTPF-DB) system [5]. Accordingly, the information of the crystal sample, from the protein sequence to the structure analysis process, is obtained in the integrated and automated manner of TERA with supervision by HTPF-DB as well.

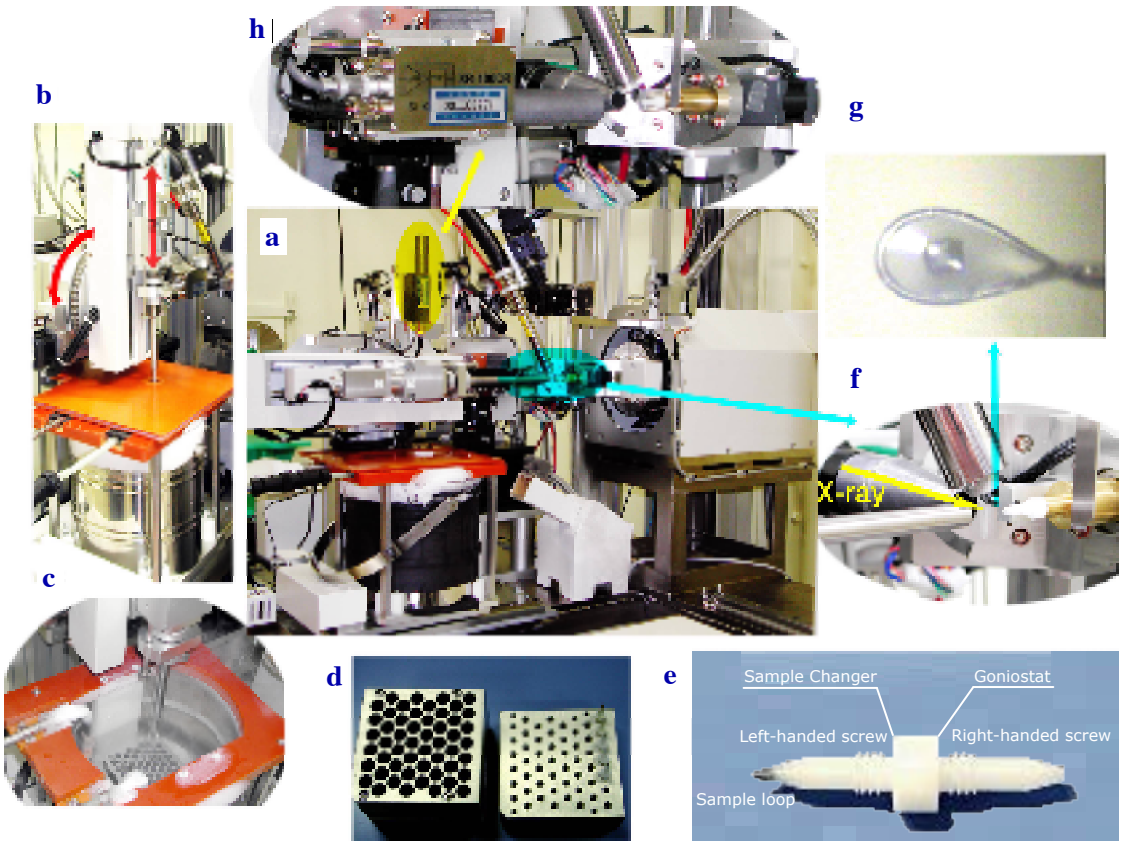

*Fig. 3. "Sample Auto Changer," a frozen crystal auto-changing system. **(a)** Sample Auto Changer and Auto Alignment Goniostat at BL26B2 station. **(b)** Crystal mounted on a Sample Pin (**e** and **g**) is picked from the tray (**d**) in liquid-nitrogen Dewer (**c**) and transferred to the goniostat head by Sample Auto Changer from left to right in panel (**a**), and its close-up view (**f**). **(e)** Sample Pin has left-handed screw and right-handed screw at each end with small nylon cryo-loop on the top for fishing the crystal. **(h)** Close-up view of XAFS measurement configuration.*

Koh Ida, Mitsuaki Sugahara, Masaki Yamamoto, and Masashi Miyano

SPring-8 / RIKEN

E-mail: yamamoto@postman.riken.go.jp and miyano@spring8.or.jp

References

[1] M. Sugahara and M. Miyano, Tanpakushitsu Kakusan Koso **47** (2002) 1026.
[2] N.E.Chayen *et al.*, J. Appl. Crystallogr. **23** (1990) 297.
[3] M. Sugahara and M. Miyano - in preparation.
[4] M. Yamamoto, G. Ueno, H. Kanda, K. Ida, T. Kumasaka, M. Miyano and T. Ishikawa - in preparation.
[5] H. Taka, R. Yoshida, E. Kanamori, Ishijima and M. Miyano - in preparation.

Nuclear Physics

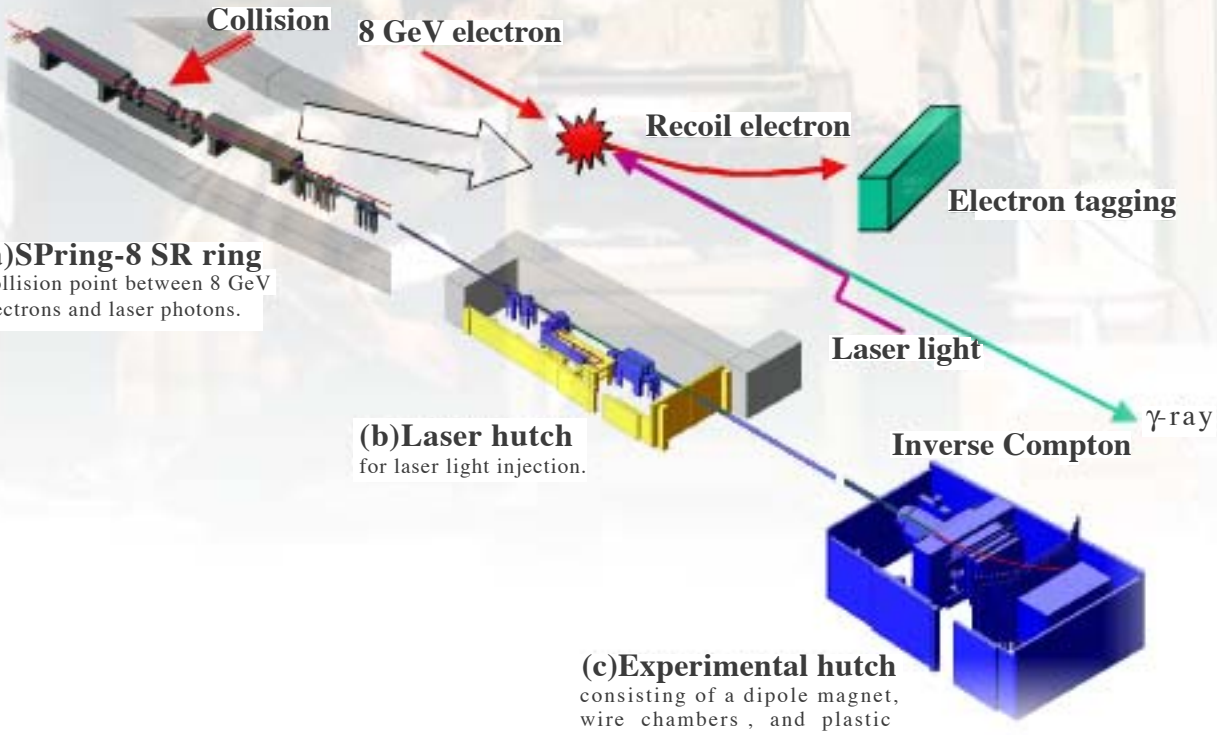

Polarization Observables in K^+-meson Photo-production at LEPS

High-energy γ-rays, called "Inverse Compton γ-rays," are generated from collisions between 8 GeV electrons and laser photons at beamline **BL33LEP**. The γ-ray can attain a maximum energy of 2.4 GeV at maximum. These γ-rays have excellent properties regarding directivity and polarization, and provide a good means to study the behavior of quark movements inside nucleons and nuclei since one of the best way to investigate the inside of hadrons is to use electromagnetic probes. This is thanks to the reduced theoretical complexity of the photonuclear reaction with real-photons. For this purpose, we constructed a detector system called the LEPS spectrometer to analyze charged particles. The LEPS spectrometer shown in Fig. 1 mainly consists of one dipole magnet with a large aperture, three drift chambers, and TOF (Time of Flight) scintillation counters. The dipole magnet is used to bend the charged particles produced by photonuclear reactions. One of the three drift chambers is located between the target and the dipole magnet. All the drift chambers are used to determine the particle trajectories. The ray-tracing technique is fully employed to determine the trajectories of charged particles, and the TOF scintillation counters serve to identify the particle mass through

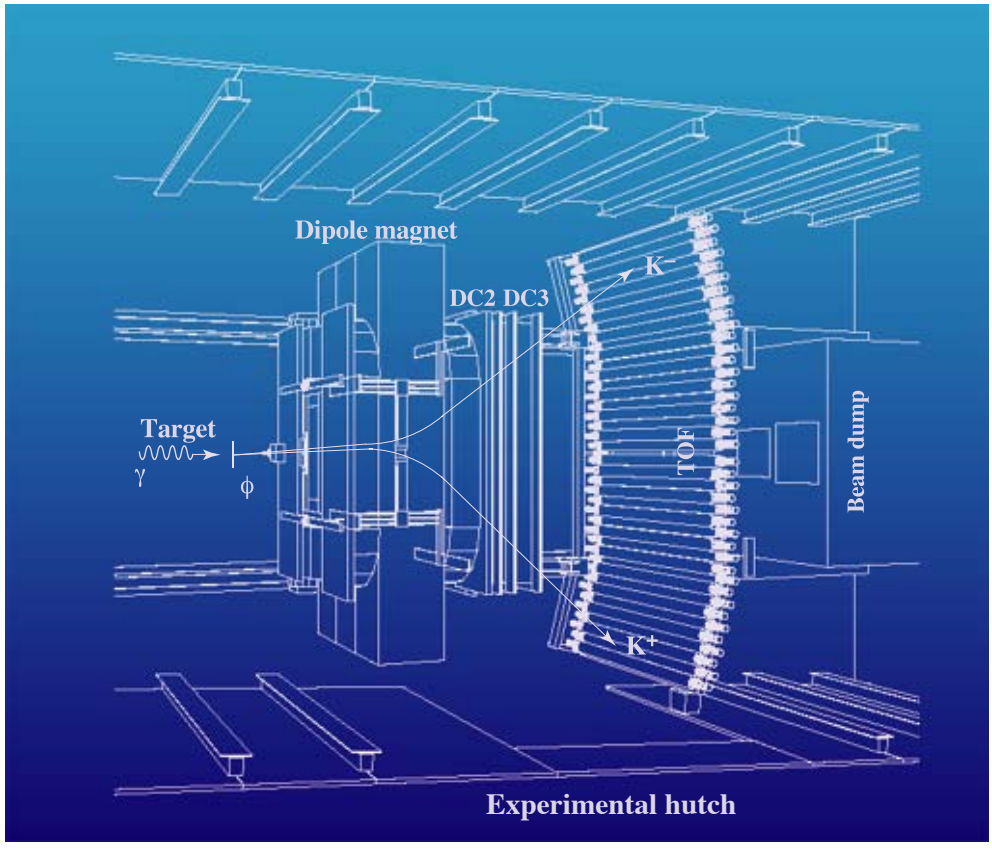

Fig. 1. Top view of the spectrometer system (LEPS) in the experimental hutch. The spectrometer mainly consists of a dipole magnet, drift-chambers, and scintillation counters for TOF measurement. High-energy γ-rays coming from the left side are stopped at the beam dump (on the right side of the figure). A typical event of $K^+ + K^-$ pairs for ϕ meson production is shown.

the measurement of the time-of-flight (TOF). In the case of ϕ meson photo-production, a ϕ-meson decays into $K^+ + K^-$ pairs when it is generated from the $\gamma + p \rightarrow p + \phi$ reaction, for example. Information on the measured magnetic fields is employed in the Runge-Kutta method to obtain the particle trajectories for the ray tracing.

In this short report, we show a typical experiment using polarized γ-rays. It is well known that a proton consists of quarks with a "*uud* " configuration, exchanging gluons (the origin of "strong force") to combine them. When a proton absorbs a high-energy γ-ray in the photo-reaction, a K^+-meson (a pair of an *u*-quark and an anti-strange s-quark) is created, leaving three quarks with a configuration of "*uds*." This system of hadrons is expected to provide us with an new aspect of studying the quark behavior, since it contains "strange quarks," which does not appear in the normal world at low temperature.

Figure 2 shows a mass identification spectrum from photonuclear reactions on protons, which demonstrates that various kinds of baryons are created with an "*uds*" quark configuration coupled to various spins and isospins. This spectrum has been obtained by measuring a K^+ meson with the LEPS magnetic spectrometer (see Fig. 1). A K^+ meson has a mass of 493.7 MeV, and mainly consists of a *u*-quark and an anti-strange $\bar{s}$-quark. When a high-energy γ-ray creates an s-$\bar{s}$ quark pair by interacting with proton, an anti-strange quark picks up the *u*-quark from the proton with a uud configuration, making a K^+ meson and leaving the Λ and Σ particles with an uds configuration. These are naive explanations for the reason why we can observe various kinds of Λ and Σ^0 particles in high-energy photoreaction. Figure 2 shows the missing mass spectrum for Λ and Σ particles produced via the processes of $\gamma + p \rightarrow K^+ + \Lambda$, $K^+ + \Sigma^0$. The Λ and Σ^0 baryons with masses of 1116, 1192, 1405, 1385, 1520 MeV are clearly identified in the spectrum.

When polarized high-energy γ-rays create the s-$\bar{s}$ quark pair as a result of the interaction with the quark-gluon field from the nucleon, the created particles tend to keep to the polarized axis and are emitted along the polarization axis of the γ-rays. This is physically natural. The quark anti-quark pair is mostly generated in the vacuum breaking process through a gluon exchange process. The distribution of created K^+ mesons have a basic pattern with respect to the linear polarization axis of γ-rays, which is predicted on the basis of quantum physics and given as

$$(d\sigma/d\Omega)_{pol} = (d\sigma/d\Omega)_{unpol} (1 + P \bullet \Sigma \cos(2\phi)),$$

where P is the polarization of the γ-ray beam, Σ is the asymmetry parameter commonly called Σ parameter, and ϕ is the deviation angle from the polarization direction of the γ-ray. We have succeeded in observing such patterns. Figure 3

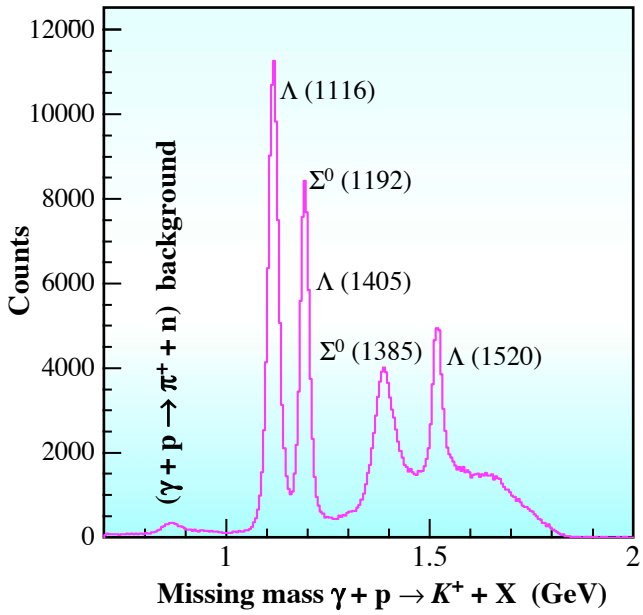

Fig. 2. Missing mass spectrum for the $\gamma + p \rightarrow K^+ + \Lambda(\Sigma^0)$ reaction. Narrow peaks for $\Lambda(1116)$, $\Sigma^0(1192)$, $\Lambda(1520)$ particles and the rather broad peaks for $\Lambda(1405)$ and $\Sigma^0(1385)$ particles can be distinguished. A small contamination for the $\gamma + p \rightarrow \pi^+ + n$ reaction is also present.

shows the measured asymmetry for the Λ(1116) and Σ^0(1192) productions. The K^+ meson production is found to be spatially asymmetric and is well described using a "cosine" curve. Its amplitude depends slightly on the type of particle production and incidence energy of the γ-rays. The amplitude of the obtained "cosine" curve depends on the interaction strengths associated with the K^+ meson creation and on the details of reaction mechanisms (*i.e.*, resonance states involved in the reaction process). These experimental results raise a somewhat controversial question, calling for theoretical challenges to describe asymmetries for Λ and Σ^0 productions.

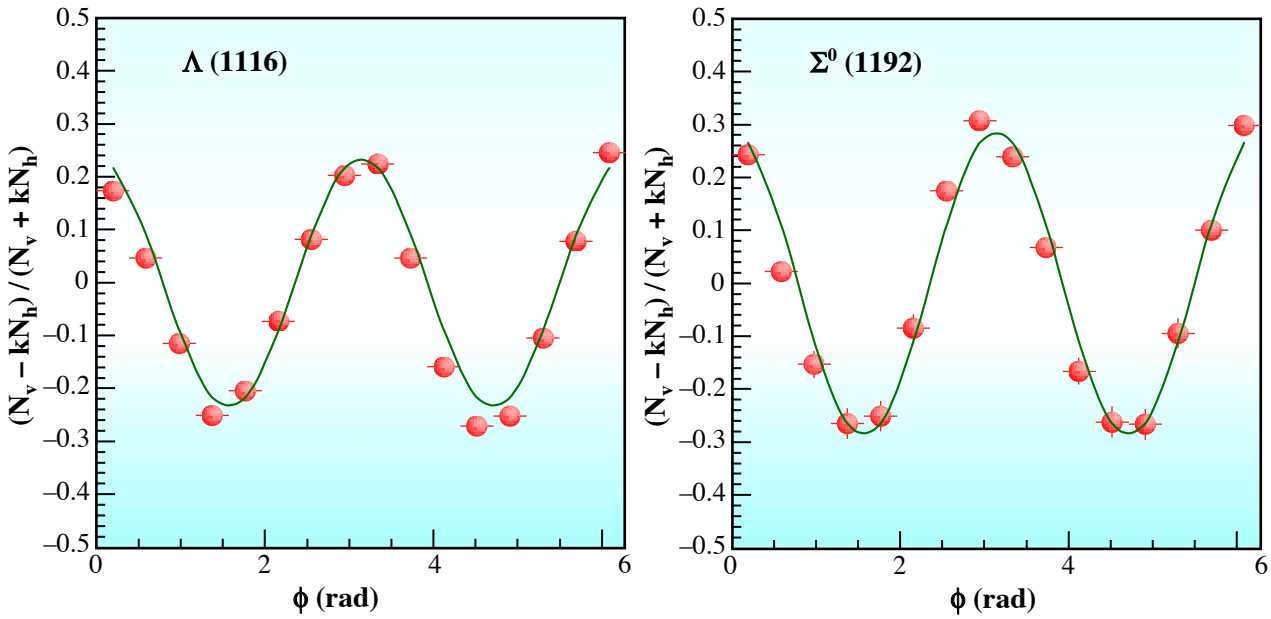

Fig. 3. Angle and energy-integrated asymmetry plots for the $\gamma + p \rightarrow K^+ + \Lambda(1116)$ reaction (left) and $\gamma + p \rightarrow K^+ + \Sigma^0(1192)$ reaction (right).

Mamoru Fujiwara[a,b]

(a) Research Center for Nuclear Physics (RCNP), Osaka University
(b) Advanced Science Research Center, JAERI (Tokai)

E-mail: fujiwara@rcnp.osaka-u.ac.jp

Accelerators Frontiers

Beam Performance and Upgrades of the Storage Ring

Orbit Stability

A beam orbit stabilization project was started in February 2001. Investigations in the first year focused on the survey of fluctuation sources, whereas in the second year, 2002, focused on suppression of the vibration sources we had found.

(i) By observing the correlation between the vacuum chamber vibration and the beam fluctuation, we found that the broad peak around 30 Hz in the vertical beam spectrum is caused by the vibration of an upstream chamber in a unit cell. The vacuum chamber vibrates in a quadrupole magnetic field, then eddy currents are induced on the vacuum chamber wall. The electromagnetic fields induced by the eddy currents shake the electron beam. We have made some improvements on the basis of these results. We reduced the vertical beam fluctuations around 30 Hz by one order of amplitude, as shown in Fig. 1. This improvement is also effective for suppressing the horizontal beam fluctuations from 50 to 100 Hz and the amplitude in this frequency range was reduced by factor three in amplitude.

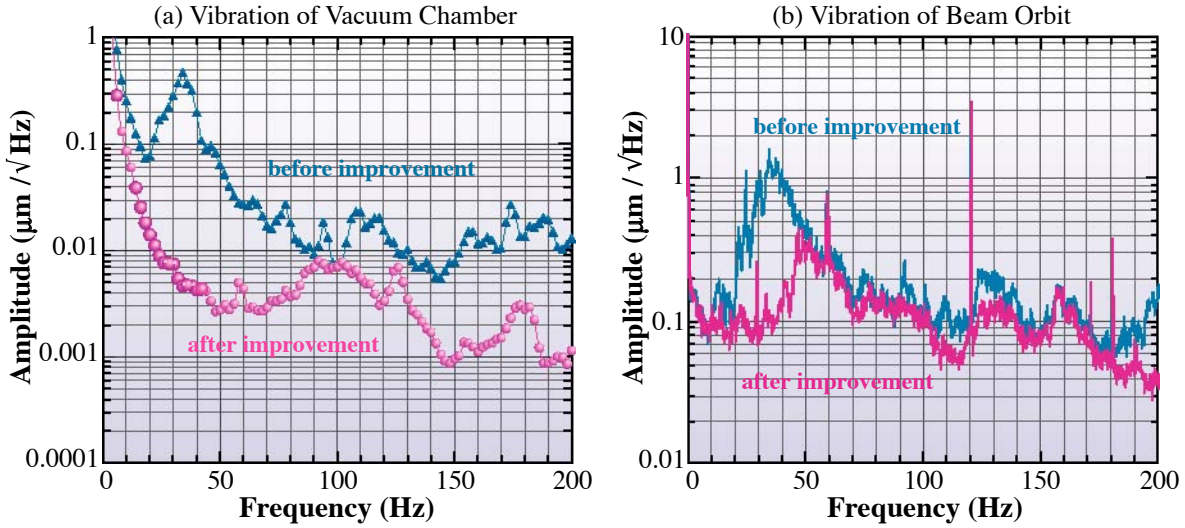

Fig. 1. Vertical vibration of the vacuum chamber and the stored electron beam before and after improvements.

(ii) To suppress the slow orbit drift, we increased the number of air-core type steering magnets with high resolution and low hysteresis from twelve to twenty-four in the summer shutdown of 2002. By this enhancement, we increase the degree of freedom for the correction phase. In principle, this is effective for reducing the slow drift. To avoid the mixing between the circumference change and orbit distortion due to the increment in the steering number, we adopted an algorithm to subtract the contribution of the energy shift from the measured orbit. By using this new periodic correction system, horizontal and vertical orbit deviations were reduced down to about 5 μm in rms for one-day operation.

Top-up Operation

Since 1999 we have been investigating the realization of "top-up operation" in the storage ring at SPring-8. In 2002, we set a target to introduce top-up operation to user time from the autumn of 2003. To meet this time schedule, we are rushing to upgrade a machine control, beam monitors, and an interlock system for radiation safety, and to design and manufacture the new injection bump magnets and their power supplies.

There are two major problems, as follows.

(i) Demagnetization of undulator magnets due to frequent beam injections: This phenomenon occurs due to the loss of injected beams at a narrow vertical aperture of the in-vacuum undulator. Considering both the experimental and simulation results, we are optimizing the design of the collimator system to be installed in the beam transport-line from the booster synchrotron to the storage ring.

(ii) Excitation of betatron oscillation of stored beam by beam injections: An off-axis beam injection is thus adopted as an injection scheme for the storage ring. The bump orbit for the injection is generated by four pulse bump magnets. The magnetic field pattern is a half-sine with a width of about 8 μs. As this bump orbit is not completely closed, the stored beam suffers error kicks while passing through the four bump magnets, and then the betatron oscillation is excited. We found that the oscillation excitation mainly occurred by two effects: (a) One is the effect of nonlinearlity due to sextupoles within the bump orbit. We are considering the correction of error kicks due to this effect by introducing compensation pulse magnets in the ring. (b) The other is caused by the existence of two types of bump magnet. These two have different eddy current patterns on the end plates of bump magnets, which change the shape of the field overshoot. We are now investigating cures for these oscillation excitations, and designing new magnets that have end plates made of insulating material to reduce eddy current effects.

New Optics

There exist several methods to reduce natural emittance. We attempted to reduce the emittance by breaking the achromatic condition imposed on Chasman-Green cells. This method is effective for the case where undulators with a moderate field are used as main insertion devices (IDs). The SPring-8 storage ring just meets this condition, and calculations show that an approximately 20% extra reduction is also obtained by closing all IDs gaps to the minimum, even after breaking the achromatic condition. In the summer shutdown, to realize the new optics we modified cabling of the quadrupoles in the dispersive arc to change the strengths of the quadrupoles while maintaining the phase matching condition over each long straight section. Since September 2002 we have been machine-tuning this new optics (Fig. 2) with the distributed dispersion. We plan to release this new optics to user operation from November 2002. The expected value of emittance is about 2.8 nm·rad with all ID gaps closed.

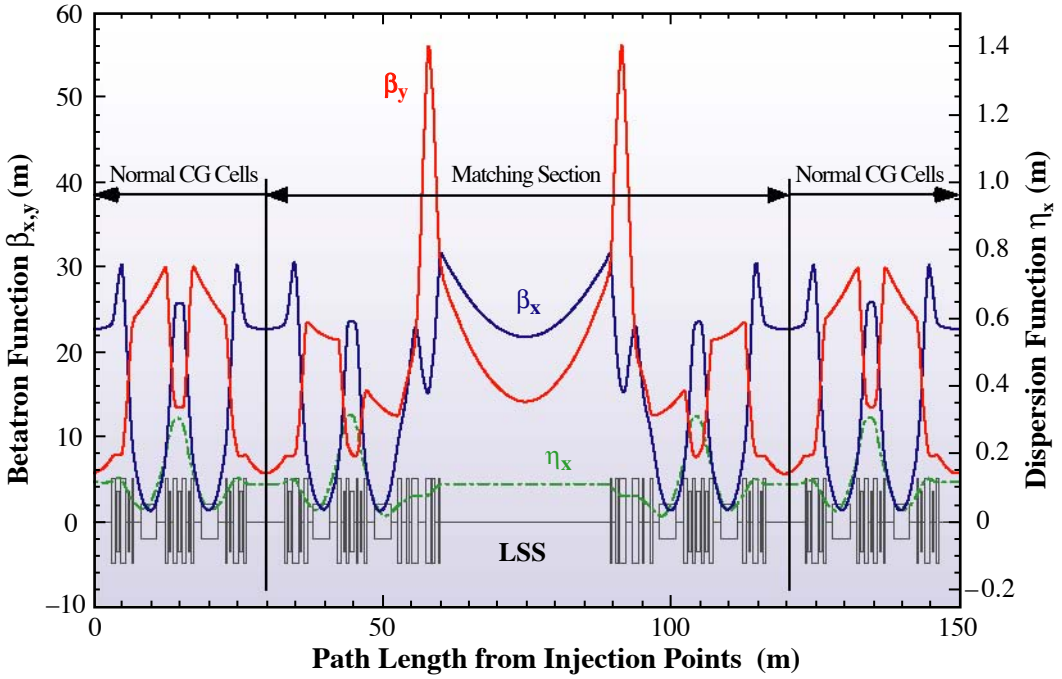

Fig. 2. Optical function for new optics.

Accelerator Diagnostics Beamlines

The accelerator diagnostics beamline #1 (BL38B2), which has a bending magnet light source, is in operation. The visible synchrotron light is used for longitudinal diagnostics of the stored electron beam, such as bunch length and single bunch impurity. Single-bunch impurity is measured by a gated photon counting method that utilizes fast pockels cells for switching light pulses. To improve the extinction ratio or isolation of the light shutter, the optical system was improved so that two pockels cells are arranged in tandem. For the main bunch, we have achieved a sensitivity to satellite bunches in the order of 10^{-10}.

A beam profile monitor based on a phase zone plate has been installed (Fig. 3). Synchrotron radiation from a dipole magnet source is imaged by a single-phase zone plate. The monochromatic X-ray is selected by a double crystal monochromator, which covers the energy range of 4 to 14 keV by Si (111) reflection, while an X-ray zooming tube observes the X-ray image of the electron beam. Results from preliminary experiments show that the observed profile of the beam is affected by a small deformation in the monochromator Si crystals, which was predicted from extensive measurements of the rocking curves of the monochromator. The experiments will resume after improvement in the crystal holders of the monochromator.

The accelerator diagnostics beamline #2 (BL05SS) has a straight section of the storage ring, where IDs for light sources can be installed. Synchrotron radiation from the edges of two bending magnets adjacent to the straight section can also be observed. In 2002, the components of the front end were designed and manufactured, and the design of radiation shielding hutches is in progress. Installation of the front end in the accelerator tunnel and the construction of the hutches will be completed in early 2003.

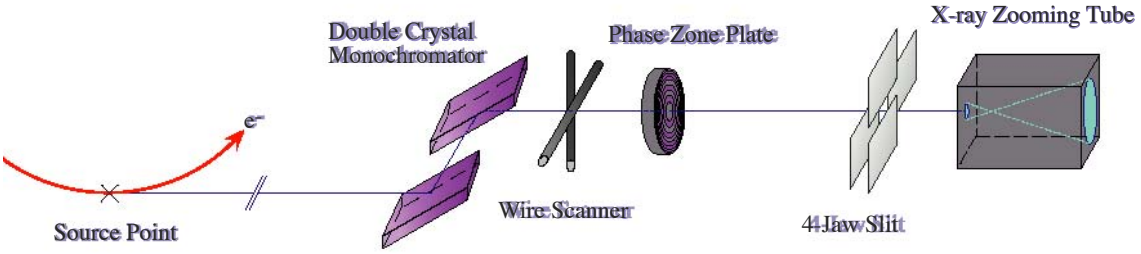

Fig. 3. Optical system of the X-ray imaging of the electron beam.

Bunch-by-bunch Feedback

A bunch-by-bunch feedback system for suppression of transverse beam instabilities is being developed for the storage ring and will be installed in the summer shutdown of 2003. Several instabilities are observed in SPring-8: a multi-bunch instability driven by vertical resistive-wall impedance of small gap in-vacuum undulators, horizontal multi-bunch instability driven by higher order mode impedance of RF cavities, of which horizontal betatron function is increased by one order of magnitude from its design value, and vertical and horizontal single-bunch mode-coupling instabilities driven by broad-band impedance of discontinuities of the beam-pipe wall of the vacuum chamber. Currently, those are suppressed by high chromaticity, 8 in the horizontal direction and 8 in the vertical direction. However, such high chromaticities reduce momentum acceptance of the ring and increases injected beam loss because of its longitudinal phase space mismatch. This beam loss is one of the most serious problems for the top-up operation.

The bunch-by-bunch feedback system uses at least four parallel modules, and each module is composed of two ADCs, one FPGA and two DACs, as shown in Fig. 4. Each module is driven by an 85-MHz clock which is one sixth of the SPring-8 RF acceleration frequency. FPGA is quite faster than DSPs and can handle two 9-tap FIR filter algorithms simultaneously with this frequency. Using this module, we successfully cured a head-tail single-bunch instability that was intentionally destabilized by setting chromaticity negative and obtaining damping time one-order of magnitude shorter than radiation damping.

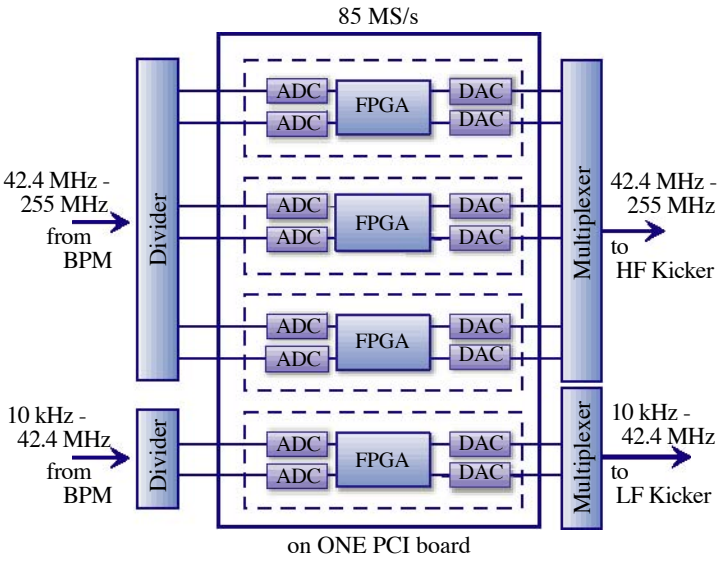

Fig. 4. Block diagram of a digital signal-processing unit with four modules on one PCI board.

Low Energy Operation

In general, the emittance of stored beam is proportional to the square of its energy, and can be reduced by lowering the beam energy. The bunch length is also reduced when we lower the energy. This reduction of emittance and bunch length will open up new opportunities for using brighter synchrotron radiation with shorter pulse lengths at SPring-8. For this aim, we ramped down the beam energy from a design value of 8 GeV and we performed beam injection at 4 GeV. In the ramping-down experiments, we first stored a low-current 5 mA beam in a multi-bunch mode then lowered the energy, step by step, to 4 GeV. At each step of beam energy we measured beam parameters, such as beam size, bunch length, synchrotron frequency, etc., and compared them with expected values obtained from a single-particle picture, as shown in Fig. 5. We found no significant difference between measured and expected values. Beam instabilities were not observed in the above-mentioned current nor in a filling mode. We then performed a beam injection at 4 GeV. To improve the efficiency of beam injection and hence increase the stored current, further studies are planned, such as optimization of the strength of harmonic sextupole magnets.

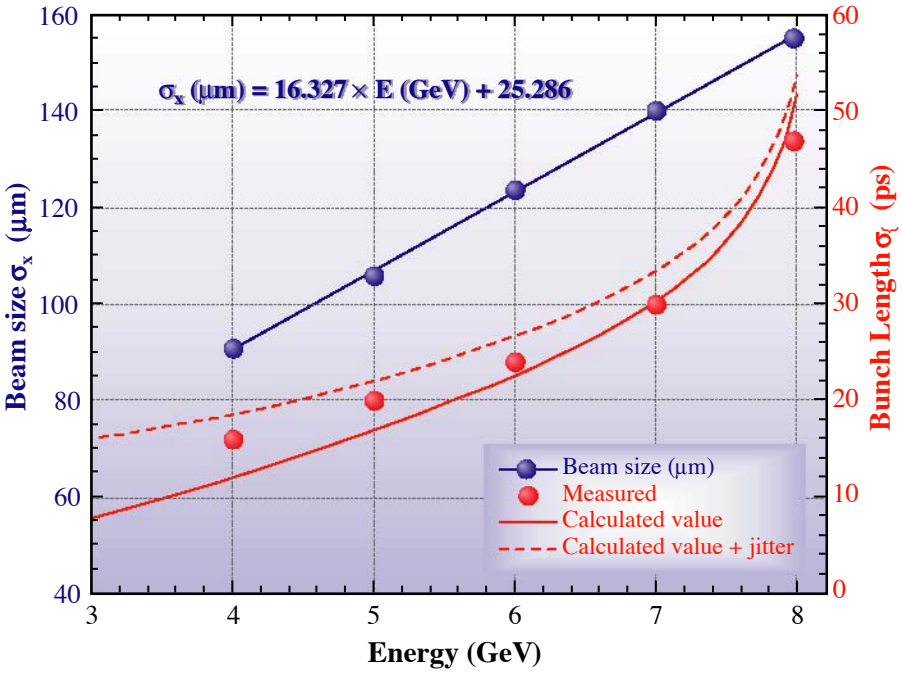

Fig. 5. Horizontal beam size and bunch length as a function of beam energy.

Developments and Upgrades of Linac

Accelerator Stabilization

A new method was invented to realize complete synchronization of the beam trigger and the linac RF, as described in the SPring-8 Research Frontiers 2000/2001. This system started to operate in 2001 and successfully reduced shot-by-shot fluctuation of the beam-energy center (Fig. 6).

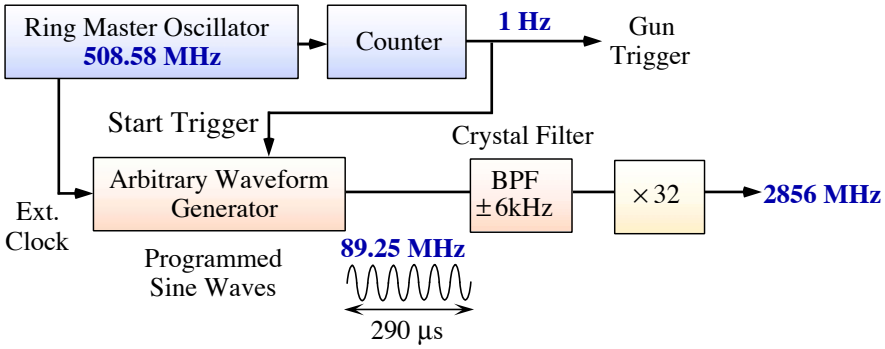

Fig. 6. Block diagram of synchronous RF reference generator.

Stability of a charged quantity of a beam bunch was examined as follows: An electron gun of the SPring-8 linac can generate a 250-ps beam. A buncher compresses almost all or a part of the 250-ps beam according to an RF phase where the beam is injected, then forms a single bunch. That is, beam timing defined in terms of the RF phase determines the beam charge. Figure 7 shows an example of beam current measurement in single-bunch acceleration. The current fluctuation observed when using the previous asynchronous system does not appear in the new synchronous system. Thus, this measurement clearly proves that the new 2856-MHz reference signal synchronizes with the beam trigger.

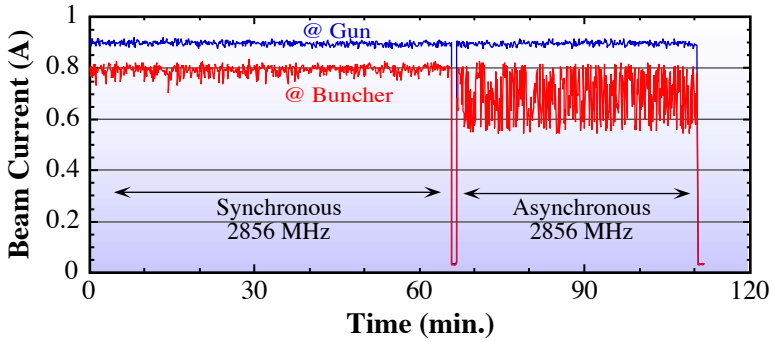

Fig. 7. Stability of single-bunched beam.

Reinforcement of Beam Monitor

A BPM system employing a strip-line type pickup and a logarithmic detection method has been developed and was installed in 2001. The system has a dynamic range wider than 45 dB and a maximum position resolution of a few tens of microns (2σ). A data acquisition system was required to process data of all the channels synchronizing with 60-Hz beam pulses to represent a one-pass beam orbit of the linac. Therefore, a shared-memory method was introduced for synchronized data acquisition by several VMEs, as shown in Fig. 8. The data acquisition system is almost completed and an automatic beam steering program has been made and is currently undergoing testing. The shared memory network will function soon.

To monitor the beam energy and energy distribution, a beam-penetration type thin foil screen monitor was introduced in the center of the ECS' chicane section where the energy dispersion is 1 m. The thin foil is a 12.5-μm thick Kapton film coated with 0.4-μm thick aluminum, and is strained on a frame. A CCD camera captures OTR (Optical Transition Radiation) emitted by beam irradiations on the screen. The captured beam images are analyzed to determine the beam energy and its spread. The 1-GeV beam has an absolute 90% emittance of 4×10^{-2} π mm•mrad and the screen increases it to 1.2×10^{-1} π mm•mrad. This emittance growth is negligible for injection into the booster synchrotron. Therefore, the screen is always inserted to monitor the beam energy during the beam injection.

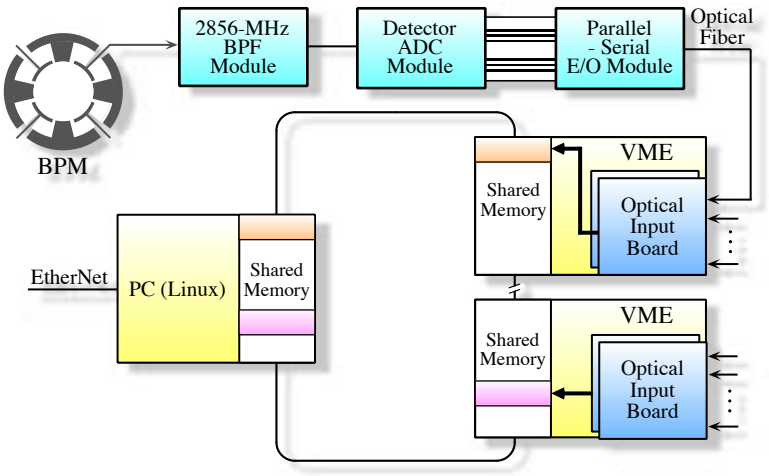

Fig. 8. Block diagram of BPM data acquisition system.

RF Gun Development

Since 1996 we have been developing a photocathode RF gun as a highly qualified electron beam source in a test facility at SPring-8. The quality of the laser beam irradiated on a cathode surface is essential for stabilizing the total system and generating a low-emittance electron beam. In particular, it needs higher pulse energy stability and improvements in the homogeneous spatial and temporal profiles of the UV-laser light source.

We shaped the laser spatial profiles with a microlens array. This microlens array is a collection of small hexagonal convex lenses with a pitch of 250 μm. The transmission of this optical array is about 80% in the ultraviolet region. It makes any shape of laser spatial profile possible, such as a Silk-hat (cylindrical flattop) with convex lens combinations, as shown in Fig. 9. The outskirts of quasi-flattop-shaped laser beam were cut through a pinhole with a diameter of 100 or 200 μm, stabilizing the energy and pointing stability of the UV-laser. This optical set-up made the experimental results reproducible. Consequently, it was possible to position the laser spot on the cathode surface accurately on an optimum beam axis, where the center axis of an RF gun cavity and the magnetic center axis of a beam focussing Helmholtz coils were aligned. As a result, we could obtain the minimum emittance value of 2π mm•mrad with a beam energy of 3.1 MeV, holding its charge to 0.1 nC/bunch.

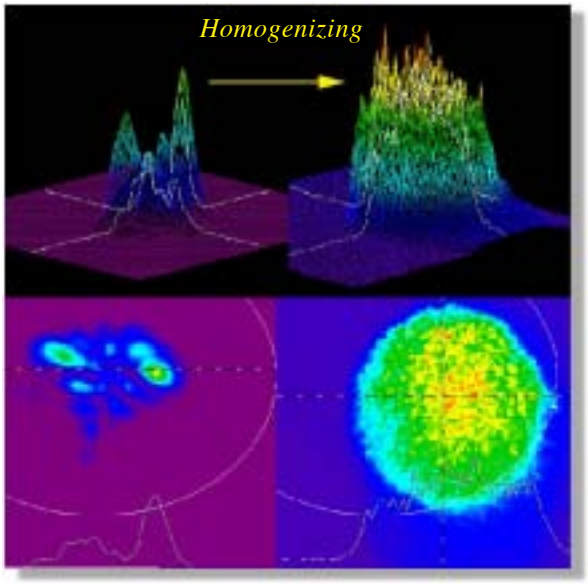

Fig. 9. Improvement of the laser spatial profile by a microlens array.

Haruo Ohkuma, Hirofumi Hanaki and Noritaka Kumagai
SPring-8 /JASRI

Facility Status

Machine Operation

Figure 1 presents the operational statistics since the operation start in October, 1997. In 2002, the SPring-8 storage ring was operated on four- or five-week period for one operation cycle. The total operation time of the accelerator complex was 5542.9 hours. Of those hours, 70.3% (3896.7 hours) were available to the users. The injection time and the down time due to failure accounted for 1.1% (60.8 hours) and 3.4% (190.5 hours) of the operation time, respectively; a great loss of user time was due to one major failure in June 2002. A cooling water leak to a vacuum vessel of the in-vacuum undulator occurred, after which the in-vacuum undulator was removed from the storage ring and replaced by a dummy vacuum chamber. As a result, 134.5 hours of user time was cancelled for the failure and replacement. The remaining 25.2% (1394.9) was dedicated to: (i) the machine and beamline study, (ii) the machine and beamline tuning, and (iii) the commissioning of new photon beamlines.

The operation modes of three different filling patterns were delivered to the user time; 35.0% in the multi-bunch mode, 47.2% in the several bunch mode such as 203-bunch mode (203 equally spaced bunches) and 84 equally spaced 4-bunch trains, and the remaining 17.8% in the hybrid filling mode such as a 2/21-partially filled multi-bunch with 18-isolated bunches. For the hybrid filling mode, 1 or 1.5 mA is stored in each isolated bunch. An isolated bunch purity of better than 10^{-10} is routinely being delivered.

Table I presents a summary of the useful beam parameters of the storage ring.

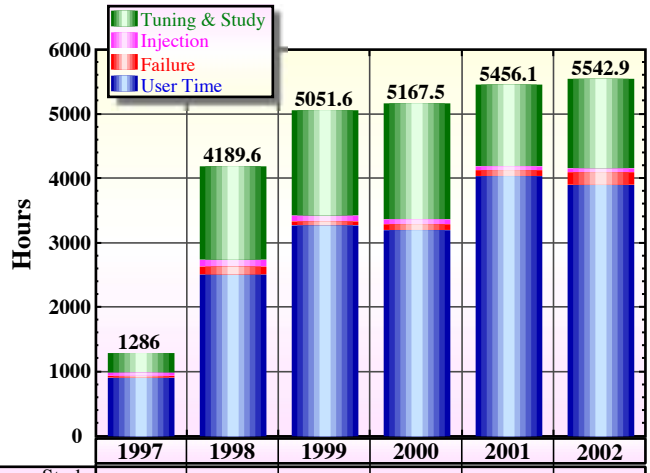

	1997	1998	1999	2000	2001	2002
Tuning & Study (Accel. & BL)	304	1457.6	1624.2	1815	1276.6	1394.9
Injection	50	110	95.2	70.4	59.3	60.8
Failure	26	110	57.2	88.7	87.1	190.5
User Time	906	2512	3275	3193.4	4033.2	3896.7

Fig. 1. Operational statistics since the facility was opened to users.

Table I. Beam parameters of SPring-8 storage ring.

Tunes (ν_x / ν_y)	40.15 / 18.35
Current[mA]: single bunch	10
multi bunch	100 (120 *1)
Bunch length (FWHM) [psec]	34
Horizontal emittance [nm•rad]	3.1 *2
Vertical emittance [pm•rad]	8.7 *3 / 3.9 *4
Coupling [%]	0.28 *3 / 0.13 *4
Beam size[μm]: (σ_x / σ_y) *5	
Long ID section	283 / 11.4
ID section	289 / 7.2
BM section	103 / 15.2
Beam Divergence[μrad]: ($\sigma_{x'}$ / $\sigma_{y'}$) *5	
Long ID section	11.9 / 0.81
ID section	11.7 / 1.3
BM section	53.8 / 0.68
Lifetime[hr]: 100 mA (multi bunch)	~ 97
1 mA (single bunch)	~ 9
Dispersion distortion[mm]:horizontal (rms)	9.3
vertical (rms)	1.1 *6
Orbit stability (tune harmonics)[μm]:	
horizontal (rms)	1.3
vertical (rms)	0.35

*1 Maximum stored beam current at machine study.
Measured by a pulse bump and scraper*2, two dimensional interferometer*3, and two photon correlation*4.
*5 Assuming that 0.2% coupling.
*6 With correction by 24 skew Q's.

BEAMLINES

The beamlines at the SPring-8 Facility are categorized into four groups as listed below:

(1) Public Beamlines,
(2) Contract Beamlines,
(3) JAERI / RIKEN Beamlines,
(4) Accelerator Beam Diagnosis Beamlines.

The public beamlines are constructed with the support of the national budget, and are open for public use. This category of public beamlines includes the R&D beamlines, which were constructed for the purpose of developing new devices and beamline equipment such as optical elements, detection systems, and so forth. Used mainly by SPring-8 staff, the R&D beamlines are also open to public. Now 25 public beamlines are operational and available for public use.

The contract beamlines are, on the other hand, facilities that are installed, owned, operated and maintained by universities, companies and other organizations. Beamline contractors can use their beamline almost exclusively. Hyogo Prefecture took the lead in the contract beamline construction. The Industrial Consortium, Institute for Protein Research (Osaka Univ.), the Research Center for Nuclear Physics (RCNP, Osaka Univ.) and National Institute for Materials Science followed in that

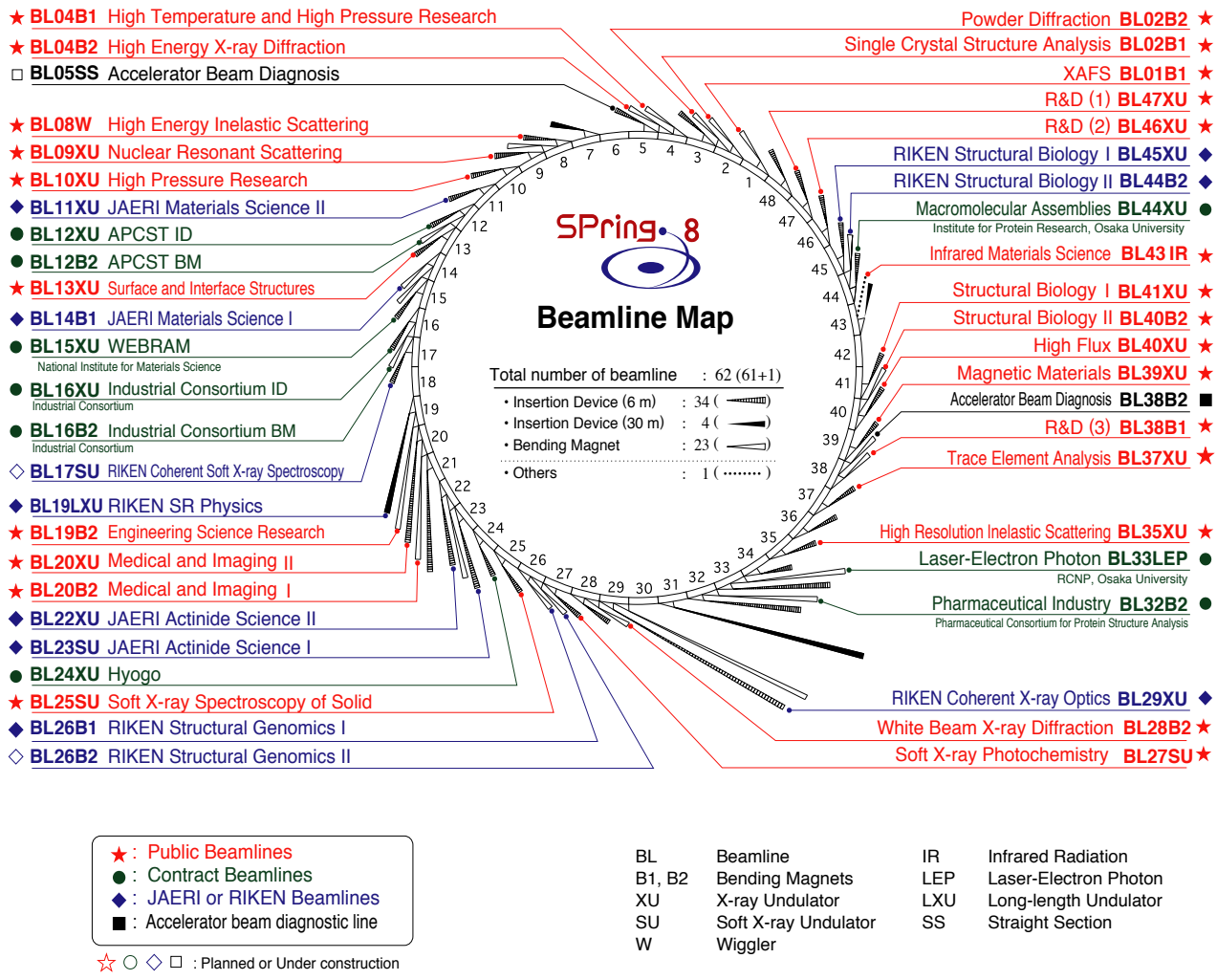

Fig. 2. Beamline Map.

order, after which the first foreign contract beamlines (BL12B2 and BL12XU) were constructed by the Asia and Pacific Council for Science and Technology of Taiwan (APCST). BL32B2, constructed by the industrial consortium that is made up of 22 pharmaceutical companies, recently joined SPring-8 contract beamlines and became operational in May 2002. Currently those nine contract beamlines are all in operation.

The JAERI/RIKEN beamlines are those constructed by JAERI and RIKEN to promote their own research activities. Nine JAERI/RIKEN beamlines have already been constructed and other two are in commissioning or under construction by RIKEN for the exclusive use of RIKEN scientists, although 20% of beam time is reserved for public use. Experimental stations of BL22XU and BL23SU are located at RI Laboratory and dedicated to research utilizing radioactive isotopes and actinide materials. BL26B1 and BL26B2 are beamlines that will be used for high throughput protein crystallography following the human genome project. BL29XU has two experimental stations, one located at the experimental hall, and the other at the end of the 1 km. Dedicated to studying the characteristics of the electron beam accumulated in the storage ring, the accelerator beam diagnosis beamlines are currently under the exclusive use of the JASRI accelerator group. As of May 7, 2003, one beamline is currently in the phase of commissioning (BL26B2) and two beamlines (BL17SU, BL05SS) are under construction.

All beamlines are shown in the Beamline Map (Fig. 2). Including the two accelerator beam diagnosis beamlines, we have beamlines, *i.e.*, about 75% of 62 beamlines that SPring-8 can accommodate.

Public Beamlines (25)

BL #	Source	Beamline Name	Status
BL01B1	BM	XAFS	in operation
BL02B1	BM	Single Crystal Structure Analysis	in operation
BL02B2	BM	Powder Diffraction	in operation
BL04B1	BM	High Temperature and High Pressure Research	in operation
BL04B2	BM	High Energy X-ray Diffraction	in operation
BL08W	W	High Energy Inelastic Scattering	in operation
BL09XU	U	Nuclear Resonant Scattering	in operation
BL10XU	U	High Pressure Research	in operation
BL13XU	U	Surface and Interface Structures	in operation
BL19B2	BM	Engineering Science Research	in operation
BL20XU	U	Medical and Imaging II	in operation
BL20B2	BM	Medical and Imaging I	in operation
BL25SU	U	Soft X-ray Spectroscopy of Solid	in operation
BL27SU	U	Soft X-ray Photochemistry	in operation
BL28B2	BM	White Beam X-ray Diffraction	in operation
BL35XU	U	High Resolution Inelastic Scattering	in operation
BL37XU	U	Trace Element Analysis	in operation
BL38B1	BM	R&D (3)	in operation
BL39XU	U	Magnetic Materials	in operation
BL40XU	U	High Flux	in operation
BL40B2	BM	Structural Biology II	in operation
BL41XU	U	Structural Biology I	in operation
BL43IR	BM	Infrared Materials Science	in operation
BL46XU	U	R&D (2)	in operation
BL47XU	U	R&D (1)	in operation

Contract Beamlines (9)

BL #	Source	Beamline Name	Status
BL12XU	U	APCST ID (APCST)	in operation
BL12B2	BM	APCST BM (APCST)	in operation
BL15XU	U	WEBRAM (National Institute for Materials Science)	in operation
BL16XU	U	Industrial Consortium ID (Industrial Consortium)	in operation
BL16B2	BM	Industrial Consortium BM (Industrial Consortium)	in operation
BL24XU	U	Hyogo (Hyogo Prefecture)	in operation
BL32B2	BM	Pharmaceutical Industry (Pharmaceutical Consortium)	in operation
BL33LEP	BM	Laser-Electron Photon (Osaka University)	in operation
BL44XU	U	Macromolecular Assemblies (Osaka University)	in operation

JAERI/RIKEN Beamlines (11)

BL #	Source	Beamline Name	Status
BL11XU	U	JAERI Materials Science II (JAERI)	in operation
BL14B1	BM	JAERI Materials Science I (JAERI)	in operation
BL22XU	U	JAERI Actinide Science II (JAERI)	in operation
BL23SU	U	JAERI Actinide Science I (JAERI)	in operation
BL17SU	U	RIKEN Coherent Soft X-ray Spectroscopy (RIKEN)	under construction
BL19LXU	U	RIKEN SR Physics (RIKEN)	in operation
BL26B1	BM	RIKEN Structural Genomics I (RIKEN)	in operation
BL26B2	BM	RIKEN Structural Genomics II (RIKEN)	in commissioning
BL29XU	U	RIKEN Coherent X-ray Optics (RIKEN)	in operation
BL44B2	BM	RIKEN Structural Biology II (RIKEN)	in operation
BL45XU	U	RIKEN Structural Biology I (RIKEN)	in operation

Accelerator Beam Diagnosis Beamline (2)

BL #	Source	Beamline Name	Status
BL05SS		Accelerator Beam Diagnosis	under construction
BL38B2	BM	Accelerator Beam Diagnosis	in operation

Table II. SPring-8 beamlines.

User Operation

In principle, SPring-8 invites proposal applications twice a year. Beam time is then allocated to selected applicants for the forthcoming SPring-8 research term. The first such term (1997B) ran from October 1997 (when the facility opened) until the end of Japan's financial year, March 1998. The second research term (1998A) ran from April 1998 until October 1998. After a somewhat longer third research term (1999A) from November 1998 until June 1999, SPring-8 roughly divided the year's user beam time into two terms with the summer shutdown in between. The proposal submission deadlines for the eighth and ninth research terms (2001B and 2002A) were May 26, 2001 and October 27, 2002, respectively. SPring-8 Proposal Review Committee approved 457 out of the 619 proposals submitted for 2001B and 520 out of 643 for 2002A. The numbers of selected proposals for proprietary research were 14 in 2001B, and 19 in 2002A, respectively. And the percentage of selected proposals from overseas was 2% for 2001B and 5% for 2002A. SPring-8 operational results for the period from 1997B to 2002A are shown in Table III. This table shows each user beam time allocated and the number of users and experiments conducted, which are illustrated in Fig. 3. For reference, the relevant data of contract beamlines is also indicated. In 2002A, SPring-8 provided users with 2,093 hours of beam time in five operation cycles and 3,246 individuals used the facility's public beamlines in 543 separate experiments. Between October 1997, opening of SPring-8 for research, and the end of 2002A, a total of 24,494 public and contract beamline users conducted 3,723 experiments.

Figures 4 and 5 indicate the numbers of selected proposals by the affiliation of applicants and by the research fields from 1997B to 2002A. As can be seen from the charts, the trend for each year has been almost the same during the period. In other words, as for the classification by the affiliations, universities have accounted for approximately 70% and other organizations have made up the rest almost equally. The same trend applies to the classification by the research fields. The ratio of Life Science, Diffraction & Scattering and others has been 1:1:1 throughout the same period. The ratio of XAFS, Spectroscopy and Method & Instrumentation, all of which are categorized as "others," has also been 1:1:1. The ratio remained the same since the inauguration of SPring-8 except for the first research term.

Research Term	User Time (hours)	Public BL		Contract BL	
		Experiments	Users	Experiments	Users
1997B: 1997.10 - 1998.03	1,286	94	681		
1998A: 1998.04 - 1998.10	1,702	234	1,252	7	
1999A: 1998.11 - 1999.06	2,585	274	1,542	33	467
1999B: 1999.09 - 1999.12	1,371	242	1,631	65	427
2000A: 2000.01 - 2000.06	2,106	365	2,486	102	794
2000B: 2000.10 - 2001.01	1,558	382	2,370	88	620
2001A: 2001.02 - 2001.06	2,381	473	2,915	103	766
2001B: 2001.10 - 2002.01	1,893	486	3,277	118	977
2002A: 2002.02 - 2002.06	2,093	543	3,246	114	1,043
TOTAL	16,975	3,093	19,400	630	5,094

Table III. SPring-8 operational results.

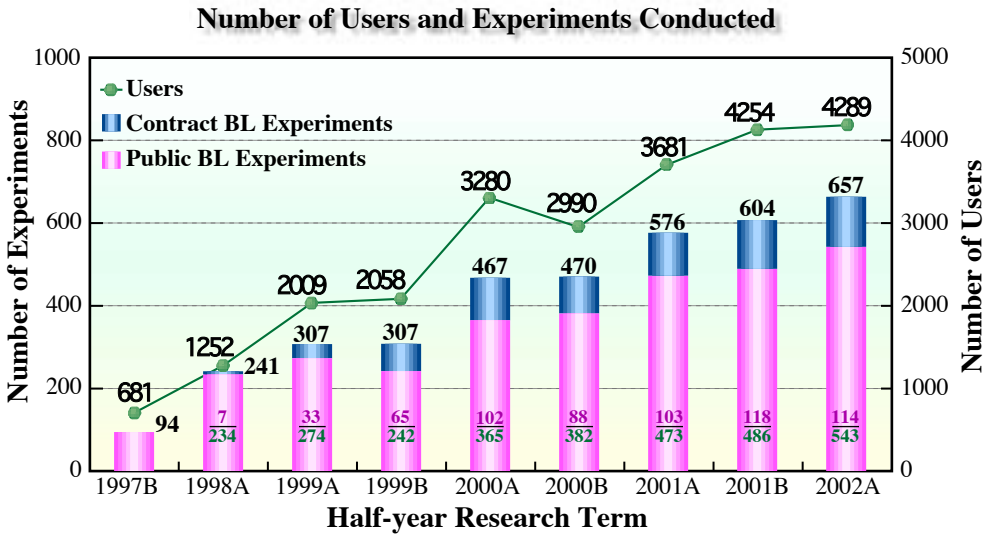

Figure 3

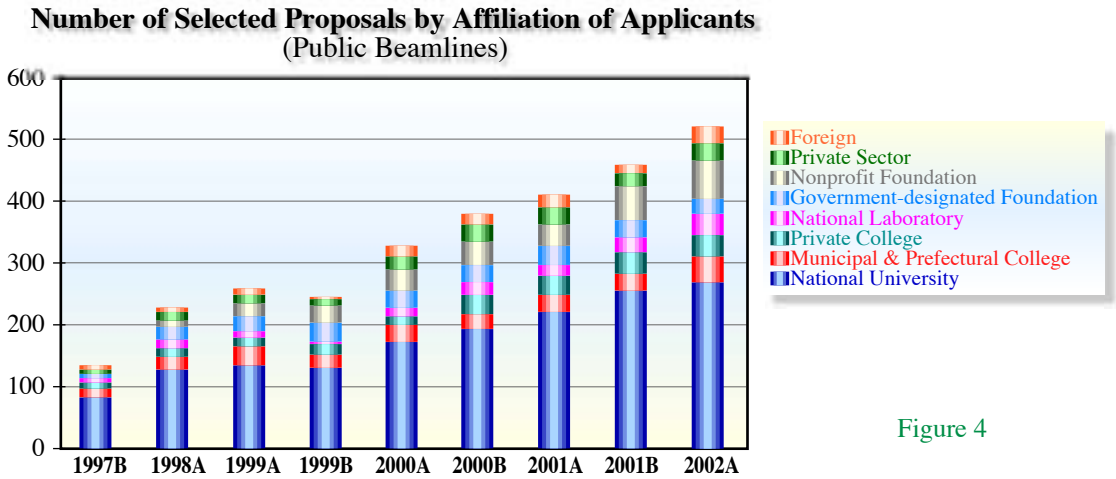

Figure 4

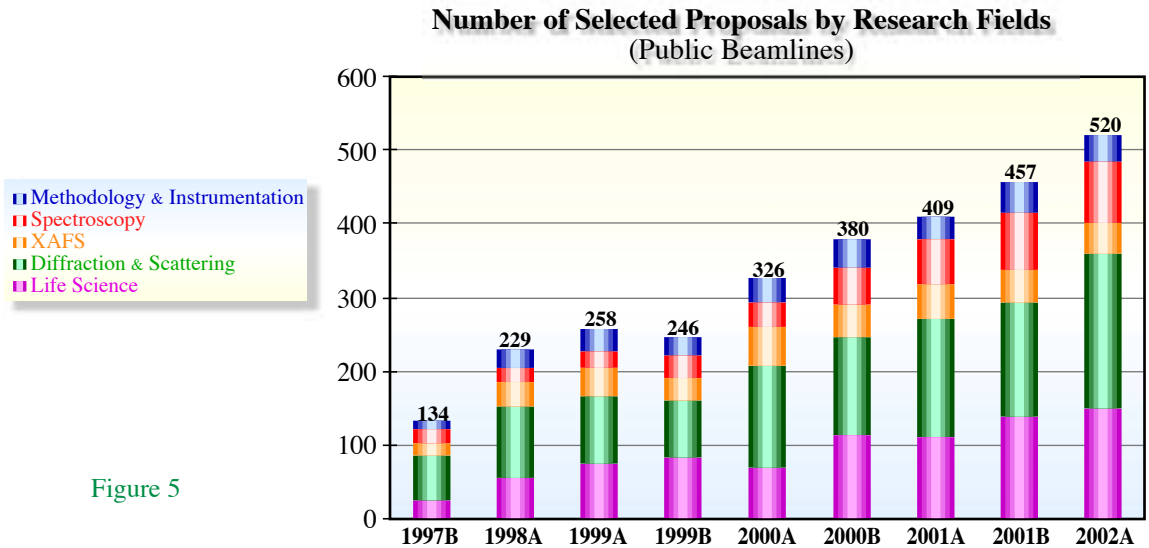

Figure 5

Proprietary Research

For proprietary research, users can keep their results by paying beam time fees. This system is useful when there is some confidential information for commercial purposes in experiments and samples and the users do not want to disclose the results. During the period from 1999B, when the system was introduced, to 2002A, 69 experiments have been carried out as proprietary research at both public and contract beamlines.

Long-term Use of Beamlines

Apart from the regular public use, SPring-8 has created a system for the long-term use of beamlines where users can secure beam time for a longer period of time. While the regular beam time is valid for six months, the beam time for long-term use is valid for up to three years. This system aims to further promote research that will produce outstanding results in the field of science and technology, that will pave the way for new research areas and research methodology and that will help improve the technology for industrial base significantly by getting the most of the characteristics of SPring-8.

Industrial Research

Together with the promotion of research activities in the field of basic science, the contribution to the reinforcement of the technological basis in industry has been one of the major aims of the SPring-8 project. Since its foundation in 1990, JASRI has sought possible ways of industrial applications of SR science.

The framework of the contract beamlines also facilitates the construction of beamlines by industries at SPring-8. Hyogo Prefecture constructed a contract beamline (BL24XU), and has been conducting experiments on protein crystal analysis, surface/interface analysis of inorganic materials, X-ray microbeam analysis, and X-ray imaging since May 1998. There have been two beamlines (BL16XU and BL16B2) constructed by the industrial consortium that is composed of thirteen companies in the fields of electronics, steel, electric power and automobiles. Since October 1999, the consortium has been carrying out its experiments on X-ray diffraction, X-ray fluorescence analysis, and X-ray microbeam experiments at the BL16XU, and XAFS and X-ray topography at the BL16B2. Another contract beamline, BL32B2, constructed by the industrial consortium that is made up of 22 pharmaceutical companies became operational in May 2002 and is expected to contribute to research on protein structure analysis for drug design. In addition, a new beamline for the industrial applications of SR science has been added to the lineup of public beamlines, which is a bending magnet beamline (BL19B2) for XAFS experiments, multipurpose X-ray diffractometry, and X-ray fluorescence spectroscopy. The BL19B2 is also in operation.

Research Results

When using SPring-8 for non-proprietary research, users are exempted from beam time fees if they submit an Experiment Report within 60 days after their experiment. JASRI has been earnestly calling on users to disclose their research results obtained through non-proprietary research in scientific journals. In cases where the results are disclosed, uses must report to JASRI and have them registered with JASRI.

The number of refereed publications produced at all beamlines is 1,043 (public BLs: 660, contract BLs: 73, JAERI & RIKEN: 163, others: 147) as of September 30, 2002.

Budget and Manpower

The SPring-8 consists of accelerators, beamlines and facilities for users, which were constructed by the JAERI-RIKEN Project Team during the period from 1991 through 1997 at the total cost of about 110 billion yen. In 1994, JASRI was designated by the "Law regarding Promotion of Common Use of the Synchrotron Radiation Facility (SPring-8)" as the Organization for the Promotion of Synchrotron Radiation Research to be responsible for managing the SPring-8. As a result, the SPring-8 research complex has been formed by JAERI, RIKEN and JASRI, and JASRI has been entrusted by JAERI and RIKEN with the operation, maintenance, improvement, upgrading, R&D and safety management of the SPring-8 as well as the technical support for the new beamline construction since the construction of main facilities and buildings at the SPring-8 was completed and the public use started in 1997.

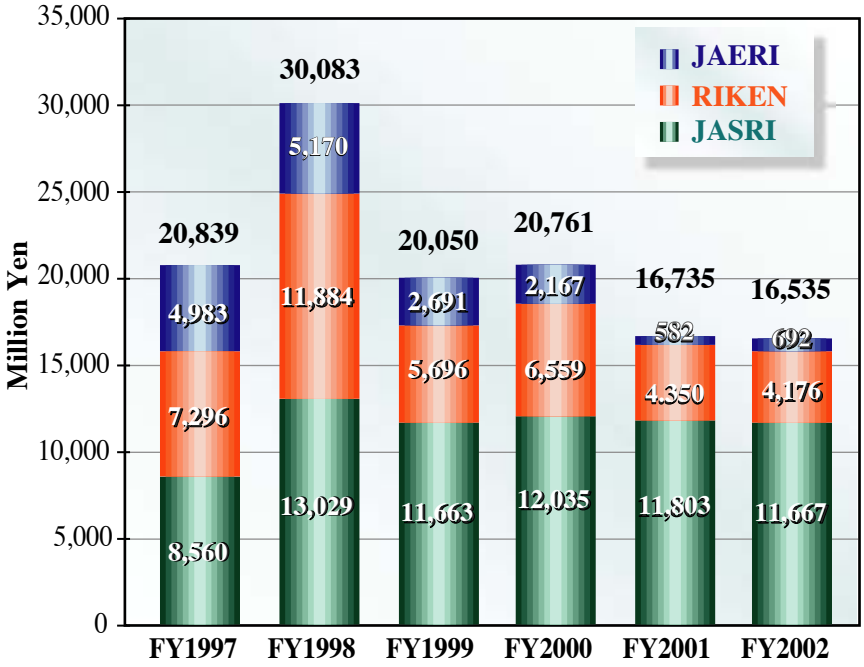

Figure 6

About 95 % of the total budget comes from the Government through JAERI and RIKEN to be appropriated for the above-mentioned missions of JASRI and the remaining 5% comes directly from the Government in the form of a grant. Figure 6 illustrates the budget at SPring-8 and it shows that the total budget for JASRI for FY2002 was 11,667 million yen and the total budgets for JAERI and RIKEN were 692 million yen and 4,176 million yen, respectively. As can be seen from the figure, the budgets for JAERI and RIKEN have been diminishing since FY2001. It is because the major unfinished construction such as utility facilities and beamlines was completed in FY2000.

When the Project Team was organized

Manpower at SPring-8
JASRI, JAERI, RIKEN

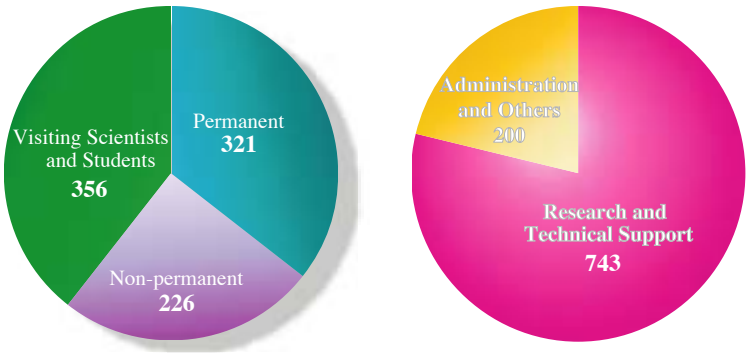

FY2002

	by Type			by Field		Total
	Permanent	Non-permanent	Visiting Scientists and Students	Research and Technical Support	Administration and Others	
JASRI	221	153	124	342	156	**498**
JAERI	42	26	7	67	8	**75**
RIKEN	58	87	225	334	36	**370**
	321	**226**	**356**	**743**	**200**	**943**

Figure 7

in October 1988, the total number of staff was 66 and the number increased to 220 by April 1, 1995. Then a certain number of the staff started to be transferred from the team to JASRI in preparation for the entrusted missions of the SPring-8. By the time the Project Team was dissolved in 1997, most of the staff had been transferred to JASRI. In FY2002, the total number of JASRI staff was 498. The total number of SPring-8 staff amounted to 943 when the number of staff at JAERI Kansai Research Establishment and RIKEN Harima Institute is combined with the number of JASRI staff. The numbers of staff by the types and fields of employment are illustrated in Fig. 7.

Organization and Committees

SPring-8 Research Complex

As mentioned earlier in the "Budget and Manpower," the SPring-8 research complex (see Fig. 8) is composed of JAERI Kansai Research Establishment, RIKEN Harima Institute and JASRI (see Fig. 9 - 11), all of which are on site. While JAERI and RIKEN conduct their own research at SPring-8, JASRI is entrusted by the two with the operation, maintenance, improvement, upgrading, R&D and safety management of the SPring-8.

The organization that JASRI has formed to accomplish those missions is shown in Fig. 9. As can be seen from the organization chart, JASRI consists of the Synchrotron Radiation Research Laboratory, the Administration Sector and the SPring-8 Safety Office.

Figure 8

Synchrotron Radiation Research Laboratory

The Synchrotron Radiation Research Laboratory is divided into five divisions, which are the Accelerator-, Beamline-, Materials Science-, Life and Environmental Science-, and Facilities & Utilities Divisions. The laboratory is responsible for operating, maintaining, and upgrading the accelerator complex and beamlines as well as for carrying out related research activities. It is also responsible for expediting scientific utilization of the facility, supporting the users methodologically and technologically, establishing a database of scientific and technical information, and keeping the SR community informed about the usage of the beamlines.

Administration Sector

The Administration Sector is made up of five divisions, which are the General Affairs-, Finance-, Planning-, User Administration- and Public Relations Divisions. The sector is responsible for the planning and coordination of research-related projects of JASRI, financial affairs, overall management, documentation, personnel supervision, welfare programs for JASRI staff, provision of information to the public, beamline management, user support and services and library information management.

in October 1988, the total number of staff was 66 and the number increased to 220 by April 1, 1995. Then a certain number of the staff started to be transferred from the team to JASRI in preparation for the entrusted missions of the SPring-8. By the time the Project Team was dissolved in 1997, most of the staff had been transferred to JASRI. In FY2002, the total number of JASRI staff was 498. The total number of SPring-8 staff amounted to 943 when the number of staff at JAERI Kansai Research Establishment and RIKEN Harima Institute is combined with the number of JASRI staff. The numbers of staff by the types and fields of employment are illustrated in Fig. 7.

Organization and Committees

SPring-8 Research Complex

As mentioned earlier in the "Budget and Manpower," the SPring-8 research complex (see Fig. 8) is composed of JAERI Kansai Research Establishment, RIKEN Harima Institute and JASRI (see Fig. 9 - 11), all of which are on site. While JAERI and RIKEN conduct their own research at SPring-8, JASRI is entrusted by the two with the operation, maintenance, improvement, upgrading, R&D and safety management of the SPring-8.

The organization that JASRI has formed to accomplish those missions is shown in Fig. 9. As can be seen from the organization chart, JASRI consists of the Synchrotron Radiation Research Laboratory, the Administration Sector and the SPring-8 Safety Office.

Figure 8

Synchrotron Radiation Research Laboratory

The Synchrotron Radiation Research Laboratory is divided into five divisions, which are the Accelerator-, Beamline-, Materials Science-, Life and Environmental Science-, and Facilities & Utilities Divisions. The laboratory is responsible for operating, maintaining, and upgrading the accelerator complex and beamlines as well as for carrying out related research activities. It is also responsible for expediting scientific utilization of the facility, supporting the users methodologically and technologically, establishing a database of scientific and technical information, and keeping the SR community informed about the usage of the beamlines.

Administration Sector

The Administration Sector is made up of five divisions, which are the General Affairs-, Finance-, Planning-, User Administration- and Public Relations Divisions. The sector is responsible for the planning and coordination of research-related projects of JASRI, financial affairs, overall management, documentation, personnel supervision, welfare programs for JASRI staff, provision of information to the public, beamline management, user support and services and library information management.

Safety Office

The Safety Office is independent from both the Synchrotron Radiation Research Laboratory and the Administration Sector. It regulates overall safety site-wide such as radiation safety, handling of chemical wastes and biohazards, and environmental preservation.

SPring-8 Advisory Committee

The SPring-8 Advisory Committee was established on the basis of the "Law regarding Promotion of Common Use of the Synchrotron Radiation Facility (SPring-8)." The committee meets at least twice a year at the request of JASRI to deliberate and makes recommendations on policy making and other important matters such as the acceptance of applications for beam time and subsequent selection of proposals to conduct experiments at the public beamlines. For the purposes, the Proposal Review Committee and the Contract Beamline Committee are sub-structured under this committee.

Proposal Review Committee

The Proposal Review Committee (PRC) was formed to report to the advisory committee on the review policy, procedures and review results. The PRC has six subcommittees to evaluate proposals in the following disciplines;

(i) Life Science,
(ii) Diffraction & Scattering,
(iii) XAFS,
(iv) Spectroscopy,
(v) Method & Instrumentation, and
(vi) Industrial Use.

In addition to the six subcommittees, a special subcommittee for long-term use was set up and the first special subcommittee was held in April 2000. The members of the PRC are mostly scientists outside the SPring-8 Facility, but one scientist from JASRI must participate in each subcommittee.

Contract Beamline Committee

This committee deliberates upon the construction of contract beamlines. It first reviews letters of intent submitted by organizations planning to construct their own beamlines and subsequently evaluates formal proposals that are submitted after the approval of letters of intent. Finally the committee reports the results of their evaluations to the SPring-8 Advisory Committee. To date, it has accepted letters of intent from nine organizations to construct eleven contract beamlines in total, and has approved seven proposals so far.

SPring-8 Three Party Steering Coordination Committee

JAERI, RIKEN and JASRI discuss important matters regarding the effective and efficient management of SPring-8 in this committee.

Beamline Advisory Committee

The committee is responsible for evaluating the proposals submitted for public beamline construction. The committee first reviews the letters of intent submitted, and will deliberate the proposals on the basis of scientific feasibility and impact on the corresponding field of science. It reports the review results to the JAERI-RIKEN-JASRI Steering Coordination Committee.

Committee of R&D on Advanced Technology and Applications

This committee promotes and enhances the in-house research program known as the R&D Project on Advanced Technology and Applications, which are to be carried out in collaboration among JAERI, RIKEN and JASRI.

R&D Beamline Program Committee

At the R&D beamlines, 30% of the beam time is reserved for public use and the remaining 70% is allocated to JAERI, RIKEN and JASRI. The R&D Beamline Program Committee was established to coordinate the management of R&D beamlines.

SPring-8 Organization

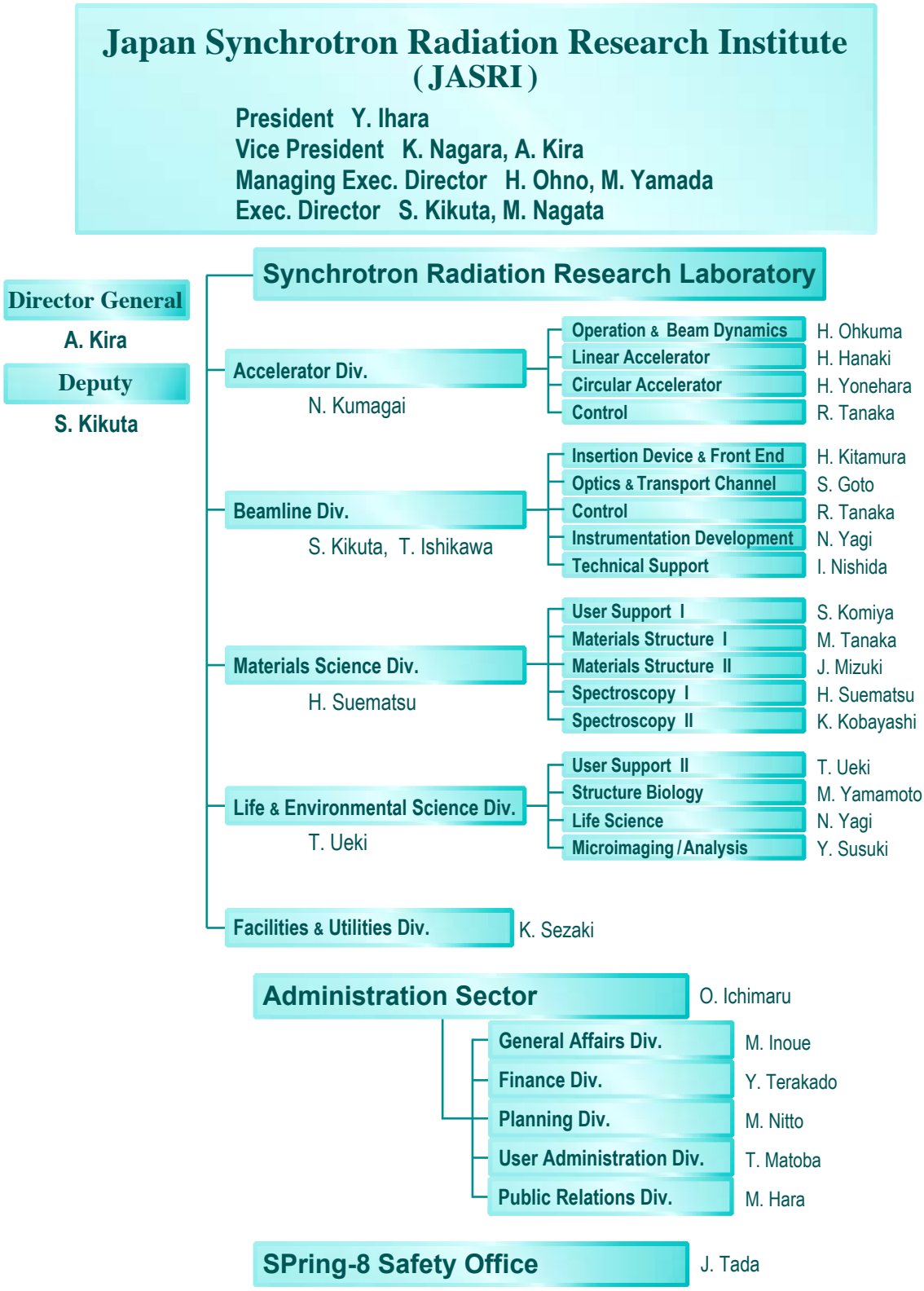

Figure 9

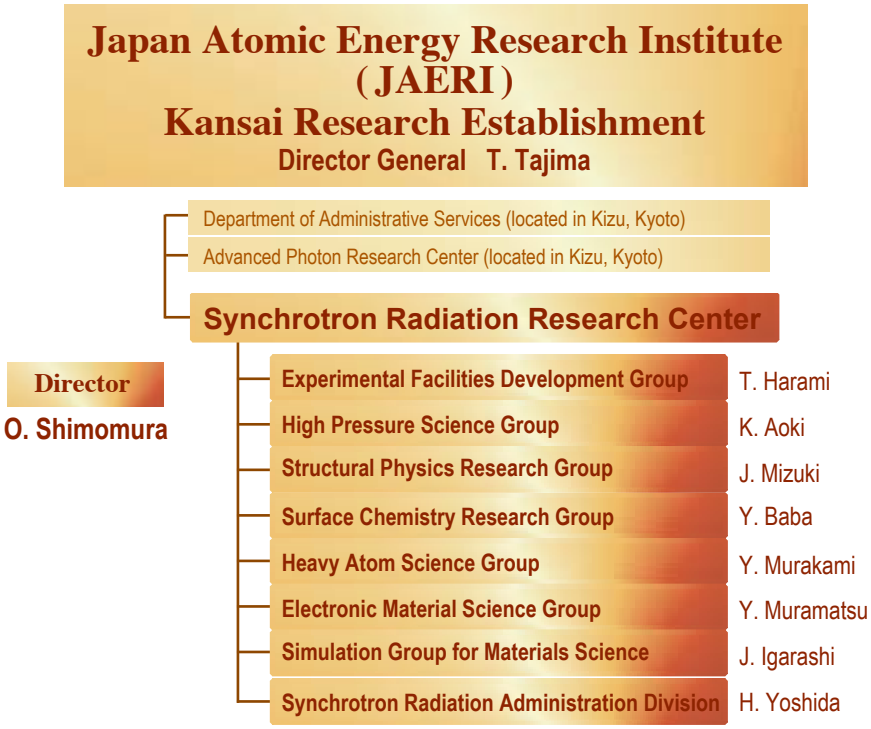

Figure 10

Figure 11

Editor
Seishi Kikuta
SPring-8 / JASRI

Editing & Layout
Marcia M. Obuti-Daté
SPring-8 / JASRI

Printing
Ono Printing Co., Ltd.

J A S R I
Users Administration Division

Kouto 1-1-1, Mikazuki, Sayo
Hyogo 679-5198, JAPAN
Tel. +81-(0) 791 58-2797 FAX: +81-(0) 791 58-2798

frontiers@spring8.or.jp
http://www.spring8.or.jp/

SPring-8/ JASRI

SPring-8

Japan Synchrotron Radiation Research Institute

Kouto 1-1-1, Mikazuki, Sayo
Hyogo 679-5198
JAPAN